On the development and investigation of the high-temperature oxidation behavior of Co-Re-base alloys

LIN WANG

UNIVERSITÄT SIEGEN

Lin Wang

On the development and investigation of the high-temperature oxidation behavior of Co-Re-base alloys

On the development and investigation

of the high-temperature oxidation behavior of

Co-Re-base alloys

genehmigte

Dissertation

zur Erlangung des Grades eines Doktors

der Ingenieurwissenschaften

vorgelegt von

M. Sc. Lin Wang

eingereicht bei der

Naturwissenschaftlich-Technischen Fakultät

der Universität Siegen

Siegen 2021

Referent: Prof. Dr.-Ing. habil. Hans-Jürgen Christ

Korreferent: Prof. Dr.-Ing. habil. Bronislava Gorr

Tag der mündlichen Prüfung: 20.12.2021

Acknowledgments

This dissertation presents the results of my activities as a research assistant and doctoral candidate at the Chair of Materials Science and Testing (Lehrstuhl für Materialkunde und Werkstoffprüfung) at the University of Siegen from 2010 to 2014. Many people helped me along the way on this journey. I would like to take this opportunity to thank them.

I would also like to thank my friends who always supported and believed in me. My special thanks go to Dr. Hao Zhuang and Dr. Qiumei Jiang for the priceless encouragement during the writing phase that helped me through the dark times.

At last but not least, I would like to thank my wife, Caiya Yu. Without her understanding, support, patience, and love, I could never have completed this work. I would also like to thank my family, especially my parents, my parents-in-law, and my son, Zimo, for always being on my side and for the lovely support in many ways.

Baunatal, May 2021   Lin Wang

Contents

Kurzfassung

Als alternative potenzielle Materialklasse, der so genannten „Beyond Ni-base Superalloys", wurden Co-Re-Basislegierungen zuerst von Rösler von der Technischen Universität Braunschweig im Jahr 2007 für Anwendungen bei Temperaturen über 1200°C vorgeschlagen. Infolgedessen wurden im Rahmen der Deutsche Forschungsgemeinschaft (DFG) Forschergruppe „FOR 727" verschiedene Studien durchgeführt, um weitere Legierungselemente zu identifizieren, mit denen sich die mechanische Eigenschaften und das Oxidationsverhalten der Legierungen verbessern lassen. Auf Grundlage früherer Studien von Gorr konzentriert sich die vorliegende Dissertation im Kern auf die Untersuchung und Entwicklung weiterer Legierungselemente (Si(-B), Cr, Al, Y und Ni) zur Verbesserung der Oxidationsbeständigkeit der Co-Re-Basislegierungen. Der Fokus liegt auf der Bildung von thermisch gewachsenen schützenden SiO_2-, Al_2O_3- und/oder Cr_2O_3-Schichten auf den Legierungsoberflächen.

Modelllegierungen Co-17Re-9Si-8B, Co-17Re-23Cr-xSi (x = 0, 1, 2, 3, 4), Co-17Re-23Cr-xAl (x = 5, 10), Co-17Re-xCr-2Si (x = 23, 25, 27), Co-17Re-25Cr-2Si-xY (x = 0.05, 0.1) und Co-17Re-23Cr-15Ni wurden schmelzmetallurgisch mittels Vakuumlichtbogenofen hergestellt und nachfolgend wärmebehandelt (Zahlen werden in At.% angegeben). Die Oxidationsversuche an diesen Legierungen wurden mit Hilfe thermogravimetrischen Messung an Luft im Temperaturbereich von 800°C bis 1300°C durchgeführt. Die Mikrostruktur der Legierungen und der Oxidationsprodukte wurde durch Röntgendiffraktometrie, Raster- und Transmissionselektronenmikroskopie, energiedispersive Röntgenspektroskopie und Elektronenrückstreubeugung charakterisiert. Thermodynamische Betrachtung zum erweiterten Verständnis der Oxidationsmechanismen wurden mit der kommerziellen Software FactSage durchgeführt.

Die Ergebnisse zeigen, dass die Bildung einer thermisch wachsenden SiO_2-Schicht durch Makrolegieren mit Si im Hinblick auf Hochtemperaturanwendungen der Co-Re-Basislegierungen kritisch zu sehen ist, da die zunehmende Si-Zugabe die Schmelztemperatur der Legierung stark absenkt. Die bevorzugte Bildung von Co_2SiO_4 während der Oxidation der Modelllegierung Co-17Re-9Si-8B behindert die Bildung einer kontinuierlichen SiO_2-Schicht. Die Zugabe von sowohl 5% als auch 10% Al verbessert die Oxidationsbeständigkeit der Referenzlegierung Co-17Re-23Cr deutlich. Während der Hauptbeitrag der Zugabe von 5% Al darin besteht, dass es als Sauerstoff-„Getter" die Bildung einer schützenden Cr_2O_3-Schicht fördert, ist die 10% Al-Zugabe fast ausreichend für die Bildung einer kontinuierlichen Al_2O_3-Schicht bis 1100°C. Die starke innere Nitrierung von Al ab 1200˚C führt mangels einer schützenden Al_2O_3-Schicht zu intensiven Oxidationsangriffen.

Die Untersuchung der Legierungsreihen Co-17Re-23Cr-(1-4)Si und Co-17Re-(23-27)Cr-2Si zeigt, dass sowohl Si als auch Cr die Bildung von spröder σ-Phase, die eine schwache Oxidationsbeständigkeit aufweist, in der Legierung fördert. Trotz des positiven Einflusses auf die isotherme

Oxidationsbeständigkeit verstärkt der zunehmende Si-Gehalt sukzessiv das Abplatzen der gebildeten Cr_2O_3-Schicht beim Abkühlen. Die geringe Zugabe von Y bis zu 0,1% verbessert die Haftung der Cr_2O_3-Schicht auf der Legierung Co-17Re-25Cr-2Si signifikant, insbesondere unter thermozyklischen Bedingungen. Es zeigt sich, dass eine Zugabe von 15% Ni zur Legierung Co-17Re-23Cr nicht nur die mechanischen Eigenschaften positiv beeinflusst, sondern auch die Oxidationsbeständigkeit deutlich verbessert. Die Verfeinerung der σ-Phase durch die Ni-Zugabe wird durch eine zusätzliche Kugelstrahlbehandlung ermöglicht, die die Bildung einer geschlossenen Cr_2O_3-Schicht auf der Legierung Co-17Re-23Cr-15Ni weiter begünstigt.

Abstract

As an alternative potential materials class of so-called "Beyond Ni-base Superalloys", Co-Re-base alloys were firstly proposed by Rösler from the Technical University of Braunschweig in 2007 for applications at temperatures beyond 1200°C. Various studies have been consequently carried out in the framework of the German Research Foundation (DFG) research group "FOR 727" aiming to find additional alloying elements to improve both the mechanical properties and oxidation performance of the Co-Re-base alloys. Based on Gorr's previous work within the framework, the study presented aims to investigate and develop further alloying concepts (Si(-B), Cr, Al, Y, and Ni) to improve the oxidation resistance of the alloy system. The focus is given to the formation of thermally grown protective SiO_2, Al_2O_3, and/or Cr_2O_3 scales on the Co-Re-base alloys.

Model alloys Co-17Re-9Si-8B, Co-17Re-23Cr-xSi (x = 0, 1, 2, 3, 4), Co-17Re-23Cr-xAl (x = 5, 10), Co-17Re-xCr-2Si (x = 23, 25, 27), Co-17Re-25Cr-2Si-xY (x = 0.05, 0.1), and Co-17Re-23Cr-15Ni were produced through arc melting followed by proper heat treatment (numbers are given in at.%). The oxidation tests of these alloys were performed in air over the temperature range from 800˚C to 1300˚C with the aid of thermogravimetry. The microstructure of the alloys and the oxidation products was characterized by X-ray diffractometry (XRD), scanning electron microscopy (SEM), energy-dispersive X-ray spectroscopy (EDS), electron backscatter diffraction (EBSD) technique, and transmission electron microscopy (TEM). Thermodynamic studies using commercial software FactSage were employed helping to establish the oxidation mechanism.

Results show that the formation of a thermally grown SiO_2 layer on the Co-Re-base alloys through macro-alloying with Si is problematic with respect to high-temperature applications of such an alloy system, since the Si addition to the Co-Re alloys strongly reduces their melting temperature. The preferential formation of Co_2SiO_4 in the model alloy Co-17Re-9Si-8B restricts the formation of a continuous SiO_2 layer. The addition of both 5% and 10% Al significantly improves the oxidation resistance of the reference alloy Co-17Re-23Cr. While the main contribution of 5% Al addition is that it acts as an oxygen "getter" promoting the formation of a protective Cr_2O_3 layer, the 10% Al addition is almost sufficient for the formation of a continuous Al_2O_3 layer up to 1100˚C. The severe internal nitridation of Al at 1200˚C and above leads to intensive oxidation attacks due to the lack of a protective Al_2O_3 layer.

The investigation of Co-17Re-23Cr-(1-4)Si and Co-17Re-(23-27)Cr-2Si alloy series indicates that both the Si and Cr significantly promote the formation of brittle and poorly oxidation-resistant primary σ phase in the alloy. Despite the positive effect on isothermal oxidation resistance, the increase of Si content successively intensifies the spallation of the Cr_2O_3 layer during cooling. The minor addition of Y up to 0.1% tremendously improves the adhesion of the Cr_2O_3 scale forming on the alloy Co-17Re-

25Cr-2Si, especially under the thermocyclic condition. A 15% Ni addition to alloy Co-17Re-23Cr is not only beneficial for the mechanical properties but also improves the oxidation resistance significantly. The refinement of the σ phase through Ni addition allows short-peening treatment to further facilitate the formation of the Cr_2O_3 scale on the alloy Co-17Re-23Cr-15Ni.

Symbols and abbreviations

Latin symbols

A	[m^2]	Surface area
A_0	[-]	Constant
a_i	[-]	Chemical activity of component i
B_0	[-]	Constant
C	[at.%]	Concentration
C_i	[at.%]	Concentration of component i
$C_O^{(S)}$	[at.%]	Oxygen solubility in alloy
D	[m^2·s^{-1}]	Diffusivity or diffusion coefficient
d	[m]	Interplanar spacing in crystals
D_i	[m^2·s^{-1}]	Diffusion coefficient of component i
D_{ii}	[m^2·s^{-1}]	Interdiffusion coefficient of component i
D_{ii}^*	[m^2·s^{-1}]	Tracer diffusion coefficient of component i
D_0	[m^2·s^{-1}]	Frequency factor of diffusivity
D_d	[m^2·s^{-1}]	Dislocation diffusivity
D_{gb}	[m^2·s^{-1}]	Grain boundary diffusivity
D_s	[m^2·s^{-1}]	Diffusivity at surfaces
E_a	[J·mol^{-1}]	Activation energy
G	[J·mol^{-1}]	Gibbs free energy
g^*	[-]	Critical volume fraction of oxide
g_{ij}	[-]	Thermodynamic factor
H	[J·mol^{-1}]	Enthalpy
J	[m^{-2}·s^{-1}]	Diffusion flux
k_{inv}	[m^{-1}]	Inverse logarithmic rate constant
k_l	[m·s^{-1}]	Linear rate constant

k_{log}	[m]	Logarithmic rate constant
k_0	[-]	Constant
k_p	[m²·s⁻¹]	Parabolic rate constant
k_p'	[kg²·m⁻⁴·s⁻¹]	Weight-change-related parabolic rate constant
M_i	[kg·mol⁻¹]	Molar masse of component i
m	[kg]	Weight
m_i	[kg]	Weight of component i
n	[-]	Natural number
n_i	[-]	Number of moles of component i
p	[bar]	Pressure
p_i	[bar]	Partial pressure of component i
p_i'	[bar]	Partial pressure of component i at the equilibrium
R	[J·mol⁻¹·K⁻¹]	Universal gas constant
S	[J·mol⁻¹·K⁻¹]	Entropy
T	[K]	Temperature
T_m	[K]	Melting temperature
T_m^i	[°C]	Melting temperature of specific matter i in Celsius
t	[s]	Time
U	[J]	Internal energy
V	[m³]	Volume
V_{CH}	[m³]	Volume of arc furnace chamber
V_m^i	[m³·mol⁻¹]	Molar volume of phase i
w_i^*	[%]	critical weight concentration of component i
X	[m]	Scale thickness
x_i	[-]	Mole fraction of component i

Greek symbols

ΔG	[J·mol⁻¹]	Change of Gibbs free energy

$\Delta G°$	[J·mol^{-1}]	Change of standard Gibbs free energy
Δm	[kg]	Weight change
η	[-]	Integration variable
θ	[˚]	Bragg angle
λ	[m]	X-ray wavelength
μ_i	[J·mol^{-1}]	Chemical potential of component i
$\mu_i°$	[J·mol^{-1}]	Standard chemical potential of component i
v	[-]	Stoichiometric constant
v_i	[-]	Stoichiometric constant of the chemical species i
π	[-]	Circular constant

Abbreviations

bcc	Body-centered cubic
BSE	Backscattered electron
CALPHAD	Calculation of phase diagrams
DFG	German Research Foundation (in German: Deutsche Forschungsgemeinschaft)
DSC	Differential scanning calorimetry
EDS	Energy-dispersive X-ray spectroscopy
EBSD	Electron backscatter diffraction
fcc	Face-centered cubic
FIB	Focus ion beam
hcp	Hexagonal close-packed
ICDD	International center for diffraction data
OAZ	Oxidation-affected zone
ppm	Parts per million
RE	Reactive element
REE	Reactive element effect
RT	Room temperature

SC   Single crystal

SE   Secondary electron

SEM   Scanning electron microscopy

TCP   Topologically closed packed

TEM   Transmission electron microscopy

TGA   Thermogravimetric analysis

XRD   X-ray diffractometry

1 Introduction and research objectives

Alloys used for high-temperature applications, such as industrial gas turbines and jet engines, require a balanced combination of excellent high-temperature mechanical properties and superior high-temperature corrosion resistance. Nickel-base superalloys are currently the dominating class of materials for applications in the hot section of turbine engines [1, 2]. For instance, Figure 1.1 illustrates the critical material classes used in the Trent 800 engine, which is the Rolls-Royce engine used mainly in the very common Boeing 777 aircraft. As probably the most well-known modern aerospace materials to the public, titanium alloys are favored in the compressor part due to their extraordinary strength to weight ratio. However, their service temperature is only up to 550°C because of its poor creep and oxidation resistance, whereas the Ni-base superalloys are the leading materials employed in the hottest section of the engine, particularly in turbine blades. The successive development of the substrate Ni-base superalloys accompanied by proper coating and cooling techniques over the last decades have allowed a steady increase in engine operating temperatures and, consequently, the continuous improvement of the engine performance and efficiency [3-6].
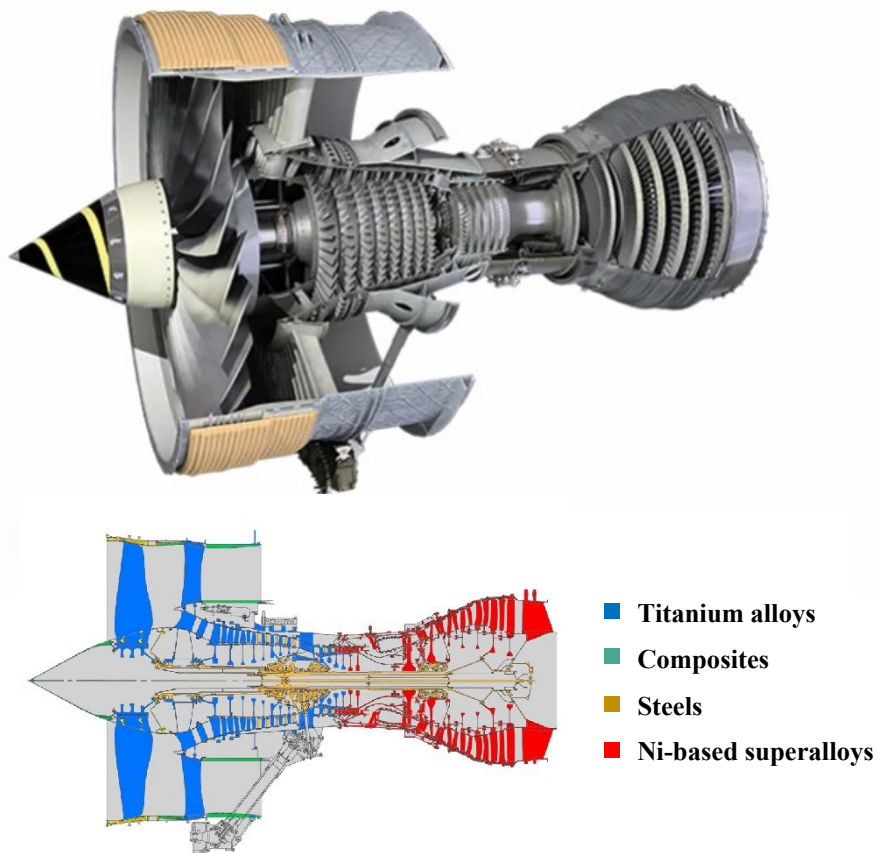
Figure 1.1: Material classes used in a Rolls Royce Trent 800 engine, based and reproduced from [7, 8]

The history of the metallurgical developments of turbine blade substrate materials, representing in their operating temperatures, is summarized in Figure 1.2. In addition to the compositional optimization, the evolution of the producing method of Ni-base superalloys from wrought through conventional casting to single crystal (SC) solidification also made a considerable contribution. The recent 6th generation Ni-base SC superalloy, TMS-238, developed by the Japanese National Institute of Materials (NIMS), has an excellent temperature capability of 1120°C, at which the alloy possesses a 1000 hours creep rupture life under stress of 137 MPa [9]. Although efforts to further improve the Ni-base superalloy are being conducted by researchers [10, 11], the potential has been getting increasingly smaller since the goal temperatures are reaching the melting point of the alloy system, which is about 1350°C [12].
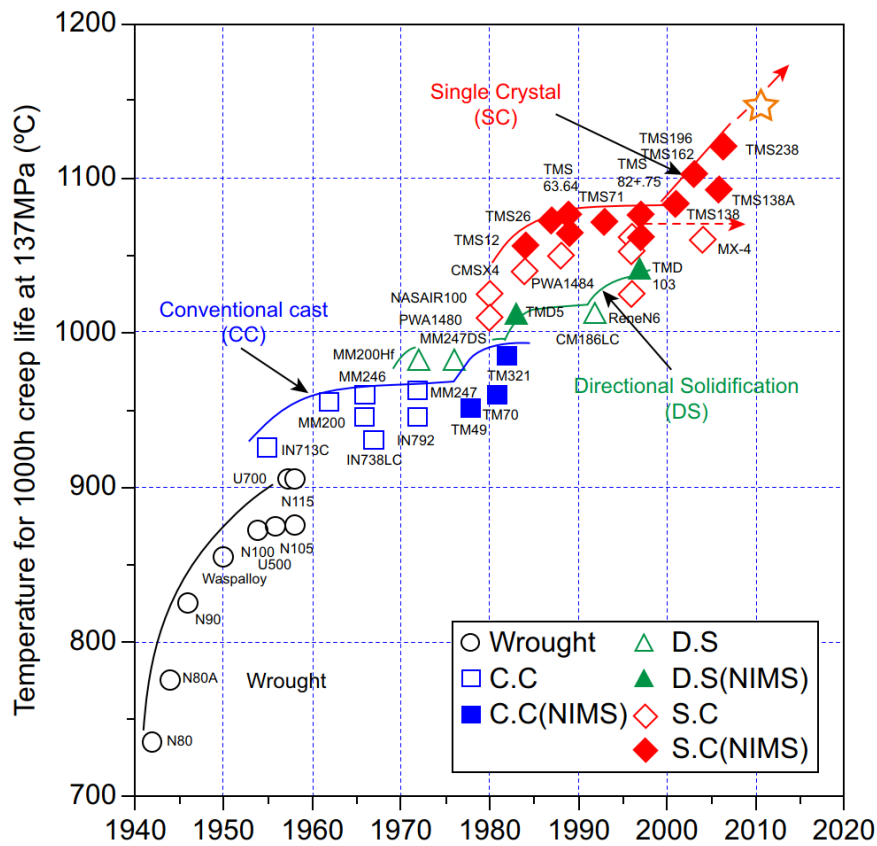
Figure 1.2:   Progressive improvement in temperature capability of superalloys for turbine engine blades in the last decades [13]. *NIMS represents the data from the National Institute of Materials (NIMS), Japan*

Hence, the seek for new substrate materials, which possess a significantly higher melting point and suitable properties at temperatures beyond the capability of Ni-base superalloys, has become a key interest of the turbine industry. Therefore, international researchers have been conducting massive investigations for years. Studies on the refractory superalloys based on noble metals such as platinum ($T_m^{Pt} = 1769°C$), rhodium ($T_m^{Rh} = 1964°C$), and iridium ($T_m^{Ir} = 2446°C$) for ultra-high-temperature use

have been noted [14-16]. As alternative systems, the niobium- and molybdenum-base alloys have also been widely investigated [17-24]. As a pure metal, both Nb ($T_m^{Nb} = 2477°C$) and Mo ($T_m^{Mo} = 2623°C$) have poor oxidation resistance. The oxide layer that forms on Nb, Nb_2O_5, does not protect the alloy from further oxidation and the oxide that forms on Mo, MoO_3, evaporates above about 700°C. Different from the Ni-base superalloys, whose oxidation resistance is derived mainly from chromium and aluminum that form protective chromia (Cr_2O_3) and alumina (Al_2O_3) layers, significant research efforts for Nb- and Mo-base alloys have been given to the formation of silica (SiO_2) layer by adding silicon. This is not only because of the slow growth rate of the SiO_2 layer but also due to the significant enhancement of the mechanical properties by strengthening intermetallic silicides. Although it is promising, many challenges still need to be overcome before Nb- and Mo-base alloys can replace the Ni-base alloys in practice.

In 2007, Co-Re-base alloys were firstly proposed by Rösler et al. [25] as another potential material class for applications at temperatures beyond 1200°C. Unlike the limited solubility of Re in Ni, complete miscibility occurs in the Co-Re system, which allows a substantial continuous increase of the melting point of Co-base alloys by arising Re addition ($T_m^{Co} = 1495°C$; $T_m^{Re} = 3182°C$) and provides a unique possibility in the development of new alloys for very high temperatures. A series of preliminary studies on these new materials have been conducted within the framework of the research group "Beyond Ni-base Superalloy", supported by the German Research Foundation.

As a part of this framework, B. Gorr [26-33] has fundamentally investigated the high-temperature oxidation of the binary Co-Re, ternary Co-Re-Cr, and quaternary Co-Re-Cr-Si alloys. It was stated that the binary Co-17Re alloy exhibits catastrophic oxidation behavior at 1000°C owing to the formation of porous cobalt oxide, resulting in severe material destruction accompanied by the evaporation of rhenium oxides. The addition of Cr is expected to improve the oxidation resistance by forming a protective chromia layer. However, it was found that even the addition of 30 at.% chromium is still insufficient to form a dense and protective Cr_2O_3 layer. Regarding mechanical properties, higher chromium content is unfavored in this alloy system. Thus, a small amount of silicon was introduced to the alloy to promote chromia formation. Gorr et al. [32] reported that the addition of 1-3 at.% Si to the Co-17Re-23Cr successively improves the oxidation resistance. A quasi-continuous chromia layer forms on the alloy Co-17Re-23Cr-3Si during exposure at 1100°C.

Based on Gorr's contribution, this work aims to further investigate and develop the intrinsic high-temperature oxidation resistance of the Co-Re-base alloy system. The main focus is given to the effects of the silicon-(boron), chromium, aluminum, yttrium, and nickel addition. Results are presented and discussed to enrich the understanding of the oxidation behavior of this alloy system. Finally, an outlook for further development is given.

2 Background of investigation

2.1 High-temperature oxidation of metals

Oxidation is one of the most basic chemical reactions in nature. When metals are exposed to air, especially in a moist environment, most of them will be oxidized, which commonly results in metal oxide formation. This process is very destructive for many metals, such as the rusting of iron. However, the oxide layer formed on the surface of some other metals, e.g., Al_2O_3 on aluminum, is very dense and continuous. It acts as a barrier separating the substrate materials from their oxidizing environment and therefore protects the metal from further deterioration. The oxidation behavior of a specific metal, however, depends not only on its chemical composition but also on many other factors such as atmosphere, temperature, etc. For metals, the term high-temperature oxidation generally refers to the reactions which take place over 500°C.

To fundamentally study the high-temperature oxidation behavior of metals, it is necessary to understand both the chemical thermodynamics of the reaction and the diffusion kinetics of the reactants, where the former determines whether the reactions can occur or not under a specific condition and the latter controls the possible oxidation process rate.

2.1.1 Chemical thermodynamics

The total Gibbs free energy, G, of a system is defined as

$$G = H - TS = U + pV - TS \tag{2.1}$$

where H is the enthalpy, T is the absolute temperature, S is the entropy, U is the internal energy, p is the pressure, and V is the volume of the system [13].

For a multi-component system containing n constituent components at constant temperature and pressure, the Gibbs free energy change is only depending on the chemical potential of the components:

$$\mathrm{d}G = \sum_{i=1}^{n} \mu_i \mathrm{d}n_i \tag{2.2}$$

where n_i is the number of moles of component i, μ_i is the chemical potential that can be expressed in its general form:

$$\mu_i = \mu_i^\circ + RT\ln a_i \tag{2.3}$$

where $\mu_i{}^\circ$ is the standard chemical potential of component i, R is the gas constant (8.314 J·K^{-1}·mol^{-1}), and a_i is the thermodynamic activity, which describes the deviation from the standard state of given species [34].

The change of Gibbs free energy (ΔG) of a reaction is further defined as:

$$\Delta G = \sum_{i=1}^{n} v_i \, \mu_i \tag{2.4}$$

Here, the v_i denotes the stoichiometric constant of the chemical species i. Substituting Equation (2.3) into Equation (2.4) leads to

$$\Delta G = \sum_{i=1}^{n} v_i \, \mu_i^\circ + RT \sum_{i=1}^{n} v_i \, \ln a_i \tag{2.5}$$

$$\Delta G = \Delta G^\circ + RT \ln \prod_{i=1}^{n} a_i{}^{v_i} \tag{2.6}$$

where ΔG° is the free energy change when all species are present in their standard states.

According to the second law of thermodynamics, a chemical reaction can occur spontaneously when $\Delta G < 0$ and is in equilibrium when $\Delta G = 0$; while the reaction is thermodynamically impossible when $\Delta G > 0$.

Take simple, pure metal (M) oxidation as an example,

$$M(s) + O_2(g) \rightleftharpoons MO_2(s) \tag{2.7}$$
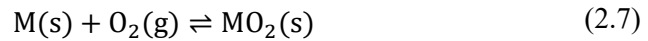
The ΔG of the reaction can be expressed as:

$$\Delta G = \Delta G^\circ + RT \ln \left(\frac{a_{MO_2}^1}{a_M^1 a_{O_2}^1} \right) \tag{2.8}$$

Assuming the metal and oxide are pure solid-state matter under the reaction condition, their activities equal 1, i.e., $a_M = a_{MO_2} = 1$, where a_{O_2} equals p_{O_2}, which is the partial pressure of oxygen, gives:

$$\Delta G = \Delta G^\circ + RT \ln \left(\frac{1}{p_{O_2}} \right) \tag{2.9}$$

when the oxidation reaction is at its equilibrium stage, $\Delta G = 0$, then:

$$\Delta G^\circ = RT \ln p_{O_2}' \tag{2.10}$$

or

$$p'_{O_2} = \exp\left(\frac{\Delta G^\circ}{RT}\right) \tag{2.11}$$

here, p'_{O_2} is the oxygen partial pressure at the equilibrium of the reaction, or namely, the dissociation pressure of the oxide at the given temperature.

Taking Equation (2.10) back into Equation (2.9), leads to:

$$\Delta G = RT\ln\left(\frac{p'_{O_2}}{p_{O_2}}\right) \tag{2.12}$$

As a result,

when $p_{O_2} > p'_{O_2}$, $\Delta G < 0$, the reaction proceeds to form the MO_2 oxide;

when $p_{O_2} = p'_{O_2}$, $\Delta G = 0$, the reaction is in equilibrium so that the metal and oxide coexist;

when $p_{O_2} < p'_{O_2}$, $\Delta G > 0$, the reaction proceeds to dissociation of the MO_2 oxide.

The corresponding value of ΔG° and p'_{O_2} under reaction conditions can be obtained from the thermodynamic data. Hence, the possibility of the oxidation reaction can be determined by calculating ΔG or by comparing the partial pressure of oxygen p_{O_2} in the environment to the dissociation pressure p'_{O_2} of the oxide at that temperature. In 1944, Ellingham plotted a diagram of standard free energy of oxide formation versus temperature so that the possibility of the reaction could be directly determined using a graphical method [35].

Besides the reaction with oxygen, metals can also be oxidized by reacting with water vapor or CO_2 as examples, shown separately in Equation (2.13) and (2.14):

$$M + 2H_2O(g) \rightleftharpoons MO_2 + 2H_2(g) \tag{2.13}$$

$$M + 2CO_2(g) \rightleftharpoons MO_2 + 2CO(g) \tag{2.14}$$
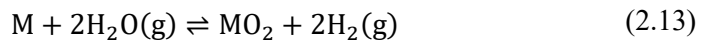
Here the oxidation process is then controlled by the oxygen partial pressure through their first-order reactions:

$$2H_2(g) + O_2(g) \rightleftharpoons 2H_2O(g) \tag{2.15}$$

$$2CO(g) + O_2(g) \rightleftharpoons 2CO_2(g) \tag{2.16}$$
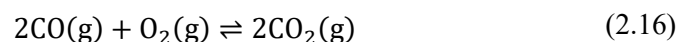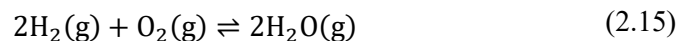
In an analog manner to the derivation from Equation (2.6) to Equation (2.11), the oxygen partial pressure at the equilibrium of the reaction (2.15) can be written as

$$p'_{O_2} = \frac{1}{\left(\dfrac{p_{H_2}}{p_{H_2O}}\right)^2} \exp\left(\frac{\Delta G^\circ}{RT}\right) \tag{2.17}$$

and of the reaction (2.16) as

$$p'_{O_2} = \frac{1}{\left(\dfrac{p_{CO}}{p_{CO_2}}\right)^2} \exp\left(\frac{\Delta G^\circ}{RT}\right) \tag{2.18}$$

Here the ΔG° in Equation (2.17) and Equation (2.18) represents the standard free energy change of the reaction in Equation (2.15) and Equation (2.16), respectively. Thus, the oxygen partial pressures in equilibrium at various temperatures can be determined as a function of p_{H_2}/p_{H_2O} or p_{CO}/p_{CO_2}. In 1948, Richardson and Jeffes [36] developed the so-called Ellingham-Richardson-Jeffes diagram by adding three auxiliary coordinates of the gas partial pressure to the original Ellingham diagram, i.e. p_{O_2}, p_{H_2}/p_{H_2O} and p_{CO}/p_{CO_2}, in which the partial pressure of oxygen in equilibrium for a given oxide at a certain temperature can be directly read from the p_{O_2} line, and the equilibrium partial pressure ratio of the gas phase components from the p_{H_2}/p_{H_2O} and p_{CO}/p_{CO_2} line, respectively, see Figure 2.1.

Taking the oxidation of Co and Cr at 1200°C as an example, the temperature normal at 1200°C intersects the line $2Co + O_2 = 2CoO$ and the line $4/3Cr + O_2 = 2/3Cr_2O_3$ at points "a" and "b" in Figure 2.1, respectively. Their corresponding values of the left vertical coordinate are the standard free energy of the formation of CoO (about -240 kJ/mol O_2) and Cr_2O_3 (about -490 kJ/mol O_2). These negative values indicate that both Co and Cr can be oxidized at 1200°C. The larger absolute value of Cr_2O_3 formation compared to CoO formation also refers to a higher oxygen affinity of Cr than Co. In other words, Cr_2O_3 is thermodynamically more stable than CoO under this condition. The straight line passing through the point "O" and the point "a" intersects with the p_{O_2} coordinate on the right-hand side, the intersecting point shows the oxygen partial pressure in equilibrium with CoO at 1200°C, which is about 5×10^{-8} atm according to Figure 2.1. This implies that the formation of CoO is thermodynamically favored at 1200°C if the oxygen partial pressures in the environment are higher than 5×10^{-8} atm. Similarly, the corresponding oxygen partial pressure in equilibrium with Cr_2O_3 can be read as 2×10^{-17} atm at 1200°C. As a result, it is easy to predict that in an environment with oxygen partial pressures between 2×10^{-17} atm and 5×10^{-8} atm at 1200°C, cobalt can thermodynamically not be oxidized, but chromium does. When the environmental oxygen partial pressure is controlled by either the p_{H_2}/p_{H_2O} or p_{CO}/p_{CO_2} ratio, the p_{H_2}/p_{H_2O} or p_{CO}/p_{CO_2} value in equilibrium with the oxide can also be similarly read from the diagram, except that the starting point of the straight line is "H" or "C" instead of "O", and their values are determined from the p_{H_2}/p_{H_2O} or p_{CO}/p_{CO_2} scale, respectively.
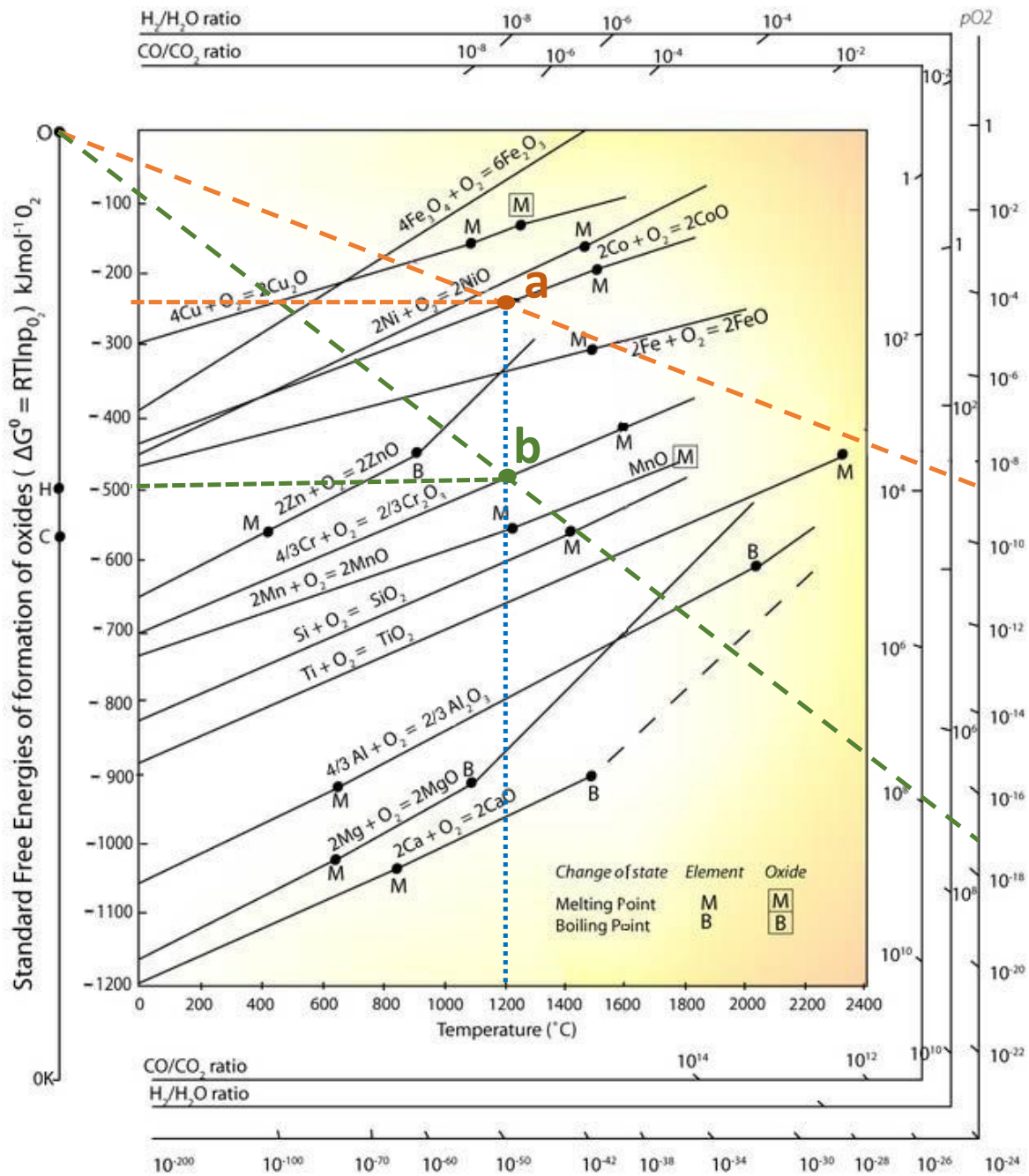
Figure 2.1: The Ellingham-Richardson-Jeffes diagram for metallurgically important oxides, reproduced from [37]

As stated above, it is very convenient to use the Ellingham-Richardson-Jeffers diagram to determine the possibility of pure metal oxidation or the stability of oxides at various temperatures and oxygen partial pressures. With the help of the CALPHAD (CALculation of PHAse Diagrams) method, different kinds of phase diagrams, including oxides, can be generated for specific purposes by using modern thermodynamic calculation programs with the corresponding database, e.g., the pure $Co-O_2$ phase diagram shown in Figure 2.2 and the isothermal alloy-oxygen phase diagram shown in Figure 2.3., etc. For alloy oxidation, the composition-dependent activity of the components has to be taken into account

for the calculation. The detailed explanation and derivation are well described and summarized elsewhere in the literature [38, 39].
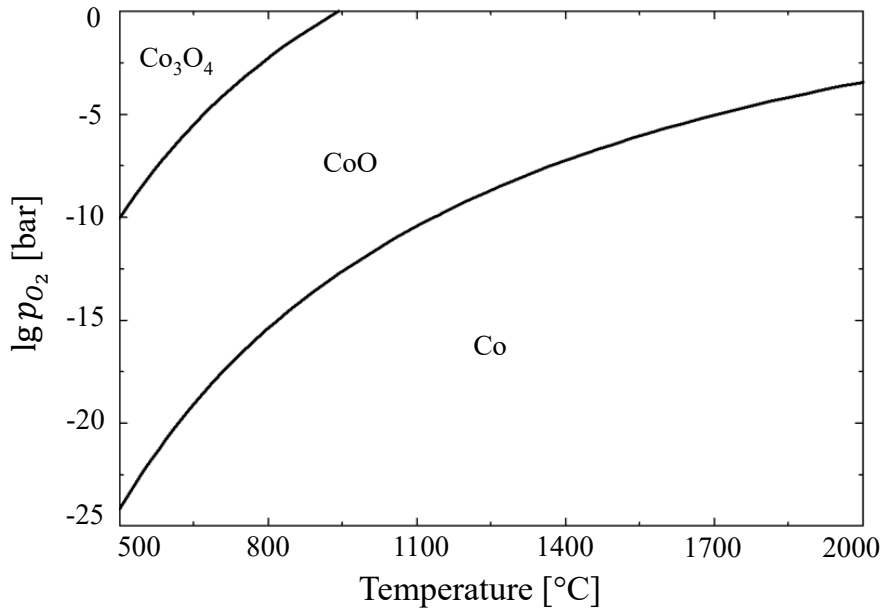
Figure 2.2: Co-O$_2$ phase diagram calculated with the commercial software FactSage
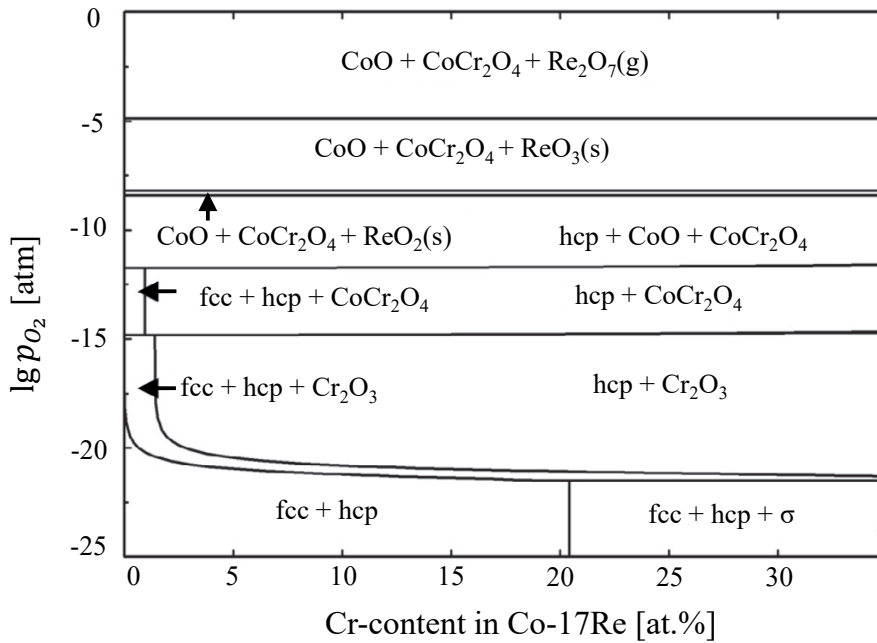
Figure 2.3:   Co-17Re-Cr-O phase diagram at 1000°C calculated with FactSage, based and reproduced from [40]

9

2.1.2 Solid-state diffusion

Diffusion is, in general, a process that leads to equalization of concentration and, therefore, occurs in response to a concentration gradient. Fick's first law of diffusion, as presented in Equation (2.19), describes the relationship between the concentration gradient and the diffusion flux, J, which is the number of particles that pass through a unit area in a unit time:

$$J = -D\nabla C \qquad (2.19)$$

where D is denoted as the diffusion coefficient or diffusivity, ∇C is the concentration gradient field. The negative sign indicates opposite directions of diffusion flux and the concentration gradient.

Fick's first law of diffusion is generally used to deal with the steady-state diffusion processes, in which concentration does not change with time, and is commonly written in its one-dimensional form:

$$J = -D\frac{\partial C}{\partial x} \qquad (2.20)$$

Considering that most of the diffusion processes during high-temperature oxidation of metals are under non-steady-state conditions, the concentration of a certain diffusion species depends not only on position (x, y, z) but also on the processing time t. It is then not practical to use Fick's first law of diffusion to describe or calculate the concentration distribution $C(x, y, z, t)$ for oxidation studies. However, the number of diffusion species in those processes is usually conserved, and therefore an equation of continuity can be formulated:

$$-\nabla \cdot J = \frac{\partial C}{\partial t} \qquad (2.21)$$

Combining the Equation (2.19) and (2.21) yields:

$$\frac{\partial C}{\partial t} = \nabla \cdot (D\nabla C) \qquad (2.22)$$

Equation (2.22) is called as Fick's second law of diffusion. From a mathematical viewpoint, if D depends on concentration, Equation (2.22) is a non-linear second-order partial differential equation and usually cannot be solved analytically. The composition-dependent diffusion coefficient is usually denoted as the interdiffusion coefficient [41]. Assuming that the diffusion coefficient D is independent of concentration, the one-dimensional form of Fick's second law can be generalized as:

$$\frac{\partial C(x,t)}{\partial t} = D\frac{\partial^2 C(x,t)}{\partial x^2} \qquad (2.23)$$

which indicates that the rate of concentration change over time at a certain point is positively correlated with the diffusion coefficient and the second derivative of the concentration gradient. With specific

initial and boundary conditions, Equation (2.23) can be solved to give the concentration as a function of position and time for unidirectional diffusion from one medium to another across a common interface:

$$C(x,t) = A_0 - B_0 \text{erf}(\frac{x}{2\sqrt{Dt}}) \tag{2.24}$$

where A_0 and B_0 are the constants to be determined from the initial and boundary conditions, more comprehensive collections of case solutions are well presented elsewhere in the literature [41]. The expression of "erf" in the above Equation is the Gauss error function, which is defined as

$$\text{erf}\left(\frac{x}{2\sqrt{Dt}}\right) = \frac{2}{\sqrt{\pi}} \int_0^{\frac{x}{2\sqrt{Dt}}} e^{-\eta^2} d\eta \tag{2.25}$$

where η is an integration variable.

From the microstructural viewpoint, diffusion in solids is the transport of matter from one point to another by the thermal motion of atoms. The Arrhenius equation:

$$D = D_0 \exp\left(\frac{-E_a}{RT}\right) \tag{2.26}$$

describes well the temperature dependence of the diffusion coefficient D. Here D_0 is the pre-exponential factor, also called as frequency factor, E_a is the activation energy. For an atom to make such a move, two conditions must be fulfilled: (i) there must be an empty adjacent site; (ii) the atom must have sufficient energy to break bonds with its neighbor atoms. At a given temperature, the diffusivity of different atoms in metals depends strongly on the mechanism by which it moves and may differ by many orders of magnitude [42, 43]. Figure 2.4 schematically illustrates two major diffusion mechanisms, the interstitial diffusion and the vacancy diffusion. The former is usually found for interdiffusion or impurities such as C, N, and O in metals, which have atoms small enough to fit into the interstitial positions in the metallic lattice. The latter involves the interchange of an atom from a normal lattice position to an adjacent vacancy and is usually found for self-diffusion and interdiffusion between elements with comparable atom sizes. Generally, interstitial atoms diffuse much faster than atoms of the host lattice because of their small sizes, allowing them to freely jump between interstices. A typical example is shown in Figure 2.5, where interstitial diffusion coefficients of C, N, and O in Nb are presented together with the Nb self-diffusion coefficient.
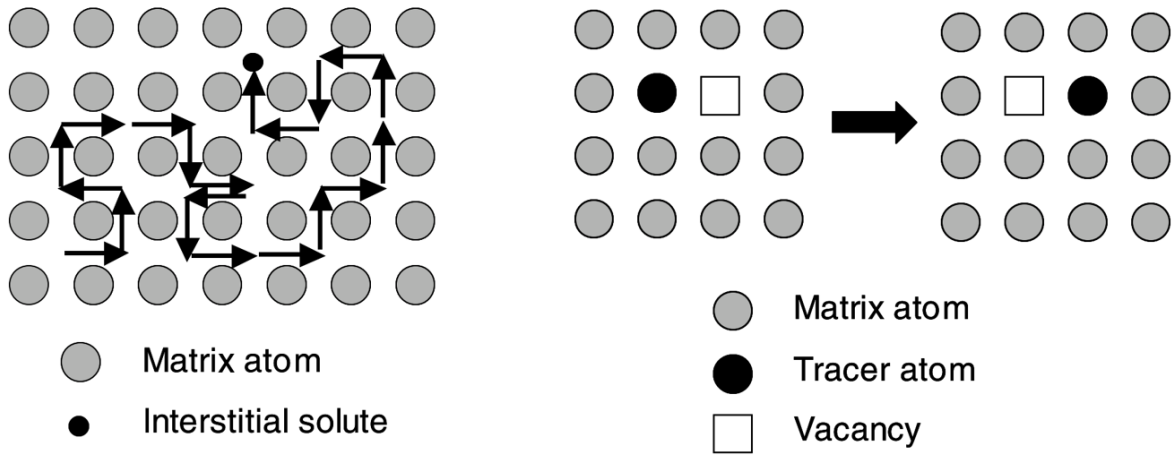
Figure 2.4:   Schematical illustration of interstitial diffusion (left) and vacancy diffusion (right) mechanism [41]
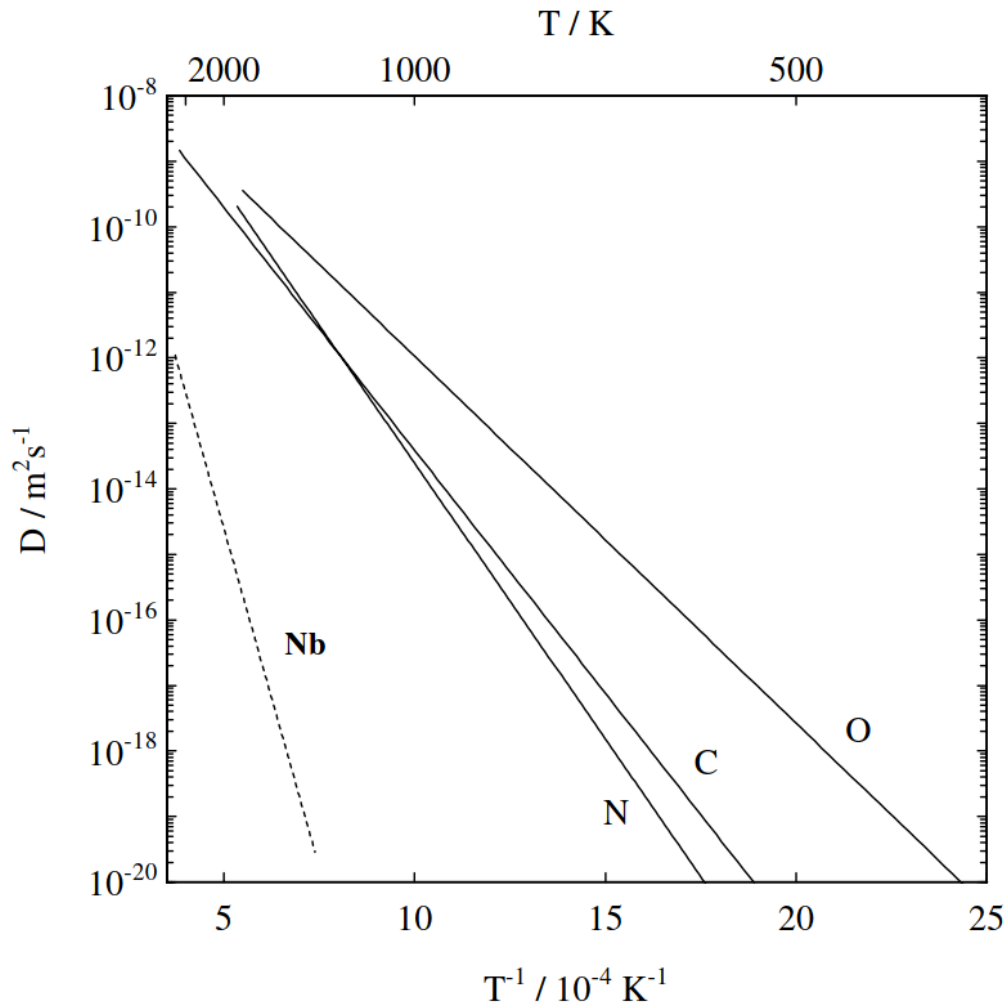
Figure 2.5: Diffusion of interstitial solutes C, N, and O in Nb compared with Nb self-diffusion [43]

Compared to lattice diffusion, the atom transports along dislocation, grain boundaries, and at free surfaces are much faster due to the increased defect density, i.e., lower activation energy E_a. These phenomena are usually called as short-circuit diffusion [44]. The diffusion spectrum for metals is shown in Figure 2.6, in which the diffusion data represent typical averages for a variety of metals and the various high-diffusivity paths, revealing the following hierarchy:

$$D \ll D_d < D_{gb} < D_s \qquad (2.27)$$

where D is the lattice diffusivity, D_d is the dislocation diffusivity, D_{gb} is the grain boundary diffusivity, and D_s is the diffusivity at surfaces.
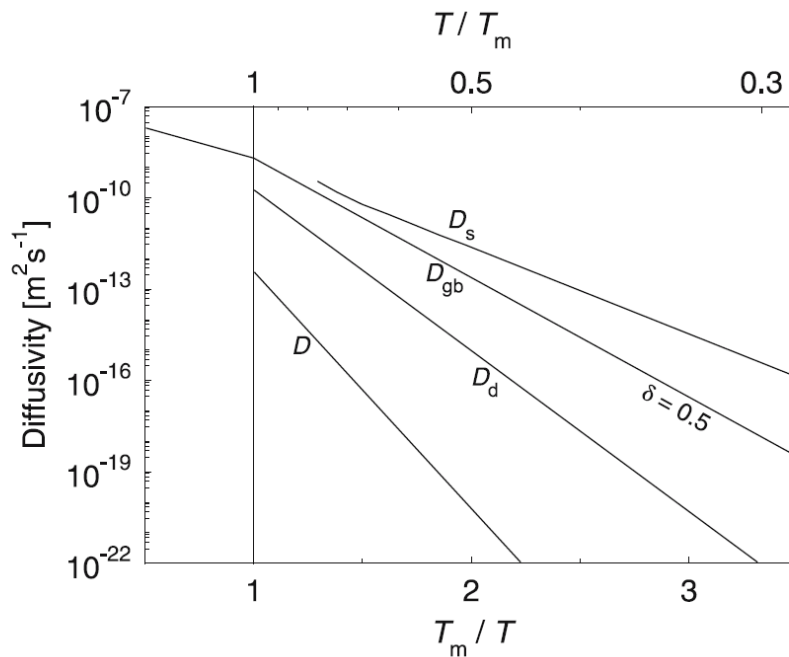
Figure 2.6: Schematic representation of the diffusion spectrum for metals in a reduced temperature scale; T_m denotes the melting temperature in kelvin [41]

The diffusion processes in crystalline oxides are basically governed by the same mechanisms as in crystalline metals as described above. There are, however, some important differences in their defect structures [43]:

- Most oxides are ionic compounds and consist of cations and anions with well defined, opposite charges.

- Crystalline oxides consist of at least two sublattices, a metal (cation) and an oxygen (anion) sublattice. Due to the opposite charges of cations and anions, diffusion always proceeds in the corresponding sublattice.

- The concentration of lattice defect depends not only on the intensive thermodynamic variables T and p, but also on the chemical potential of the component oxygen, i.e., the oxygen partial pressure p_{O_2}.

2.1.3 Oxidation kinetics

Alternatively to oxidation rate, the term "oxidation kinetics" concerns more specifically the understanding of the reaction rate, including investigations of how oxidation conditions influence the speed of the reaction and information about the oxidation mechanisms.

In general, the oxidation of metals at high temperatures involves the adsorption, dissociation, and chemisorption of oxygen on the metal surface at the initial reaction stage. The chemisorbed oxygen can be absorbed by those metals with oxygen solubility, or it remains on the surface where additional oxygen is chemisorbed to form an oxide with the metal [45]. Once the oxide formed separates the metal and oxygen, the transfer of metal and/or oxygen through the oxide barrier is required for further growth. Figure 2.7 schematically illustrates two types of such transportation mechanisms as well as the corresponding interfacial reactions. The intrinsic difference between them is the oxidation front site. If the metallic cations diffuse through the oxide scale faster than oxygen anions, the oxide scale grows predominately at the outer oxide/gas interface. Inversely, if the oxygen anions diffuse through the oxide scale faster than metallic cations, the oxide scale then grows predominately at the inner metal/oxide interface.

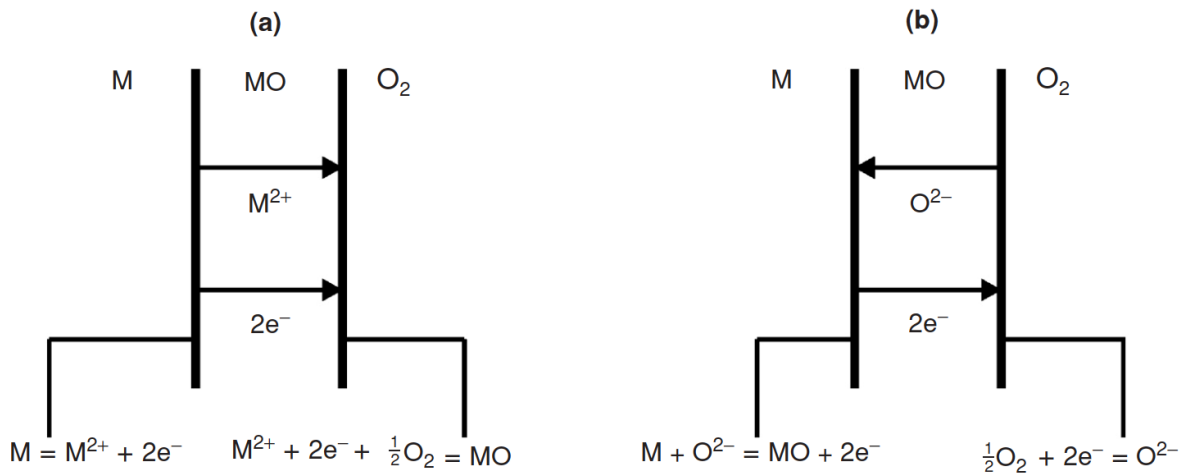Figure 2.7: Interfacial reactions and transport processes for high-temperature oxidation mechanisms: (a) cation mobile and (b) anion mobile [34]

Therefore, the defect-structure-dependent particle diffusivities within the oxide scale play a key role in the oxidation mechanism and scale growth. If the scale formed is compact and coherent, its growth is

then essentially controlled by the diffusion processes, and the rate of scaling commonly follows a parabolic law [13]:

$$\frac{dX}{dt} = \frac{k_p}{X} \tag{2.28}$$

which in integrated form reads:

$$X^2 = 2k_p t \tag{2.29}$$

where X is the thickness of the oxide scale, k_p is the parabolic rate constant, and t is the exposure time. Equation (2.29) presents that the scaling rate decreases with increasing time as the oxide scale thickness, i.e., the ion diffusion distance, increases.

In practice, the oxide scale thickness can be directly measured by examining the cross-sectional microscopic images. Alternatively, the continuous gravimetric recording of the mass gain through oxygen uptake, described in detail in Chapter 3, offers a unique opportunity to in-situ investigate the oxidation kinetics during the entire process without damaging the specimen. The corresponding parabolic law of oxidation can be then expressed as:

$$(\frac{\Delta m}{A})^2 = 2k_p' t \tag{2.30}$$

where Δm is the weight change of specimen, A is the sample surface area, and k_p' is the weight-change-related parabolic rate constant. Moreover, $\frac{\Delta m}{A}$ is generally denoted as specific weight change or specific mass change.

If the scaling mechanism remains identically within a certain temperature range, the temperature dependence of parabolic rate constants at constant ambient oxygen pressure can be written in an Arrhenius-type equation [46]:

$$k_p = k_0 \exp(\frac{-E_a}{RT}) \tag{2.31}$$

where k_0 is a constant.

Figure 2.8 schematically illustrates the temperature-dependent parabolic rate constant of several oxides, which are of great importance to modern structural materials. As can be seen from the data presented in Figure 2.8, the growth rate of these oxides at a constant temperature can differ by several orders of magnitude due to the nature of their defect structure.

However, it is important to point out that the derivation of the parabolic rate law is based on many ideal assumptions, which Birks and Meier well summarized as follows [34]:

- The oxide scale is compact and adherent.

- Migration of ions or electrons across the scale is the rate-controlling process.

- Thermodynamic equilibrium is established at both the metal/scale and scale/gas interface.

- The oxide scale shows only small deviations from stoichiometry and, hence, the ionic fluxes are independent of position within the scale.

- Thermodynamic equilibrium is established locally throughout the scale.

- The scale is thick compared with the distances over which space charge effects (electrical double layer) occur.

- Oxygen solubility in the metal may be neglected.
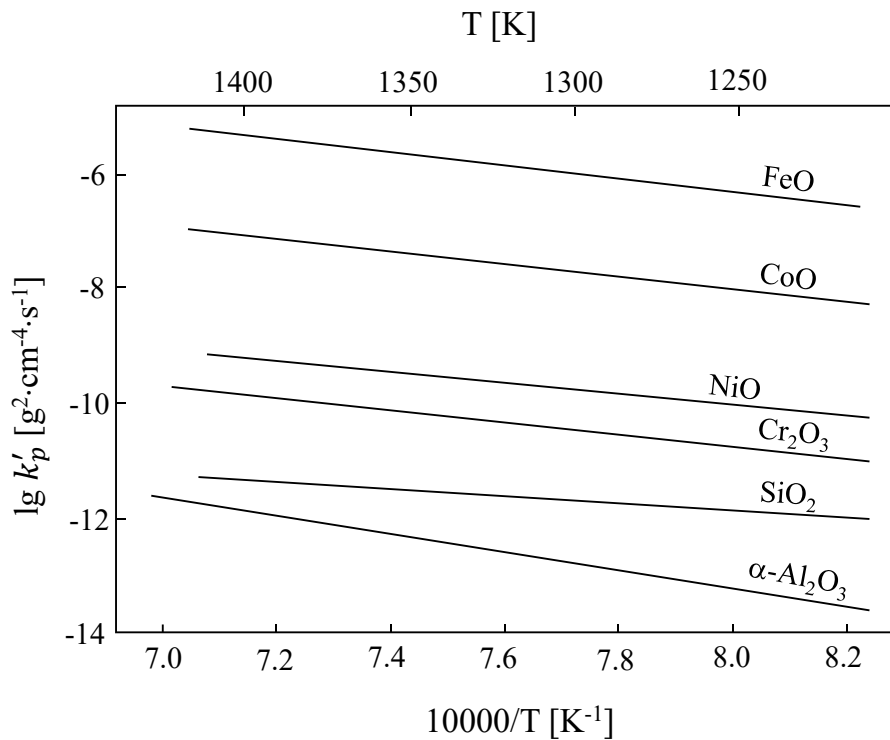

Figure 2.8:   Temperature dependence of the weight-change-related parabolic rate constants of several oxides, based and reproduced from [34]

When the oxide scale forming on the metal surface provides no diffusion barrier due to pores, oxide cracking and spalling, volatile oxides, etc., a linear kinetic rate can be observed:

$$X = k_l t \tag{2.32}$$

where k_l is the linear rate constant.

Besides, logarithmic or inverse logarithmic kinetics are commonly found when oxidation occurs at temperatures below 400°C or the oxide film thickness is about 100 nm or less. The logarithmic rate law can be expressed by:

$$X = k_{log} \log(A_0 t + 1) \tag{2.33}$$

where k_{log} is the logarithmic rate constant, and A_0 is a simple constant.

The inverse logarithmic rate can be expressed by:

$$\frac{1}{X} = B_0 - k_{inv} \log(t) \tag{2.34}$$

where k_{inv} is the inverse logarithmic rate constant, and B_0 is a simple constant.

In practice, some other empirical rate laws including, but not limited to cubic and paralinear, which are combinations of the ideal rate laws as mentioned above, have also been observed and reported [47].

2.1.4 Alloy design against oxidation

Although engineering materials used for high-temperature applications are generally ennobled by coating technology against oxidation, superior inherent oxidation resistance is still required for the bulk materials to defense against coating damage or spallation. The oxidation resistance of alloys relies mainly on forming a compact, adherent, and slow-growing external oxide scale, which limits the further degradation of the base materials. For this purpose, the most effective scales are the chromia, the alumina, and the silica scales [48].

Indeed, the development of high-temperature alloys usually involves a satisfactory compromise between oxidation resistance and mechanical properties. A general concept in improving alloy inherent oxidation resistance is to increase the concentration of the protective scale-forming elements, i.e., Cr, Al, and Si singly or mixed. Figure 2.9 schematically illustrates the Cr content dependence of forming a continuous and protective chromia scale on the surface of Fe-Cr alloys. However, high Cr content often leads to damage to mechanical properties by forming brittle phases or decreasing creep strength [49, 50]. Without such restriction in mechanical properties, Cr content can even go as high as 53 at.% for coating applications [51]. In this connection, the study of the critical concentration of the protective scale former plays a crucial role in developing alloys for high-temperature applications.

Considering a binary A-B alloy system, component A is the base material, and component B is the solute element with a higher oxygen affinity than A. The following Equation (2.35) describes the relationship between the decisive factors and the critical concentration of solute B (C_B) to form an external BO$_v$ scale instead of internal oxide precipitations according to Wagner [52] and Birks [34]:

$$C_B > \left[\frac{\pi g^*}{2v} C_O^{(S)} \frac{D_O V_m^M}{D_B V_m^{OX}} \right]^{\frac{1}{2}} \tag{2.35}$$

where π is the circular constant, g^* is the critical volume fraction of oxide, v is the stoichiometric constant of oxide BO_v, $C_O^{(S)}$ is the oxygen solubility in the alloy, D_O is the diffusion coefficient of oxygen and D_B is the diffusion coefficient of solute B in the alloy, and V_m^M and V_m^{OX} are the molar volumes of the alloy and oxide, respectively.
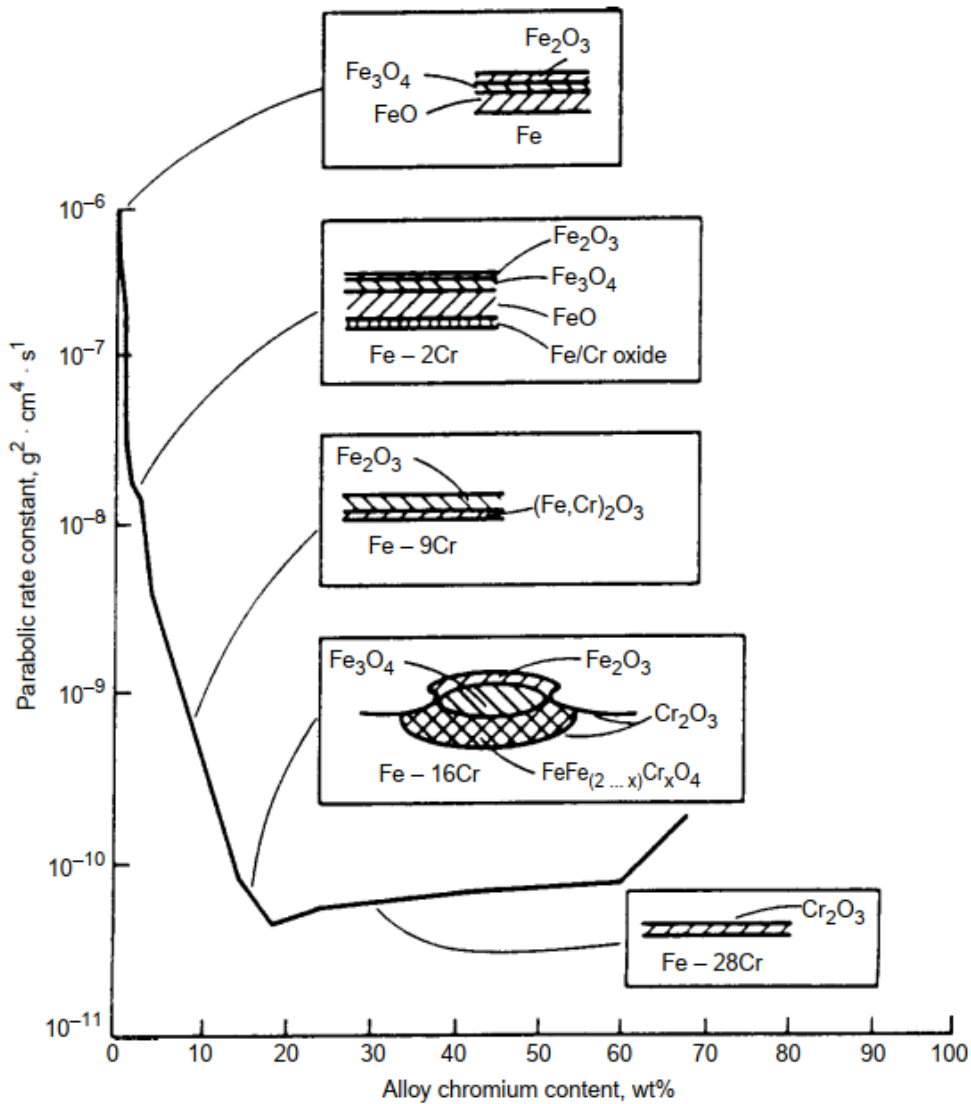

Figure 2.9: Effect of Cr content on scale formation of Fe-Cr alloys at 1000°C in 0.13 atm O_2 [47]

However, Equation (2.35) is derived under ideal conditions where only component B can be oxidized. Under conditions where both components can be oxidized, the transient oxidation of component A must

18

also be considered. Gesmundo and Viani [53] extended Wagner's original analysis and showed that the formation of an outer AO scale tends to produce an increase in the critical concentration C_B, essentially as a result of a decrease of the enrichment of A in the internally oxidized region. Accordingly, the critical concentration C_B becomes larger as the rate constant for the growth of the outer AO scale increases under constant values of the other parameters involved.

Once a continuous and protective external BO_v scale is formed, a sufficient supply of solute B, at least at the rate it is being consumed by scale growth, must be fulfilled to maintain the protectiveness of the scale. This requirement leads to another criterion for the critical concentration C_B and may be expressed as [54]:

$$C_B > \frac{V_m}{32v}\left(\frac{\pi k_p}{D_B}\right)^{\frac{1}{2}} \qquad (2.36)$$

where k_p is the parabolic rate constant for growth of the external scale, measured in terms of scale thickness.

Combining Equation (2.35) and Equation (2.36), it becomes clear that an increase of bulk diffusivity of the protective scale former, D_B, is benifical for reducing the critical concentration required to develop and maintain a continuous and protective external scale. It is also generally believed that the provision of a greater number of short-circuit diffusion paths tends to increase D_B more than D_O [51]. Therefore, the critical concentration C_B can be effectively decreased by reducing the alloy grain size [55] or increasing the dislocation density at the alloy surface by mechanical deformation through abrasion, shot-peening [56], etc.

So far, the most widely used high-temperature alloys are Fe- or Ni-base alloys that form a protective Cr_2O_3 scale during exposure. However, the protectiveness of the chromia scale is weakened when the exposure temperature is too high. It is usually postulated that the outer part of the Cr_2O_3 scale continuously reacts with oxygen to form a new oxide CrO_3, which is volatile and leaves the scale in a gaseous form when the temperature exceeds 1000°C, resulting in a rapid oxidation attack [57]. This phenomenon is even worse in the presence of water vapor due to the additional formation of volatile $CrO_2(OH)_2$ [58]. Similarly, the formation of volatile SiO also partly restricts the use of SiO_2 as a protective scale [34]. Whereas such vapor species influence the protectiveness of chromia at high oxygen partial pressures, the effect for silica is vital at low oxygen partial pressures.

For application at higher temperatures, the alumina scale becomes more preferred due to its high-temperature stability and the extremely slow growth rate (see Figure 2.8) relating to its highly stoichiometric structure. For instance, alloys of the type Fe-20Cr-5Al (in wt.%), which are generally used as alloy foil in automotive catalytic converters, are among the most oxidation-resistant metallic materials by forming protective Al_2O_3 scale at temperatures above 1000°C [59]. Examples of Ni-base

alloys are Rene N5 [60], Nicrofer 6025 HT [61], Haynes HR-224 [62], etc. The main weakness of Al_2O_3 scales is their susceptibility to cracking and spalling [63, 64]. During high-temperature exposure, Al is depleted in the alloy subsurface due to its selective oxidation into the external protective scale. This depletion can be enlarged by repeated spallation and re-healing of the scale under thermocyclic conditions. If the Al concentration is decreased beneath a critical level, severe oxidation occurs due to the formation of other rapidly growing oxides. Such kind of rapid increase in the oxidation rate is generally called as "breakaway oxidation".

To overcome this issue, the addition of reactive elements (RE), such as yttrium, cerium, hafnium, etc., has become a common method in developing modern high-temperature alloys. It has been widely reported [65-74] that the small addition of these elements can, to some extent, reduce the growth rate and remarkably improve the adhesion of chromia or alumina scales on the base alloy. Even a unique term of "reactive element effect" (REE) is given to these extraordinary effects of RE in the high-temperature oxidation community.

As mentioned above, typical of any alloy development, the recurring issue with the addition of protective scale-forming elements is a balance of properties. Whether to form chromia, alumina, or silica protective scale is the best solution for a specific high-temperature alloy against oxidation depends not only on its application environment but also on how the critical concentration of the scale-forming element affects other properties of the alloy.

2.2 Co-Re alloy system

Essentially, Co-base alloys were widely used in turbines many decades ago. They exhibit excellent thermal shock resistance and are easy to manufacture [75]. However, they lack the strength of γ′-hardened Ni-base superalloys, and thereby their development in turbine blades has gradually faded from the competition. Although the recently developed Co-Al-W alloys by Sato et al. [76] showed a γ/γ′ structure similar to the Ni-base superalloys, the low solvus temperature of the γ′ phase limits their application temperature as for the Ni-base superalloys [77].

One major event in the history of the Ni-base superalloys was the introduction of Re into their SC system, which has effectively enhanced the strength and creep resistance of the alloys further [78, 79]. Even the so-called "generations" of the SC superalloys are mainly characterized by their Re content, e.g., the first-generation of SC superalloys is Re-free, the second-generation contains about 3 wt.% Re, and the third-generation contains about 6 wt.% Re [80]. However, a further increase of Re by a significant amount is unfavorable, since it promotes the formation and precipitation of brittle topologically closed packed (TCP) phases. Although the occurrence of a moderate amount of the TCP phases does not significantly degrade the alloy properties, the overmuch present still need to be avoided [81].

In contrast to Ni, the unlimited solubility of Re in Co, as shown in Figure 2.10a, provides an extensive range of possibilities to substantial solid solution strengthen the Co-Re alloy matrix and simultaneously increase the melting temperature of the alloy by increasing the amount of Re. Mukherji et al. [82] reported that the addition of 17 at.% rhenium to cobalt increases the melting temperature of the alloy to above 1700°C. Nevertheless, Co has an allotropic transformation from hexagonally close-packed (hcp) ε phase to face-centered cubic (fcc) γ phase. The transformation temperature of pure Co is 417°C. The addition of Re, which has an hcp structure, strongly increases the transformation temperature in the binary Co-Re system.

Similar to the conventional Co-base superalloys, Cr is added to the Co-Re alloy system aiming to improve mechanical properties through solid solution strengthening and oxidation resistance by forming a protective Cr_2O_3 scale [83]. At the first development stage, the alloy Co-17Re-23Cr (all concentrations in this work related to Co-Re-base alloys are given in atomic percent unless otherwise stated), which shows an onset melting temperature of 1543°C through differential scanning calorimetry (DSC) measurement [84], was designed as a reference alloy for the subsequent development of the Co-Re-Cr-base system by means of further alloying additions (e.g., B, C, Si, Ta, Ni, etc.) trying to establish sufficient strength and oxidation resistance at elevated temperatures [85].

As shown in Figure 2.10b, the addition of Cr greater than 20% to the alloy Co-17Re can significantly promote the formation of σ phase. Microstructural study on the reference alloy Co-17Re-23Cr directly after arc-melting reveals the presence of fcc phase apart from the hcp and the σ phases, which implies that the phase transformation from fcc to hcp is retarded due to the fast cooling system within the arc furnace. After a proper solution heat treatment at 1450°C followed by Ar-quench with a moderate cooling rate, hcp phase and σ phase are the only phases that can be observed in the alloy, where the σ phase populates at the grain boundaries of the hcp matrix in a blocky morphology. Additionally, the precipitation of fine dispersed lamellar secondary σ phase in the supersaturated hcp grains during further annealing or exposure process is a general observation in the Co-Re-Cr-base alloys. The detailed microstructural analyses of the Co-Re-Cr-base alloys were presented by Depka et al. [86, 87] elsewhere.

The topologically closed packed σ phase in the Co-Re-Cr-base alloys is Cr-Re-rich (Cr_2Re_3-type) and has a very high hardness (~1500 HV), but unfortunately, it is very brittle [88]. Moreover, the slightly detrimental effect of the σ phase on oxidation resistance in the Co-Re-Cr-base alloys has also been reported [28].
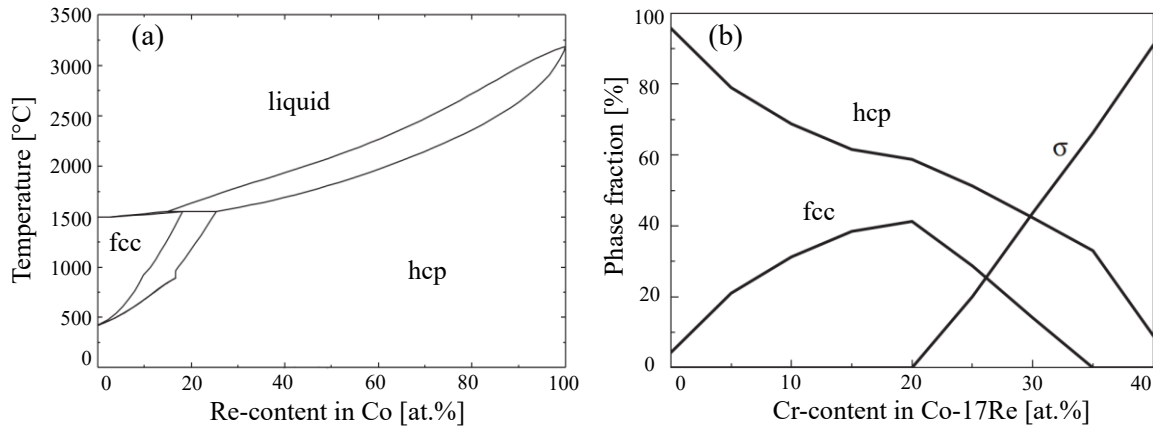
Figure 2.10: Phase diagram calculated with FactSage: (a) binary Co-Re; (b) chromium dependent phase distribution in Co-17Re at 1000°C (both diagrams are based and reproduced from [40])

Nevertheless, the σ phase volume fraction and morphology can be considerably adjusted by proper control of the chemical composition and thermal treatment [40, 89]. Mukherji and Rösler [90] reported that the addition of 15% Ni to the alloy Co-17Re-23Cr can significantly refine the particle size of the σ phase down to about 100 nm, enhancing the intrinsic ductility of the alloy without weakening its strength, as shown in Figure 2.11. Since the σ phase in the Co-Re-Cr alloys is relatively stable at high temperatures up to 1300°C, a novel strengthing strategy in the development of Co-Re-base alloys addresses the utilization of the high strength σ particles for composite strengthening [90].

Figure 2.11: Comparison of microstructure and hardness indents (a) of alloy Co-17Re-23Cr showing cracks in large σ particles (bright) and slip bands (arrows) in the hcp matrix and (b) of alloy Co-17Re-23Cr-15Ni showing no cracks in σ phase, which is finely dispersed in the matrix [88]

Another strengthening strategy involved in the development of the Co-Re alloy system is precipitation hardening by carbides. By introducing 2.6% C to the reference alloy, lamellar $Cr_{23}C_6$-type carbides in the form of thin plates (~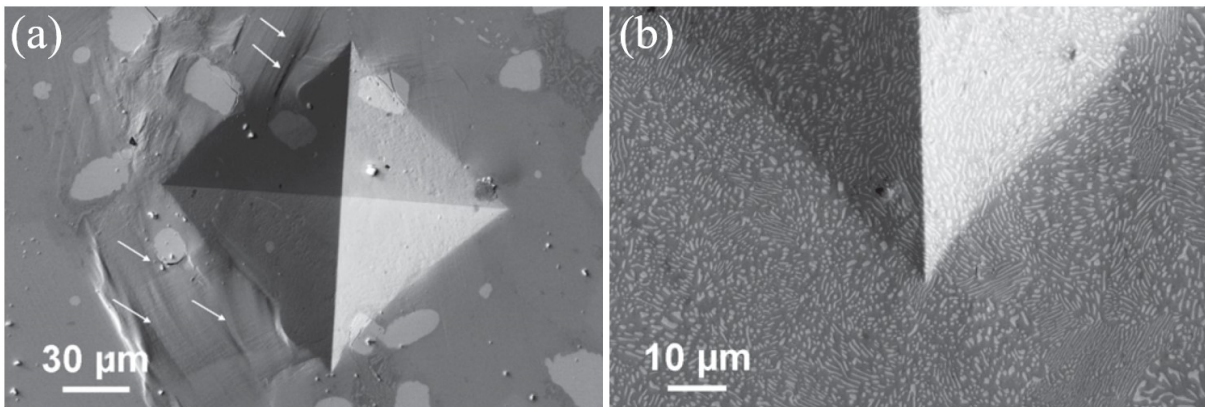40 nm thick) presents in the hcp matrix in addition to the massive $Cr_{23}C_6$-type carbide precipitates at grain boundaries with several micrometers in size. In alloy Co-17Re-23Cr-1.2Ta-2.6C, a very fine dispersion of TaC-type MC carbide forms additionally [85]. These fine TaC dispersions are found to be stable up to temperatures above 1200°C. Although they coarsen on long exposures, they remind still fine enough to be an effective barrier for dislocations and interact with dislocations during creep exposure [91, 92].

Moreover, investigations on cast polycrystalline Co-Re-base alloys showed a critical grain boundary embrittlement, limiting both the strength and the ductility of the alloys at room and high temperatures [84]. The addition of B in a small amount (50-1000 wt.ppm) to the Co-Re-base alloys changes the fracture mode from intergranular to transgranular and thereby tremendously improves the strength and ductility. An example is given in Figure 2.12.
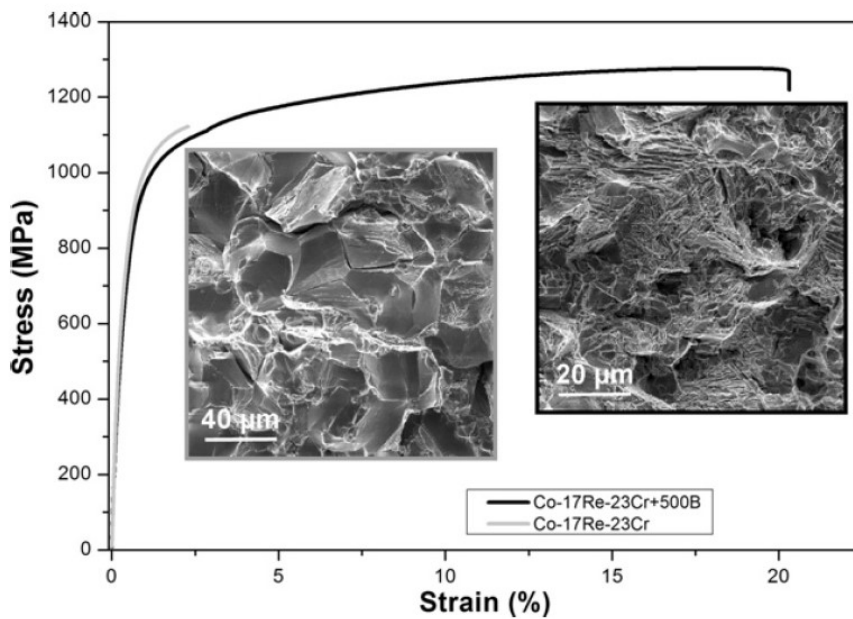

Figure 2.12: Tensile test results at RT on alloys Co-17Re-23Cr and Co-17Re-23Cr + 500B (500 wt. ppm) with the corresponding fracture surface images [93]

2.3 High-temperature oxidation of Co-Re-base alloys

2.3.1 Oxidation of binary Co-Re alloys

Although the Co-Re-base alloys possess a higher melting point than Ni-base superalloys and the potential to achieve good mechanical properties at high temperatures, one essential challenge in the development of these alloys is their relatively poor oxidation resistance.

Gorr et al. [28] studied the oxidation behavior of binary alloy Co-17Re and reported a catastrophic oxidation behavior of the alloy during exposure to laboratory air at 1000°C. Figure 2.13 shows the cross-sectional micrograph of an oxidized Co-17Re specimen. The oxide scale consists of pure CoO with different morphologies, i.e., an outwardly grown layer with columnar grains and an inwardly grown layer with equiaxed grains, showing a non-protective nature. Apart from the intrinsic high growth rate of the CoO grains, the noticeable pores and microchannels between these grains provide fast access for gaseous oxygen to transport inwardly. Consequently, the oxidation of rhenium takes place at the scale/alloy interface. Due to the high volatility of Re oxides [94], Re is continuously lost via the evaporation of its oxides through those pores and microchannels in the CoO scale, resulting in massive weight loss during oxidation even despite the uptaking of oxygen by forming CoO.
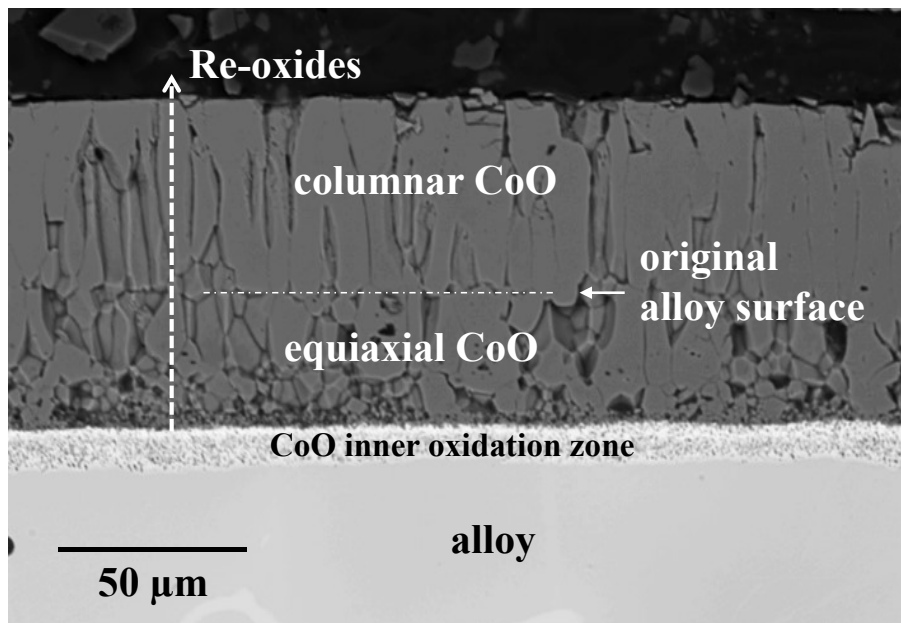

Figure 2.13: Cross-sectional image showing the constitution of the oxide scale formed on alloy Co-17Re after exposure to laboratory air at 1000°C for 1 h, reproduced from [28]

2.3.2 Oxidation of Co-Re-Cr alloys

In principle, Cr is added to the Co-Re alloys to improve their oxidation performance. However, the ternary alloy Co-17Re-23Cr shows even a more inadequate short-term oxidation resistance than the binary Co-17Re alloy since it forms a very porous $CoCr_2O_4$ spinel layer underneath the CoO layer, as shown in Figure 2.14.

The increase of Cr from 23% to 30% to Co-17Re can also not effectively improve the oxidation resistance but significantly increases the particle size and volume fraction of the primary σ phase, which is preferentially attacked during initial exposure compared to the hcp matrix. The oxide scale structure on alloy Co-17Re-30Cr is quite similar to that on alloy Co-17Re-23Cr. Due to the lack of a protective Cr_2O_3 layer, massive weight loss kinetics can still be observed for alloy Co-17Re-30Cr, although the $CoCr_2O_4$ spinel layer formed contains less porosity as compared to Co-17Re-23Cr.

Experimental results [27] also showed that the addition of C to ternary Co-Re-Cr alloys for improving mechanical properties does not play a significant role in the oxidation behavior. A slower internal oxidation rate at grain boundaries than the grain interior is only observed in a short oxidation period for the quaternary alloy Co-17Re-23Cr-2.6C. This phenomenon disappears, however, significantly with the increasing time of oxidation.
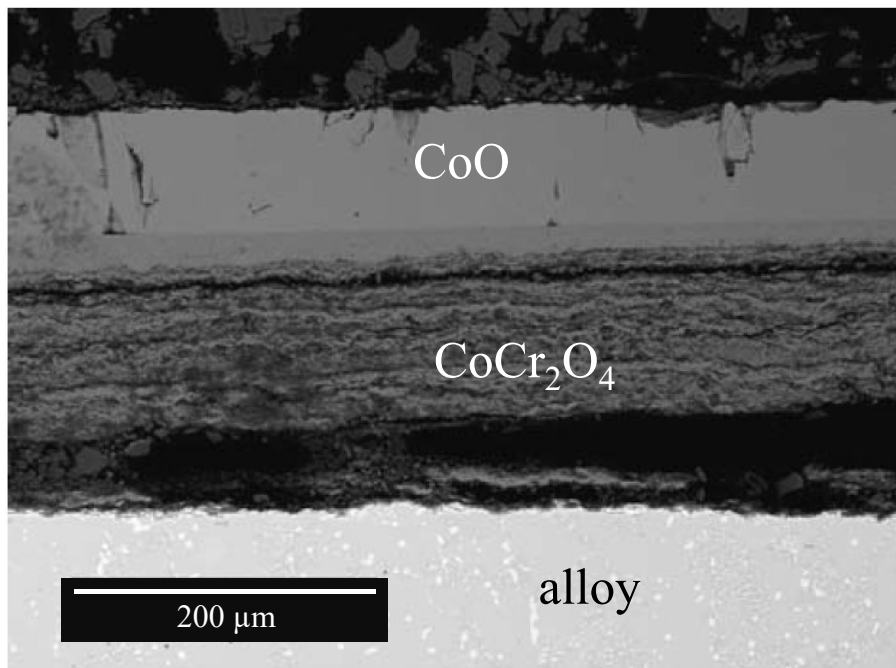

Figure 2.14: Cross-sectional image showing the constitution of the oxide scale formed on alloy Co-17Re-23Cr after exposure to laboratory air at 1000°C for 7 h, reproduced from [28]

2.3.3 Oxidation of Co-Re-Cr-Si alloys

Numerous studies indicate that a small amount of silicon addition can significantly improve the oxidation resistance of Co-Cr-base alloys [95-97]. One of the generally accepted theories on this phenomenon proposes that Si or firstly formed silica acts as nucleation sites reducing the distance between Cr_2O_3 nuclei and promoting the rapid formation of a continuous and protective chromia layer. Some other authors also reported that the addition of silicon improves the oxidation resistance of alloys through the formation of an amorphous silica layer between the outer oxide layer and the alloy substrate, inhibiting the outward diffusion of metal cations to the outer oxide scale as well as the inward diffusion of oxygen anions [98, 99].

Inspired by this, Gorr et al. [32] investigated the influence of Si on the oxidation behavior of Co-Re-Cr alloys and reported that the oxidation resistance of alloy Co-17Re-23Cr can be successively enhanced by increasing the Si content from 1% to 3%. Figure 2.15a presents the weight change of the alloys Co-17Re-23Cr-xSi with different amounts of Si content during exposure to laboratory air at 1000°C. The oxidation kinetics of these alloys are all affected by the evaporation of Re oxide. However, the weight loss rate decreases strongly and successively with increasing Si content.

Microstructural examination by Gorr et al. [32] revealed that the oxide scale formed on alloy Co-17Re-23Cr-1Si at 1000°C consists of an outermost CoO layer, a porous $CoCr_2O_4$ layer, and a thin discontinuous inner Cr_2O_3 layer. A similar scale structure can be observed in certain areas on alloy Co-17Re-23Cr-2Si, while the rest of the alloy is covered by locally continuous Cr_2O_3. A completely different oxide structure, which consists of an outer $CoCr_2O_4$ layer and a relatively thick inner Cr_2O_3 layer, is found on alloy Co-17Re-23Cr-3Si, see Figure 2.15b. However, this scale is still not compact enough to completely prevent Re oxide evaporation resulting in a slight weight loss kinetics.
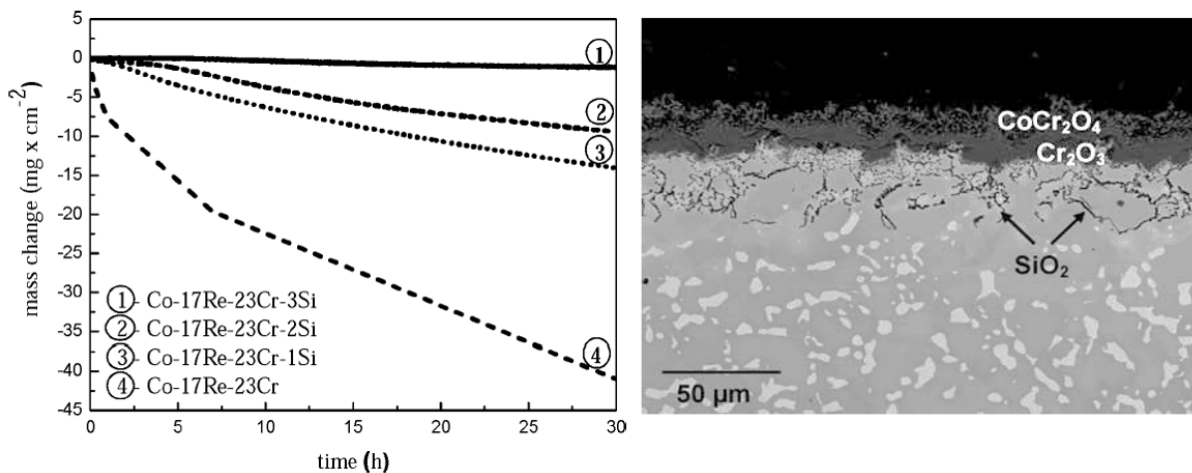
Figure 2.15: Oxidation behavior of the alloy Co-17Re-23Cr-xSi: TGA results at 1000°C (left) and cross-sectional image of the alloy Co-17Re-23Cr-3Si after oxidation at 1100°C in air for 7 h (right) [32]

As a result of the increase in Cr content from 23% to 30%, a slight mass gain is detected on alloy Co-17Re-30Cr-2Si during exposure to air at 1000°C and 1100°C (see Figure 2.16a). The oxidation kinetics at 1000°C obeys the parabolic rate law, indicating a protective oxide scale. Microstural examination on the oxidized specimen confirms the formation of a dense and continuous chromia layer, which prohibits the evaporation of Re oxides (see Figure 2.16b).

In all Si-containing Co-Re-Cr alloys investigated, SiO_2 precipitates are found as internal oxidation products beneath the scale formed. The amount of SiO_2 precipitates increases with increasing Si-content.
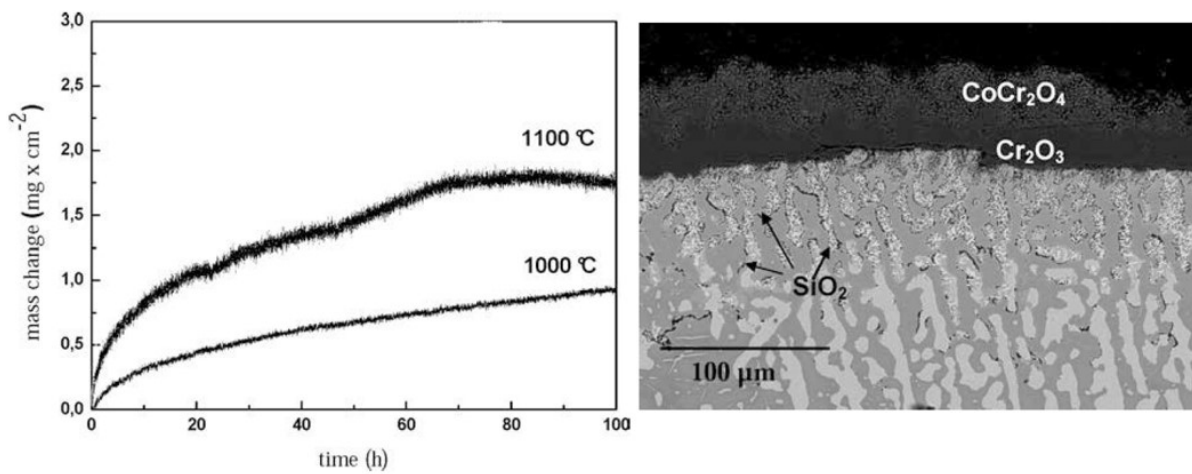
Figure 2.16: TGA results of alloy Co-17Re-30Cr-2Si (left) and cross-sectional image of the alloy Co-17Re-30Cr-2Si after oxidation at 1000°C in air for 72h (right) [94]

3 Materials and examination methods

To further study the oxidation behavior of Co-Re-base alloys, especially the effect of the element additions aiming to improve the oxidation resistance, various model alloys were produced for oxidation tests. Kinetic studies and the subsequent examination and analysis of oxidation products were carried out. Further, thermodynamic studies were performed and microstructural changes of the model alloys were investigated for establishing the oxidation mechanisms.

3.1 Materials and specimen preparation

3.1.1 Material production and chemical compositions

The materials investigated in this work were provided by the Institute for Materials at the Technical University of Braunschweig as part of the DFG research group "FOR727". These alloys were produced by vacuum arc-melting using elementary substances with high purity (>99.98%) and cast in bar form with a general dimension of 11mm × 11mm × 50mm, as shown in Figure 3.1. Most of the cast bars were stepwise annealed in a vacuum furnace for homogenization. Their chemical compositions, together with the heat treatment conditions, are listed in Table 3.1. At the end of the annealing, the bars were quenched by argon flow within the vacuum furnace.

Figure 3.1: Cast alloy bar after heat treatments

Table 3.1: Chemical compositions (at.%) and heat treatment conditions of alloys investigated

Alloys	Co	Re	Cr	Si	Al	B	Y	Ni	Heat treatment
Co-17Re-9Si-8B	bal.	17	-	9	-	8	-	-	as cast
Co-17Re-23Cr	bal.	17	23	-	-	-	-	-	ST1*
Co-17Re-23Cr-2Si	bal.	17	23	2	-	-	-	-	ST1
Co-17Re-23Cr-3Si	bal.	17	23	3	-	-	-	-	ST1
Co-17Re-23Cr-4Si	bal.	17	23	4	-	-	-	-	ST1
Co-17Re-25Cr-2Si	bal.	17	25	2	-	-	-	-	ST1
Co-17Re-27Cr-2Si	bal.	17	27	2	-	-	-	-	ST1
Co-17Re-23Cr-5Al	bal.	17	23	-	5	-	-	-	ST2*
Co-17Re-23Cr-10Al	bal.	17	23	-	10	-	-	-	ST2
Co-17Re-25Cr-2Si-0.05Y	bal.	17	25	2	-	-	0.05	-	ST1
Co-17Re-25Cr-2Si-0.1Y	bal.	17	25	2	-	-	0.1	-	ST1
Co-17Re-23Cr-15Ni	bal.	17	23	-	-	-	-	15	ST1
Co-17Re-23Cr-15Ni-AT	bal.	17	23	-	-	-	-	15	ST1+ AT*

*   ST1 represents for solid solution heat treatment condition 1 (1350°C/5 h + 1400°C/5 h + 1450°C/5 h), ST2 represents for solid solution heat treatment condition 2 (1350°C/7.5 h + 1400°C/7.5 h), and AT represents for annealing heat treatment (1050°C/4 h).

3.1.2 Specimen preparation

Specimens with about 2 mm in thickness were cut from the received bars by wire-cut electrical discharge machining. It is well-known that surface roughness plays an essential role in the high-temperature oxidation behavior of metals, especially in the early stage of reaction [100]. Hence, like those investigated in Gorr's previous work, samples for the oxidation test in this work were stepwise wet-ground down to 1200 grit using silicon carbide abrasive paper to provide a reasonable comparison. The edges of specimens were slightly ground to minimize the edge effect on oxidation. Before the oxidation test, samples were ultrasonically cleaned in acetone and ethanol and finally dried.

For microstructural characterization, samples were in general wet-ground down to 4000 grit followed by polishing using diamond suspension down to 1 μm. In the case of EBSD (electron backscatter diffraction) measurements, the grinding/polishing-induced residual stresses on the alloy surface were removed by a final vibratory polishing for about 10 hours, using a colloidal silica suspension with a particle size of 0.02 μm.

3.1.3 Shot-peening

To study the influence of bulk material diffusion on the oxidation behavior of Co-Re-base alloys, shot-peening treatment using ceramic balls (125-250 μm) was carried out on selected specimens after standard groundwork (down to 1200 grit). The setup as well as the parameters are shown in Figure 3.2. The benefit of this approach is that the shot-peening process brings random microplastic deformation on the alloy surface, which increases the dislocation density in the subsurface region. This subsurface dislocation-network is generally considered as a fast diffusion path for the protective oxide-scale forming elements, such as Al and Cr.
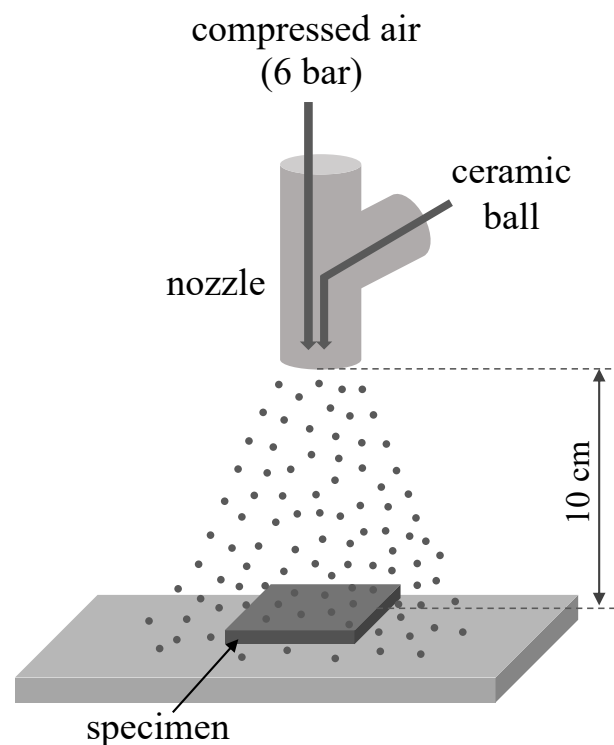
Figure 3.2: Setup of the shot-peening treatment

3.1.4 Hardness test

The Vickers small load hardness tester (Struers Duramin) was used to characterize the shot-peening-induced residual stress underneath the sample surface. This was done by making a series of hardness measurements from the edge of the cross-sectioned sample towards the center. The small size of the microhardness indents produced by this technique provides a unique possibility to measure in different phases at a specific position separately. At least five measurements were carried out for each area of interest to minimize the error.

3.2 Oxidation tests

Continuous thermogravimetric analysis (TGA) was used as the most crucial method to assess the reaction kinetics. Figure 3.3 illustrates the fundamental setup of the TGA apparatus, where the specimen was suspended to an automatic recording electromagnetic microbalance (accuracy 10^{-6}g) within a reaction chamber. During the oxidation tests, the weight change of specimen through gas uptake (i.e., oxygen and nitrogen), scale spallation, or the evaporation of oxidation products (i.e., Re oxides) was continuously recorded as a function of time. Most of the TGA measurements in this work were conducted in quasi-static laboratory air. The gaseous mixture of He, He/H_2, and H_2O was used to provide a low oxygen partial pressure atmosphere for some specific measurements. The oxygen partial pressure was set through the ratio H_2/H_2O and was continuously monitored by a lambda sensor direct under the specimen.

In addition to the stationary experiment, a thermocyclic oxidation test is necessary for studying the adhesion behavior of the oxide scale. The magnetic levitation thermobalance from Rubotherm (accuracy $0.1\mu g$) used in this work enables a fully automatic cyclic testing process including the continuous monitoring of the weight change of specimen.

While TGA measured the continuous weight changes, discontinuous isothermal oxidation experiments were performed to investigate the oxide morphology toward establishing the oxide scale growth mechanism. For this purpose, samples were exposed to laboratory air at 800-1300°C in a stationary annealing furnace for different durations, such as 5 min, 1 h, 5 h, 24 h, 72 h, etc. After the exposure time, the samples were directly taken out from the furnace and cooled in air. For each exposure time, a separate specimen was used.
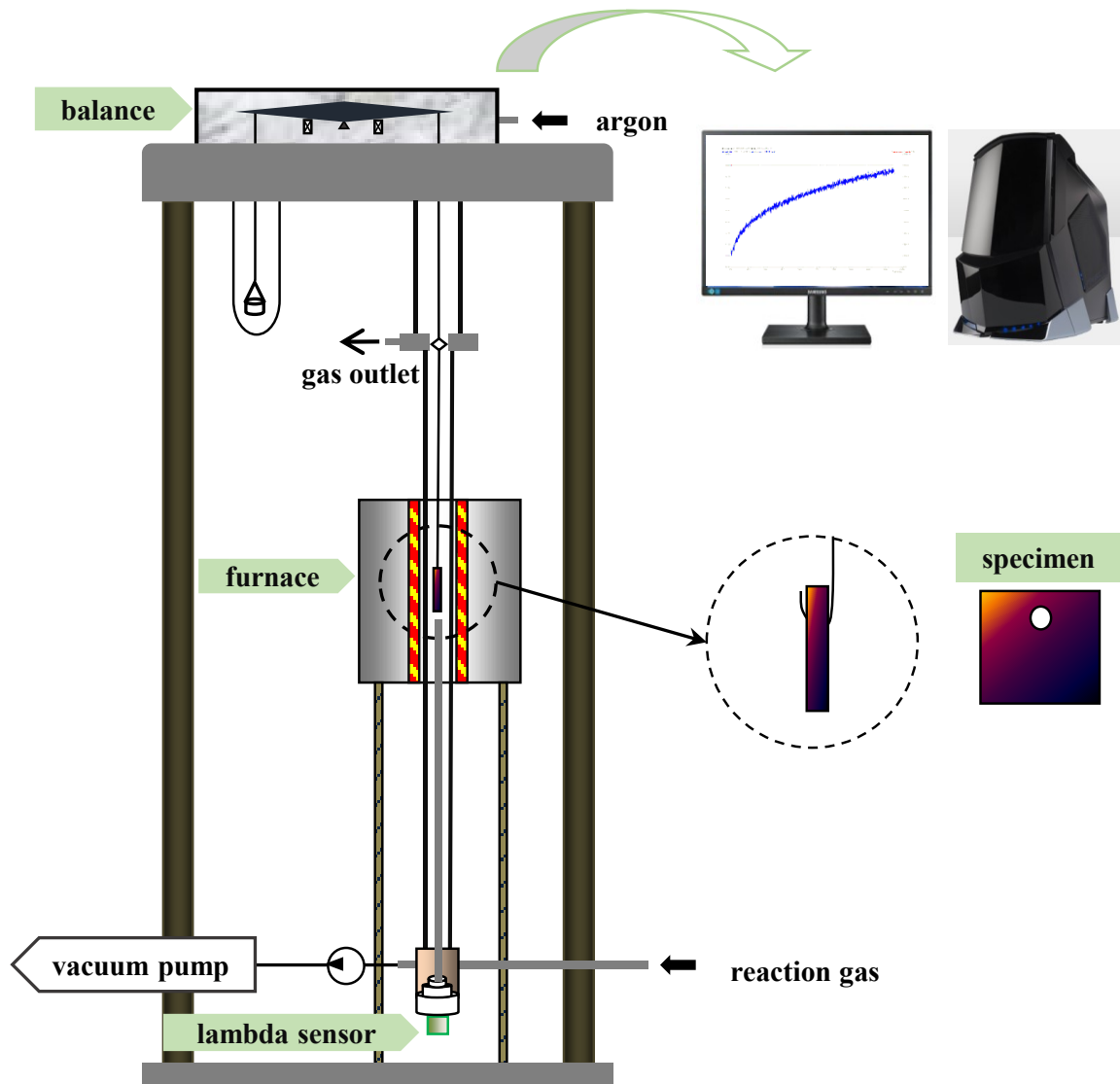
Figure 3.3: Schematic illustration of a TGA apparatus for measuring weight change during the high-temperature reaction in a controlled gas atmosphere

3.3 Microstructural characterization

3.3.1 X-ray diffraction

X-ray diffractometry (XRD) was employed to determine the crystalline structure of the alloys and the oxides formed on the specimens. To do so, an X'Pert X-ray diffractometer with a position-sensitive detector from Panalytical was used. The working principle of XRD is based on Bragg's law, which shows how the interplanar spacing in a crystal relates to the diffraction angles:

$$n\lambda = 2d\sin2\theta \qquad (3.1)$$

where n is an integer, λ is the X-ray wavelength, d is the interplanar spacing of the examined crystal, and θ is the incident angle (Bragg angle).

XRD measures the intensity distribution of the elastically scattered X-rays and demonstrates the detected intensity as a function of scattering angle in a profile, in which when the Bragg's law is fulfilled, diffraction peaks can be detected. The peak position can be used to determine the spacing between various lattice planes. Comparing the measured locations of the X-ray peaks (i.e., the Bragg angles) with the commercial database from the International Center for Diffraction Data (ICDD) allows identifying the phases that exist in the specimen.

3.3.2 Scanning electron microscopy

Scanning electron microscopy (SEM) was intensively used to investigate the oxide morphology and the microstructural changes of the alloys after oxidation. Most of the SEM investigations in this work were carried out on an ultra-high field emission SEM of type Helios NanoLab 600, which is equipped with the function of energy-dispersive X-ray spectroscopy (EDS), electron backscatter diffraction (EBSD), and focus ion beam (FIB).

Generally, specimens for surface characterization were directly investigated after the oxidation tests, whereas the specimens for cross-sectional investigations were Au-spattered and electroplated with a protective nickel-layer followed by embedding, grinding, and final polishing. The specimens for cross-sectional characterization in the Helios NanoLab 600 were then divested of the embedding materials to avoid unexpected contamination. Some of the specimens, which are generally covered by either extremely thick or brittle oxide layers, were directly embedded and investigated in another SEM (Philips XL30). The Au-spattering and Ni-plating as well as the divestment from the embedding materials were unnecessary for such cases.

Depending on perspective, an appropriate signal/detector was applied. The secondary electron (SE) detector was used to image the surface morphology, since the secondary electrons emerged from the regions near the sample surface. In contrast, the backscattered electron (BSE) detector was used for qualitative observation of the chemical element distribution in the microstructure because the backscattered electrons were reflected by elastic scattering and related to the average atomic number of the material. Heavy elements, e.g., Re, strongly backscatter electrons. Hence, those areas rich in Re appear brighter. Lighter elements, e.g., O, tend to absorb electrons and thus appear darker. For this reason, the BSE images were mainly taken for the cross-sections, where the oxide layers appear darker than the substrate. Consequently, the morphology and distribution of the Re-rich σ phase in alloys could be directly observed using the BSE signal.

3.3.3 Energy-dispersive X-ray spectroscopy and electron backscatter diffraction

The energy-dispersive X-ray spectroscopy (EDS) was used for quantitative chemical analysis. The way EDS analysis works is that the electron beam hits and knocks out an electron from the inner shell of an atom, leaving an electron vacancy. To maintain a stable state, an electron from the outer higher-energy shell tends to transit into the inner lower-energy shell of the atom. The energy difference can then be released as an X-ray emission. Since the emitted X-ray energy is unique to the specific element and transition, these X-ray quanta are collected according to energy and number by a silicon drift detector. From this signal, the chemical composition and the element distribution can be calculated. This technique is of great importance to study the cross-section of oxidized specimens by identifying the chemical constitution of the multi-layer oxide scales. Three different EDS scan modes, i.e., point-analysis, line-scan, and 2D-mapping, were optional for specific interests. In combination with the electron backscatter diffraction (EBSD) technique used for the crystallographic microstructural investigation, it was possible to identify the alloy phase transformation during oxidation, especially in the subsurface region.

In contrast to the XRD technique, which characterizes the sample grains globally, the EBSD technique can provide local phase information and crystal orientation of individual grains. The working principle of EBSD is that the backscattered electrons can be diffracted by atomic lattice planes in the crystalline materials that meet the Bragg diffraction condition. The diffracted electrons hit the built-in phosphor screen and generate a pattern of Kikuchi bands, the width of which are dictated by the Bragg Law and the distance between the specimen and the phosphor screen. From the geometry of the Kikuchi bands, the crystallographic phase and orientation can be determined by comparison with the database.

3.3.4 Transmission electron microscopy and focus ion beam

Compared to SEM, transmission electron microscopy (TEM) provides a possibility for high-resolution microstructural analysis in the nanometer range and allows for a deep insight into the oxidation products. One of the unique functions of the Helios NanoLab 600 is the integrated FIB technique, which is of great importance for the preparation of TEM samples (electron transparent foils) containing oxide scales. As an example, the TEM lamella prepared by FIB from an oxidized Co-17Re-25Cr-2Si-0.1Y specimen is shown in Figure 3.4. The TEM investigations in this work were carried out in a high-resolution TEM of type Philips CM200-FEG in the Juelich Research Centre.

Furthermore, the FIB technique was also used as a specific preparation method for the cross-sectional SEM investigations at selected positions, avoiding damage to the oxide layer caused by the general sample preparation techniques during embedding, grinding, and polishing.
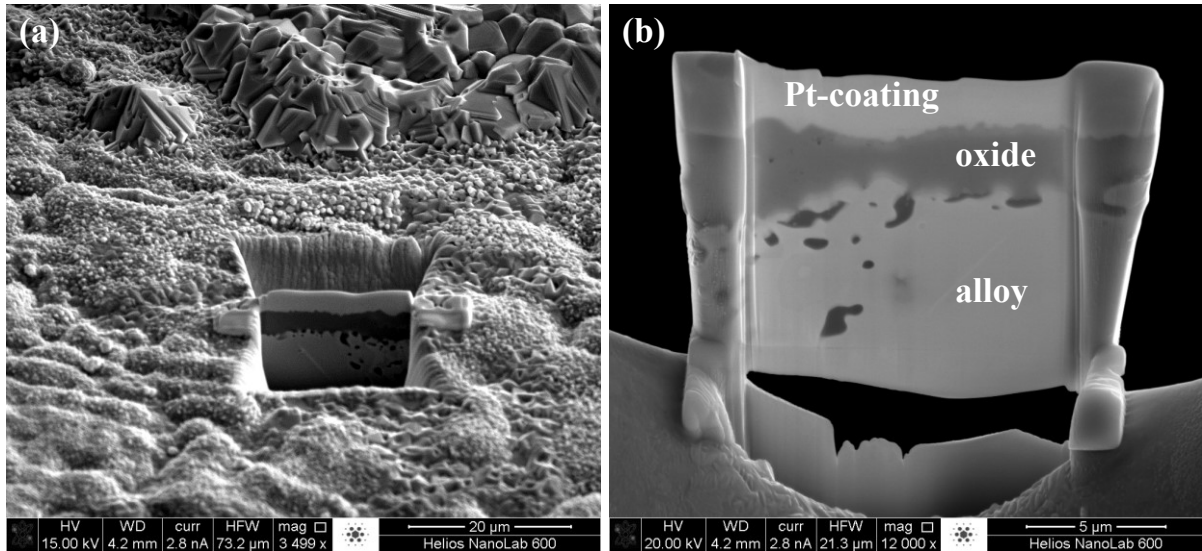
Figure 3.4:   TEM lamella prepared by FIB from alloy Co-17Re-25Cr-2Si-0.1Y oxidized at 1000°C for 24 h; (a) TEM-lamella incised by Ga-ion beam after deposition of a protective platin coating and (b) TEM-lamella cut free and finally polished by Ga-ion beam

3.4 Thermodynamic calculation

To better understand the oxidation behavior of the alloys, thermodynamic calculations were conducted with commercial software FactSage (Version 5.4) based on the so-called CALPHAD (CALculation of PHAse Diagram) methodology. The CALPHAD methodology provides analytical expressions of all thermodynamic state functions of a system and is used to minimize the Gibbs energy. The Gibbs energy of the phases of a system is calculated as a function of the state variables (temperature, pressure, concentration) using a variety of mathematical models (e.g. model of the ideal and non-ideal solution, sublattice model, etc.), which are not presented in this thesis. The essential theoretical background, practical assignments, and guided instruction are given elsewhere by FactSage-Teach [101]. Some application examples for the Co-Re-base alloys can be found in ref. [40].

4 The effect of Si (-B) alloying

Previous research by Gorr [26] has established that the addition of 1-3% silicon to the Co-17Re-23Cr model alloy significantly and successively improves its oxidation resistance. A quasi-continuous chromia layer can be observed on alloy Co-17Re-23Cr-3Si after oxidation at 1000°C in air. Compared to chromia, a silica layer formed on an alloy surface is generally considered to be more protective against long-term oxidation at elevated temperatures due to its slower growth rate. Regarding the silicon effect on the oxidation behavior, the first set of questions is, whether an intrinsic protective SiO_2 layer can form on the Co-Re-base alloy or not? Are the potential concepts harmful to other properties of the alloy? Is there any possibility of balancing them?

4.1 Silicon in ternary Co-Re-Cr alloys

Based on these questions above and the fact that the addition of 3% silicon to the reference alloy Co-17Re-23Cr is insufficient to form a silica layer, but rather it forms SiO_2 internal oxide particles underneath a quasi-continuous Cr_2O_3 scale, the model alloy Co-17Re-23Cr-4Si with 4% silicon was additionally investigated in this work. The results, in combination with the previous studies, will be presented and discussed in the following.

4.1.1 Alloy Co-17Re-23Cr-*x*Si

Figure 4.1 shows the microstructure in BSE images of the reference alloy Co-17Re-23Cr and the alloys Co-17Re-23Cr-*x*Si containing different Si content (1-4%). Like the Si-free alloy Co-17Re-23Cr, all Si-containing alloys consist of hcp matrix and σ phase. It is noticed that the microstructure in Figure 4.1 in terms of the distribution of the primary σ phase is significantly affected by the increase of the Si content. Automated image analysis applying the software Image J was conducted to measure the volume fraction of the primary σ phase. Five images were taken from different areas of each sample to obtain average values. As presented in Figure 4.1f, the σ phase volume fraction increases from about 2% in the Si-free alloy Co-17Re-23Cr to around 23% in alloy Co-17Re-23Cr-4Si. It is important to point out that such measurements were carried under the as-received condition of the alloys (see Table 3.1), which is very likely not in the equilibrium state. Moreover, a significant positive correlation between the Si content and the average particle size of the primary σ phase is observed.
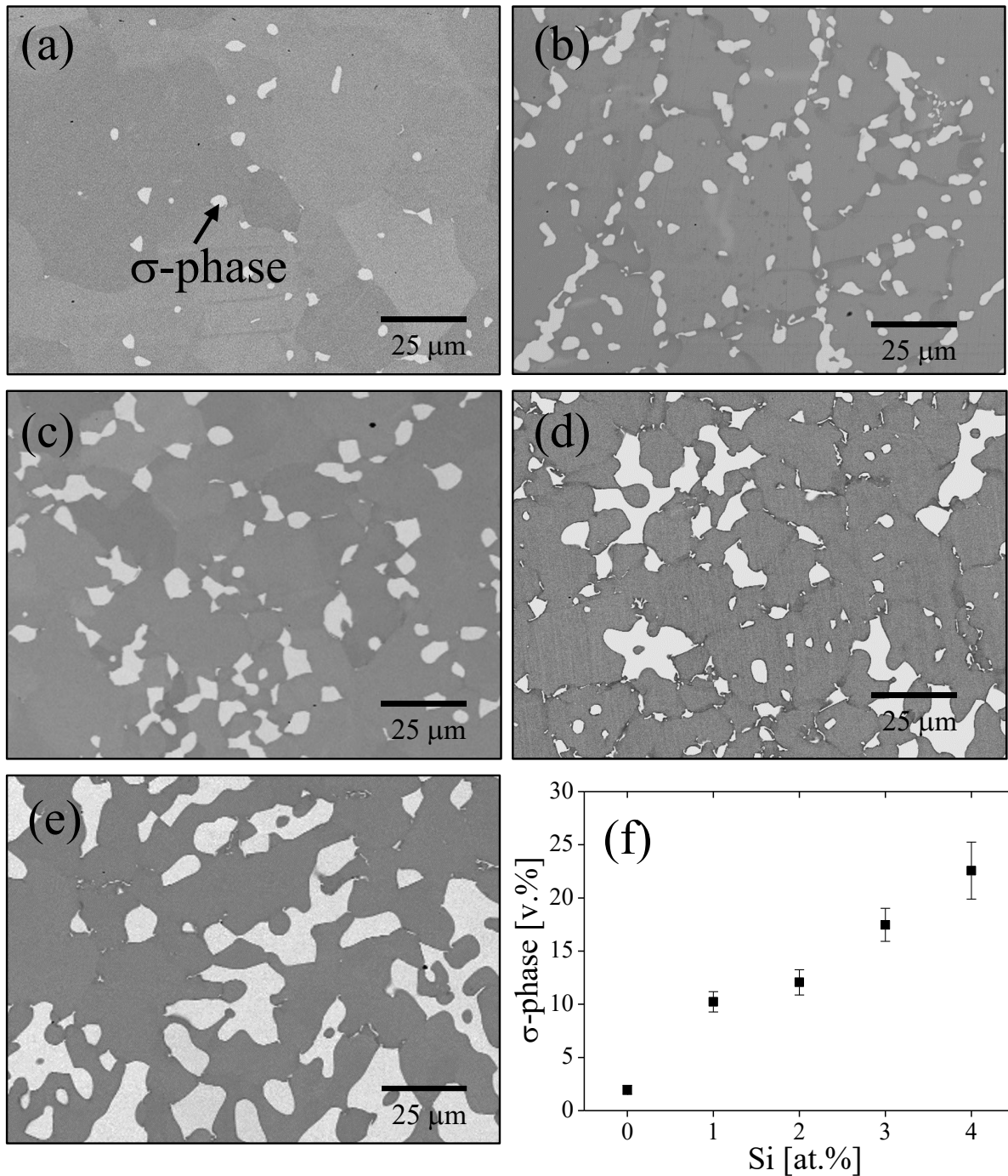
Figure 4.1: Microstructure comparison of the model alloys Co-17Re-23Cr-*x*Si with different Si content, (a) without Si; (b) with 1% Si; (c) with 2% Si; (d) with 3% Si; (e) with 4% Si; (f) measured volume fraction of the σ-phase in the corresponding alloys

4.1.2 Oxidation results

The specific weight change, i.e., the weight change per unit surface area, of the alloys Co-17Re-23Cr-(0-4)Si during the oxidation test at 1000°C is compared in Figure 4.2. The addition of 4% Si obviously

significantly changes the oxidation kinetics from weight loss to weight gain. Additionally, the weight gain curve of the alloy Co-17Re-23Cr-4Si shows a parabolic manner, which is a typical indication of the growth of the compact oxide scale.
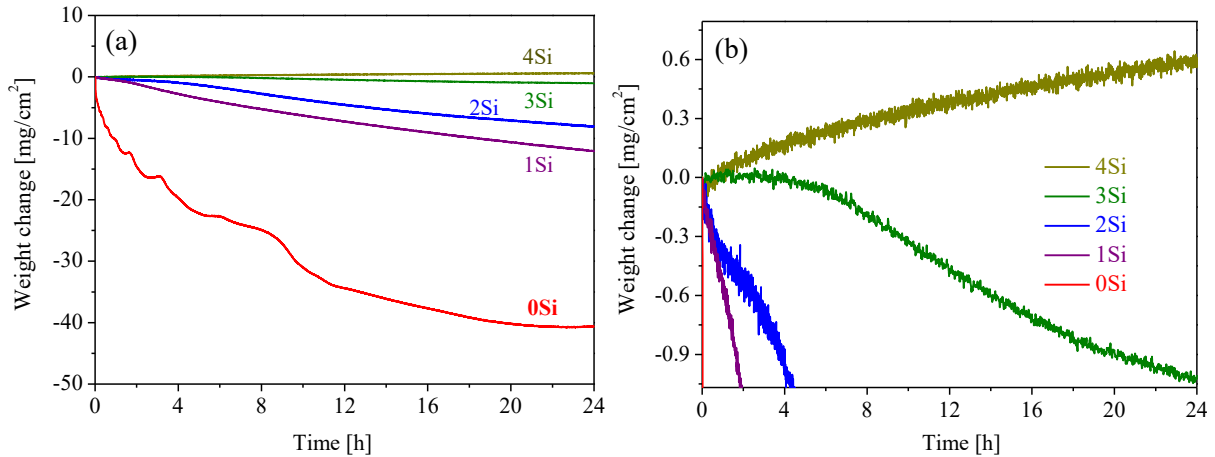

Figure 4.2:   (a) Comparison of the thermogravimetric data of Co-17Re-23Cr-xSi alloys during oxidation at 1000°C in air; (b) higher magnification (data partially taken from [32])

Figure 4.3 shows the surface morphology of the alloys Co-17-23Cr-3Si and Co-17Re-23Cr-4Si after oxidation at 1000°C for 100 h. During the cooling process after the isothermal oxidation tests, cracking and spallation of the oxide layer occurred on both alloys. It can be seen from Figure 4.3a and c that the oxide layer on alloy Co-17Re-23Cr-3Si is partially spalled off, whereas the one on alloy Co-17Re-23Cr-4Si is almost entirely spalled off, leaving behind few of the oxide debris on the surface. By further examining the remaining oxide scales under higher magnification, the outermost oxide-layer on alloy Co-17Re-23Cr-3Si is found to be composed of two distinct types of oxide, one with coarse grains and the other with fine equiaxed grains, as shown in Figure 4.3b. Chemical analysis by EDS indicates that the coarse-type is pure cobalt oxide and reveals O, Cr, and Co in the fine-type, where the Cr intensity is very strong. Unlike Co-17Re-23Cr-3Si, the oxide surface morphology on alloy Co-17Re-23Cr-4Si is relatively uniform, and its chemical content is found to be similar to that of the fine-grain-oxides on alloy Co-17Re-23Cr-3Si by EDS.

Figure 4.4 shows the cross-sectional BSE image of both alloys after oxidation at 1000°C for 100 h. It is seen that the scale formed on alloy Co-17Re-23Cr-3Si is rather nonuniform but can be roughly classified into two types. This appears to make sense and to be compatible with the surface observation in Figure 4.3b. The XRD and EDS analysis suggest that the area with thick oxide scale is quite similar to the scale on Co-17Re-23Cr-1Si reported by Gorr et al. [32], consisting of outermost CoO with a coarse grain structure, porous $CoCr_2O_4$ spinel, and semi-continuous and thin Cr_2O_3 layer at the alloy/scale interface. SiO_2 precipitates are found underneath the oxide scale. However, the nature of such a multi-layer scale is non-protective and allows further deterioration of the base alloy, resulting from the evaporation of Re

oxide. To simplify the description, this kind of non-protective oxide scale constitution will be named as "typical multi-layer scale" in the following part of this work. In the other area, as magnified in Figure 4.4a, a dense and continuous chromia layer is observed underneath a thin outermost $CrCo_2O_4$ layer. Beneath the external oxide scale, SiO_2 internal precipitates in this region are more laterally connected than that in the region with the typical multi-layer scale. Although the oxide layer of the Co-17Re-23Cr-4Si was almost wholly broken away during cooling, it is clear to see that the base alloy was barely destructed compared to the alloy Co-17Re-23Cr-3Si. Based on the evidence of the parabolic thermogravimetric data and the oxide surface morphology, it can be proposed that a homogeneous protective Cr_2O_3 layer was formed on the alloy Co-17Re-23Cr-4Si under the experimental conditions, and thus this layer prevented the oxidation of Re and the evaporation of its oxide. Further, many secondary σ precipitates are found in both alloys substrate after the oxidation test.
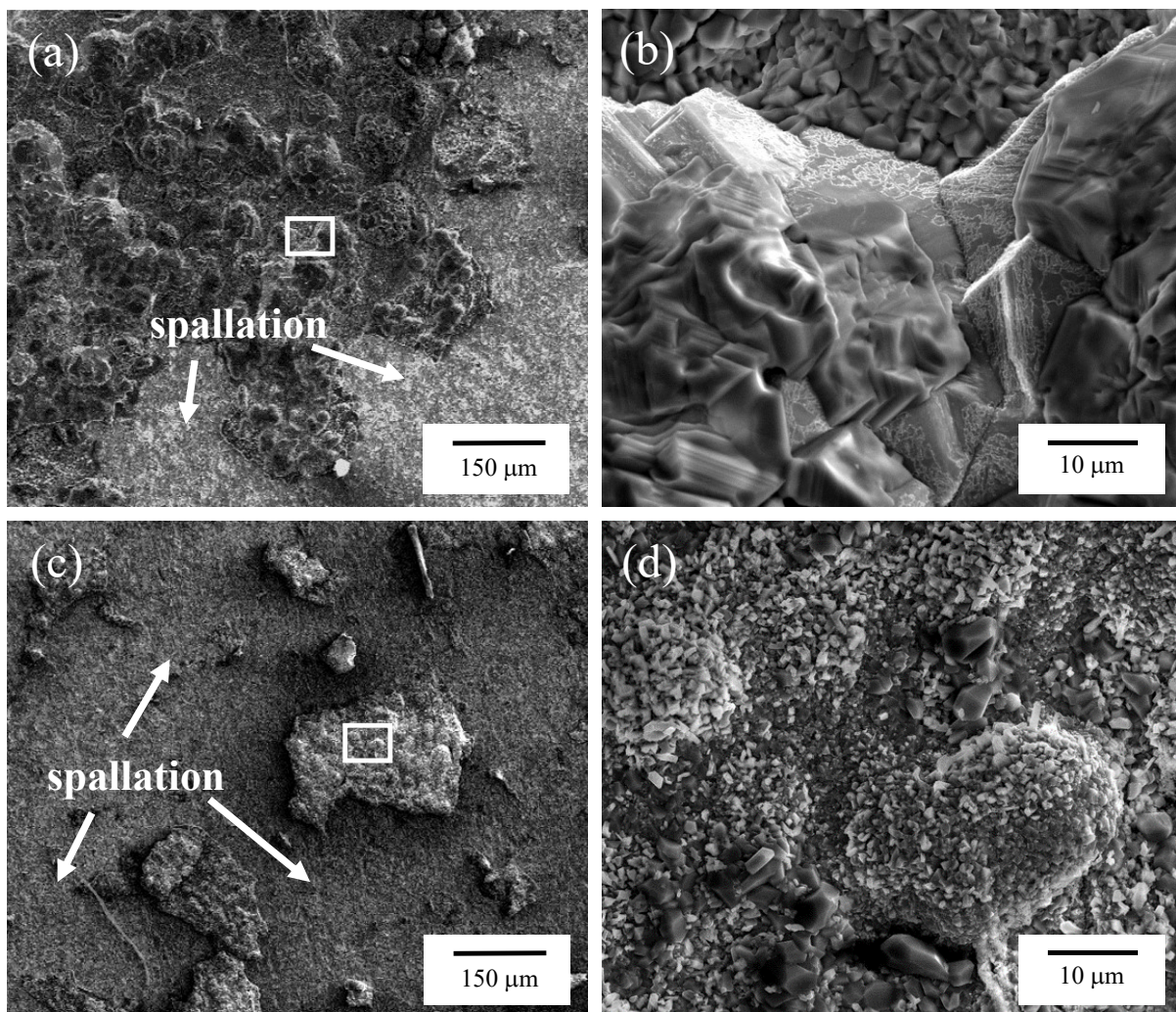

Figure 4.3:   SE-SEM surface images of alloy Co-17Re-23Cr-3Si (a & b) and alloy Co-17Re-23Cr-4Si (c & d) after oxidation at 1000°C for 100 h; (b) and (d) with higher magnification taken from the marked area in (a) and (c), respectively
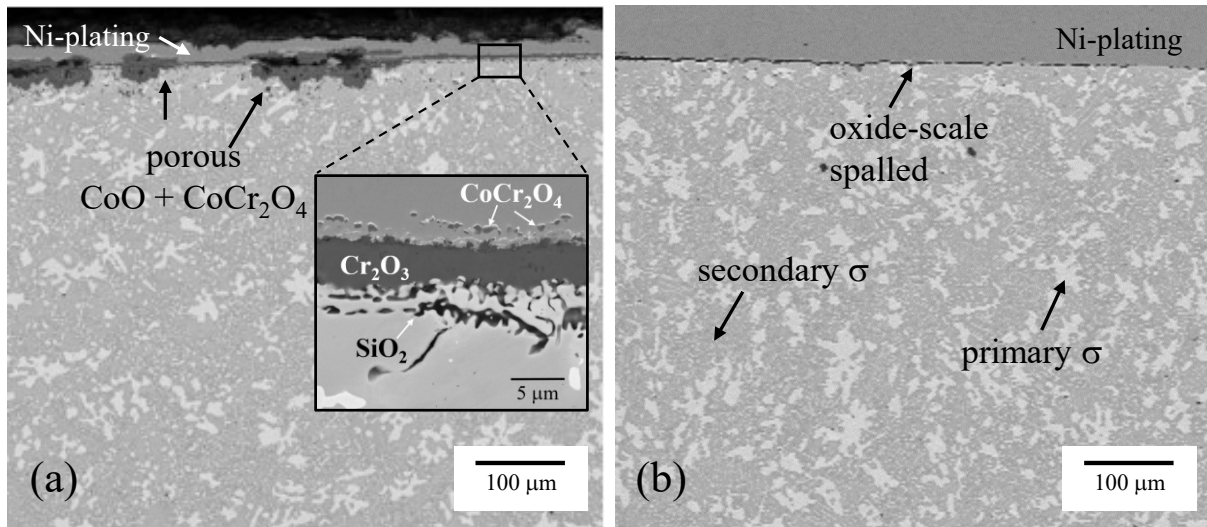
Figure 4.4:   Cross-sectional BSE-SEM images after oxidation at 1000°C for 100 h; (a) Co-17Re-23Cr-3Si and (b) Co-17Re-23Cr-4Si

Weight change data of alloy Co-17Re-23Cr-3Si and alloy Co-17Re-23Cr-4Si at 900°C is shown in Figure 4.5. Both curves consist of a rapid initial weight loss and a following relatively constant state. It is assumed that the evaporation of rhenium oxide dominates the specimen weight change in the early stage of oxidation. As the process continues, the oxide scales formed on both alloys are getting more protective but are still insufficiently dense to completely prevent the oxidation of rhenium, resulting in a balance between the weight loss through the evaporation of rhenium oxide and the weight gain through oxygen uptaking by oxidation. The initial weight loss of alloy Co-17Re-23Cr-3Si is more than twice compared to that of alloy Co-17Re-23Cr-4Si. Nevertheless, a slight tendency to further weight loss is observed on alloy Co-17Re-23Cr-4Si. This should not be attributed to any oxide spallation during the test because of the absence of a sudden weight change, but rather a balance shift to slower oxygen uptake and/or accelerated rhenium oxide evaporation seems to occur.

As the pictures of the oxidized specimens shown in Figure 4.5, the entire oxide scale formed on alloy Co-17Re-23Cr-3Si exhibits excellent adhesion behavior, while the alloy Co-17Re-23Cr-4Si suffers from the spallation during cooling after the oxidation test. The comparison of the cross-sectional BSE images of both specimens, shown in Figure 4.6, indicates that the scale formed on alloy Co-17Re-23Cr-3Si is relatively homogeneous, consisting of a typical non-protective multi-layer structure whereas that on alloy Co-17Re-23Cr-4Si is composed of two distinct scale morphologies. Besides the typical non-protective multi-layer scale (left part in Figure 4.6b), a region with a thin and compact chromia layer is observed on Co-17Re-23Cr-4Si.
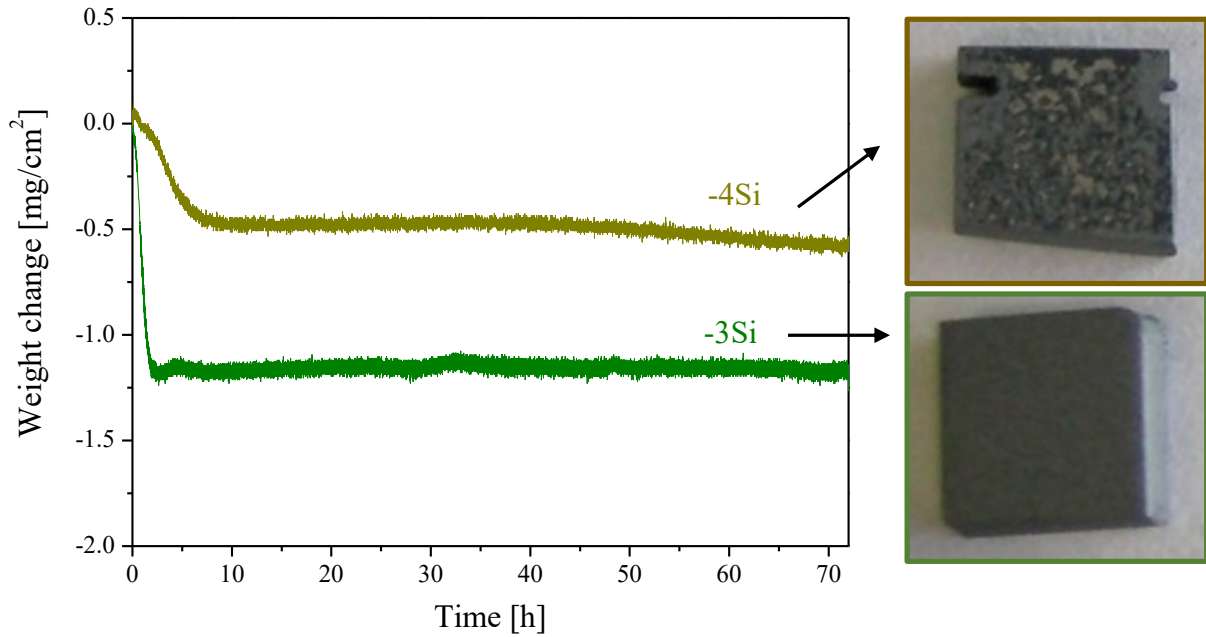
Figure 4.5:   Specific weight change data in combination with sample images of Co-17Re-23Cr-3Si and Co-17Re-23Cr-4Si after oxidation at 900°C in air for 72 h
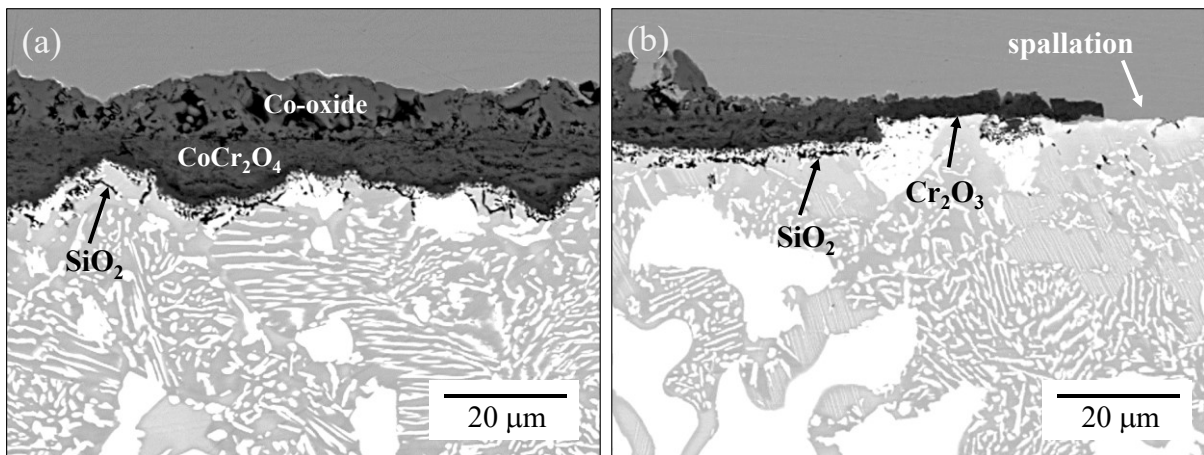
Figure 4.6:   Cross-sectional BSE-SEM images after oxidation at 900°C for 72 h; (a) Co-17Re-23Cr-3Si and (b) Co-17Re-23Cr-4Si

It is worth noticing that the substrate material underneath the dense external Cr_2O_3 layer on alloy Co-17Re-23Cr-4Si is barely attacked. Rarely internal SiO_2 precipitates can be observed in the vicinity of the chromia/alloy interface. Another critical note must also be made here, namely that the oxide scale spallation during cooling mainly happens in the chromia-forming region, which is about half of the entire sample surface. This observation is similar to the phenomenon observed at 1000°C, where the scale is almost entirely spalled off.

At 1100°C, the scales formed on both alloys suffer the same severe spallation, as shown in Figure 4.7. This evidence suggests that as the temperature and Si content increase, a thin SiO_2 layer might form at the chromia/alloy interface during oxidation, which later intensifies the external chromia scale spallation during cooling. In support of this hypothesis, it has been reported by Douglass and Armijo [102] that a continuous film of silica was observed under the chromia layer on the alloy Ni-20Cr-3Si containing 3 wt.% Si, whereas a 1 wt.% concentration of silicon in alloy Ni-20Cr-1Si was insufficient to form a continuous SiO_2 layer at 1200°C. The scale formed on Ni-20Cr-3Si was reported to spall extensively during cooling and was found to be extremely sensitive to thermal shock. Another study by Evans et al. [103] reported that the stainless steel with a higher silicon amount released far more spall than the steel containing lower silicon content.
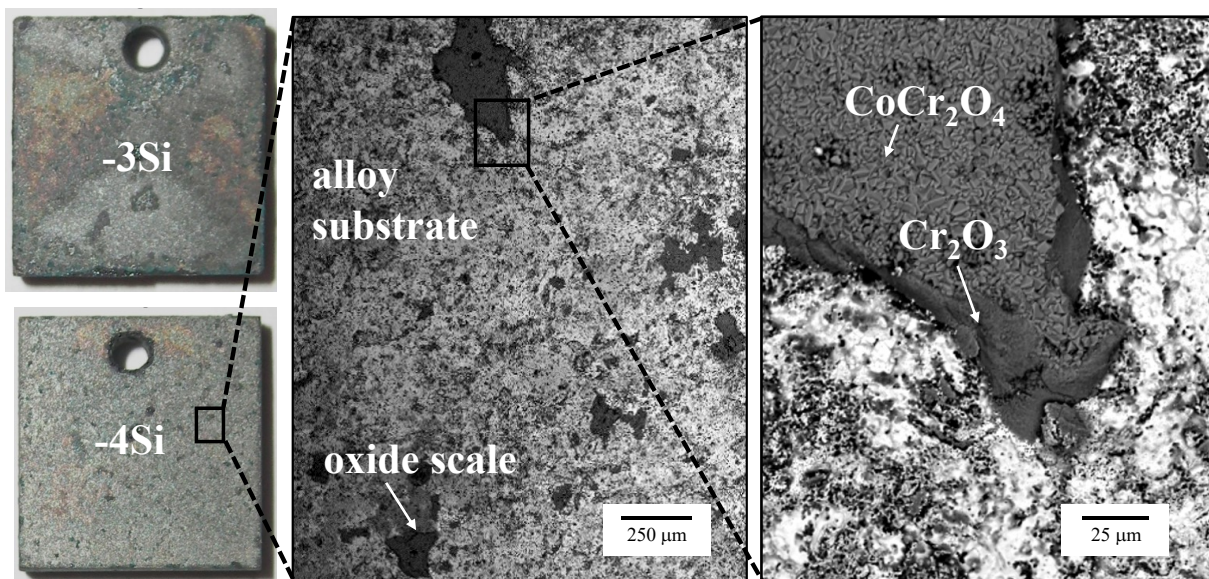
Figure 4.7:   Pictures and BSE-SEM surface images of Co-17Re-23Cr-3Si and Co-17Re-23Cr-4Si after oxidation at 1100°C in air for 72 h, showing severe spallation of the oxide scale

4.2 The Si-B effect

As presented above, the Si addition significantly improves the isothermal oxidation resistance of the reference alloy Co-17Re-23Cr by facilitating a chromia scale formation. However, the evidence also reveals that the increase of Si content in alloy Co-17Re-23Cr from 1% to 4% dramatically increases the volume fraction and particle size of the primary σ phase, which cannot be reduced or refined by further annealing heat treatment and is, therefore, undesired from the viewpoint of mechanical properties. Besides, high silicon content enhances the spallation of the protective scale formed. Considering all the above, a further increase of Si content to the ternary Co-Re-Cr system towards forming a dense, protective, and adhesive silica layer is not reasonable.

Within the framework of the DFG research group "FOR 727", Burk [104] reported that a dense protective B_2O_3-SiO_2 layer was formed on alloy Mo-9Si-8B in the temperature range 1100-1300°C due to the simultaneous additions of Si and B. In light of this, a preliminary study on the quaternary model alloy Co-17Re-9Si-8B without Cr was carried out, aiming to examine the applicability of this concept to the Co-Re alloy system. The results of the isothermal oxidation behavior are shown below.

4.2.1 Alloy Co-17Re-9Si-8B

Unlike the other alloys dealt with in this work, the alloy Co-17Re-9Si-8B was directly studied after arc-melting without the typical heat treatment up to 1450°C. The alloy ingot was remelted several times during arc-melting to avoid inhomogeneity. The microstructure of the alloy Co-17Re-9Si-8B as received in the BSE-SEM/EDS analysis combination is shown in Figure 4.8. It is seen that the overall microstructure of the alloy is homogeneous but quite complex. At least four different phases, including some eutectic morphology, could be identified. It should be mentioned that the quantitative analysis of the light element boron through the EDS technique employed is quite difficult. The EDS results were therefore integrated without B and might not be precise. However, the relative element distribution of Co, Re, and Si in the presented phases could still be meaningful.

Element	Wt%	At%
SiK	2.29	9.78
CoK	19.53	39.79
ReL	78.19	50.43

Element	Wt%	At%
SiK	18.60	32.41
CoK	81.40	67.59

Element	Wt%	At%
SiK	2.85	9.57
CoK	37.53	60.17
ReL	59.63	30.26

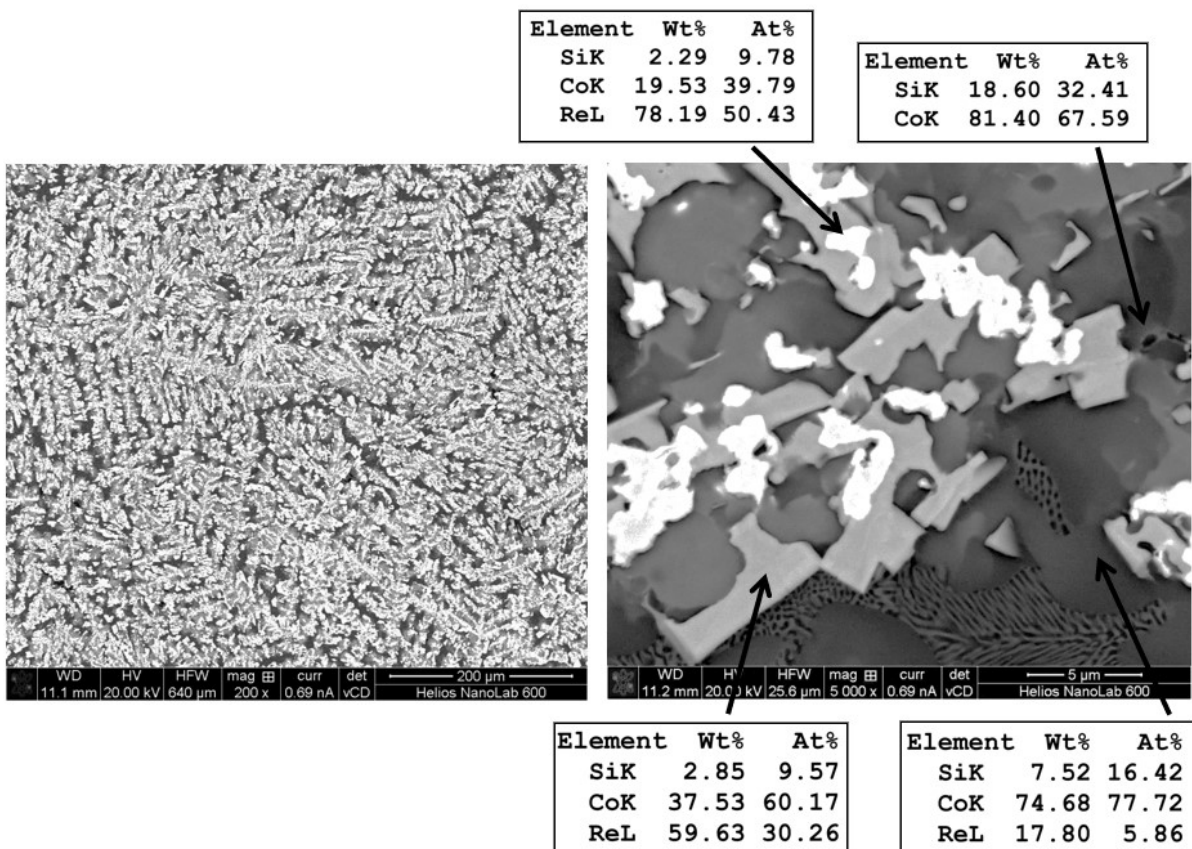| Element	Wt%	At%
SiK	7.52	16.42
CoK	74.68	77.72
ReL	17.80	5.86

Figure 4.8: Microstructural BSE-SEM images of the alloy Co-17Re-9Si-8B in combination with chemical analysis results by EDS

4.2.2 Oxidation results

The weight change vs. time plot of Co-17Re-9Si-8B during exposure to air at 900-1100°C is presented in Figure 4.9. It is seen that a significant change in oxidation behavior occurs when the oxidation temperature increases from 900°C to 1100°C. While the TGA curve at 900°C is nearly flattened and mass gain kinetics is observed at 1000°C, severe weight loss occurs at 1100°C after a short but fast weight-gaining period.
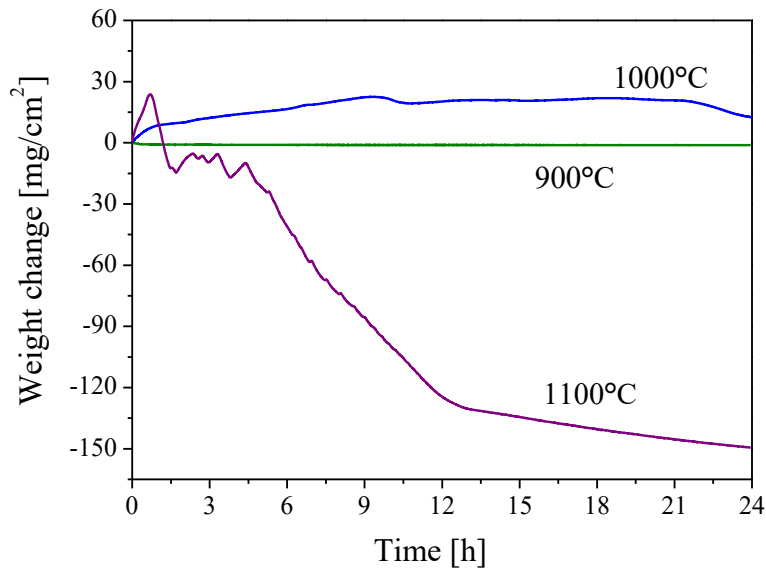

Figure 4.9: Specific weight change vs. time for the alloy Co-17Re-9Si-8B oxidized in laboratory air

The microstructure examination of the oxidized specimens reveals that the oxide scale formed at 900°C is basically composed of an outer Co oxide layer followed by a compact Co_2SiO_4 layer, as shown in Figure 4.10. In addition to a semi-continuous SiO_2 layer at the scale/alloy interface, many Si-O-rich spheres are found over the outermost oxide layer. BSE-SEM image of a short-term oxidized specimen (Figure 4.10c) indicates that those spheres form directly above the Si-rich Co-silicide (probably also rich in B). A similar morphology is observed in Mo-Si-B alloys and reported to be borosilicate [20]. The enrichment of Re (brighter contrast in Figure 4.10b) directly underneath the scale implies the protectiveness of the scale against Re oxidation and its evaporation.
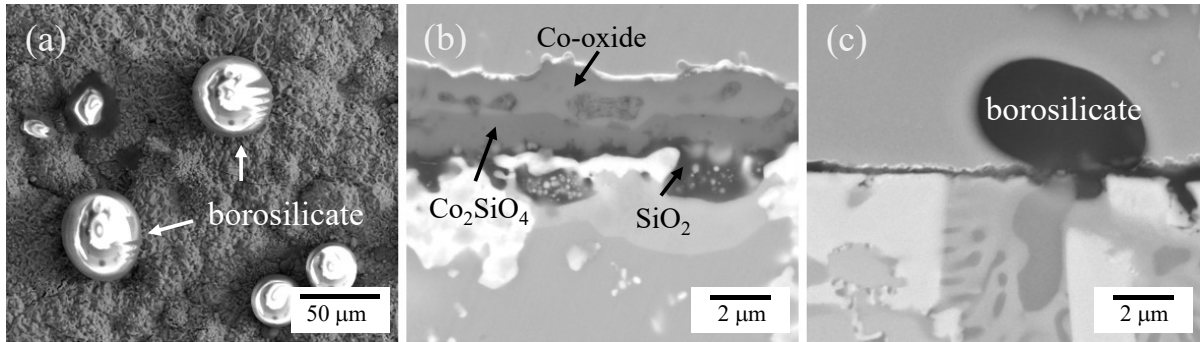
Figure 4.10: Microstructural images of oxides formed on alloy Co-17Re-9Si-8B at 900°C: (a) Surface SE-SEM image; Cross-sectional BSE-SEM image after oxidation for 72 h (b) and for 10 min (c)

During oxidation at 1000°C, the growth of the Co_2SiO_4 layer predominates the alloy scaling process. The semi-continuous SiO_2 layer at the scale/alloy interface does not provide sufficient protectiveness as a diffusion barrier for both the outward transport of Co and the inward transport of oxygen. A large amount of SiO_2 internal oxidation particles forms consequently in the vicinity of the alloy surface, resulting in a depletion of the Co-silicide zone in the alloy subsurface region, as shown in Figure 4.11. Again, the Co_2SiO_4 layer appears continuous and dense, partly preventing the oxidation of Re and thereby leading to an overall mass gain.
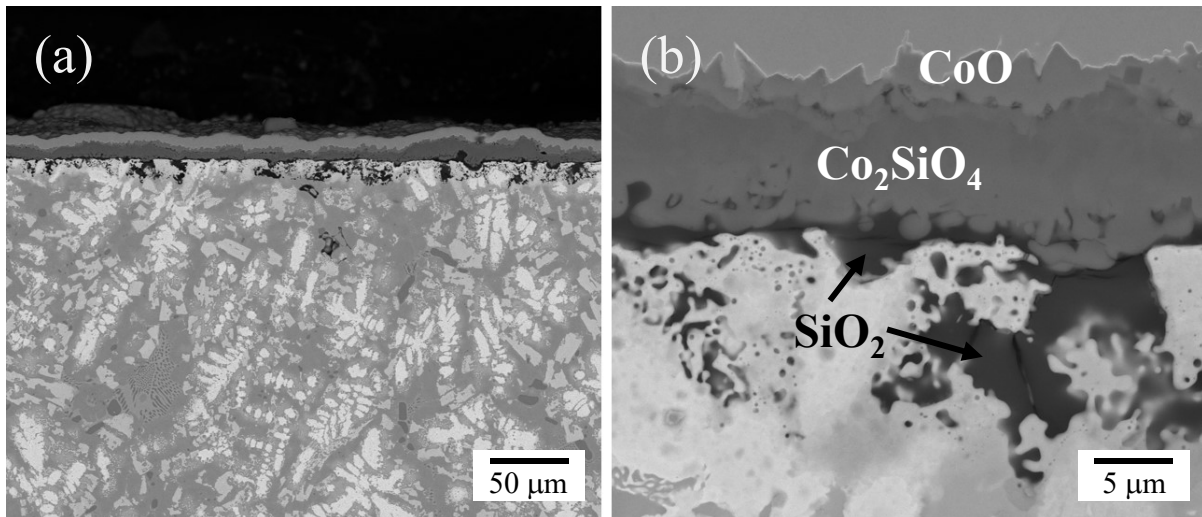

Figure 4.11: Cross-sectional BSE-SEM images of alloy Co-17Re-9Si-8B after oxidation at 1000°C for 1 h

However, if the oxidation temperature is increased further to 1050°C, the supply of Si from the alloy towards the scale/alloy interface becomes insufficient to maintain the accelerated growth of Co_2SiO_4.

Therefore, the scaling process tends to be predominated by the growth of the non-protective CoO layer, resulting in severe internal oxidation of SiO₂. The oxidation of Re and the evaporation of its oxides take place simultaneously. As the oxidation process proceeds, oxygen diffuses inwardly and continuously. Once the local oxygen activity exceeds the equilibrium value for Co_2SiO_4, the following reaction takes place:

$$SiO_2 + 2Co + 2O \rightarrow Co_2SiO_4 \qquad (4.1)$$
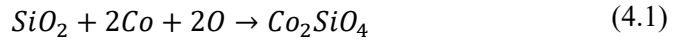
The corresponding thermodynamic calculation in the combination of the well-matched experimental results is shown in Figure 4.12.

At 1100°C, the specimen did not survive the 100 h exposure, as shown in Figure 4.13.
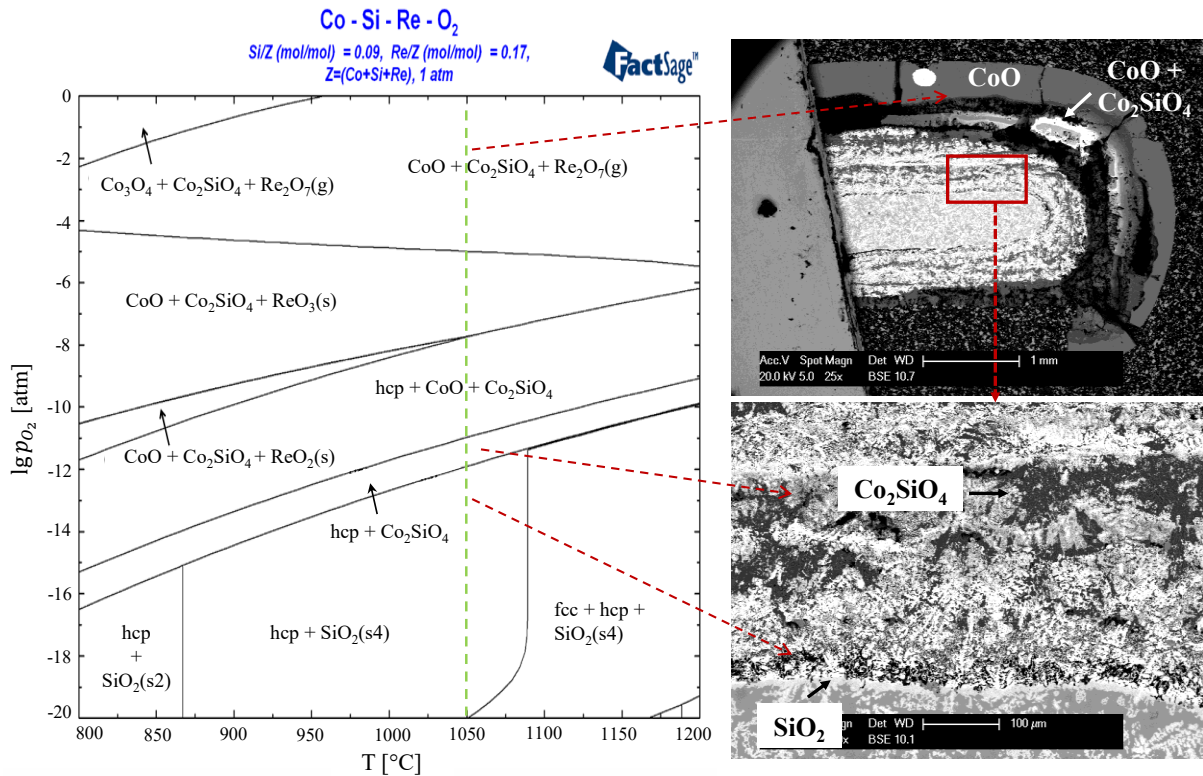

Figure 4.12: Cross-sectional micrographs of alloy Co-17Re-9Si-8B after oxidation at 1050°C for 72 h in combination with the corresponding thermodynamically calculated phase diagram
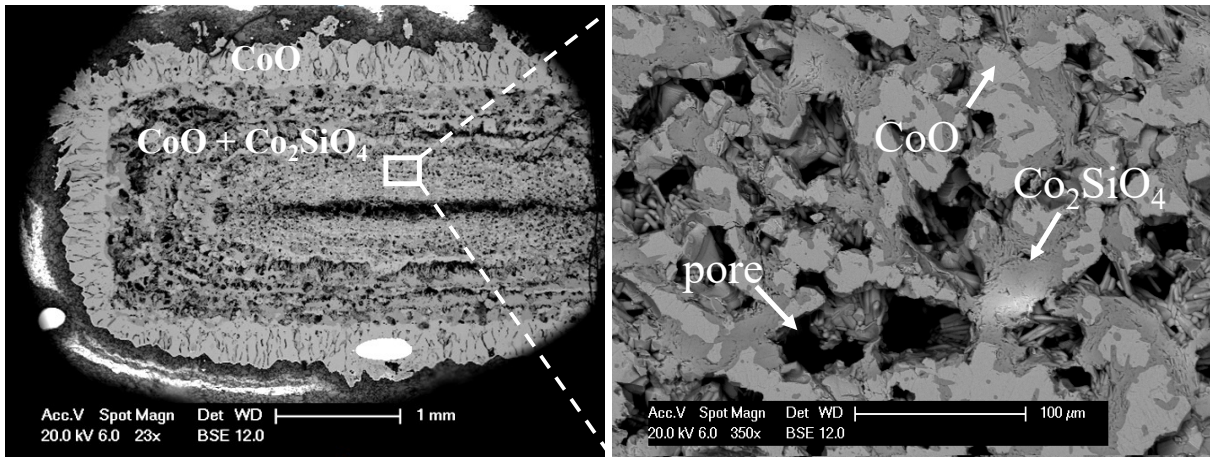
Figure 4.13: Cross-sectional micrographs of alloy Co-17Re-9Si-8B after oxidation at 1100°C for 100 h

4.3 Summary and discussion

As shown above, it is beneficial to add Si in a small amount to ternary Co-Re-Cr alloys, promoting the formation of the Cr_2O_3 scale through selective oxidation. However, an over-addition should be avoided since this evidently enhances the spallation of the chromia scale formed and, moreover, significantly increases the volume fraction as well as the particle size of the primary σ phase, which is known to be detrimental to the mechanical properties.

The preliminary study on the model alloy Co-17Re-9Si-8B shows unfortunately an unsatisfactory potential to form an intrinsic SiO_2 scale on Co-Re-base alloys by macro-alloying Si(-B) for high-temperature applications. Compared to Mo-Si-B alloys, the critical shortcoming of Si-B addition to the Co-Re alloys is related to the formation of non-protective but thermodynamically stable Co_2SiO_4, which constantly consumes Si or SiO_2 formed in the alloy and thereby retards the formation of a protective external SiO_2 scale.

Unfortunately, the available and applied analytical techniques in this study are not able to reasonably detect the presence and distribution of boron. This element is of great importance for the reduction of the viscosity of silica formed on Mo-Si-B alloys so that SiO_2 can easily cover the alloy surface. However, for the Co-Re-Si-B system, it can be assumed that the influence of boron is less meaningful because of the ease of Co_2SiO_4 formation.

Moreover, the thermodynamic calculation also implies that the addition of Si to binary Co-17Re strongly reduces the alloy melting temperature, as shown in Figure 4.14. This behavior fundamentally restricts the potential to form a protective SiO_2 scale through macro-alloying with silicon.

Taking together, it seems that the formation of the intrinsic silica layer on the Co-Re-base alloys is quite unpractical. Therefore, the further development in oxidation resistance of Co-Re-base alloys for very

high-temperature applications should be mainly focused on other candidates, e.g., the Al_2O_3 and/or Cr_2O_3 scales.
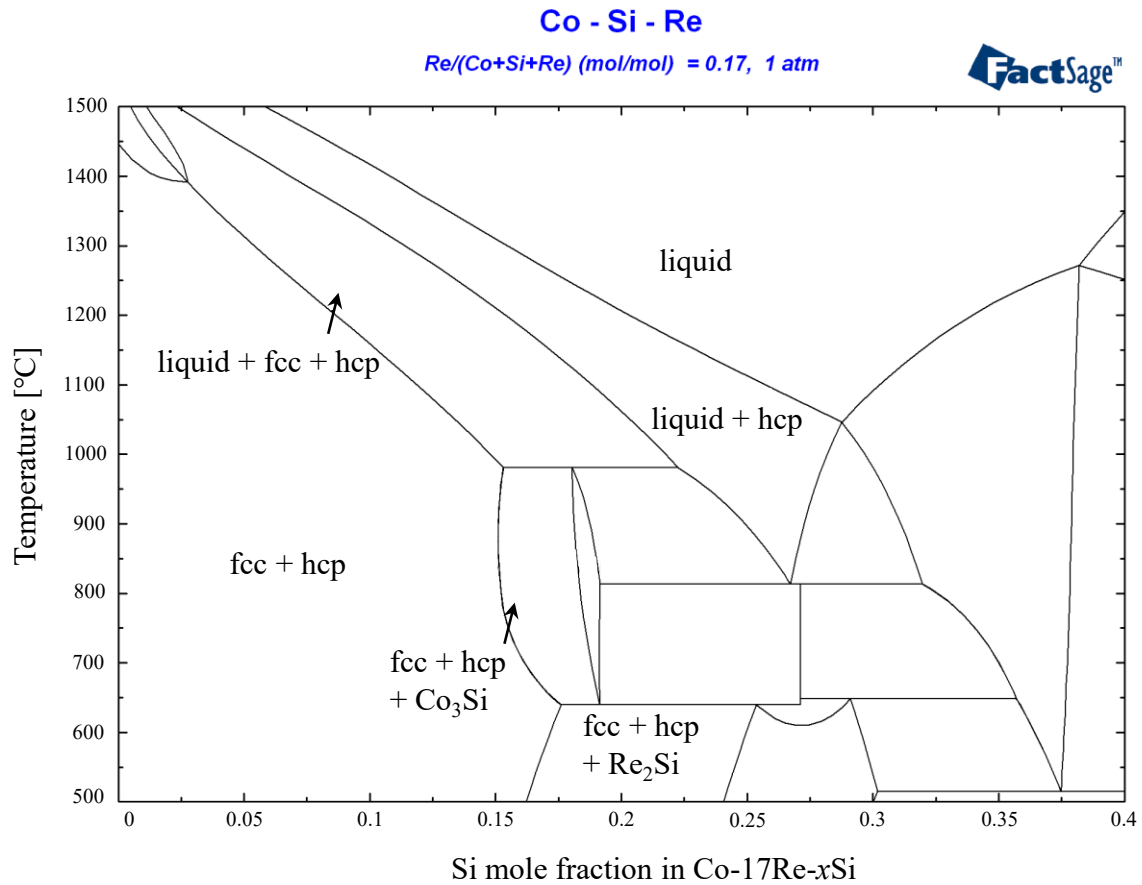

Figure 4.14: Phase diagram of Co-17Re-xSi calculated with FactSage showing Si addition (0-15%) strongly reduces the melting temperature of the alloy

5 Approaches to form Al₂O₃ layer

As an alternative to silica, alumina is so far the most effective oxide for protection against high-temperature oxidation. To study the possibility of forming a protective Al_2O_3 scale and the influence of aluminum addition on the Co-Re-base alloy system, two model alloys, Co-17Re-23Cr-5Al and Co-17Re-23Cr-10Al, containing 5% and 10% aluminum, respectively, were fabricated and investigated. The essential results and their interpretation are presented in the following.

5.1 Alloy Co-17Re-23Cr-5/10Al

The microstructure of the investigated model alloys Co-17Re-23Cr-5Al, Co-17Re-23Cr-10Al, and the aluminum-free reference alloy Co-17Re-23Cr, are shown as BSE-SEM images in Figure 5.1. The corresponding EDS analysis of specific microstructural features is presented in Table 5.1.

The two typical major phases, i.e., the hcp matrix and the primary σ phase, can be generally identified in all three alloys. In addition, a third phase enriched in cobalt and aluminum presents in the alloy Co-17Re-23Cr-10Al. According to the ternary Co-Cr-Al phase diagram [105] and the TEM diffraction pattern shown in Figure 5.1d, this (Co, Al)-rich phase is supposed to be a CoAl-type bcc phase (B2). It is clearly visible that the overall microstructure in Figure 5.1, in terms of σ phase distribution, is significantly affected by the increase of the Al content in the alloy. Quantitative analysis of the as-received (see Table 3.1) alloys shows that the σ phase volume fraction increases from about 2% in Co-17Re-23Cr to around 24% and 37% in Co-17Re-23Cr-5Al and Co-17Re-23Cr-10Al, respectively. The average size of the primary σ phase in both Al-containing alloys is noticeably larger than that found in the reference alloy Co-17Re-23Cr. It is also important to note that the content of Al in the σ phase is generally lower than that in the hcp matrix in both Al-containing alloys, which is opposed to the distribution of Cr content.
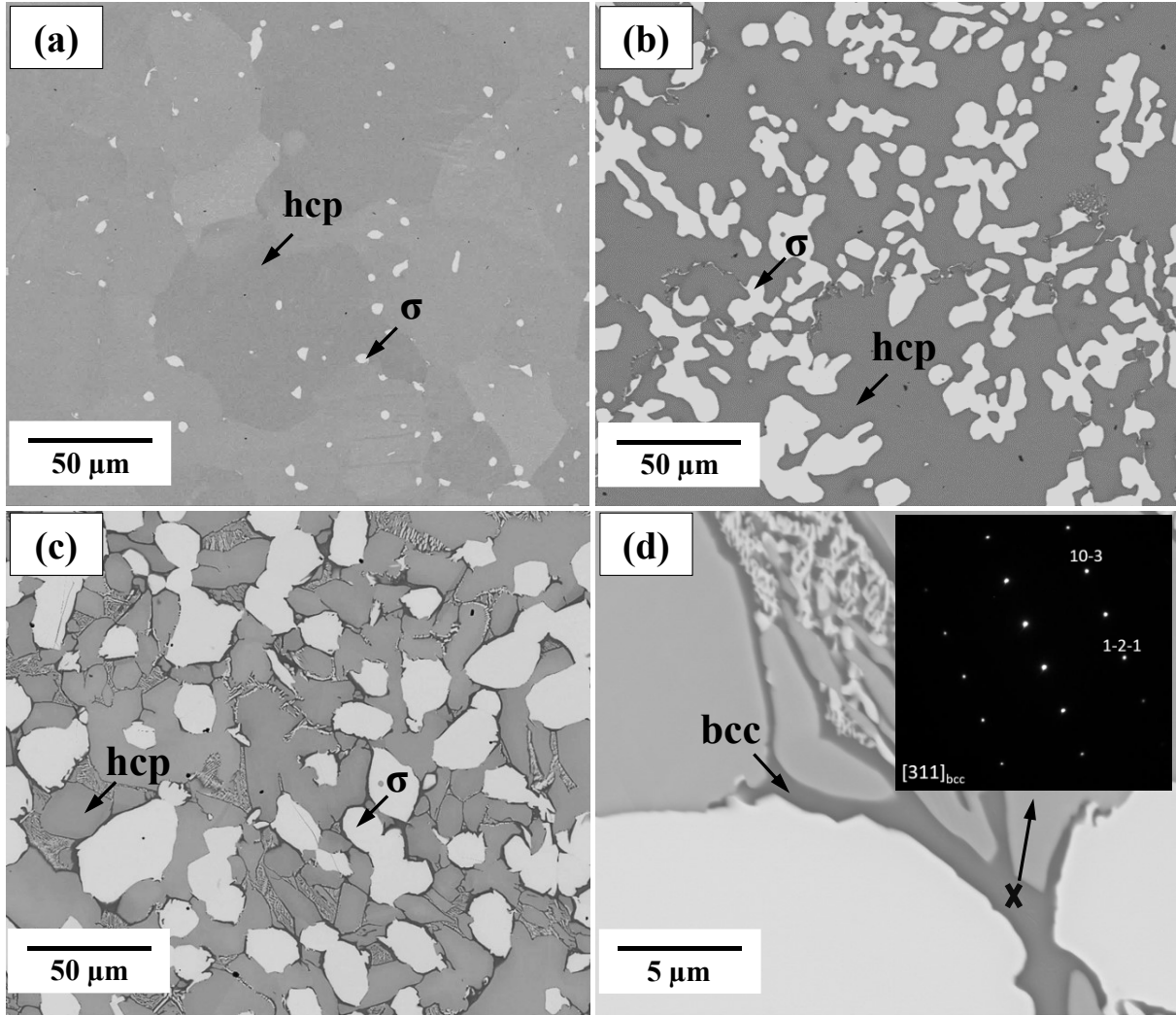
Figure 5.1:   SEM (BSE mode) micrographs of the alloys: (a) Co-17Re-23Cr; (b) Co-17Re-23Cr-5Al; (c) Co-17Re-23Cr-10Al; (d) Co-17Re-23Cr-10Al in higher magnification including a selected area diffraction pattern of the position labeled

Table 5.1:   Mean volume fraction (V.%) and EDS analysis results of the alloy phases, showing elemental concentrations in at.%

Alloy	Phase	Co	Re	Cr	Al	V.%
Co-17Re-23Cr	hcp	58.5	19.2	22.3	-	98.1 ± 0.4
	σ	38.8	30.8	30.4	-	1.9 ± 0.4
Co-17Re-23Cr-5Al	hcp	57.8	14.9	20.6	6.7	76.2 ± 1.7
	σ	35.1	31.4	28.5	5.0	23.8 ± 1.7
Co-17Re-23Cr-10Al	hcp	56.8	12.3	19.6	11.3	53.8 ± 2.5
	σ	33.9	32.7	26.6	6.8	37.1 ± 1.3
	bcc	54.6	2.5	12.7	30.2	9.1 ± 2.2

5.2 Oxidation results

Isothermal oxidation tests in air were carried out for both aluminum-containing alloys at various temperatures between 800°C and 1300°C. This section illustrates the results in three parts based on their distinctiveness in the oxidation mechanism at different temperatures.

5.2.1 Oxidation at 800-900°C

Figure 5.2 shows the thermogravimetrically measured weight change kinetics of the tested alloys at 800°C and 900°C. It is seen that weight losses occurred for all four cases. Nonetheless, a period of weight gain is observed on alloy Co-17Re-23Cr-5Al at 800°C before it turns into the negative direction, whereas the same alloy at 900°C shows a constant weight loss character and the rate of weight loss slows down with oxidation time. Looking at the weight change curves of Co-17Re-23Cr-10Al at both 800°C and 900°C and comparing them to that of the alloy Co-17Re-23Cr-5Al at 900°C, it becomes clear that a period of negligible net weight change is achieved after a certain transition time. This transition time at 900°C is about 1 hour and is way shorter than that of about 10 hours at 800°C. The values of the weight loss during this transition time at both temperatures are, however, very similar.
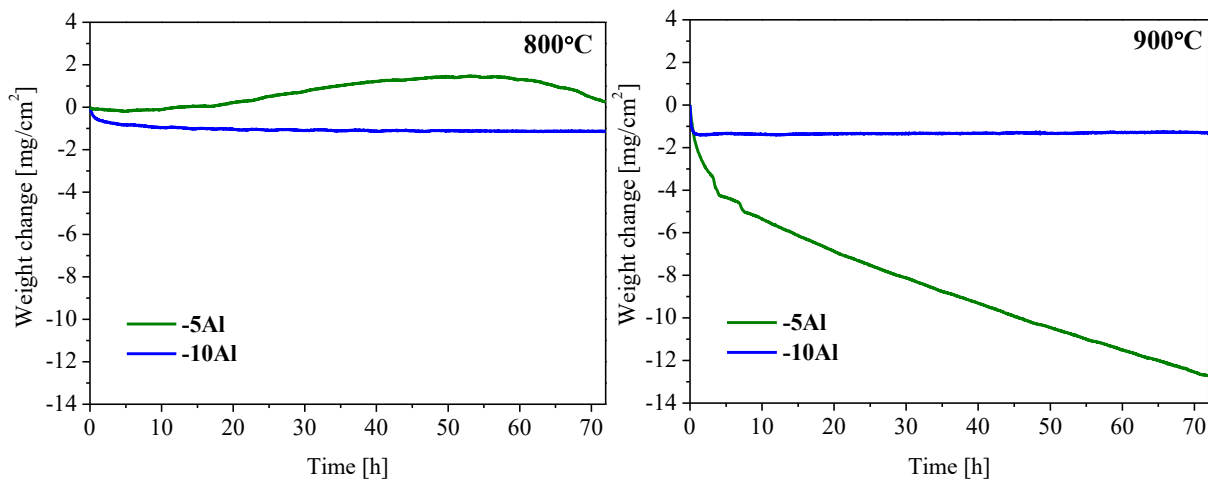
Figure 5.2:   Thermogravimetrically measured weight change versus oxidation time for Al-alloyed Co-17Re-23Cr-xAl alloys at 800°C (left) and 900°C (right)

Microstructural examination of oxidized alloy surfaces, depicted in Figure 5.3, shows distinct morphology differences between the alloy Co-17Re-23Cr-5Al and Co-17Re-23Cr-10Al. On alloy Co-17Re-23Cr-5Al, both the oxide surfaces formed at 800°C (Figure 5.3a) and 900°C (Figure 5.3c) appear to be homogeneous. EDS and XRD analyses reveal that the surface oxide formed at 800°C is pure Co$_3$O$_4$, whereas at 900°C it is composed of CoO and Co$_3$O$_4$. This is thermodynamically reasonable according to the Co-O$_2$ phase diagram shown in Figure 2.2. On the contrary, the oxide surfaces on alloy Co-17Re-

23Cr-10Al formed at 800°C and 900°C are inhomogeneous. The morphological patterns are inherited from the alloy substrate, in which the island-shaped brighter areas (Figure 5.3b and d) are observed to be correlated to the σ phase in the base alloy (Figure 5.1c). EDS analysis detected the presence of Cr, Co, and O in these island-shaped brighter areas, with Co and O being most abundant. Compared with the brighter areas, the darker areas appear significantly thinner, and the oxide grains are finer. Even the grinding pattern from sample preparation before oxidation can still be observed. Chemical analysis by EDS on these areas reveals the presence of Co, Cr, Re, Al, and O, and the Al peaks are very strong, indicating that the scale is predominantly composed of an Al-rich oxide.

Figure 5.3:   Secondary-electron SEM images of surfaces on Al-alloyed Co-17Re-23Cr-5Al (a and c) and Co-17Re-23Cr-10Al (b and d) after oxidation for 72 h at 800°C and 900°C

Figure 5.4 shows the cross-sectional BSE-SEM images of both alloys after oxidation at 800°C and 900°C for 72 hours. For the alloy Co-17Re-23Cr-5Al, neither the Cr nor the Al concentration is sufficient to form a slow-growing Cr$_2$O$_3$ or Al$_2$O$_3$ layer that can protect the substrate under the testing conditions. In these cases, the oxide scales formed consist of an outer layer composed of solely cobalt oxide and an inner layer enriched in Cr and Al due to the formation of the spinel phase Co(Cr,Al)$_2$O$_4$. The outer cobalt oxide layer growth is controlled by outwards diffusion of Co, whereas the inner spinel

layer grows inwardly. However, both layers are non-protective and thus allow inward transport of oxygen and reaction with Re to form the volatile rhenium oxide. An increase of temperature from 800°C to 900°C accelerates the oxidation velocity, leading to a more severe weight loss of the alloy through the Re oxide evaporation. The thickness of the total oxide scale at 900°C (158.6 ± 2.9 μm) is measured to be about three times larger than that of the oxide scale formed at 800°C (53.1 ± 5.8 μm).
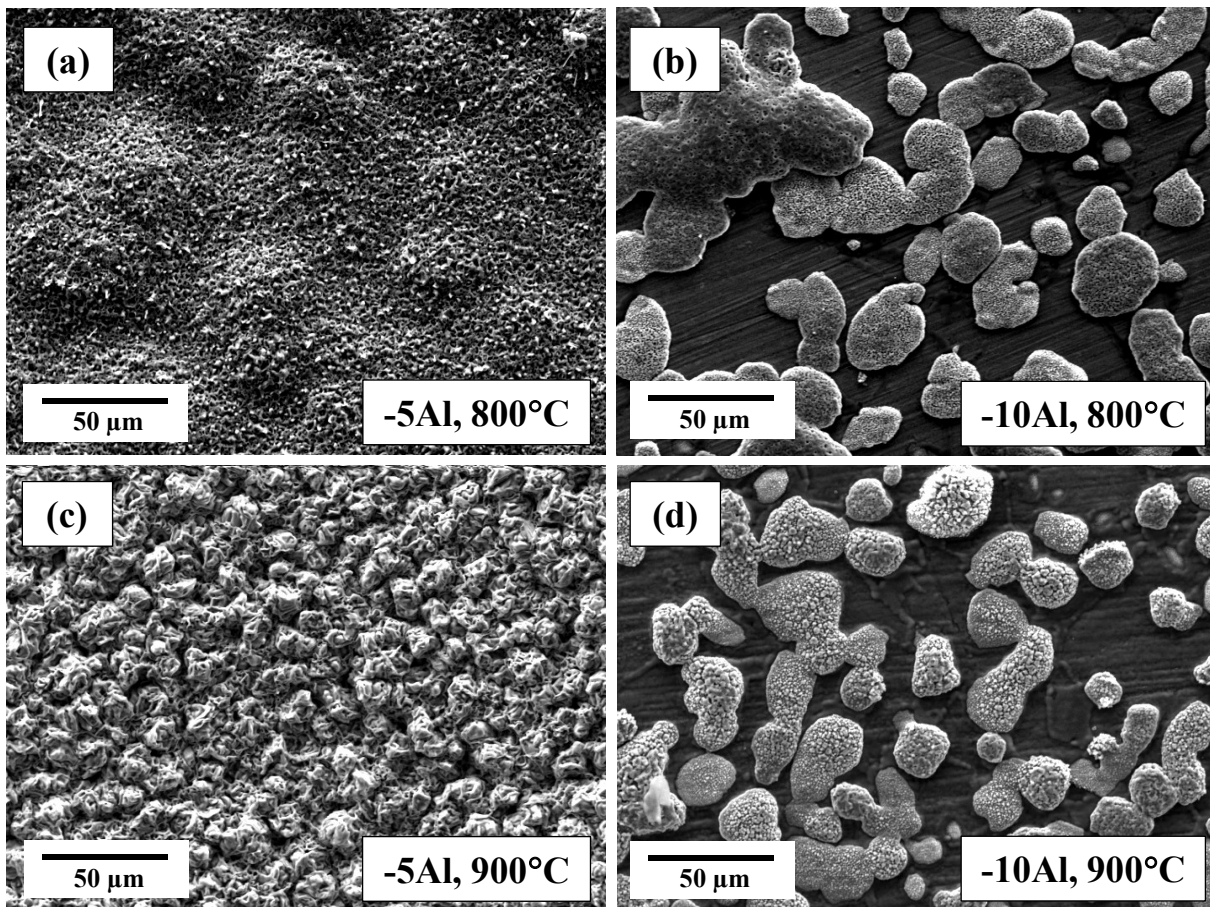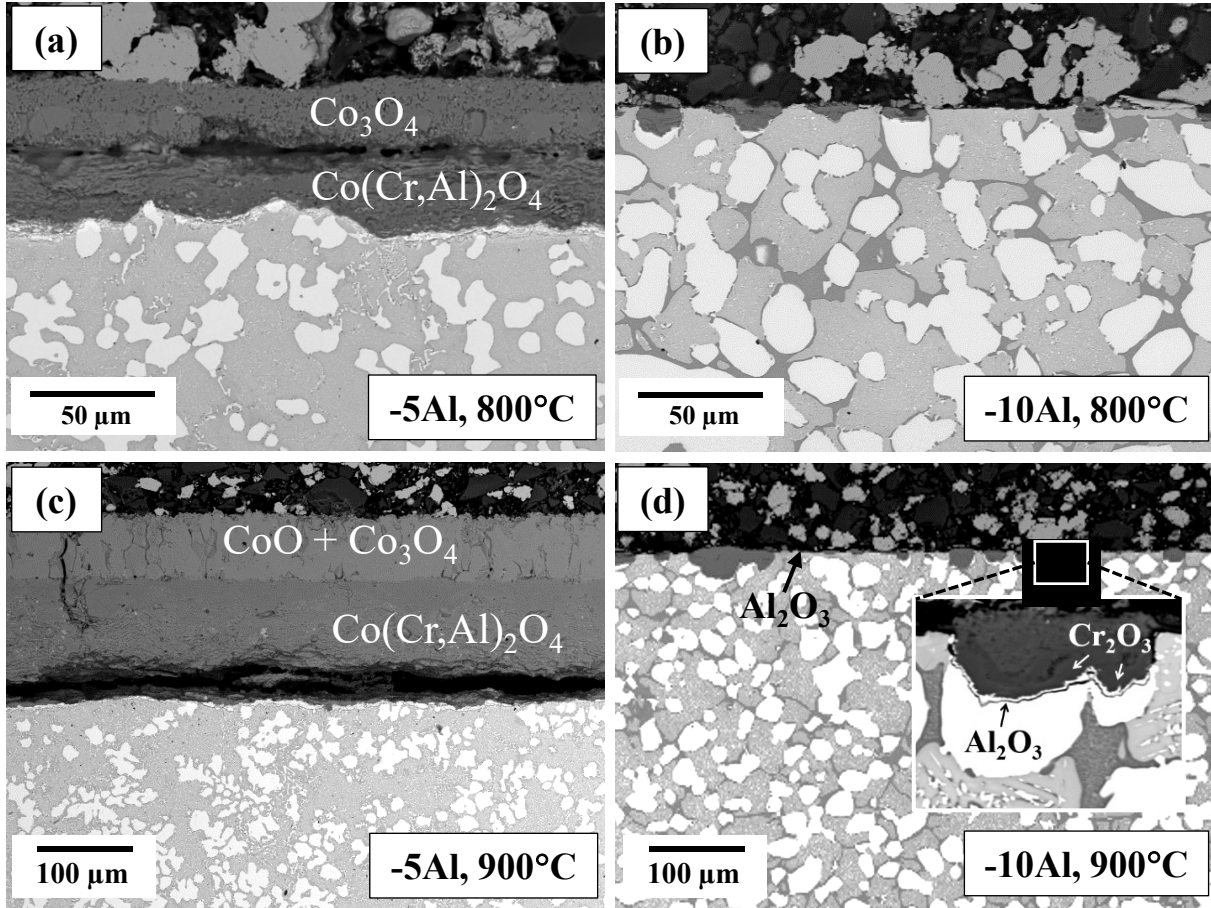

Figure 5.4: Cross-sectional BSE-SEM images of Al-alloyed Co-17Re-23Cr-5Al (a and c) and Co-17Re-23Cr-10Al (b and d) after oxidation for 72 h at 800°C and 900°C (the upper side of all images corresponds to the embedding material)

Compared to the low Al-containing alloy Co-17Re-23Cr-5Al, the oxide scales formed on alloy Co-17Re-23Cr-10Al at both temperatures are relatively thin, as shown in Figure 5.4b and d. However, the scales appear rather nonuniform and can be distinguished in two types, both being correlated to the matrix (incl. bcc phase) and the σ phase. The scale formed on the matrix is extremely thin (less than 1 μm) and seems to consist entirely of Al$_2$O$_3$. In contrast, the scale formed on the σ phase is relatively thick and is determined to be a Co(Cr,Al)$_2$O$_4$/Cr$_2$O$_3$/Al$_2$O$_3$ multi-layer scale (ordered in the direction from gas phase to alloy). The Al$_2$O$_3$ formed underneath the chromia layer is semi-continuous, whereas the Cr$_2$O$_3$ layer itself is continuous and dense, showing a protective nature.

53

Consequently, the further degradation of the σ phase is strongly retarded. In combination with the information revealed from the thermogravimetric experiments, the results indicate that the oxidation of Re and the evaporation of its oxide from the σ phase occurs simultaneously during the early reaction stage of alloy Co-17Re-23Cr-10Al, resulting in the initial weight loss represented in the oxidation kinetics. Once the continuous and compact chromia layer is formed in the σ phase region, the oxidation rate is subsequently controlled by the growth of a Cr_2O_3 scale (on σ phase) and an Al_2O_3 scale (on matrix). It is also worth to point out that the increase of temperature from 800°C to 900°C does not significantly affect the oxidation mechanism, but somewhat reduces the transition period by accelerating the formation of the protective chromia layer on the σ phase.

5.2.2 Oxidation at 1000-1100°C

Figure 5.5 shows separately the weight change measurements of the tested alloys in air at 1000°C and 1100°C. Despite a weight loss at the very early reaction stage, substantial weight gain in a parabolic manner is observed during the steady-state period for all four cases. The total weight losses of alloy Co-17Re-23Cr-10Al at the very early stage are more significant than those of the alloy Co-17Re-23Cr-5Al. One other observation of interest that should be noted is that the weight gain rates of both alloys during the steady-state oxidation increase with increasing reaction temperature. Moreover, the weight gain rate of alloy Co-17Re-23Cr-10Al is observed to be lower than that of alloy Co-17Re-23Cr-5Al, especially at 1100°C.

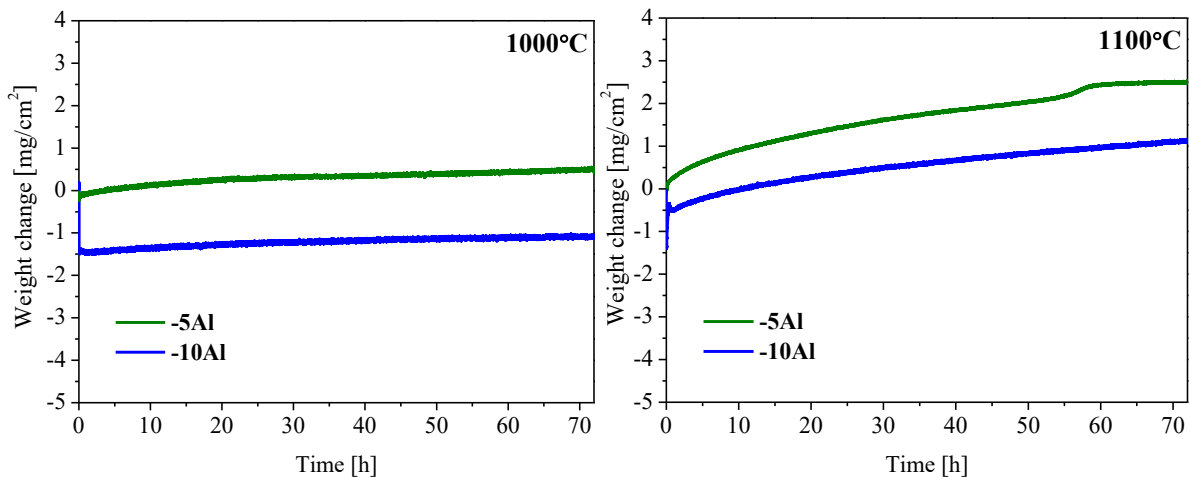Figure 5.5:   Specific weight change vs. time for the aluminum-alloyed Co-17Re-23Cr-xAl at 1000°C (left) and 1100°C (right)

Surface examination of oxidized alloy Co-17Re-23Cr-5Al shows that the outermost oxide formed at 1000°C consists of CoO and $CoCr_2O_4$, while that formed at 1100°C consists of Cr_2O_3 and $CoCr_2O_4$. Examples are shown in Figure 5.6a and c. EDS measurement on both oxidized surfaces showed a very

strong Cr peak no matter in which region the measurement was conducted. This implies that the outermost oxide layer is relatively thin, and a Cr-rich oxide layer is formed underneath.

On alloy Co-17Re-23Cr-10Al, the surface morphology after oxidation at 1000°C is similar to that formed at lower temperatures. Due to its large bandgap, Al$_2$O$_3$ possesses weak electric conductivity, resulting in an accumulation of beam electrons on the sample surface. This effect appears more substantial on the specimen oxidized at 1100°C, leading to a difficult morphological analysis using the secondary electron signal, as shown in Figure 5.6b and d.

Figure 5.6:   Secondary-electron SEM image of surfaces on Al-alloyed Co-17Re-23Cr-5Al (a and c) and Co-17Re-23Cr-10Al (b and d) after oxidation for 72 h at 1000°C and 1100°C

The comparison of the corresponding cross-sectional micrographs is shown in Figure 5.7. It is seen that a continuous and protective external oxide scale formed on all four specimens. The external scales formed on alloy Co-17Re-23Cr-5Al both at 1000°C and 1100°C are homogeneous and composed mainly of pure Cr$_2$O$_3$ (Figure 5.7a and c), whereas the scales formed on alloy Co-17Re-23Cr-10Al appear again

as nonuniform, i.e., the thin and compact Co(Cr,Al)$_2$O$_4$/Al$_2$O$_3$ double-layer scale on the matrix and the relatively thick Co(Cr,Al)$_2$O$_4$/Cr$_2$O$_3$ double-layer scale on the σ phase. This result is reasonable, since the Al content in the σ phase is only half of that in the hcp matrix (Table 5.1) and must be considered insufficient for forming an external Al$_2$O$_3$ scale under the experimental condition. A clear representation of such different oxidation behavior between the matrix and the σ phase on alloy Co-17Re-23Cr-10Al is given in Figure 5.8, where additionally to the microstructural information the corresponding elemental distribution maps are shown.

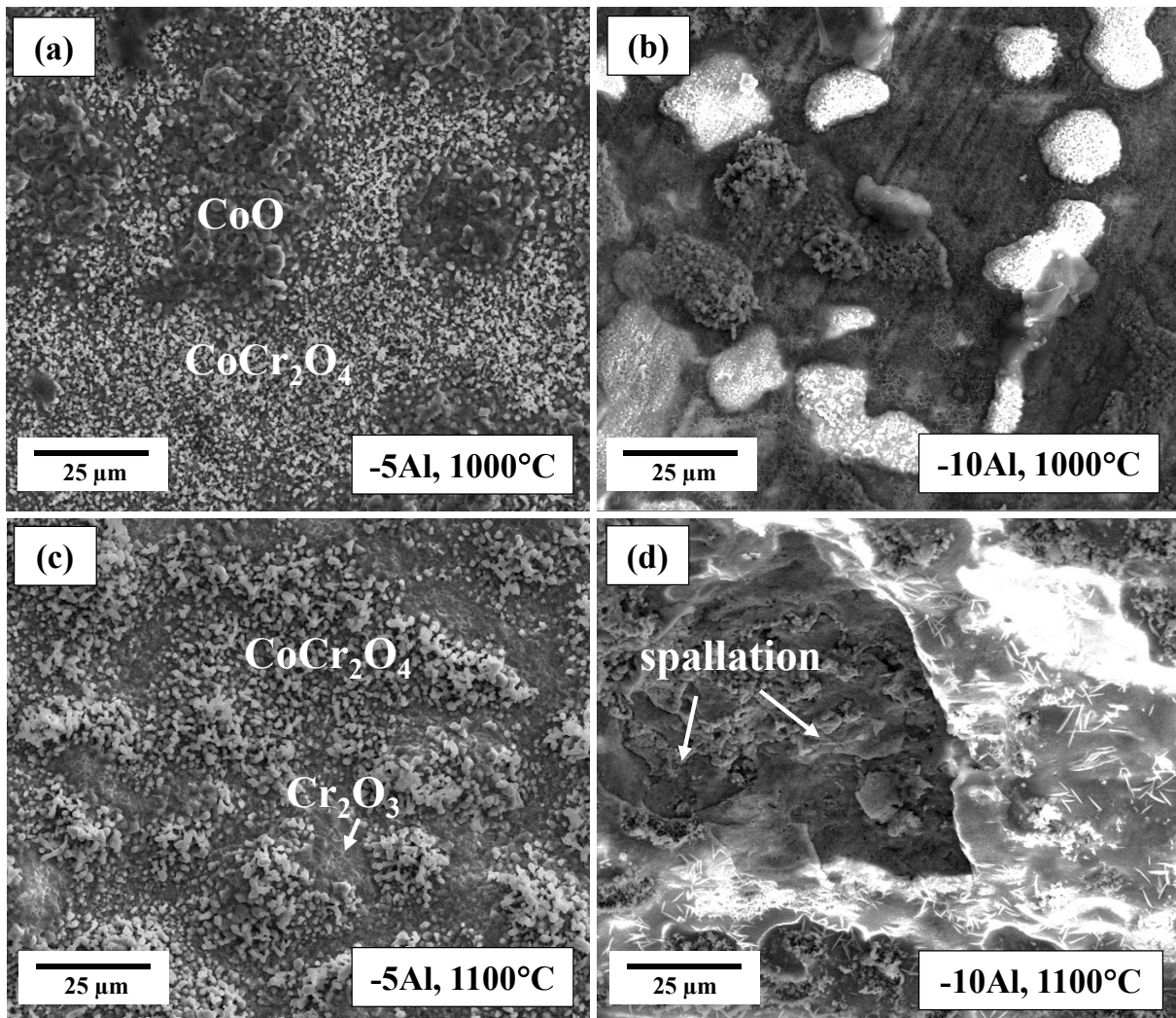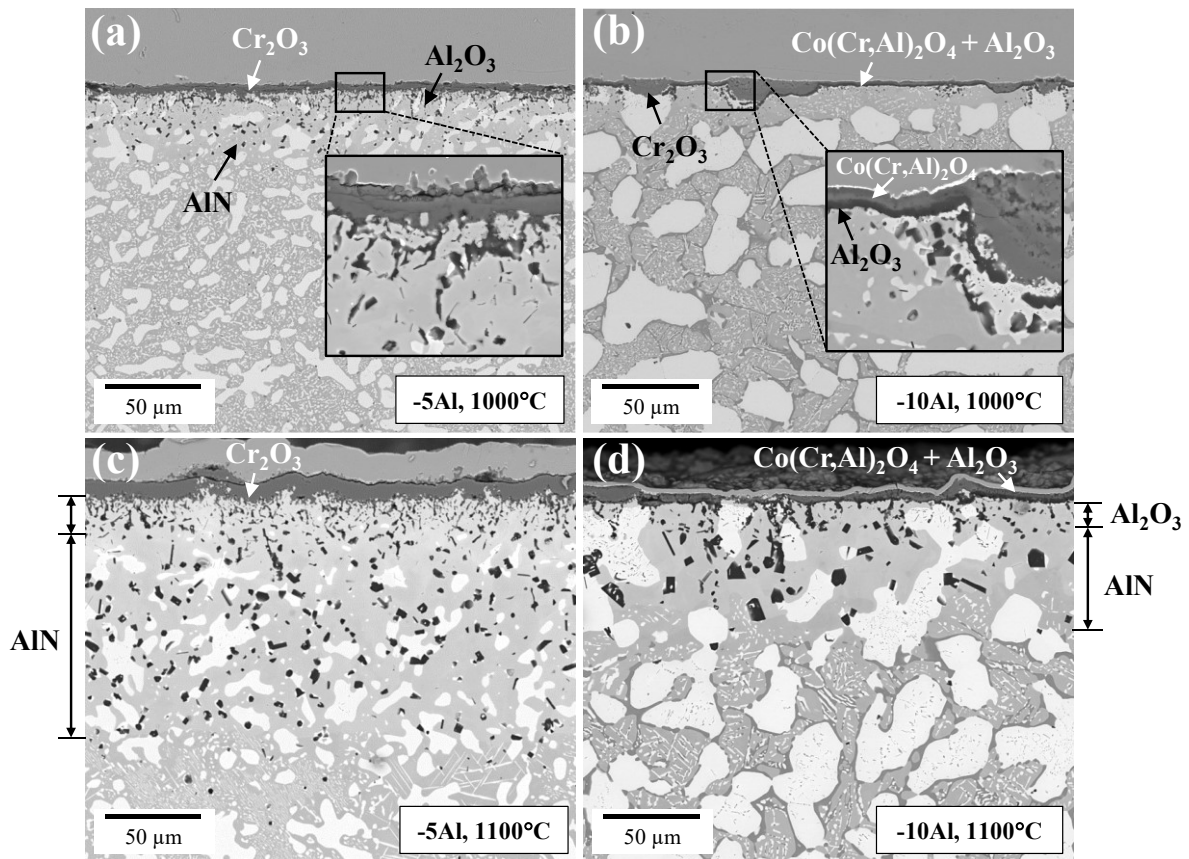

Figure 5.7:   Cross-sectional BSE-SEM images of Al-alloyed Co-17Re-23Cr-5Al (a and c) and Co-17Re-23Cr-10Al (b and d) after oxidation for 72 h at 1000°C and 1100°C (oxidized specimens were Ni-plated)

Except for the cross-section of the alloy Co-17Re-23Cr-10Al oxidized at 1000°C, large quantities of internal precipitation products are observed in the subsurface region of the other three cases. EDS and TEM analyses imply that the irregular precipitates directly underneath the scale are Al$_2$O$_3$, and the precipitated angular particles deeper in the alloy are AlN. In all examined specimens, the mean particle size of the internal AlN precipitates generally increases with increasing penetration depth. A similar observation in Ni-Cr-Al alloys has been reported by other authors [106, 107], in which they explained

that the formation of fine AlN precipitates near the exposed surface is due to the higher nitrogen flux and correspondingly the easier nitride nucleation. Besides, the AlN precipitates formed within the σ phase are observed to be much more finner than that formed in the matrix. Depletion of Cr and Al through oxide-scale growth and internal precipitation results in a dissolution of the σ phase in the subsurface region. Additionally, the Al-rich bcc phase in alloy Co-17Re-23Cr-10Al is dissolved for the same reason.
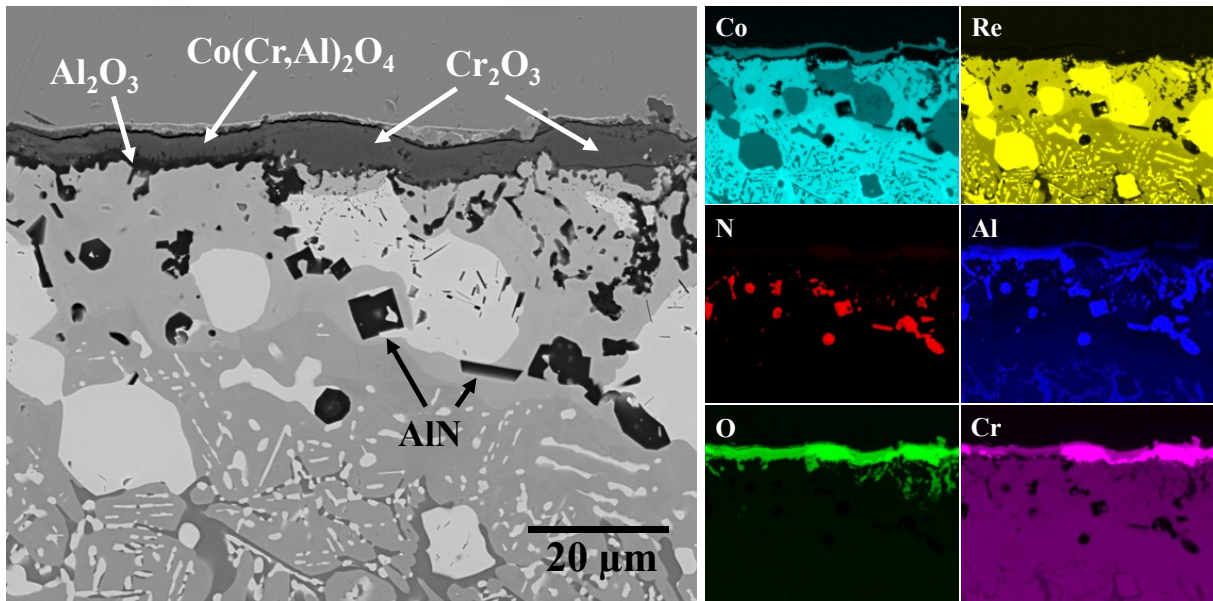

Figure 5.8:   Cross-sectional BSE-SEM image (left) together with the corresponding element distribution maps (right) of alloy Co-17Re-23Cr-10Al after exposure to air at 1100°C for 24 h

Upon the microstructural analyses above, it becomes clear that the overall weight gain shown in Figure 5.5 results from simultaneous growth of the external scale and the simultaneous formation of internal precipitates. To analyze the reaction kinetics more in detail, oxide scale thickness and precipitation depth of Al$_2$O$_3$ and AlN were measured as a function of reaction time through discontinuous tests. All the measurements were primarily carried out in the matrix region to avoid the misinformation by the irregular distribution of the σ phase. The results are shown in Figure 5.9 and Figure 5.10.

As shown in Figure 5.9, all scale growth data obey a parabolic rate law, and the corresponding Arrhenius plot indicates a slower growth rate and a lower temperature dependence of the scale formed on alloy Co-17Re-23Cr-10Al compared to that on alloy Co-17Re-23Cr-5Al. Except for alloy Co-17Re-23Cr-10Al oxidized at 1000°C, which possesses merely internal oxide, the general pattern of internal oxidation is parabolic, whereas that of the internal nitridation is parabolic in the initial stages but follows a linear kinetics later on, most pronounced by the alloy Co-17Re-23Cr-10Al oxidized at 1100°C. Analysis of the discontinuously oxidized specimens reveals that a continuous Al$_2$O$_3$ layer is formed

initially at the scale/alloy interface even on the σ phase region strongly retarding the inwards transport of nitrogen through the scale. Hence, diffusion-controlled kinetics of AlN formation is in effect in this transient state. As the process proceeds, the scale thickening becomes predominated by the growth of the Cr$_2$O$_3$ layer, and the Al$_2$O$_3$ layer becomes discontinuous. As a result of the non-protective nature of chromia against nitrogen compared to alumina [108, 109], nitrogen penetrates then more rapidly into the alloy and therefore leads to an approximately linear kinetics of nitridation in the long term.
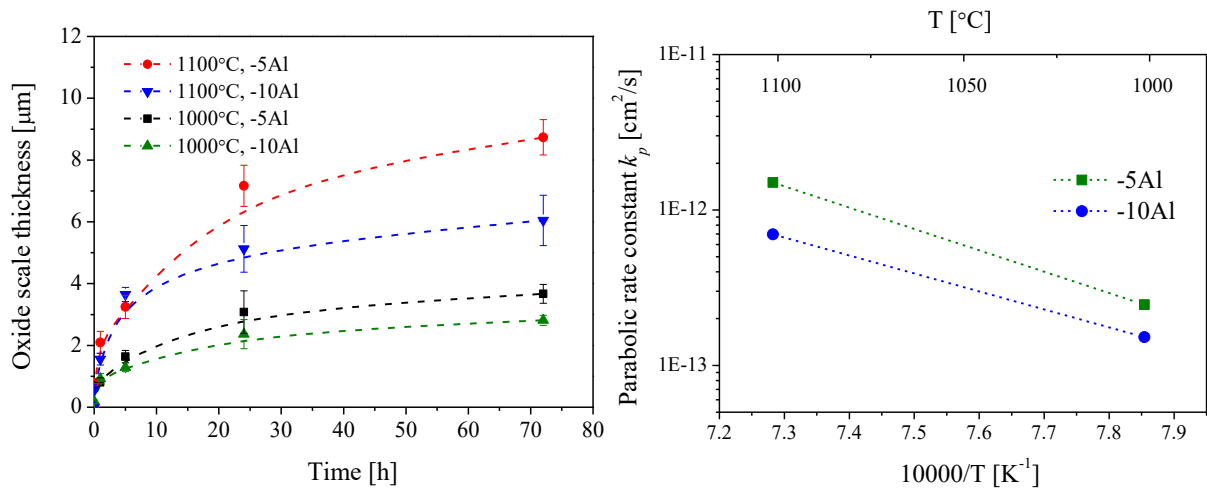

Figure 5.9:   External oxide scaling kinetics of alloys Co-17Re-23Cr-*x*Al presented in scale thickness versus time (left) and the corresponding Arrhenius plot of the parabolic rate constant (right)
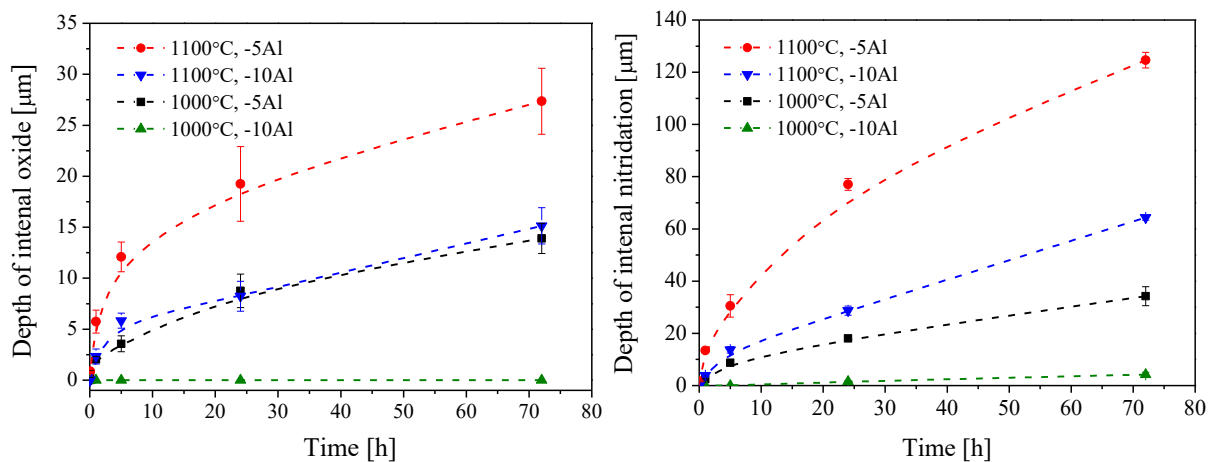

Figure 5.10: Internal oxidation kinetics (left) and internal nitridation kinetics (right) of alloys Co-17Re-23Cr-*x*Al

5.2.3 Oxidation at 1200-1300°C

Figure 5.11 shows the continuously measured weight change of Al-containing alloys during exposure to air at 1200°C and 1300°C. Due to the high evaporating rate of Re oxides, which simultaneously recondense on the upper part of the suspension hook and create falsified results, the measurements at 1300°C were interrupted after 10 hours. Massive weight loss kinetics are observed for alloy Co-17Re-23Cr-5Al at both temperatures, and the weight loss rate increases dramatically by raised temperature. For alloy Co-17Re-23Cr-10Al, the curve at 1200°C initially exhibits a parabolic weight gain kinetics in the first 30 hours. After that, weight loss occurs. At 1300°C, substantial weight loss takes place immediately, but the curve turns to behave in a weight gain manner only after about half an hour.
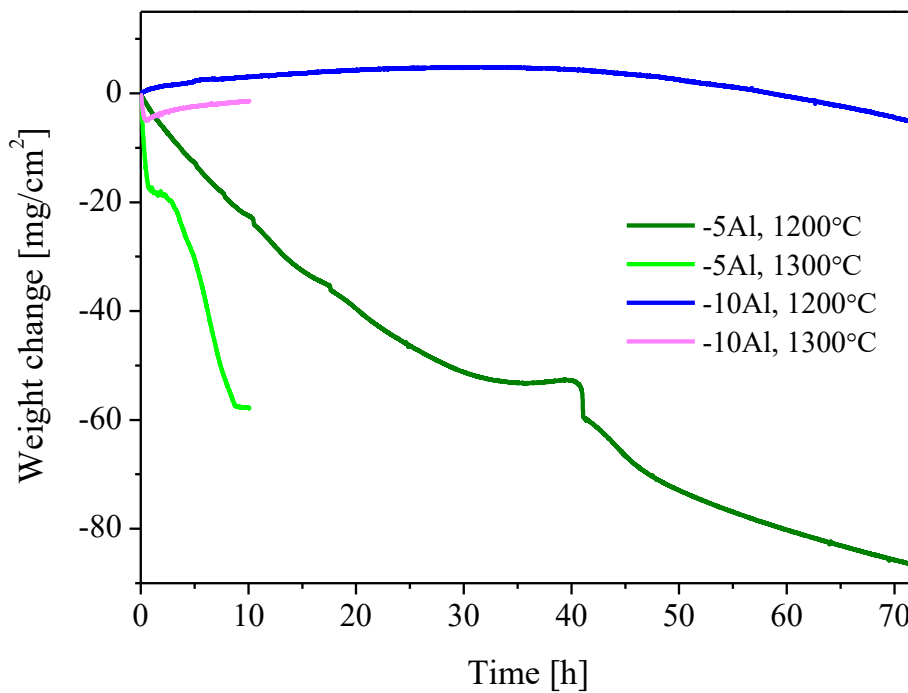
Figure 5.11: Weight change versus oxidation time for the aluminum-alloyed Co-17Re-23Cr at 1200°C and 1300°C

Microstructural examination on cross-sections of the oxidized alloy Co-17Re-23Cr-5Al reveals that the scale formed at 1200°C is no longer protective compared to that formed at 1000°C and 1100°C. As shown in Figure 5.12, the scale consists of an outermost pure CoO layer and a mixed inner layer composed of CoO and Co(Cr,Al)$_2$O$_4$. Neither Cr$_2$O$_3$ nor Al$_2$O$_3$ layer is formed at the scale/alloy interface. An internal AlN precipitation zone appears directly under the scale. Internal Al$_2$O$_3$ precipitates could be barely found in this case. It is worth to point out that although the scale morphology here is observed to be similar to that formed at 900°C (Figure 5.4), the inner layer is more porous and with an additional presence of CoO. This kind of scale constitution is generally considered as a sign of non-protectiveness,

which allows the fast inwards transport of gaseous oxygen to the oxidation front, i.e., the oxide/alloy interface.

Consequently, Re is continuously oxidized and evaporates as volatile oxides, resulting in the massive weight loss of the TGA measurement. The total thickness of the scale is around 1 mm. More than half of the specimen is consumed after the 72-hourly test (Figure 5.12). At 1300°C, the process is accelerated, and the investigated specimen is completely oxidized after 72 h exposure, as shown in Figure 5.13.
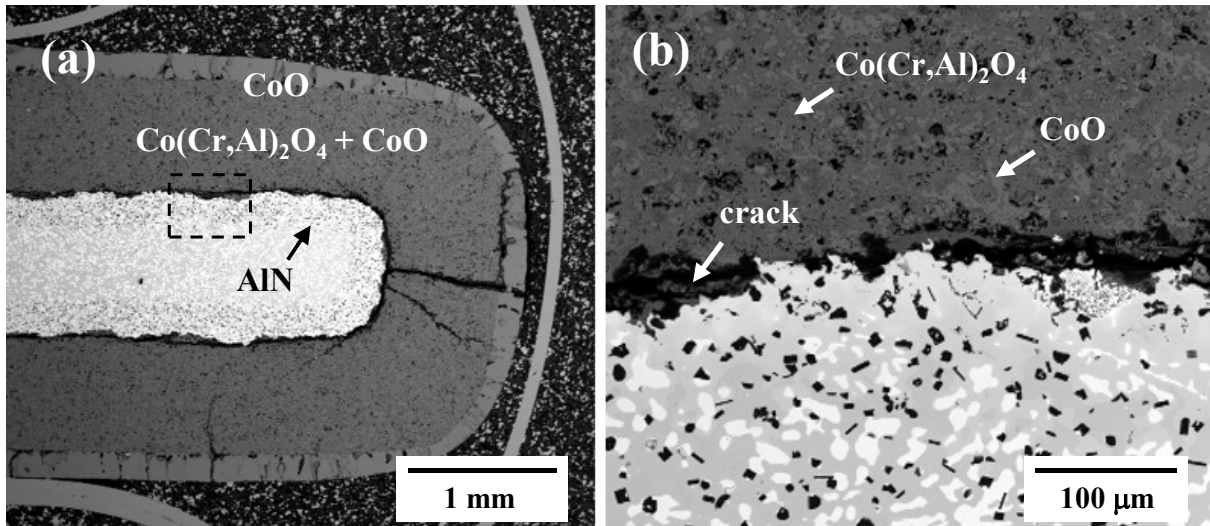

Figure 5.12: BSE-SEM images of the cross-section of alloy Co-17Re-23Cr-5Al after exposure to air at 1200°C for 72h. (a) overview; (b) higher magnification of the region marked in (a)
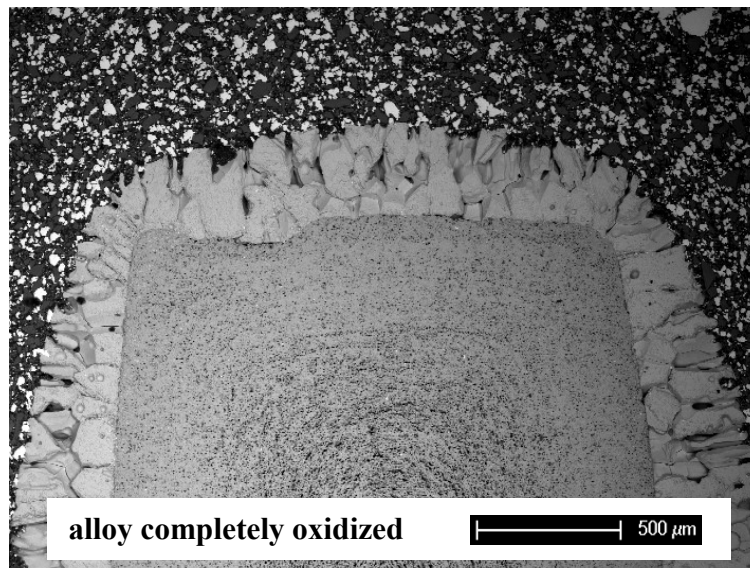

Figure 5.13: BSE-SEM images of the oxidation product of alloy Co-17Re-23Cr-5Al after exposure to air at 1300°C for 72h

On alloy Co-17Re-23Cr-10Al, severe spallation of oxide scale occurs during cooling process after oxidation tests at 1200°C and 1300°C. Figure 5.14 shows both the surface and cross-sectional micrographs of alloy Co-17Re-23Cr-10Al after oxidation at 1200°C for 72 h. It is seen that a large area of oxide scale is completely spalled off, leaving behind many pieces of cracked Cr$_2$O$_3$ directly on the alloy surface. The retained intact scale is found mainly at the edge of the specimen and is characterized as a mixture of CoO and Co(Cr,Al)$_2$O$_4$ spinel phase covered by outermost, discontinuously distributed coarse CoO grains. The scale constitution in the retained areas is quite similar to that formed on alloy Co-17Re-23Cr-5Al under the same condition (Figure 5.12), but with a significantly smaller total thickness, i.e., about 200 μm (Co-17Re-23Cr -10Al) as compared to 1 mm (Co-17Re-23Cr -5Al). No inwardly grown spinel layer is found in the spalled area, rather some cracked Cr$_2$O$_3$ remainings exist on the alloy surface. Massive internal Al$_2$O$_3$ and AlN precipitates are found beneath the surface. Based on the TGA data and the microstructural examination of specimens of discontinuous tests, it can be inferred that the growth of the chromia layer initially dominates the scaling process until breakaway oxidation occurs in the edge area, which results in evaporation of Re oxide subsequently. At 1300°C, the investigated Co-17Re-23Cr-10Al specimen shown in Figure 5.15 shows no breakaway oxidation. Although the specimen with 10% Al survives to a great extent compared to Co-17Re-23Cr-5Al under the same condition, the absence of a protective external Al$_2$O$_3$ scale leads to a severe internal nitridation at this elevated temperature.

Figure 5.14: SEM micrographs of alloy Co-17Re-23Cr-10Al after exposure to air at 1200°C for 72 h. (a) surface view using SE signal; (b) cross-section view using BSE signal
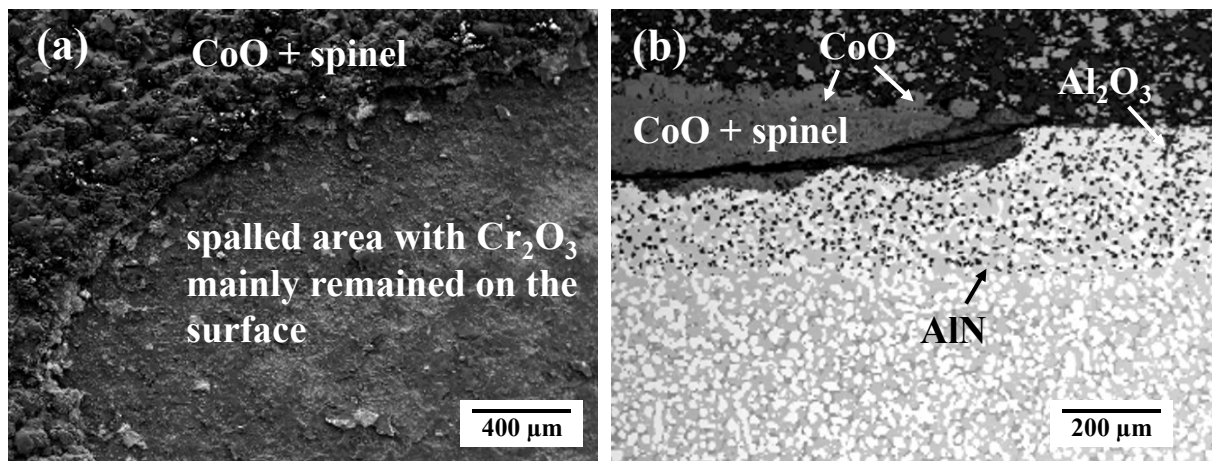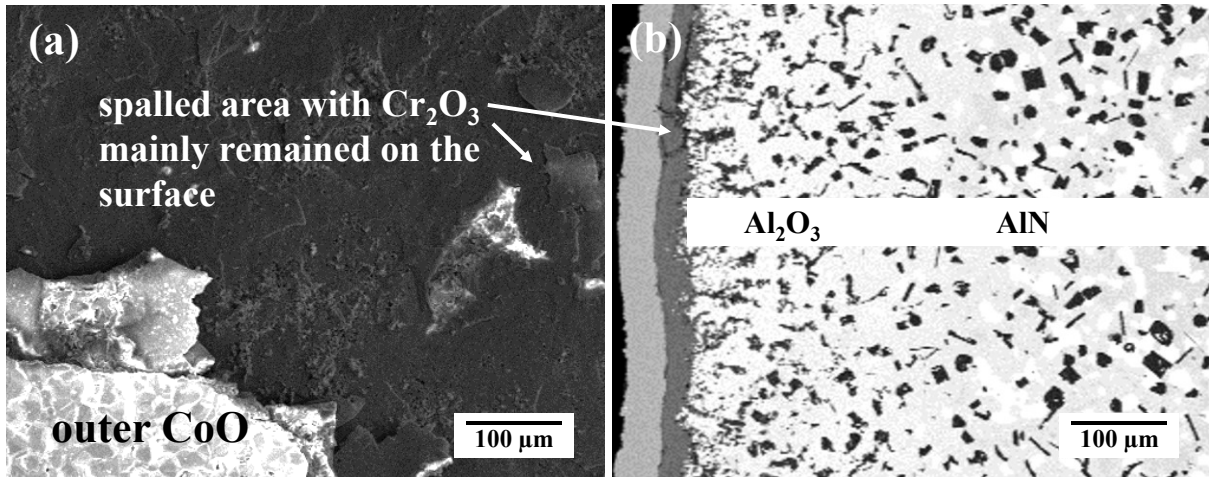
Figure 5.15: SEM micrographs of alloy Co-17Re-23Cr-10Al after exposure to air at 1300°C for 72 h: (a) surface view using SE signal; (b) cross-section view of the spalled area using BSE signal.

5.3 Summary and discussion

The isothermal oxidation behavior of the two Al-alloyed model alloys Co-17Re-23Cr-5Al and Co-17Re-23Cr-10Al have been investigated in the temperature range 800-1300°C. Table 5.2 summarized the dominating external scales formed in each case. Looking at the thermogravimetric data and the microstructural analyses presented above and comparing them with the reference alloy Co-17Re-23Cr [27], it becomes evident that the addition of Al up to 10% significantly improves the oxidation resistance of the alloy by promoting the formation of protective Cr$_2$O$_3$ and/or Al$_2$O$_3$ scales. Alloy Co-17Re-23Cr-10Al with a higher Al content shows, in general, a better oxidation resistance than alloy Co-17Re-23Cr-5Al at all temperatures investigated in this study.

Upon initial exposure of the alloy Co-17Re-23Cr-xAl to air, the transient oxides such as CoO (or Co$_3$O$_4$ at 900°C and below), Cr$_2$O$_3$ and Al$_2$O$_3$ singly or in solid solution, and probably as well as the spinel phase rapidly nucleate on the alloy surface. Re oxidizes and evaporates simultaneously. Once these transient oxides cover the alloy surface, the oxygen activity at the oxide/alloy interface becomes much lower so that preferential oxidation of Al, and to a lesser extent Cr, tends to occur. Nevertheless, the fast-growing transient cobalt oxide can overgrow and undercut these Al-rich and Cr-rich nuclei and incorporate them into the scale before they can develop laterally to give a complete layer. Whether or not Al/Cr can succeed in forming a protective external layer, or just an internal oxide zone, depends not only on their concentration but also on the relative diffusivity of Al/Cr and oxygen in the alloy.

Table 5.2: Consitution of external scales formed on both investigated Al-containing alloys in the temperature range 800-1300°C

Temperature [°C]	Co-17Re-23Cr-5Al	Co-17Re-23Cr-10Al
800	Co$_3$O$_4$, spinel	Al$_2$O$_3$, minor Cr$_2$O$_3$ (on σ phase)
900	CoO+Co$_3$O$_4$, spinel	Al$_2$O$_3$, minor Cr$_2$O$_3$ (on σ phase)
1000	Cr$_2$O$_3$	Al$_2$O$_3$, minor Cr$_2$O$_3$ (on σ phase)
1100	Cr$_2$O$_3$	Al$_2$O$_3$, Cr$_2$O$_3$ (on σ phase)
1200	CoO, spinel+CoO	CoO, spinel+CoO, Cr$_2$O$_3$
1300	CoO, spinel+CoO	CoO, spinel+CoO, Cr$_2$O$_3$

The results show that the addition of 5% Al in the alloy Co-17Re-23Cr-5Al is insufficient to form an external Al$_2$O$_3$ layer in the entire temperature range 800-1300°C. The contribution of the 5% Al in the alloy is that it "getters" the oxygen by preferential internal oxidation in the narrow region beneath the alloy surface, and thereby Al reduces the effective oxygen flux into the alloy and allows the outwards diffusion of Cr to form a complete external Cr$_2$O$_3$ layer. However, at 800°C and 900°C, the temperature-dependent Cr diffusivity in the alloy is not high enough to supply the necessary amount of Cr to form an external Cr$_2$O$_3$ layer. As the temperature increases to 1000°C and 1100°C, a sufficient supply of Cr through the accelerated Cr diffusion finally conduces to form a protective chromia layer.

Nonetheless, the increasing temperature also increases the growth rate of the chromia scale, from $k_p = 2.46 \times 10^{-13}$ cm^2/s at 1000°C to $k_p = 1.50 \times 10^{-12}$ cm^2/s at 1100°C. At 1200°C and 1300°C, although an incipient layer of Cr$_2$O$_3$ is formed at the early oxidation stage, the competition between the effective flux of Cr up to the alloy surface and the rapid consumption of Cr through scale growth, which is probably also associated by the formation and evaporation of CrO$_3$, still results in a transition of the scale into non-protective, and consequently, a rapid oxidation attack.

The increase of Al content from 5% to 10% significantly enhances the oxidation resistance of the alloy, especially at 800°C and 900°C. It appears that 10% Al is almost, but not fully, sufficient to enable the formation of a complete Al$_2$O$_3$ layer on the alloy Co-17Re-23Cr-10Al up to 1100°C. Only in certain areas on the σ phase, the scaling process is predominated by the growth of the Cr$_2$O$_3$ layer, under which Al$_2$O$_3$ is precipitated as internal oxide. The degree of such discontinuity of the Al$_2$O$_3$ layer increases with increasing temperature. At 1200°C and above, Al$_2$O$_3$ can only be found as internal oxides in the vicinity of the scale/alloy interface. The factors restricting an external Al$_2$O$_3$ layer to form on alloy Co-17Re-23Cr-10Al at elevated temperatures are not similar to those restricting the Cr$_2$O$_3$ layer to form on

alloy Co-17Re-23Cr-5Al under the same condition. The formation of the Al$_2$O$_3$ layer on alloy Co-17Re-23Cr-10Al is strongly affected by another oxidant, namely nitrogen.

Thermodynamically, aluminum does not only possess high oxygen affinity but also belongs to the strongest nitride formers at high temperatures, as shown in Figure 5.16. Since nitrogen and oxygen are the two most essential air constituents, the nitridation of the protective oxide layer formers, i.e., Al and Cr, should be seriously considered in the alloy development. The more those components are consumed by internal nitridation, the harder the corresponding external protective oxide scale forms. In both Al-containing alloys in this study, the chemical affinity of Al to N is much higher than that of Cr, and as such, only AlN formation is observed under the presented experimental conditions. As shown in the Al-O$_2$-N$_2$ phase diagram (Figure 5.17), Al$_2$O$_3$ is thermodynamically the only stable phase in air, while AlN can only be formed, if the nitrogen partial pressure p_{N_2} is way higher than the oxygen partial pressure p_{O_2}. For example, at 1000°C almost a twenty orders of magnitude higher p_{N_2} than p_{O_2} is required for the formation of AlN.
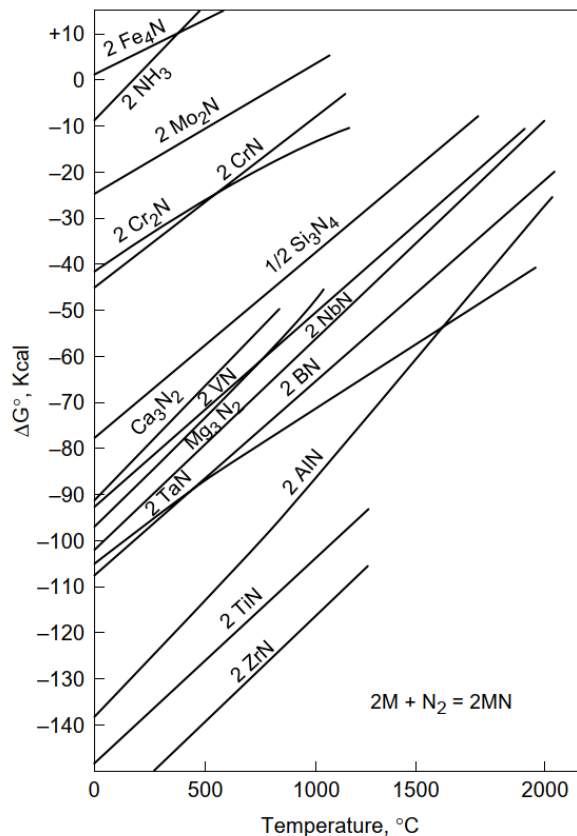

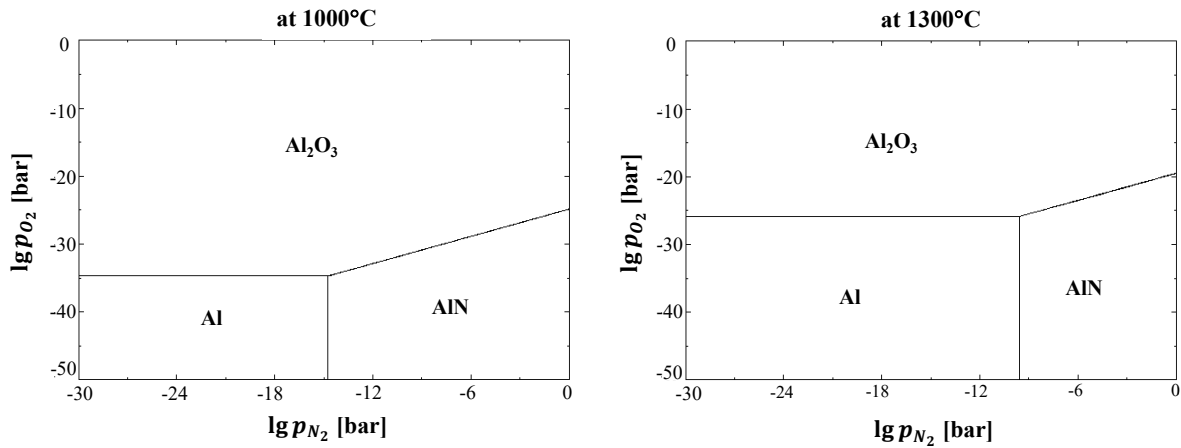Figure 5.16: Standard free energy for the formation of selected nitrides per mol N$_2$ [47]

Figure 5.17: The Al-O$_2$-N$_2$ phase stability diagram at 1000°C (left) and at 1300°C (right) calculated with FactSage

Therefore, the formation and arrangement of internal Al$_2$O$_3$ and AlN are essentially a consequence of the competition between the inwards diffusion of oxygen and nitrogen. At the boundary between the internal Al$_2$O$_3$ and AlN precipitation zones, the following local equilibrium is established:

$$2AlN + 3O \rightleftharpoons Al_2O_3 + 2N \tag{5.1}$$
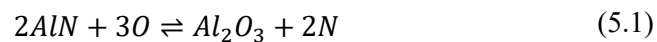
The kinetic studies and microstructural examinations indicate that the Cr$_2$O$_3$ scale possesses a much weaker protectiveness against nitrogen penetration than the Al$_2$O$_3$ scale. Other researchers have reported the same phenomenon, but there is no consistent theoretical explanation so far. Litz et al. [110] proposed that the formation of internal Al$_2$O$_3$ beneath the Cr$_2$O$_3$ scale caused a volume increase leading to compressive stresses in the internal oxidation zone and tensile stresses in the scale. Consequently, these processes led to scale cracking, giving gaseous nitrogen in air the chance to enter the metal and form internal nitrides. However, the more recent study by Geers et al. [109] showed that the oxide scale formed on FeCrAl alloy Kanthal APMT was penetrated by nitrogen exclusively at chromia domains without any evidence of micro-cracks that could serve as points-of-entry for nitrogen. In their study, they also employed density functional theory to investigate decisive nitrogen surface chemistry and transport properties in chromia and alumina and reported that the complex redox chemistry of Cr^{3+}, as opposed to Al^{3+}, was a sufficient discriminating factor between alumina and chromia, facilitating N$_2$ dissociation and mobility of N in chromia.

Looking at the microstructure of both Al-containing Co-Cr-Re-base alloys (Figure 5.1) and carefully comparing the Cr and Al concentrations in the σ phases (Table 5.1), it becomes apparent that the increase of Al content from 5% to 10% does not effectively raise the Al content in the σ phase, but rather, raises the volume fraction and particle size of the primary σ phase. The measured Al content in the σ phase of alloy Co-17Re-23Cr-10Al, which is about 6.8%, is almost the same as the Al content in the hcp matrix

in alloy Co-17Re-23Cr-5Al. This may partially explain their similarity in poor oxidation/nitridation resistance by forming a Cr$_2$O$_3$ layer instead of an external Al$_2$O$_3$ layer due to the lack of sufficient Al supply during exposure. Therefore, a reduction in both the volume fraction and the size of the σ phase should be considered as a potential strategy for further development, for example, by decreasing the Cr content or through suitable heat treatment.

Moreover, whether or not the addition of other elements with higher nitrogen affinity (e.g., Ti or Zr) could act as "nitrogen-getters" and therefore promote the outwards diffusion of Al to form a complete and protective Al$_2$O$_3$ layer should also be taken into consideration in the further development of the Co-Re-base alloys. An example is given in Figure 5.18, in which the inward diffused nitrogen was removed by chemical combination with Ti in the alloy, forming an internal TiN zone and an external Al$_2$O$_3$ layer.

Figure 5.18: Cross-sectional micrograph of SC Ni-base superalloy SRR99 (approximately Ni-10W-8Cr-6Al-5Co-3Ta-2Ti in wt.%) after exposure to air at 1000°C for 100 h [107]

6 Cr$_2$O$_3$ layer stability

During the preliminary studies which attempt to form silica or alumina scale on the Co-Re-base alloys for application at elevated temperatures, efforts focusing on the chromia formation were conducted in parallel for intermediate temperature applications. The corresponding key results are presented and discussed in this chapter.

6.1 Oxidation mechanism of Co-Re-Cr-Si alloys

As discussed in Chapter 4, the addition of Si in a small amount to the alloy Co-17Re-23Cr has markedly improved its oxidation resistance by facilitating the formation of the Cr$_2$O$_3$ layer through selective oxidation. Although such effect is positively correlated to the amount of silicon added, high Si content in the alloy system still needs to be avoided, since (i) it strongly reduces the melting point of the alloy; (ii) it promotes the formation of the brittle σ phase; (iii) it enhances the spallation of the chromia layer formed.

Besides, Gorr et al. [32] reported that the increase of Cr content from 23% to 30% in the alloy Co-17Re-xCr-2Si also resulted in a significant improvement in oxidation resistance. While the scale formed on alloy Co-17Re-23Cr-2Si was porous and non-protective, a dense and protective chromia scale was observed on alloy Co-17Re-30Cr-2Si during exposure to air at 1000°C. This has been the first time in the history of Co-Re-base alloys development that a protective Cr$_2$O$_3$ scale could be achieved.

However, such a high Cr content is undesired from the viewpoint of mechanical properties, and the studies on the oxidation mechanism of this relatively unknown alloy system are so far still inadequate. Against this background, a set of Co-Re-base alloys containing moderate Si (2%) and varying Cr content (23-27%) were investigated aiming at an optimization of the Cr content and trying to elucidate the relevant oxidation mechanisms of the Co-Re-Cr-Si alloys, in order to develop strategies for further improvement of the oxidation resistance.

6.1.1 Effect of chromium concentration

The microstructure of the investigated alloys Co-17Re-23Cr-2Si, Co-17Re-25Cr-2Si, and Co-17Re-27Cr-2Si are shown in Figure 6.1. All three alloys are composed of the two typical phases, i.e., the hcp matrix and the σ phase. The volume fraction of the primary σ phase in each alloy after solution heat treatment was measured and compared in Figure 6.2. It is seen that the volume fraction of the σ phase increases significantly from about 12% to about 36% with increasing Cr content by just 4% from 23%

to 27%. This observation is in very reasonable agreement with the thermodynamic calculation for the Co-17Re-xCr alloy system at 1000°C, as shown in Figure 2.10. In addition, the average particle size of the primary σ phase is observed to be positively correlated to the Cr content.
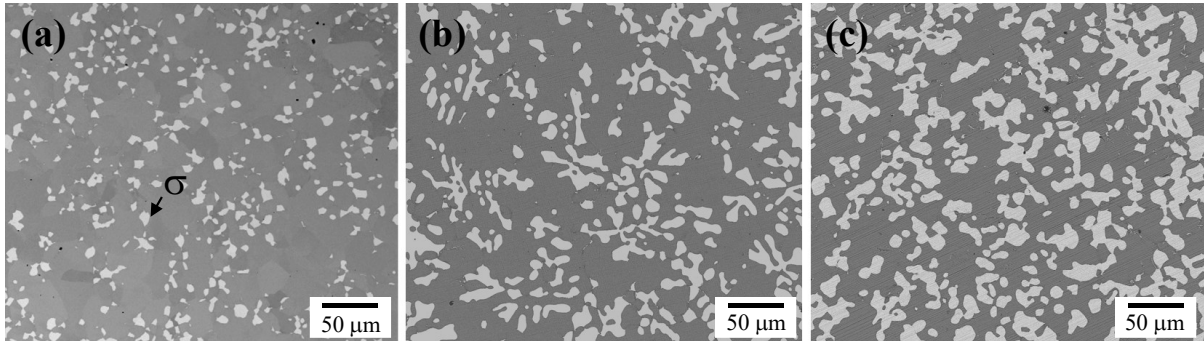

Figure 6.1:   Microstructural images of alloys Co-17Re-xCr-2Si showing significant differences in the distribution of the σ-phase: (a) -23Cr; (b) -25Cr; (c) -27Cr
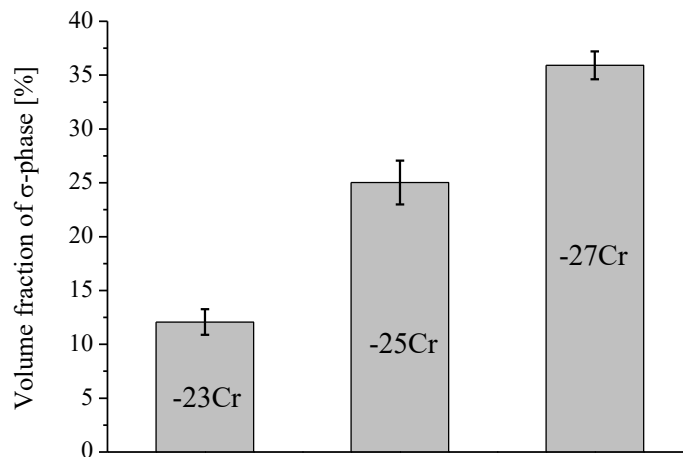
Figure 6.2:   Observed volume fractions of the σ-phase in the alloys Co-17Re-xCr-2Si after solution heat treatment

The thermogravimetric results of the alloys Co-17Re-xCr-2Si during exposure at 1000°C are shown in Figure 6.3. As the Cr content changes from 23% to 27%, two distinct types of oxidation kinetics are observed. While the weight change curve of the alloy Co-17Re-23Cr-2Si is extensively influenced by the volatilization of Re oxide, weight gain kinetics are observed both on alloy Co-17Re-25Cr-2Si and alloy Co-17Re-27Cr-2Si. The kinetic curve of alloy Co-17Re-27Cr-2Si shows a parabolic behavior in the oxidation test, and the thermogravimetric course of alloy Co-17Re-25Cr-2Si shows a near-parabolic behavior in the steady-state stage. It is worth mentioning that the kinetic behavior of alloy Co-17Re-25Cr-2Si, especially the behavior in the early reaction stage, depends sensitively on the sample condition.

Any minor differences in microstructure near the sample surface (σ phase distribution) or roughness at the specimen edges may lead to strongly different kinetic results. Nevertheless, all of the kinetic results of alloy Co-17Re-25Cr-2Si obtained at 1000°C exhibit in general a slowly increasing weight gain.
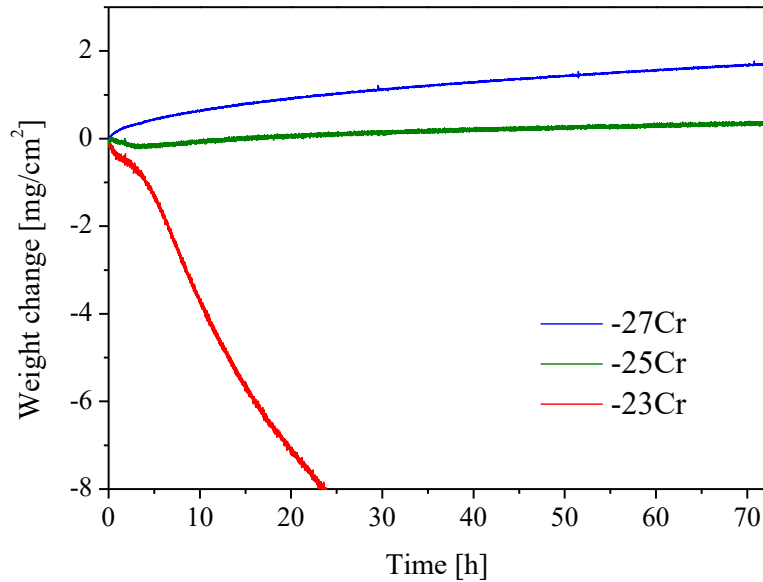

Figure 6.3: Thermogravimetric data from oxidation tests at 1000°C on Co-17Re-xCr-2Si alloys containing different Cr-contents

Cross-sectional examination of the oxidized specimens implies that the scale morphology on alloy Co-17Re-25Cr-2Si and Co-17Re-27Cr-2Si are rather similar. Figure 6.4 compares the cross-sections of oxidized Co-17Re-23Cr-2Si and Co-17Re-25Cr-2Si. It is apparent that the increase of the Cr content from 23% to 25% significantly changes the oxidation mechanism under the experimental conditions.

The oxide scale formed on Co-17Re-23Cr-2Si, shown in Figure 6.4a, is thick and can be essentially identified to consist of three layers, i.e., the outermost CoO layer, the $CoCr_2O_4$ spinel layer, and the quasi-continuous Cr_2O_3 layer at the oxide/alloy interface. SiO_2 is observed as internal precipitates beneath the scale formed. On the contrary, the scale formed on alloy Co-17Re-25Cr-2Si is relatively thin and consists mainly of a dense and continuous Cr_2O_3 layer, over which an extremely thin outermost $CoCr_2O_4$ layer is found. Beneath the Cr_2O_3 layer, SiO_2 internal precipitates exist primarily as clusters in the σ phase and along the phase boundaries between the σ phase and the alloy matrix.
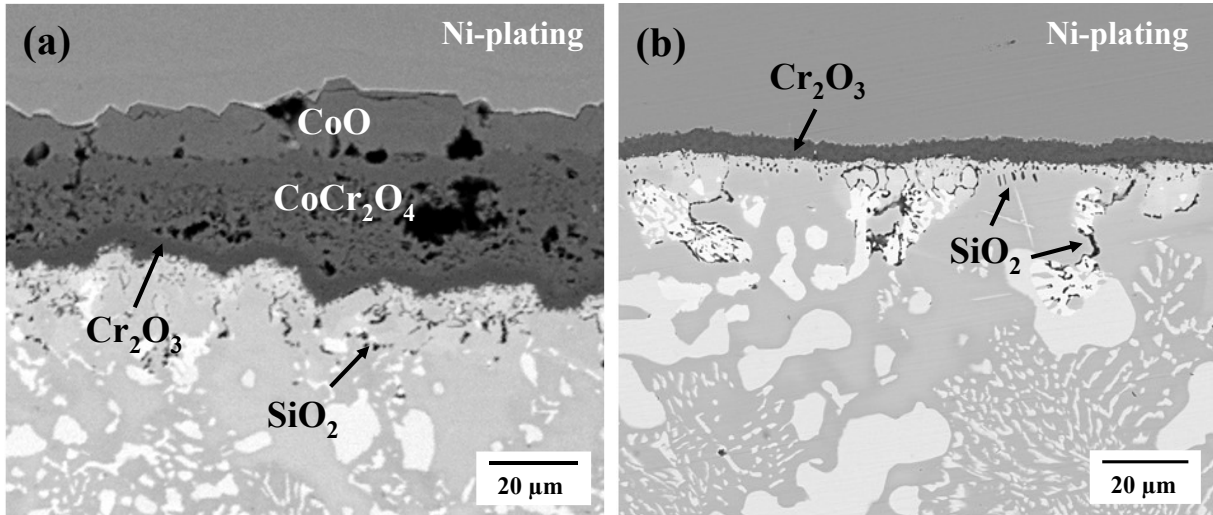
Figure 6.4:   Cross-sectional BSE-SEM images of alloys after exposure in air at 1000°C for 72h: (a) Co-17Re-23Cr-2Si; (b) Co-17Re-25Cr-2Si

Combining the TGA findings and the microstructural observations presented above, it can be stated that the increase of the Cr from 23% to 25% has significantly improved the oxidation resistance of alloy Co-17Re-xCr-2Si by forming a dense and protective Cr$_2$O$_3$ layer. Furthermore, 25% Cr seems to be the critical concentration to form a continuous external chromia layer at 1000°C. Alloy Co-17Re-25Cr-2Si and alloy Co-17Re-30Cr-2Si form a continuous and protective Cr$_2$O$_3$ scale at 1000°C. However, it is important to point out that the volume fraction of the σ phase in alloy Co-17Re-25Cr-2Si (~25%) is only about half of that in alloy Cr-17Re-30Cr-2Si (~44%) [111]. Such reduction is undoubtedly beneficial in terms of mechanical properties.

Therefore, further studies on alloy Co-17Re-25Cr-2Si were conducted to understand the oxidation mechanism more in detail to develop strategies to form a stable chromia scale on Co-Re-base alloys.

6.1.2 Temperature dependence

Figure 6.5 shows the TGA measurements of alloy Co-17Re-25Cr-2Si during exposure to air at various temperatures from 800-1100°C. At 800°C, a small positive weight change caused by the initial oxygen uptake is only observed at the initial stage of oxidation. After this extremely short period, the weight change curve tends toward the negative direction, demonstrating the non-protective nature of the oxide scale formed. The evaporation of Re oxides is not prevented.

Similarly, the negative weight change behavior of the alloy is also observed at 900°C. However, the weight loss rate in the first few hours is much higher and follows an almost linear time law. After a turning point at around 5 h, the weight loss rate is tremendously slowed down.

On the contrary, the TGA data obtained at 1000°C and 1100°C exhibit significantly different behavior. Despite a slight negative weight change in the initial period at 1000°C, both TGA curves exhibit a weight gaining behavior at the steady oxidation stage, which to some extent follows a parabolic rate law.
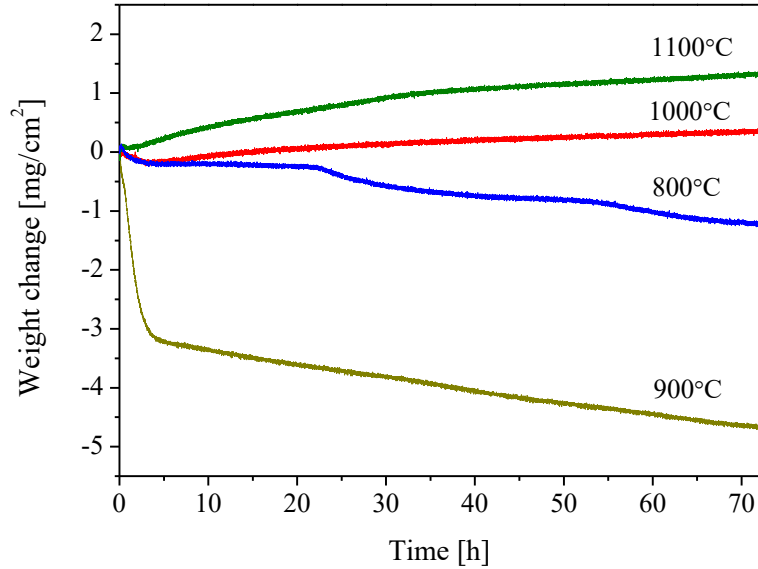

Figure 6.5:   Thermogravimetric data of the alloy Co-17Re-25Cr-2Si during exposure to laboratory air at 800-1100°C

Figure 6.6 shows the surface micrographs of alloy Co-17Re-25Cr-2Si after exposure to air for 72 h at 800-1100°C. It is seen that the outermost oxide layer formed at 800°C is porous and fine-grained, while that formed at 900°C is dense and relatively large-grained. Both oxide surfaces appear uniform. In combination with XRD and EDS analysis, as shown in Table 6.1, the outermost oxide layer formed at 800°C is identified as pure Co_3O_4, whereas the one formed at 900°C is identified as a mixture of Co_3O_4 and CoO.

However, the outermost oxide layer formed at 1000°C is inhomogeneous. Significant differences are found at lower magnification (see Figure 6.6c), showing darker areas whose distribution resembles the σ phase distribution in the alloy matrix. The oxide grain size in the darker areas is slightly larger than that in the brighter area. EDS analysis shows a high Cr signal for both areas, but the darker area contains more cobalt than the brighter area, as presented in Table 6.1.

At 1100°C, the oxide surface is homogeneous and appears similar to that formed on the brighter area at 1000°C. XRD analyses on both oxide surfaces show strong peaks of Cr_2O_3 with a minor presence of $CoCr_2O_4$. The grain sizes of the outermost oxide layers formed at 1000°C and 1100°C are also finer compared to those formed at 900°C. Additionally, the oxide scales formed at 1000°C and 1100°C appear to be denser.
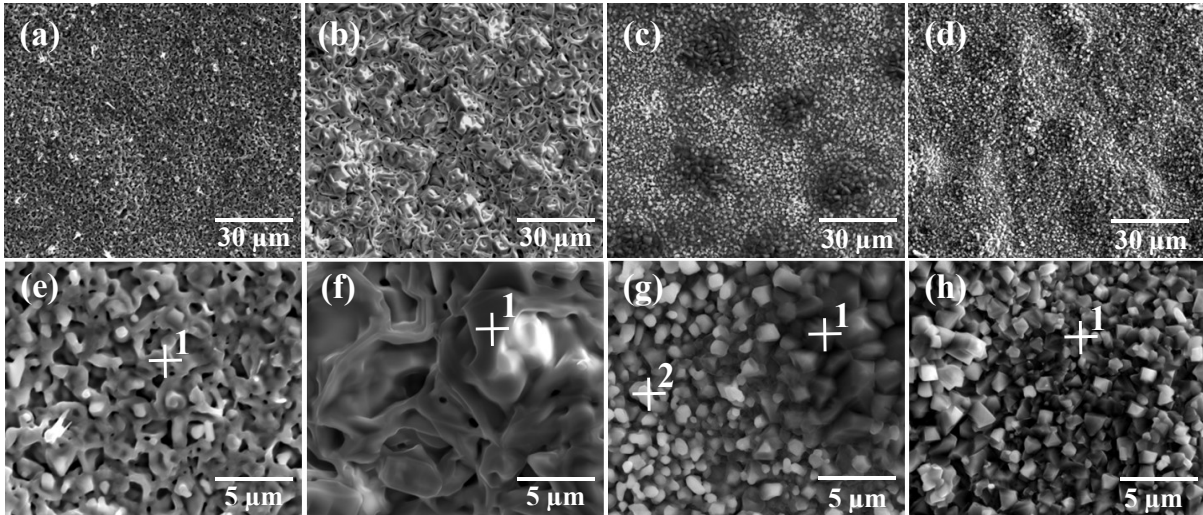
Figure 6.6: SE-SEM images of the oxide surface formed on alloy Co-17Re-25Cr-2Si after exposure to air for 72 h: (a, e) 800°C; (b, f) 900°C; (c, g) 1000°C; (d, h) 1100°C.

Table 6.1: EDS (positions in Figure 6.6) and XRD characterization of the oxide surfaces formed on alloy Co-17Re-25Cr-2Si

Temperature	EDS results in at.%				Phase detected by XRD
	Position	Co	Cr	O	
800°C	e-1	49.7	-	50.3	Co$_3$O$_4$
900°C	f-1	48.9	-	51.1	Co$_3$O$_4$, CoO
1000°C	g-1	7.9	33.7	58.4	Cr$_2$O$_3$ (major), CoCr$_2$O$_4$ (minor)
1000°C	g-2	1.2	39.3	59.5	Cr$_2$O$_3$ (major), CoCr$_2$O$_4$ (minor)
1100°C	h-1	1.3	39.7	59.0	Cr$_2$O$_3$ (major), CoCr$_2$O$_4$ (minor)

The cross-sectional micrographs of the oxide scale in combination with EDS line scans are shown in Figure 6.7. It is seen that both of the scales formed at 800°C and 900°C reveal two oxide layers, an outer Co oxide layer followed by a CoCr$_2$O$_4$ spinel layer, in which few SiO$_2$ particles are found to be embedded. The higher Cr intensity in the combination of the sudden drop of the Co intensity at the scale/alloy interface at 800°C and 900°C implies the presence of a relatively discontinuous and thin Cr$_2$O$_3$ layer. Although the spinel layer formed at 900°C is denser than that formed at 800°C, the accelerated inward diffusion of oxygen by raised temperature and the lack of protective Cr$_2$O$_3$ layer still result in a thicker spinel layer.

The oxide scales formed at higher temperatures show a distinct structure. EDS line scans reveal that both scales formed at 1000°C and 1100°C consist mainly of a single-phase layer identified as Cr$_2$O$_3$. Only an extremely thin CoCr$_2$O$_4$ layer forms at the scale/air interface. SiO$_2$ precipitates are found as internal oxidation products at both temperatures.
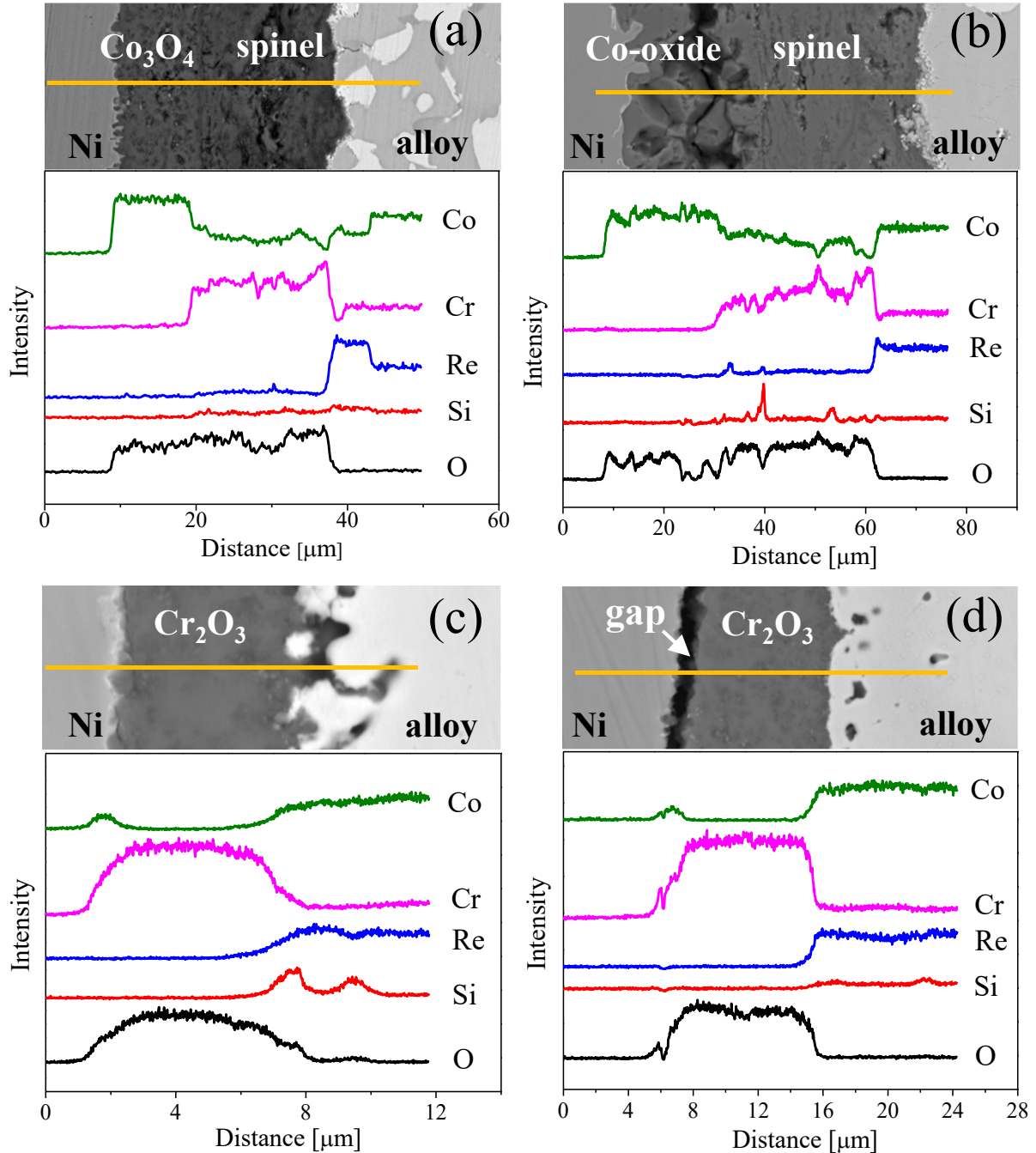

Figure 6.7: Cross-sectionnal SEM images (BSE) in combination with corresponding EDS line scans through the oxide scale formed on alloy Co-17Re-25Cr-2Si after oxidation for 72 h: (a) 800°C; (b) 900°C; (c) 1000°C; (d) 1100°C

Several authors have carried out studies on the high-temperature oxidation behavior of binary Co-Cr alloys and Co-Cr-based alloys [83, 112-117]. Most of these studies were conducted at temperatures around 1000°C. At these temperatures, it is a common observation that a non-protective double-layered oxide scale, which consists of an outer CoO layer and an inner mixture of $CoCr_2O_4$ and CoO, forms on alloys containing Cr less than the critical concentration required for the formation of a closed Cr_2O_3 layer. If a Co-Cr alloy possesses sufficient Cr-concentration, a dense Cr_2O_3 layer may develop with an associated reduction in the oxidation rate. In addition to the variation of the Cr content, Kofstad and Hed [118] reported that the transition from the non-protective to the protective oxidation products also depends sensitively on the oxygen partial pressure. Nevertheless, there is rare information reports on the temperature effect on the oxidation mechanism, especially with respect to the oxide products transition of Co-Cr-based alloys.

Despite the possibility of Re oxidation and the corresponding volatilization of its oxide, scales formed on Co-Re-Cr-base alloys are generally similar to those formed on the conventional Co-Cr-base alloys at around 1000°C. Results shown above clearly reveal that a transition of the oxidation products on the alloy Co-17Re-25Cr-2Si from non-protective double layers to a dense and slow-growing Cr_2O_3 external layer occurs as the oxidation temperature changes from 900°C to 1000°C. From the thermodynamic point of view, Cr_2O_3 is always much more stable than Co oxides in the temperature range investigated [119]. Hence, it can be assumed that the strong temperature dependence of the prevailing oxidation products on alloy Co-17Re-25Cr-2Si is controlled by kinetics, specifically, by the Cr diffusivity in the alloy.

The Arrhenius plot of the Cr diffusion coefficient in the binary Co-Cr alloy system shown in Figure 6.8 indicates that the diffusivity of Cr increase by almost three orders of magnitude when the temperature increases from 800°C to 1100°C. With the aid of silicon, which chemically bonds the inwardly diffusing oxygen, the accelerated diffusional flux of Cr at increased temperature facilitates the formation of a continuous chromia layer on the alloy surface.
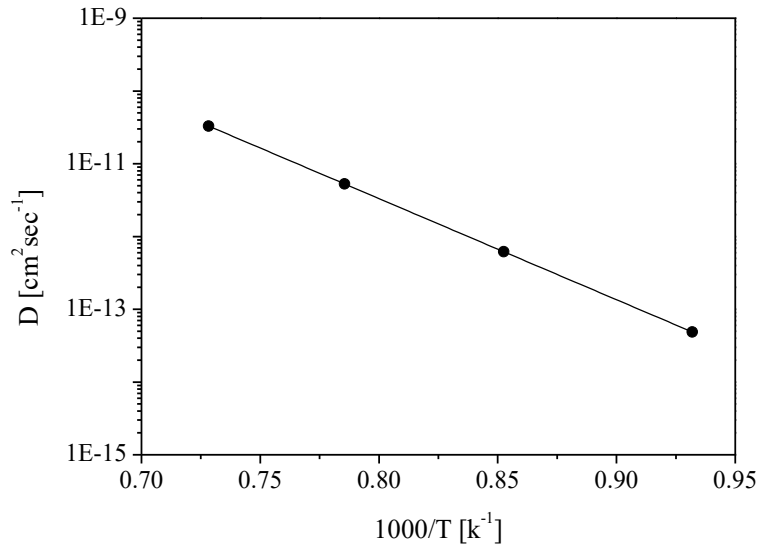
Figure 6.8:   Arrhenius plot of the Cr diffusion coefficient in a Co-Cr solid solution (0-40 at.% Cr) in the temperature range 800-1100°C based on data from [120]

6.1.3 Alloy microstructural changes

Figure 6.9 shows the cross-sectional images of oxidized Co-17Re-25Cr-2Si specimens demonstrating oxidation products and the metallic substrate. The total scale thickness and the corresponding depth of the internal oxidation zone are summarized in Table 6.2. Although the scale constitutions at 1000°C and 1100°C are similar, the Cr$_2$O$_3$ scale formed at 1100°C is about twice as thick as that formed at 1000°C. In addition, the amount of SiO$_2$ internal precipitates underneath the oxide scale increases with increasing oxidation temperature. At 1000°C, most of the internal oxidation particles are formed in the σ phase. In contrast, the SiO$_2$ particles formed at 1100°C are much more homogeneously distributed in the alloy subsurface.

Moreover, secondary σ phase precipitates are found in each alloy substrate after isothermal oxidation tests at 800-1100°C. However, the amount, form, and distribution of these secondary σ particles are different after oxidation at different temperatures. The aggregated volume fraction of the σ phase after oxidation tests in the alloy substrate is summarized in Table 6.2. Considering the volume fraction of the primary σ phase in the alloy prior to oxidation is about 25%, only 3% is additionally precipitated as the secondary σ phase along the grain boundaries of the hcp matrix at 800°C. At 900°C, the secondary σ phase also precipitates in the hcp matrix grains, and the volume fraction of the secondary σ phase increases by up to 10%. The secondary σ phase formed at 1000°C has similar morphology as that formed at 900°C but exhibits a higher volume fraction. At 1100°C, the precipitated secondary σ phase becomes coarse and spheroidal-shaped after oxidation.

75
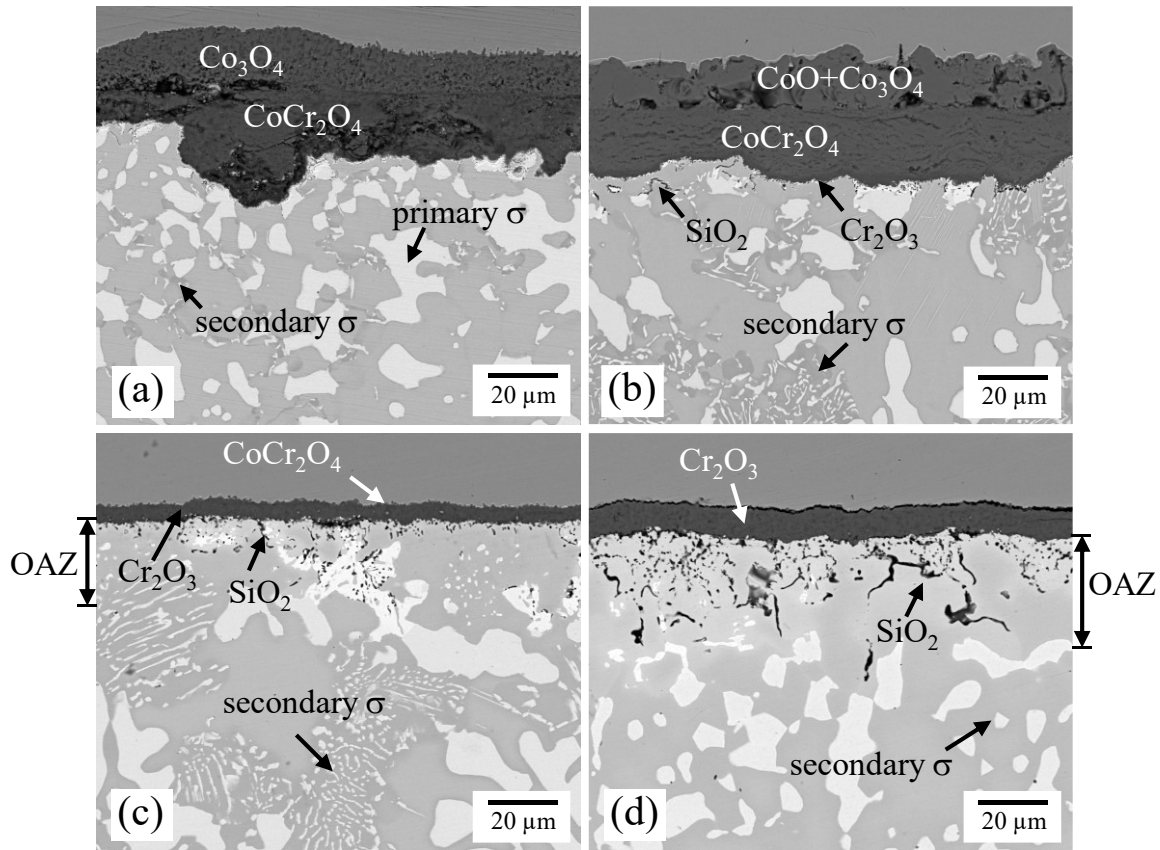
Figure 6.9:   Cross-sectional BSE-SEM micrographs of alloy Co-17Re-25Cr-2Si after exposure to air for 72 h indicating the oxidation-affected zone (OAZ): (a) 800°C; (b) 900°C; (c) 1000°C; (d) 1100°C

Table 6.2: Cross-sectional characterization on alloy Co-17Re-25Cr-2Si after oxidation for 72 h

Temperature [°C]	Scale thickness [μm]	Depth of the internal oxidation [μm]	Total σ phase volume fraction [%]
800	26.8 ± 3.6	-	28.6 ± 1.4
900	35.6 ± 3.4	3.3 ± 1.3	34.0 ± 2.1
1000	5.1 ± 0.8	12.9 ± 6.7	37.8 ± 2.1
1100	9.5 ± 0.6	30.9 ± 10.7	36.9 ± 3.0

Beneath the oxide scale, a dissolution of the primary σ phase is observed after oxidation at 1000°C and 1100°C. The reason for this phenomenon is suggested to be the consumption of Cr in this region, which has stabilized the primary σ phase before. This phenomenon can be more clearly observed on specimens that are oxidized at 1100°C due to the faster growth of the Cr$_2$O$_3$ scale. Figure 6.10 shows a cross-

sectional EDS mapping of a specimen oxidized at 1100°C. The elemental distribution of Cr indicates an approximately 50 µm deep Cr depletion zone underneath the Cr$_2$O$_3$ layer. The primary σ phase in this region dissolves consequently, forming a Re-rich subsurface. The enrichment of Re at the subsurface also implies the protective nature of the scale, avoiding the formation and evaporation of rhenium oxide. Moreover, the diffusion of Co from the original hcp matrix into the region of the dissolved σ phase at the subsurface is observed.
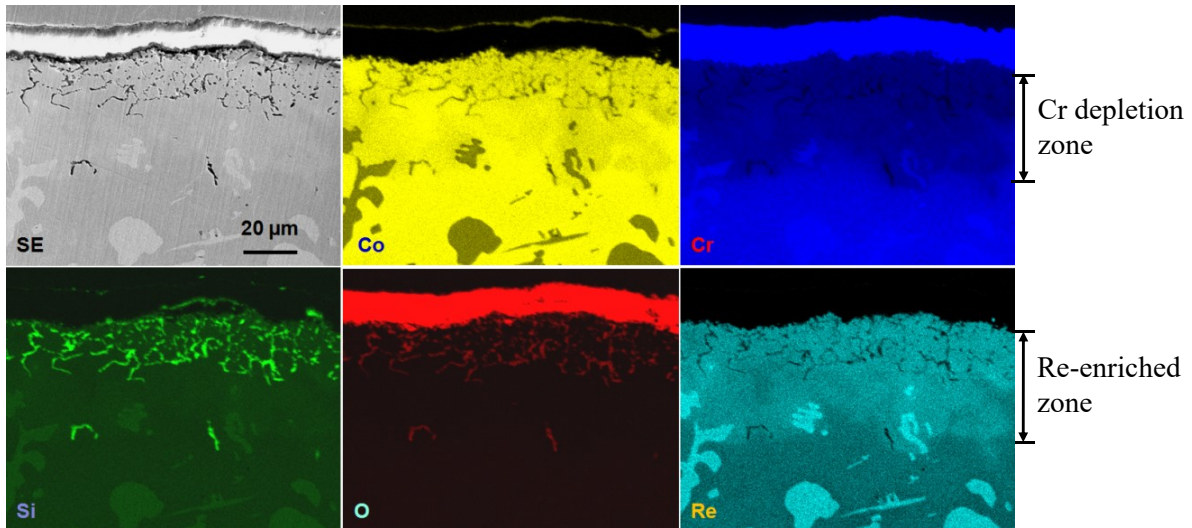

Figure 6.10: The element distribution maps of a cross-section of Co-17Re-25Cr-2Si alloy after exposure in air at 1100°C for 72 h

Additionally, SiO$_2$ particles form in the oxidation-affected zone both at 1000°C and 1100°C. However, the distributions of these oxides are different. For samples oxidized at 1000°C for 72 h, SiO$_2$ primarily forms in the region where the primary σ phase dissolves. However, also SiO$_2$ particles precipitate in the hcp matrix (Figure 6.9c). A similar SiO$_2$ distribution is observed in the specimen oxidized at 1100°C after a short period of oxidation. Nevertheless, after a long exposure period at 1100°C, the SiO$_2$ particles distribute homogeneously underneath the Cr$_2$O$_3$ scale (Figure 6.9d).

EBSD examination (Figure 6.11) of the oxidation-affected zone reveals that a fine-grained hcp phase region newly forms underneath the oxide scale after oxidation. Interestingly, it is also found that most of the SiO$_2$ particles form exactly along the grain boundaries of these new grains. The elementary distribution obtained by EDS scan (Figure 6.12) indicates a noteworthy difference in chemical composition between the newly formed hcp grains and the initial hcp grains in the alloy. Lower Cr and Co but higher Re contents are found in the new hcp grains.
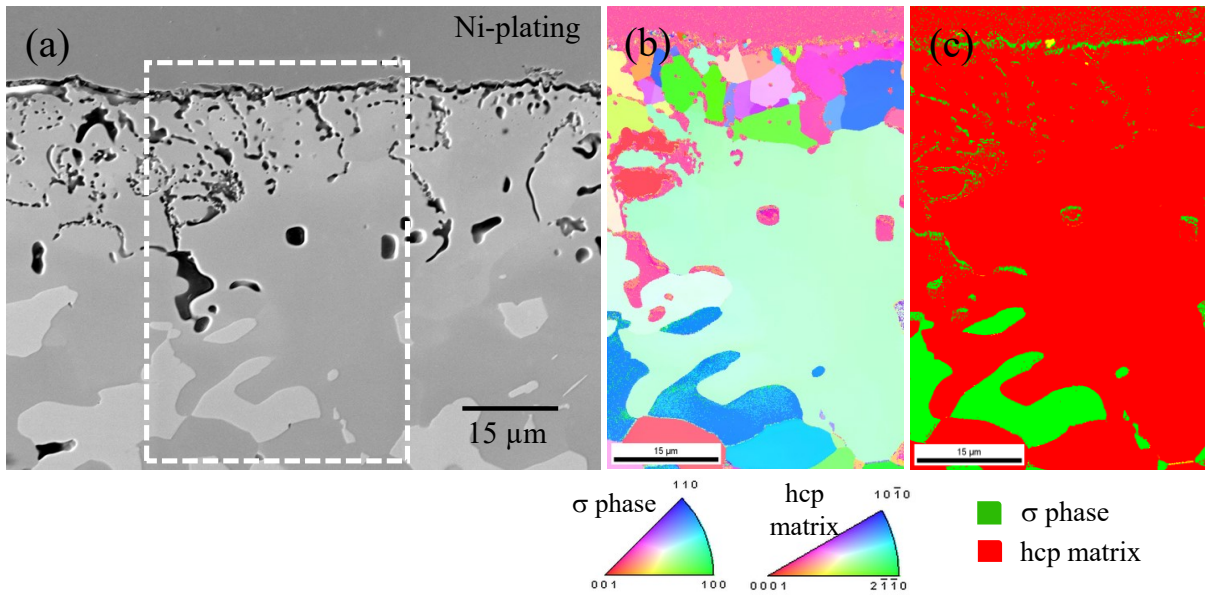
Figure 6.11: SEM images of the cross-section of alloy Co-17Re-25Cr-2Si after oxidation at 1000°C for 72 h, where the external oxide scale is completely spalled off: (a) BSE micrograph; (b) EBSD grain orientation map of the framed area marked in (a); (c) EBSD phase map
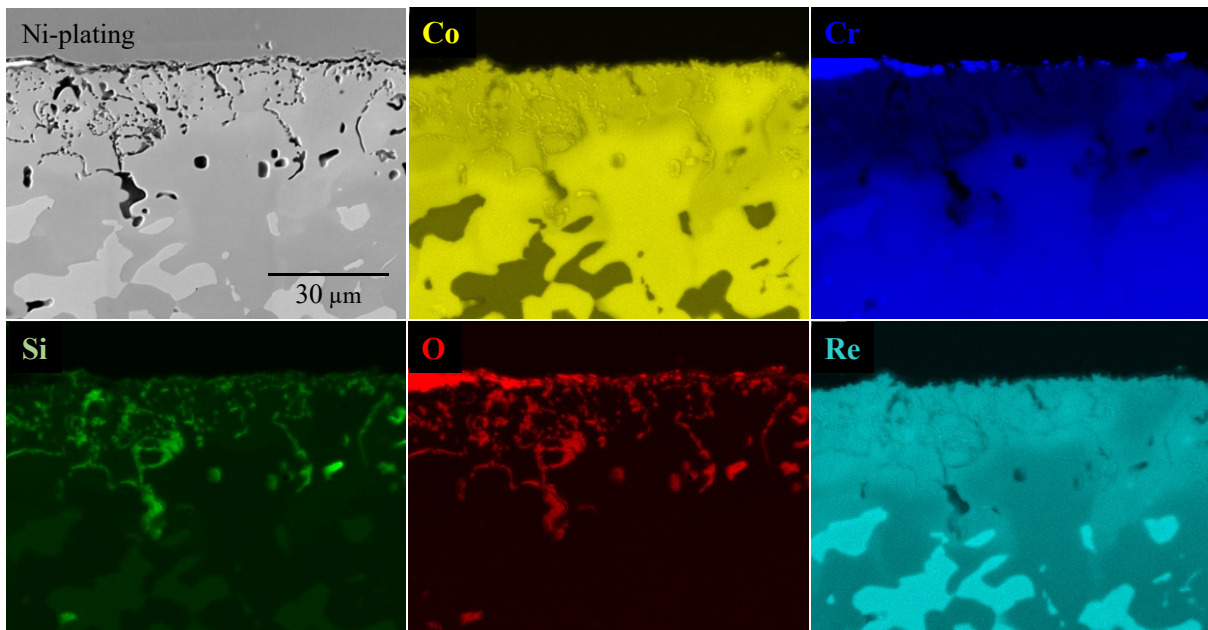
Figure 6.12: EDS mappings of Co-17Re-25Cr-2Si subsurface after oxidation in air for 72 h. The area shown corresponds to that depicted in Figure 6.11

As shown in Figure 6.11, it seems that the formation of the new small hcp grains in the vicinity of the alloy surface is attributed to the classical recrystallization phenomenon since the material in the near-surface region exhibits a relatively high dislocations density as a result of the grinding process before

oxidation test and, consequently, is in a relatively high strain energy state. However, it should be kept in mind that dissolution of σ phase may also lead to the formation of the new hcp grains. To verify whether the microstructural changes are driven by strain energy stored in dislocations or by the Cr-depletion induced σ phase dissolution, a Co-17Re-25Cr-2Si specimen was ground down to 1200 grid as usual and then exposed to an atmosphere with low oxygen partial pressure at 1000°C for 72 h. The setting conditions should primarily prevent the oxidation of Cr and, most importantly, the dissolution of the σ phase in the subsurface region.

The corresponding EBSD analysis was carried out after the exposure, and the results are shown in Figure 6.13. Although the oxidation of Cr could not be prevented completely, the dissolution of the σ phase has been significantly retarded. SiO$_2$ internal precipitation along the grain/phase boundaries implies the relatively faster short-circuit diffusion of oxygen into the alloy than that of Si towards the alloy surface. Comparing the EBSD results after oxidation in air (Figure 6.11) and in low oxygen partial pressure (Figure 6.13), it becomes clear that the formation of small hcp grains is the result of σ phase dissolution.
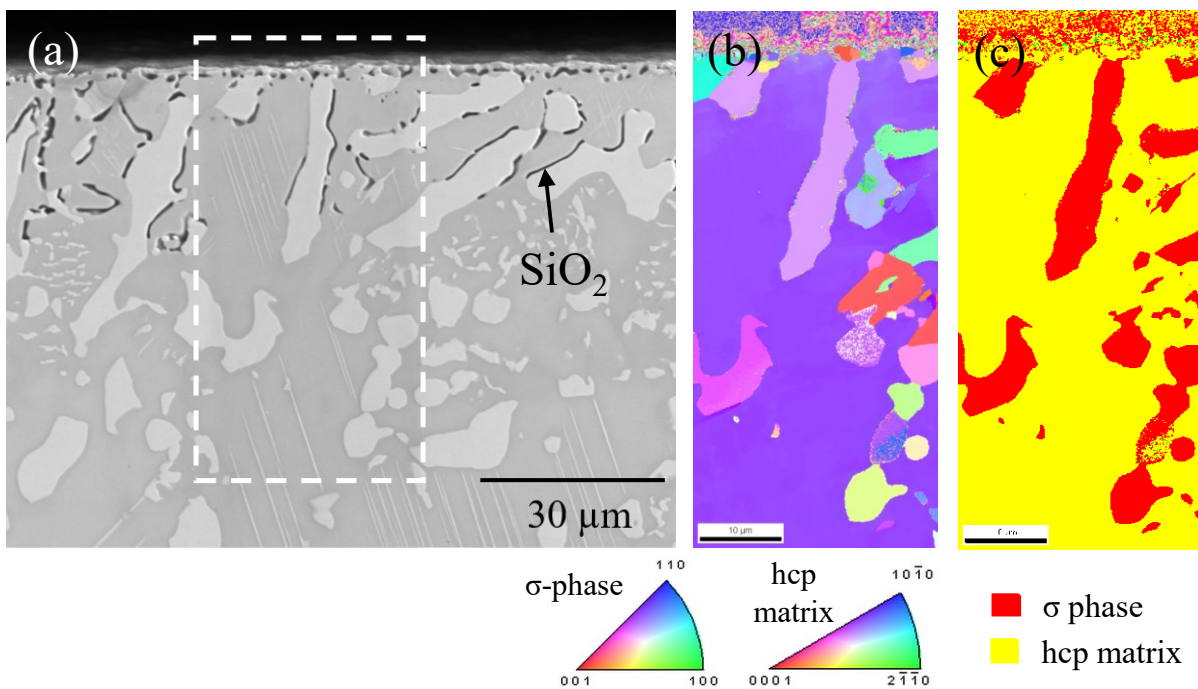
Figure 6.13: SEM analysis of the cross-section of the alloy Co-17Re-25Cr-2Si after exposure to Ar-H$_2$/H$_2$O atmosphere (p(O$_2$) = 10^{-19} bar) at 1000°C for 72 h: (a) BSE image; (b) grain orientation map of the frame area marked in (a); (c) phase map

6.1.4 Scaling mechanism

Figure 6.14 shows the scales formed on alloy Co-17Re-25Cr-2Si after a short exposure to air at 800°C, 1000°C, and 1100°C, respectively. It is seen that a thin Cr$_2$O$_3$ layer forms quickly on the hcp grain at

the early oxidation stage at all temperatures. However, the oxides formed on the σ phase are different from external Cr$_2$O$_3$. Even though the σ phase contains more Cr than the hcp phase, no protective Cr$_2$O$_3$ layer is formed on the σ phase at 800°C. Instead, a thick and porous Co$_3$O$_4$/spinel double-layer scale forms. Cr$_2$O$_3$ and SiO$_2$ internal precipitates are found underneath the oxide scale (see Figure 6.14a).

When the temperature increases to 1000°C, the accelerated Cr diffusion in the σ phase promotes a dense and semi-continuous Cr$_2$O$_3$ layer to form at the scale/alloy interface after only 20 min (see Figure 6.14b). The non-protective nature of the oxide scale formed during the transient oxidation period leads to the oxidation of Re and consequently the evaporation of its oxides, which corresponds to the initial negative weight change of the TGA curve shown in Figure 6.5. Once the complete continuous Cr$_2$O$_3$ layer formed, the Re oxides evaporation is retarded, resulting in weight gain kinetics. At 1100°C, a compact protective Cr$_2$O$_3$ layer forms on the σ phase almost as quickly as it forms on the hcp phase. The oxidation of Re and the evaporation of its oxides are directly retarded at the very initial stage of oxidation (Figure 6.14c).

These results clearly show that the oxidation behavior of the σ particles plays a crucial role in scale development, especially in the transient oxidation period. Consequently, reducing the volume fraction or particle size of the primary σ phase is supposed to be a necessary strategy for the further development of the alloy.
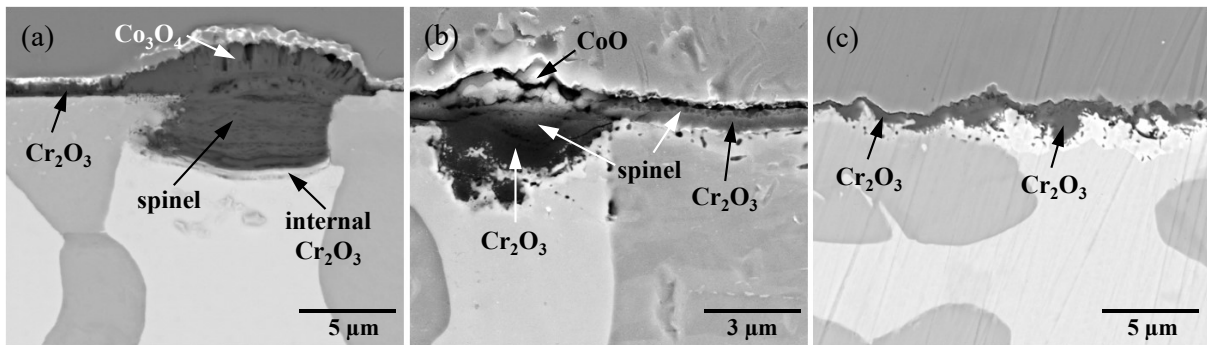
Figure 6.14: Cross-sectional images of the oxide scales formed on alloy Co-17Re-25Cr-2Si at (a) 800°C for 2 h; (b) 1000°C for 20 min; (c) 1100°C for 5 min

Marker experiments were carried out to determine the growth mechanism of the oxide scales formed. Au markers, spattered on the alloy surface before oxidation, remind at the Co oxide/spinel interface after exposure to air at 900°C for two hours (Figure 6.15a), indicating that the outer Co oxide layer grows by the outward migration of cobalt cations and the inner spinel layer grows by the inward migration of oxygen. A similar result was obtained at 800°C.

To avoid confusion caused by the standard sample preparation in this work, where the oxidized specimens for cross-sectional examination are normally Au-sputtered before Ni-plating, and by the low melting point of Au (1064°C), Pt markers were used for experiments at 1000°C and above. Since the

spinel phase, as a transient product, does not form a continuous dense outer oxide layer, platinum markers are observed on the oxide surface (Figure 6.15b) as well as at the spinel/Cr$_2$O$_3$ interface (Figure 6.15c). This observation suggests that the Cr$_2$O$_3$ layer grows predominantly via inward transport of oxygen through the Cr$_2$O$_3$ layer being in contrast to many Cr$_2$O$_3$ forming alloys [121] but in accordance with alloys containing reactive elements [74].
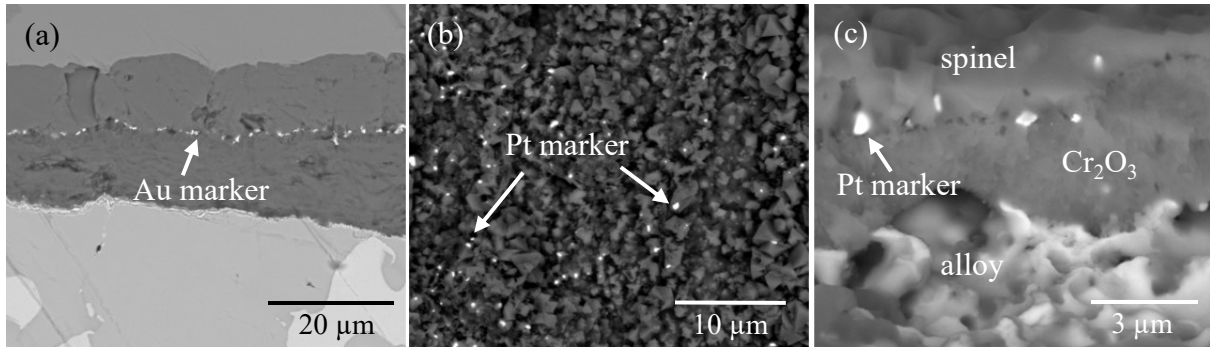
Figure 6.15: Markers in the oxide scales of Co-17Re-25Cr-2Si: (a) cross-sectional BSE image after oxidation at 900°C for 2 h; (b) top view (BSE) of the sample surface after oxidation at 1100°C for 8 h; (c) cross-sectional view of the cracked oxide scale shown in (b)

Figure 6.16 presents the BSE images of the oxide scale formed on the alloy Co-17Re-25Cr-2Si at 1100°C in high contrast. Rapid transient oxidation produces an extremely thin spinel layer at the scale/gas interface. Within the Cr$_2$O$_3$ layer, relatively small grain size is found at the scale/alloy interface, indicating that the formation of new Cr$_2$O$_3$ grains mainly takes place at the oxide/alloy interface (see Figure 6.16a). As the arrows in Figure 6.16b indicate, many bright particles are found at the oxide grain boundaries. EDS analysis shows a relatively high intensity of Re. The segregation of rhenium at the chromia grain boundaries might impede the outward transport of Cr, leading to an inward oxygen-transport-predominated scale growth.
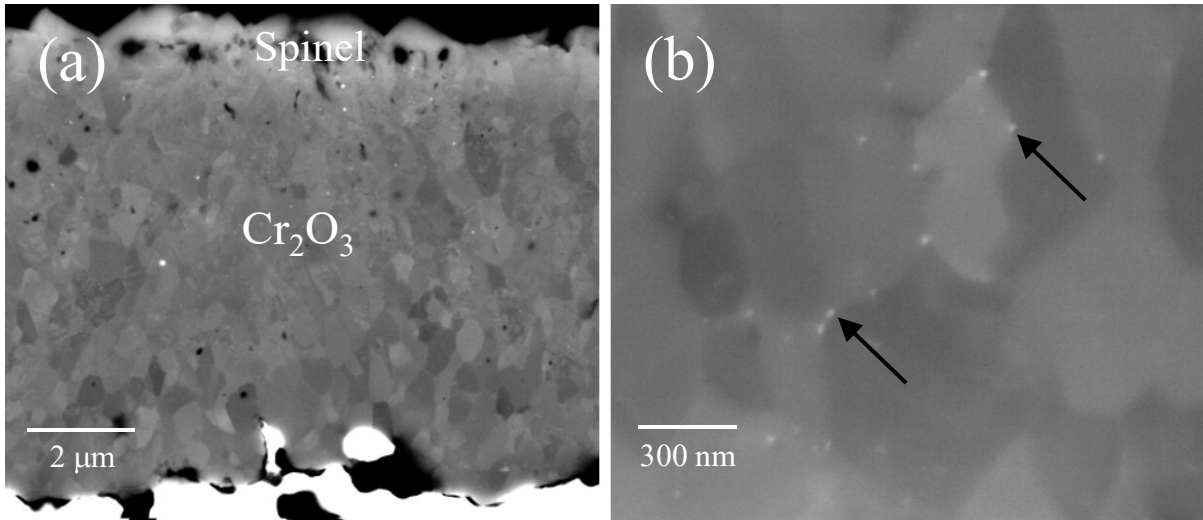
Figure 6.16: High contrast BSE-SEM micrograph of chromia scale formed on alloy Co-17Re-25Cr-2Si after exposure to air at 1100°C for 72h: (a) the total scale; (b) highly magnified chromia layer

In terms of scale adhesion, alloy Co-17Re-25Cr-2Si possesses, in general, a better performance compared to the high silicon-containing alloys. However, as the chromia thickens, increasingly severe spallation of the scale during cooling can be observed. This is, for instance, shown in Figure 6.17.
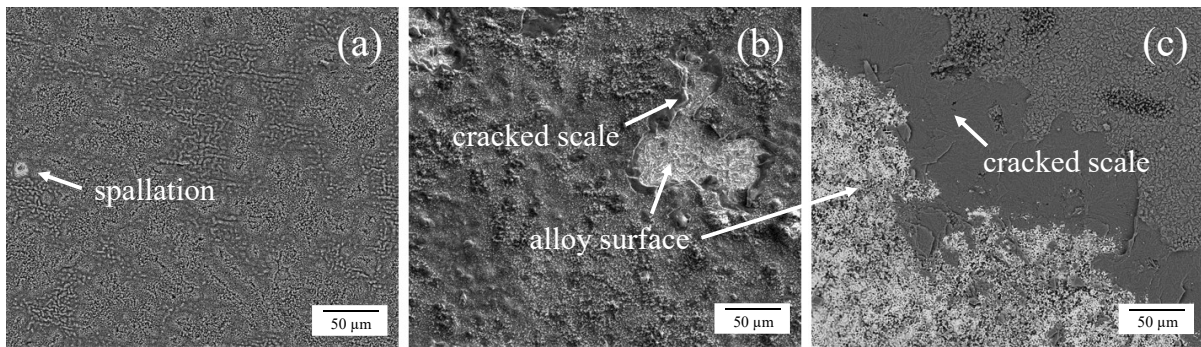
Figure 6.17: Surface images of alloy Co-17Re-25Cr-2Si after oxidation at 1100°C for different times: (a) 1 h; (b) 5 h; (c) 72 h

6.1.5 Discussion

Based on the results shown above, Figure 6.18 schematically illustrates two different possibilities of scale development on Co-17Cr-xCr-2Si alloys. Upon initial exposure, the transient oxides such as CoO, Cr$_2$O$_3$, and SiO$_2$ rapidly nucleate on the alloy surface. Re oxidizes and evaporates simultaneously. Although the nucleation of chromia and silica are thermodynamically preferred, a significant amount of

CoO can still overgrow the transient nuclei since CoO grows much more rapidly than Cr$_2$O$_3$ and SiO$_2$. Thereafter, a continuous Cr$_2$O$_3$ layer can form if the Cr$_2$O$_3$ nucleus can grow laterally fast enough. Otherwise, prior formed Cr$_2$O$_3$ kernels are quickly engulfed by the fast-growing cobalt oxide and ensue to form the spinel phase.

Figure 6.18: Schematic illustration of the two characteristic types of scale development on alloy Co-17Re-*x*Cr-2Si.

The nucleation rate of Cr$_2$O$_3$ and the supply of Cr to the reaction front are the two important factors, which decide, whether or not the Cr$_2$O$_3$ grows laterally fast enough to form a continuous external layer. In addition to the synergetic effects of Cr and Si, where Si/SiO$_2$ is believed to act as nucleation sites for Cr$_2$O$_3$, the increase of the Cr content from 23% to 25% significantly furt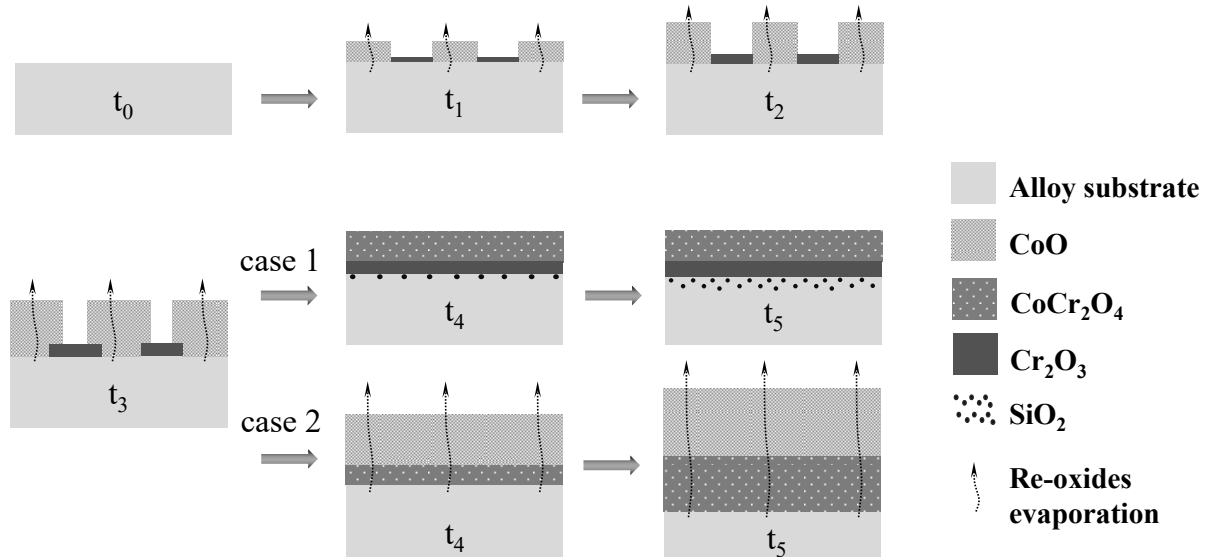her improves the oxidation behavior of alloy Co-17Re-*x*Cr-2Si by facilitating the formation of a dense and compact chromia layer. Although alloy Co-17Re-30Cr-2Si possesses similar excellent oxidation behavior, the volume fraction of the primary σ phase in alloy Co-17Re-25Cr-2Si is only half of that in alloy Co-17Re-30Cr-2Si.

The oxidation mechanism of the alloy Co-17Re-25Cr-2Si is strongly temperature-dependent in the temperature range 800-1100°C. The alloy exhibits relatively poor oxidation resistance at 800°C and 900°C mainly due to the slow and therefore insufficient supply of Cr from the substrate to the reaction front to form a continuous Cr$_2$O$_3$ layer. At 1000°C and 1100°C, accelerated Cr diffusional flux in the alloy facilitates the formation of a protective Cr$_2$O$_3$ scale. However, the growth of the Cr$_2$O$_3$ layer is rate controlled by the inwards transport of oxygen. The depletion of Cr caused by the external chromia scale growth leads to the dissolution of the σ phase and the formation of refined hcp grains in the alloy subsurface region. Apart from the subsurface microstructural changes, secondary σ phase precipitation

in the alloy substrate during oxidation occurs at all temperatures investigated, indicating the high-temperature stability of the σ phase.

Experimental observation suggests that oxygen penetration into σ particles is much faster than in the hcp alloy matrix grains. Hence, it is more difficult for an external chromia scale to develop on the σ phase despite the higher Cr content as compared to the hcp phase. Reducing the volume fraction and/or the particle size of the primary σ phase is believed to be beneficial for both the oxidation and mechanical properties of the alloy. It is also important to point out that even though a protective chromia scale could develop on alloy Co-17Re-25Cr-2Si, the relatively massive scale spallation during cooling (Figure 6.17) might still lead to severe material consumption under cyclic oxidation conditions. Thus, a closer consideration of the scale adhesion behavior must be taken into account to develop the alloy system further.

6.2 Effect of yttrium addition

To study the reactive element effect (REE) in Co-Re-base alloys aiming at an improvement of the scale adhesion, two Y-containing alloys, Co-17Re-25Cr-2Si-0.05Y and Co-17Re-25Cr-2Si-0.1Y, were fabricated and investigated.

Microstructural analyses on the alloys Co-17Re-25Cr-2Si, Co-17Re-25Cr-2Si-0.05Y, and Co-17Re-25Cr-2Si-0.1Y indicate that the addition of a small amount of Y up to 0.1% did not evidently change the alloy microstructure. However, in both Y-containing alloys, a small amount of fine and homogenously distributed Y-rich particles are observed in both the matrix and the σ phase with a preference of the matrix. No significant differences can be identified in the distribution of such Y-rich particles in alloy Co-17Re-25Cr-2Si-0.05Y and Co-17Re-25Cr-2Si-0.1Y. Examples are given in Figure 6.19, in which some of these Y-rich particles are indicated with arrows. EDS analyses imply that almost all these particles are in addition to yttrium also enriched in oxygen and sulfur. Moreover, in a few cases, aluminum is also detected (see Figure 6.20).
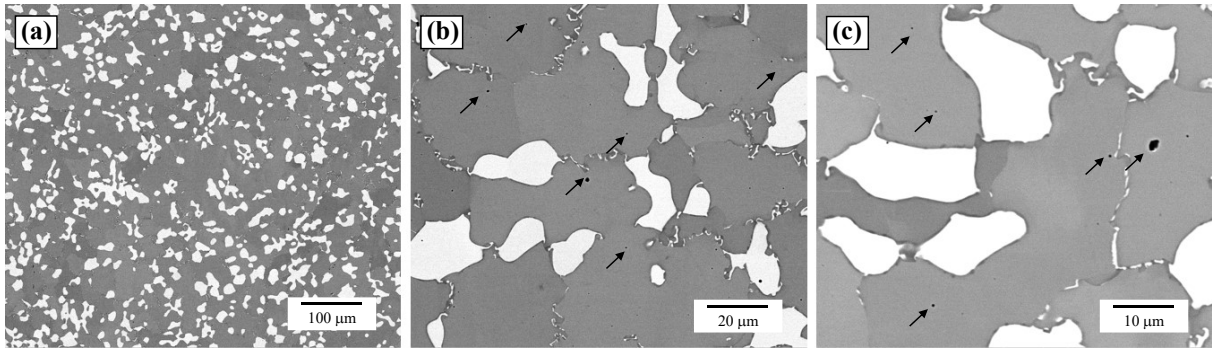
Figure 6.19: Microstrucal BSE-SEM images of alloy Co-17Re-25Cr-2Si-0.1Y in different magnifications: (a) ×200; (b) ×1000; (c) ×2000
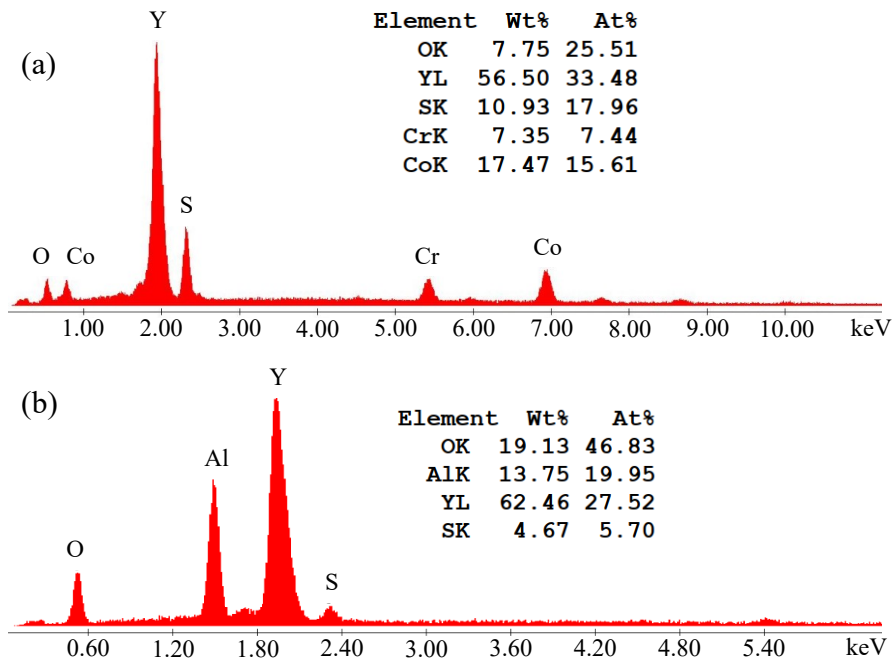
Figure 6.20: EDS analyses of the Y-rich particles: (a) major cases (the Cr and Co signals are from the matrix); (b) minor cases (usually relatively bigger particle size and thus no influence by the matrix)

6.2.1 Isothermal oxidation

Figure 6.21 shows the thermogravimetric data of the alloy Co-17Re-25Cr-2Si, Co-17Re-25Cr-2Si-0.05Y, and Co-17Re-25Cr-2Si-0.1Y during exposure to air at 900°C. The oxidation curves of both Y-containing alloys exhibit very similar behavior. All three curves show a continuous mass loss in the first few hours due to the formation of volatile Re oxides, implying the non-protective nature of the oxide

scale formed. Compared to Y-free alloy Co-17Re-25Cr-2Si, a significant reduction in the quantity of mass loss is observed for both Y-containing alloys. After the distinct mass loss period, the oxidation curves of the Y-containing alloys flatten, while that of the Y-free alloy Co-17Re-25Cr-2Si continues to exhibit a weight loss nature.
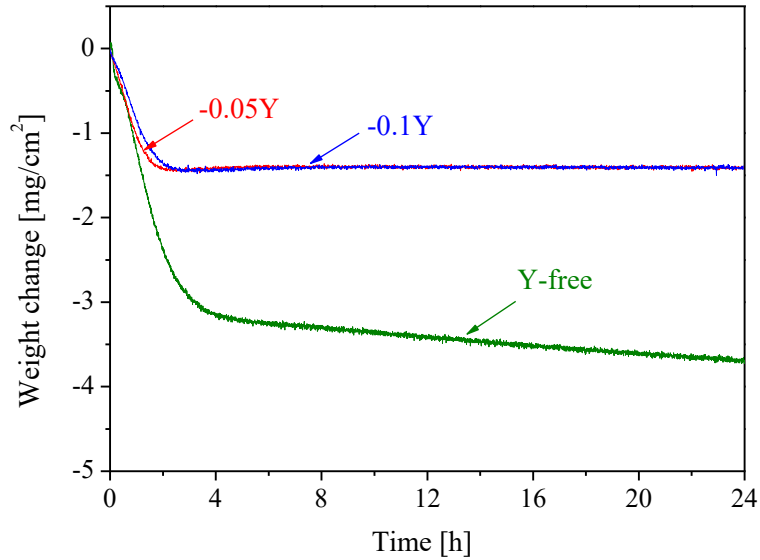
Figure 6.21: Thermogravimetrically measured weight change versus oxidation time for alloys Co-17Re-25Si-2Si-xY at 900°C

The cross-sectional micrographs of the alloys Co-17Re-25Cr-2Si-xY (x = 0, 0.05, and 0.1) after oxidation at 900°C for 72 h are shown in Figure 6.22. The oxide scales formed on both Y-containing alloys are very similar as is their oxidation kinetics, and their total layer thickness is only one-third of that formed on the Y-free alloy Co-17Re-25Cr-2Si, which yields a thickness of approximately 60 μm. XRD and EDS analyses indicate that the constitution of oxide scales formed on all three alloys resemble an outer Co oxides layer, an inner CoCr$_2$O$_4$-type spinel layer, and a semi-continuous Cr$_2$O$_3$ layer at the scale/alloy interface. Comparing the EDS line-scans through the oxide scale formed on alloy Co-17Re-25Cr-2Si-0.1Y (Figure 6.23) and the one on alloy Co-17Re-25Cr-2Si (Figure 6.7b), it is apparent that the Cr content in the spinel layer on the Y-containing alloy increases with increasing penetration depth, indicating a strong tendency to form a complete Cr$_2$O$_3$ layer.
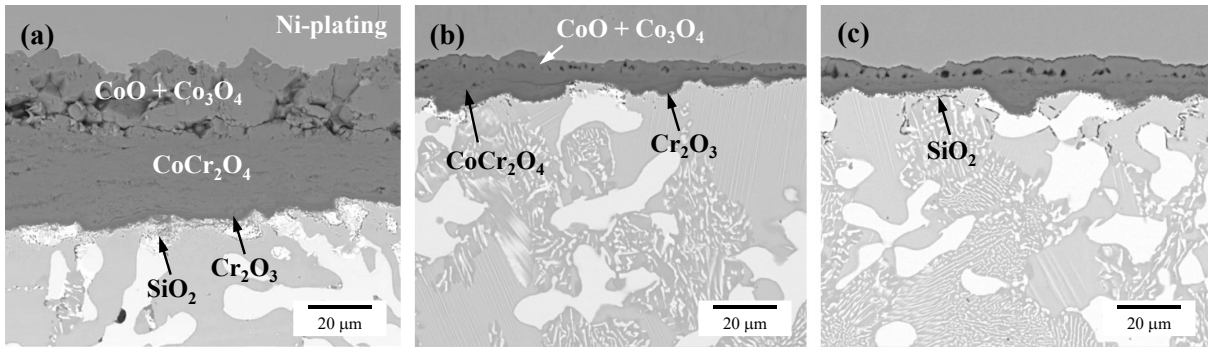
Figure 6.22: Cross-sectional BSE-SEM images of alloys after exposure to air at 900°C for 72 h. (a) Co-17Re-25Cr-2Si; (b) Co-17Re-25Cr-2Si-0.05Y; (c) Co-17Re-25Cr-2Si-0.1Y
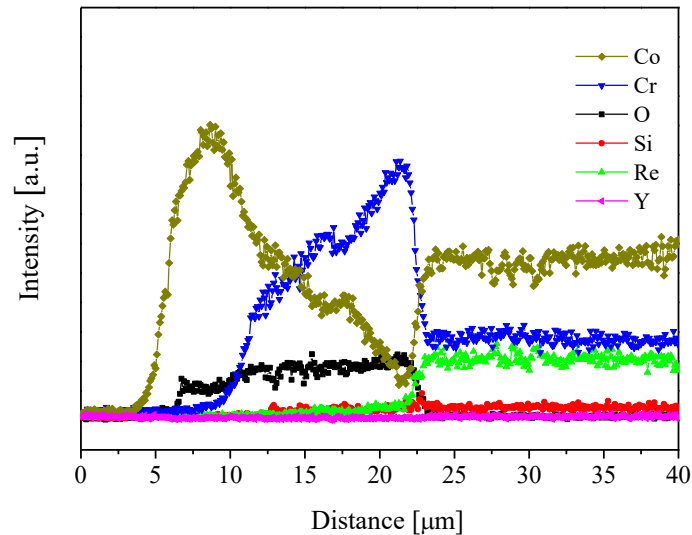
Figure 6.23: Cross-sectional chemical analysis using EDS line scan through the oxide scale formed on alloy Co-17Re-25Cr-2Si-0.1Y after oxidation at 900°C for 72 h

Figure 6.24 shows the thermogravimetric data of the alloys Co-17Re-25Cr-2Si and Co-17Re-25Cr-2Si-0.1Y during exposure to air at 1000°C. Both curves exhibit a parabolic weight gain, whereas the weight gain rate of alloy Co-17Re-25Cr-2Si-0.1Y is comparatively lower than that of the Y-free alloy. Nevertheless, it is important to remind that the kinetic behavior of alloy Co-17Re-25Cr-2Si depends sensitively on the sample condition at 1000°C, any minor differences in microstructure (σ phase distribution) or variations in roughness at the specimen edges may lead to different kinetics results.

Surface examination of Co-17Re-25Cr-2Si and Co-17Re-25Cr-2Si-0.1Y specimens after exposure at 1000°C for 24 h does not show a significant difference in oxide morphology. However, the scale formed on Y-containing alloy seems to possess a better spallation resistance. The corresponding cross-sectional micrographs are shown in Figure 6.25. In agreement with the gravimetric results, a continuous and

protective Cr$_2$O$_3$ layer can be found on both alloys. Although the Cr$_2$O$_3$ layer formed on the Y-containing alloy Co-17Re-25Cr-2Si-0.1Y (2.53 ± 1.00 μm) is statistically thinner than that formed on the Y-free alloy (3.48 ± 0.27 μm), it is important to point out that the chromia layer formed on the Y-free alloy is uniform whereas that formed on the alloy Co-17Re-25Cr-2Si-0.1Y is irregular. At some areas on alloy Co-17Re-25Cr-2Si-0.1Y, which are mainly located at the hcp grain boundaries, the scale is very thin compared to the rest. The internal oxidation depth in the Y-containing alloy (16.96 ± 4.27 μm) is found to be twice that in the Y-free alloy (8.12 ± 2.01 μm). Besides, the internal SiO$_2$ particles in the Y-containing alloy are observed to be more preferentially precipitated at the hcp grain boundaries or alloy/scale interface instead of within the hcp grains.

Figure 6.24: Thermogravimetrically measured weight change versus oxidation time for alloys Co-17Re-25Si-2Si-xY at 1000°C
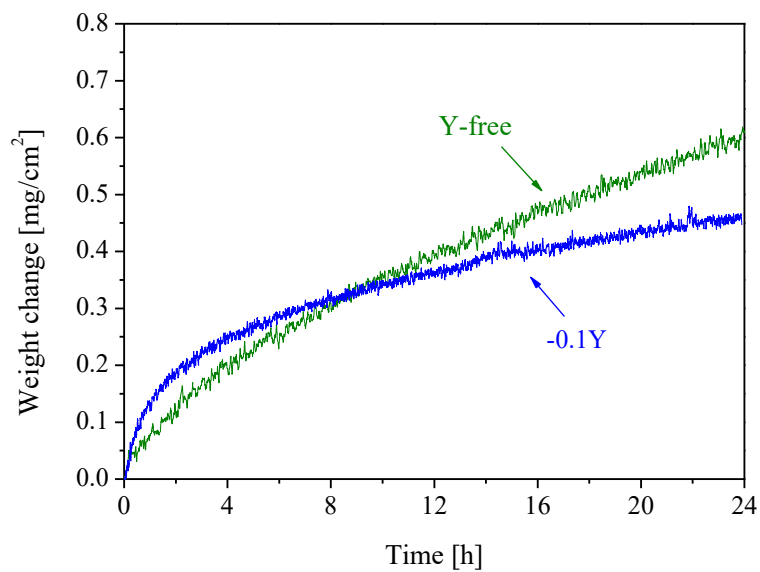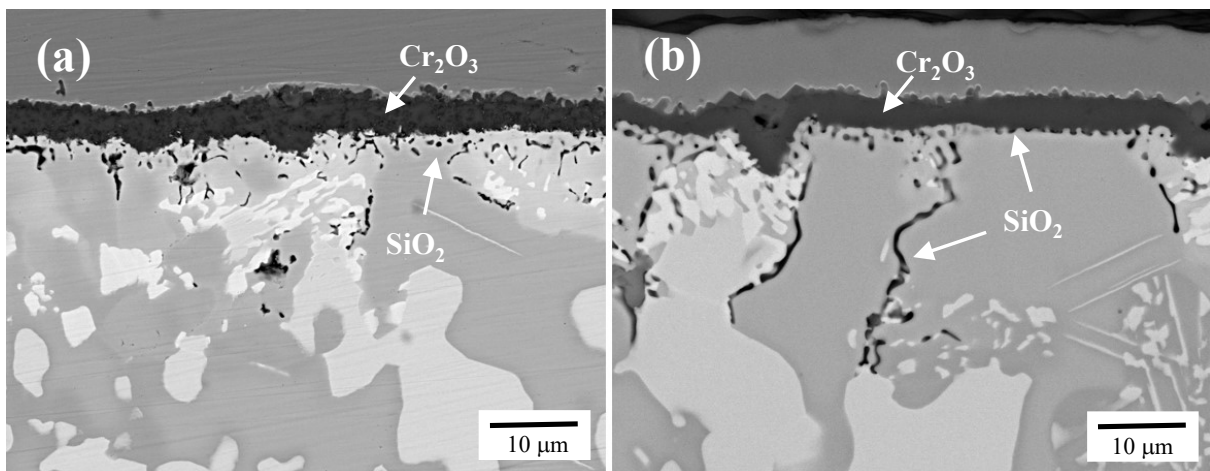

Figure 6.25: Cross-sectional BSE-SEM images of alloys (a) Co-17Re-25Cr-2Si and (b) Co-17Re-25Cr-2Si-0.1Y after exposure to air at 1000°C for 24 h

6.2.2 Cyclic oxidation

To study the effect of Y addition on the scale adhesion property under thermocyclic conditions, cyclic oxidation tests were conducted on the Y-free alloy Co-17Re-25Cr-2Si and the Y-containing alloy Co-17Re-25Cr-2Si-0.1Y. The cyclic thermogravimetric measurements were carried out by driving the specimen into a pre-heated furnace and hold for 2 h followed by lifting out and cooling it at room temperature for 20 min. This temperature cycle was repeated 50 times. The results are shown in Figure 6.26. It is seen that the weight change curve of both alloys follows near-parabolic kinetics in the first part of the experiment. However, a significant continuous weight loss kinetics is observed for the Y-free alloy after about 80 h while the near-parabolic weight gain behavior of alloy Co-17Re-25Cr-2Si-0.1Y continues.
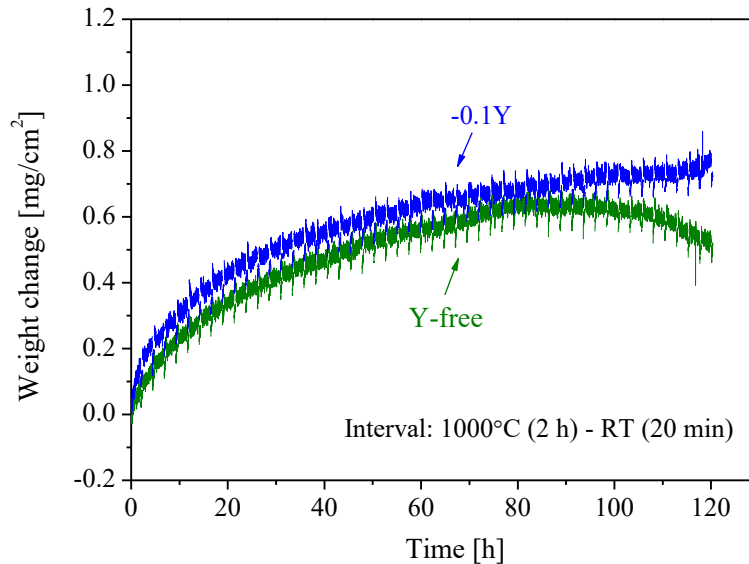
Figure 6.26: Cyclic oxidation kinetics of Y-free alloy Co-17Re-25Cr-2Si and alloy Co-17Re-25Cr-2Si-0.1Y

Microstructural analyses of the specimen surface after the cyclic tests show a markedly different morphology between the Y-free and the Y-containing alloys, as shown in Figure 6.27. While the scale formed on the Y-containing alloy is found to be homogenous and shows no spallation, many CoO islands with different sizes are found on the Y-free alloy, and the spallation of the scale is evident.

Looking at the thermogravimetric data shown in Figure 6.26 and comparing the cross-sectional micrographs of both alloys under isothermal (Figure 6.25) and thermocyclic (Figure 6.28) conditions, a significant improvement of Y addition in scale adhesion can clearly be stated. At the early stage of the cyclic oxidation tests, a protective Cr$_2$O$_3$ layer is formed on both tested specimens. However, the thermally grown Cr$_2$O$_3$ layer on the Y-free alloy is repeatedly spalled during the cooling process but rebuilt immediately in the following heated exposure period. Once the Cr concentration in the subsurface

is depleted under the critical value for external Cr$_2$O$_3$ to form, the formation of a non-protective CoO/spinel scale occurs and consequently results in a massive weight loss through the evaporation of rhenium oxides. The rapid growth of CoO, which is governed by the outwards diffusion of cobalt cations to the oxide/air interface, leads to the formation of the protrusion islands on the surface.

On the contrary, the scale formed on the Y-containing alloy Co-17Re-25Cr-2Si-0.1Y shows high resistance against spallation during the entire cyclic test. The full scale is homogeneously composed of a chromia layer and is thinner than that formed on alloy Co-17Re-25Cr-2Si in the spallation-free regions. Furthermore, the scale on alloy Co-17Re-25Cr-2Si-0.1Y shows an atypical "buckling" pattern (Figure 6.27b). A similar morphology is observed on alloy Co-17Re-25Cr-2Si but only on the hcp phase at the very early reaction stage due to the compressive growth stress within the chromia scale. A closer look at the scale cross-section documents that the reason for those "buckling" morphology on alloy Co-17Re-25Cr-2Si-0.1Y is not caused by growth stress but instead results from a local scale thickness variation. Figure 6.29 clearly represents this phenomenon, where the chromia scale formed over the alloy grain boundaries is found to be far thinner than that formed over the alloy grains. The areas between the thicker scale segments are supposed to be beneficial for a reduction of the growth stress within the scale. A release through plastic deformation can avoid the spallation of the scale. Moreover, both in quantity and penetration depth, a greater extent of internal oxidation is found in alloy Co-17Re-25Cr-2Si-0.1Y compared to the Y-free alloy.
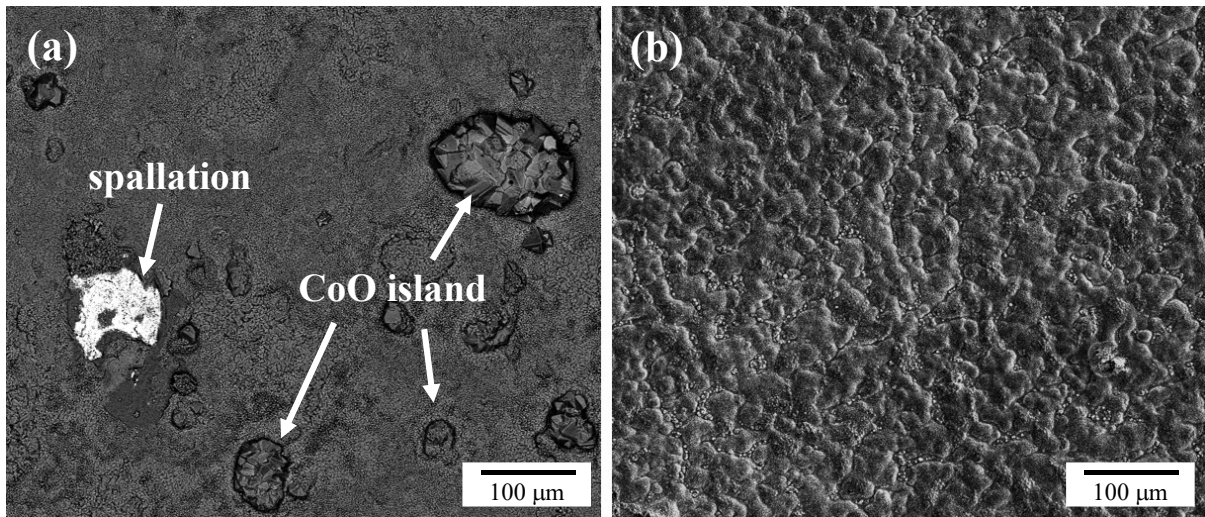
Figure 6.27: SEM surface micrographs of (a) Y-free alloy Co-17Re-25Cr-2Si (BSE contrast) and (b) alloy Co-17Re-25Cr-2Si-0.1Y (SE contrast)

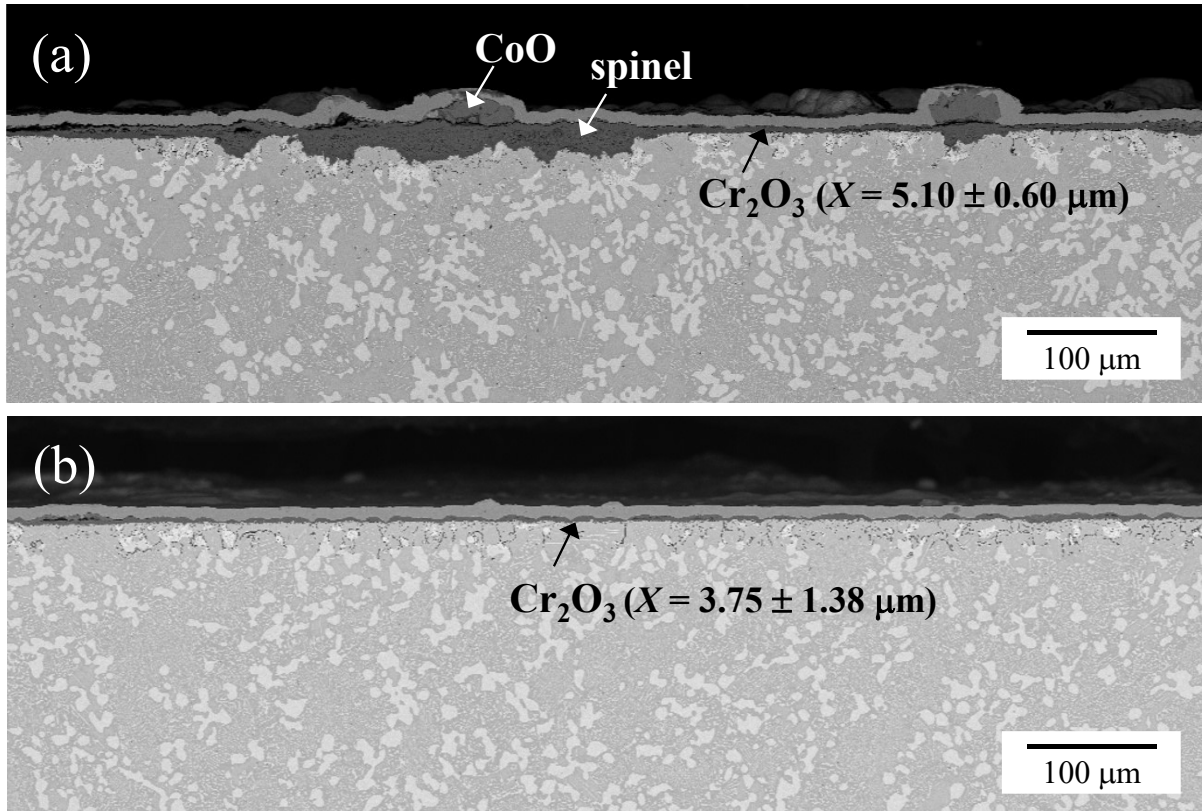Figure 6.28: Comparision of the cross-sectional micrographs of (a) Y-free alloy Co-17Re-25Cr-2Si and (b) alloy Co-17Re-25Cr-2Si-0.1Y after cyclic oxidation
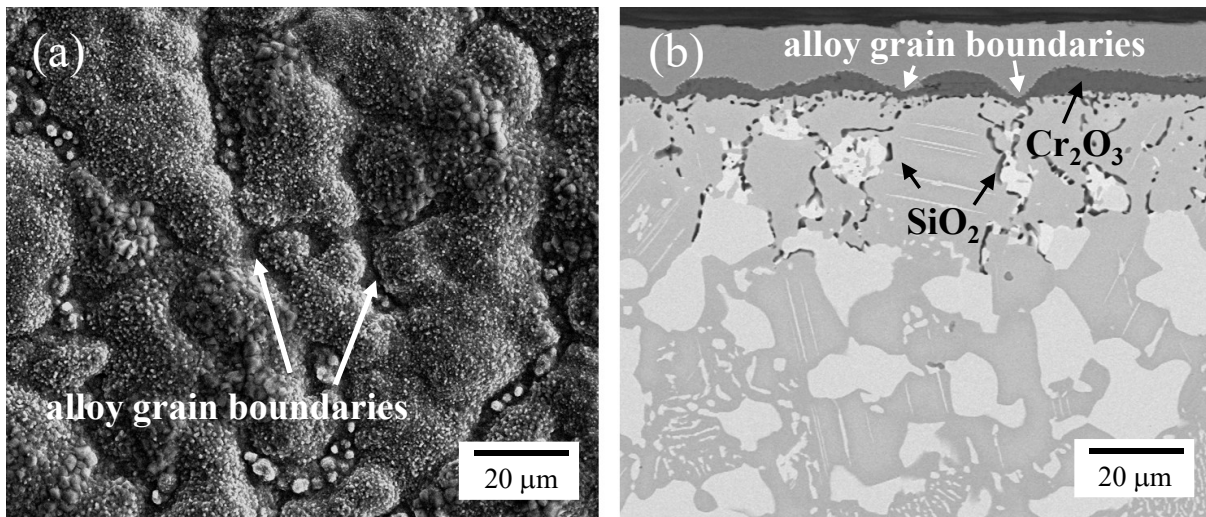

Figure 6.29: Surface (a) and cross-sectional (b) micrographs of cyclic oxidized Co-17Re-25Cr-2Si-0.1Y at 1000°C showing comparably thinner chromia layer above the alloy grain boundaries

6.2.3 Discussion

The experimental results clearly show that the minor addition of Y to the model alloy Co-17Re-25Cr-2Si effectively improves the oxidation resistance by facilitating the Cr$_2$O$_3$ scale formation and enhancing the scale adhesion, especially under thermocyclic conditions. The Y concentration difference between 0.05% and 0.1%, at least in this study, has no significant impact on the oxidation behavior.

The beneficial effects of reactive elements (Y, Ce, Zr, etc.) on the oxidation behavior of Cr$_2$O$_3$ and Al$_2$O$_3$ scale forming alloys have been known for many decades since the work of Griffiths and Pfeil [122]. Despite a large number of subsequent research in various alloy systems that have been published and have coherently shown that the REE manifests itself particularly in a reduced isothermal oxidation rate and an improvement of scale adhesion under thermocyclic conditions, a general agreement in the exact mechanism is not yet achieved though several hypotheses have been proposed. The results of these studies and the corresponding hypotheses have been extensively reviewed by Hou et al. [123] and could be summarized as follows:

- **Promoting selective oxidation**. Any element can be considered "reactive" if it is more oxygen active than the scale-forming elements, e.g., Cr or Al. Reactive elements with much higher oxygen affinity than that of Cr or Al act as oxygen "getters" in the alloy and thereby promote the external Cr$_2$O$_3$ or Al$_2$O$_3$ scale to form, resulting in a reduction of the critical concentration of Cr or Al in the alloy necessary to develop external protective scales or in a reduction of the formation time of these scales for alloys that already have sufficient amounts of Cr or Al.

- **Reducing growth rate and changing growth direction**. Many two-stage oxidation studies using oxygen isotopes have indicated that the reduction in Cr$_2$O$_3$ or Al$_2$O$_3$ growth rate in the presence of reactive elements is due to the unilaterally and significantly inhibited outward transport of cation through the oxide scale without affecting the inward transport of oxygen. This effect naturally changes the growth direction of the Cr$_2$O$_3$ scale, since the growth of Cr$_2$O$_3$ is normally governed by the cation outward diffusion. However, the overall growth direction of the Al$_2$O$_3$ scale is not changed because the inward oxygen diffusion essentially predominates its growth. Using high-resolution analytical TEM, reactive elements have been observed to be segregated at Cr$_2$O$_3$ or Al$_2$O$_3$ scale grain boundaries by many studies (e.g., Figure 6.30). Despite the different opinions on the driving force for the segregation of RE, it is a general understanding that the RE at grain boundaries blocks the outward diffusion of Cr or Al through the grain boundaries.

- **Improving scale adhesion**. At present, the most accepted mechanism by which RE affects scale adhesion is related to the reduction of sulfur segregation at the scale/alloy interface. This hypothesis is that the oxide/alloy interfacial bonding is intrinsically strong but could be significantly weakened by the segregation of indigenous S in the alloy to the interface during

oxidation. The role of RE, which possesses a strong sulfide forming ability, is to bind S impurity in the alloy and thereby to prevent S from the segregation at the scale/alloy interface, resulting in a significant improvement in scale adhesion. Apart from this RE-S interaction hypothesis, it has also been argued that the change in growth mechanism also inhibits the interfacial void formation and thus improves scale adhesion.
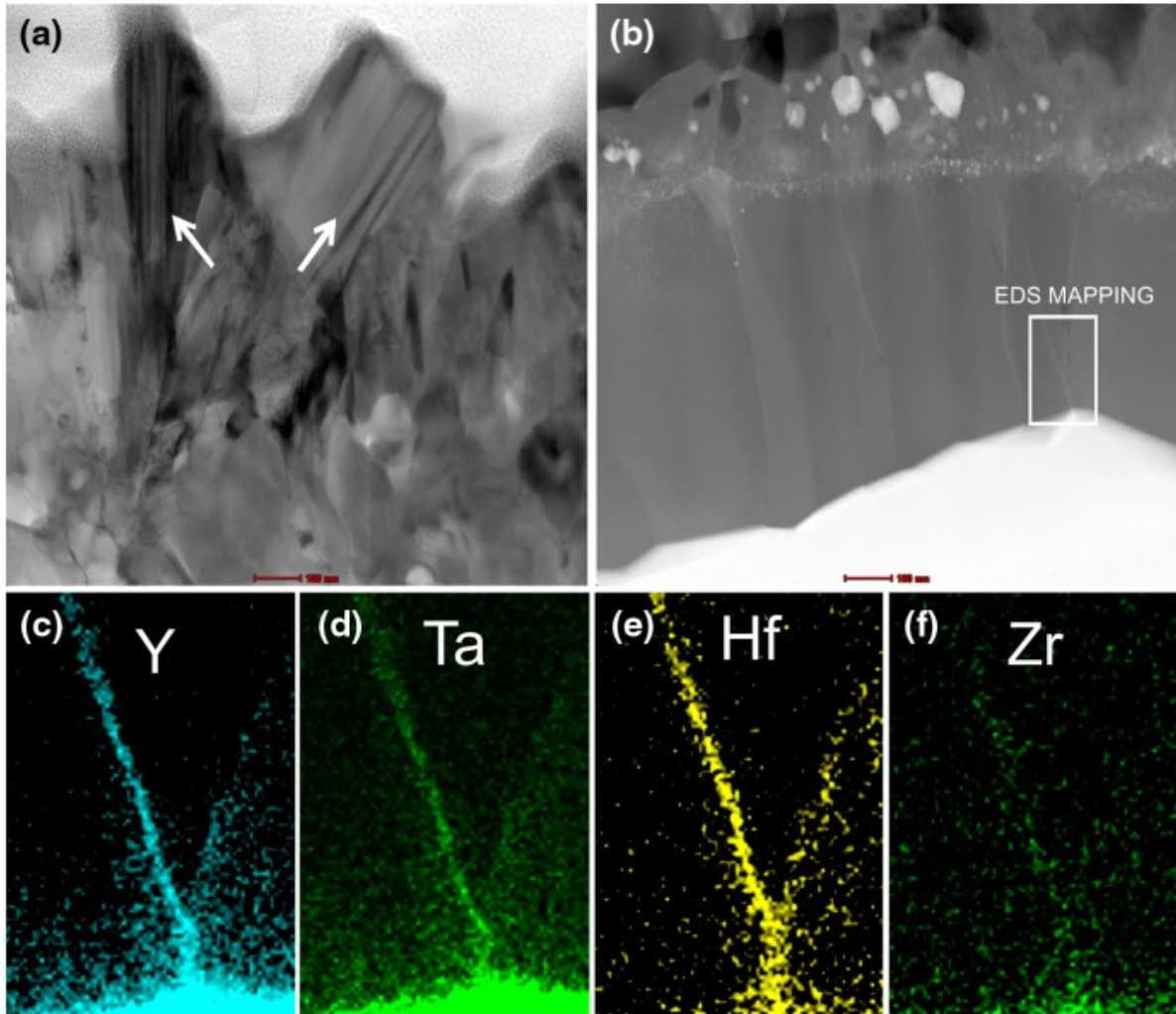
Figure 6.30: Microstructure of the oxide scale formed on a Ni-base superalloy during isothermal oxidation at 1100°C for 100 h: STEM-BF (a) image of Al_2O_3 grains in the outer zone of the scale and (b) inner columnar Al_2O_3 grains along with elemental mapping of Y (c), Ta (d), Hf (e) and Zr (f) [124]

Micrographic analysis revealed that the grain morphology of the oxide scale formed on alloy Co-17Re-25Cr-2Si-0.1Y (Figure 6.31) at 1000°C is similar to that formed on the Y-free alloy Co-17Re-25Cr-2Si (Figure 6.16) under the same conditions, where relatively smaller chromia grains are observed at the scale/alloy interface, indicating that the inward anion diffusion predominates the Cr_2O_3 scale growth on

both alloys. Besides, no Y could be detected within the chromia scale or at the scale/alloy interface by the techniques employed in this work.
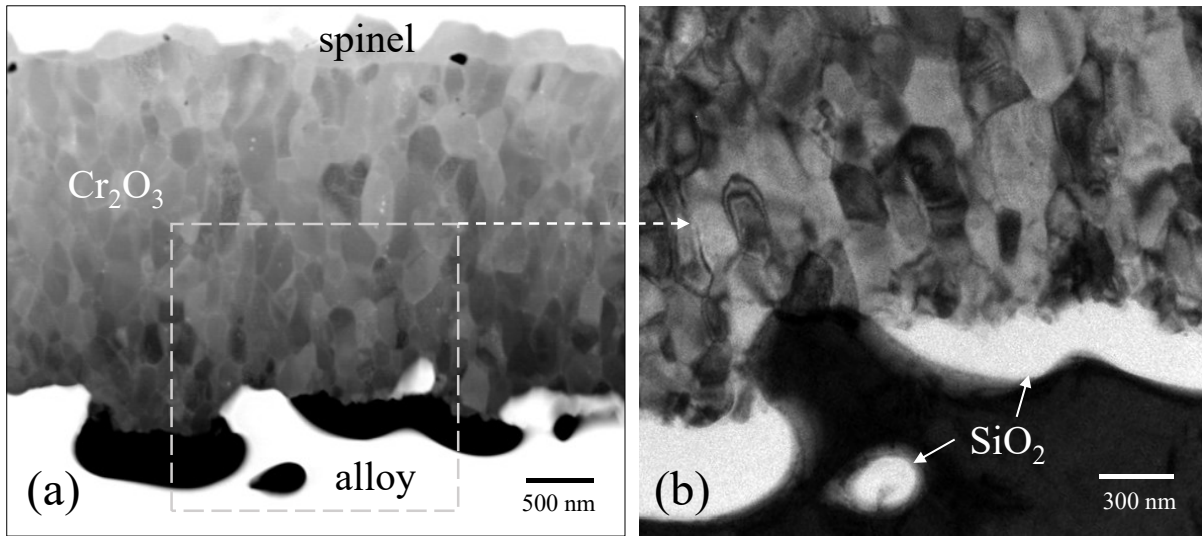
Figure 6.31: Micrographs of scale formed on alloy Co-17Re-25Cr-2Si-0.1Y after oxidation at 1000°C for 24 h: (a) high contrast BSE-SEM image; (b) TEM image

Looking at the EDX analyses of the Y-rich particles in Figure 6.20, it appears that the addition of Y to alloy Co-17Re-25Cr-2Si has bonded S from the alloy by forming Y-S-(O)-compound. The presence of oxygen in these particles is probably due to yttrium oxide formation during the melting process. Even though the alloy fabrication processes were carried out under vacuum or argon-protected conditions, the ambient oxygen partial pressure, which was about 10^{-6} bar, was still high enough for Y to be oxidized. To a certain extent, the indigenous Al as an impurity in the alloy has been involved in forming a stable yttrium-aluminum-oxide. Figure 6.32 shows the comparison of the optical images of Y-free and Y-containing alloys after solution heat treatment. It is apparent that relatively severe oxidation occurred on the Y-containing alloys during fabrication, forming a darker and thicker oxide surface compared to the Y-free alloy. Since the alloys with 0.05% Y and 0.1% Y investigated in this study show a very similar oxidation behavior, it is necessary to question whether or not the Y added in these two alloys were in fact massively removed from the alloy through oxidation during the manufacturing process.

For an ingot or bar of alloy Co-17Re-25Cr-2Si-0.1Y with a weight of 100 g, the total amount of Y within the alloy is about 0.1136 g, i.e., 1.28×10^{-3} mol (using the molar masse of Y of 88.91 g/mol). Assuming that Y in the alloy is completely exhausted through the formation of Y_2O_3, which can be expressed as

$$4Y + 3O_2 = 2Y_2O_3 \tag{6.1}$$

the necessary amount of oxygen, n_{O_2}, can be calculated through Equation (6.2).

$$n_{O_2} = \frac{3}{4} \, n_Y = \frac{3}{4} \times 1.28 \times 10^{-3} \, mol = 9.6 \times 10^{-4} \, mol \qquad (6.2)$$

where n_Y is the amount of Y in mole in the alloy.
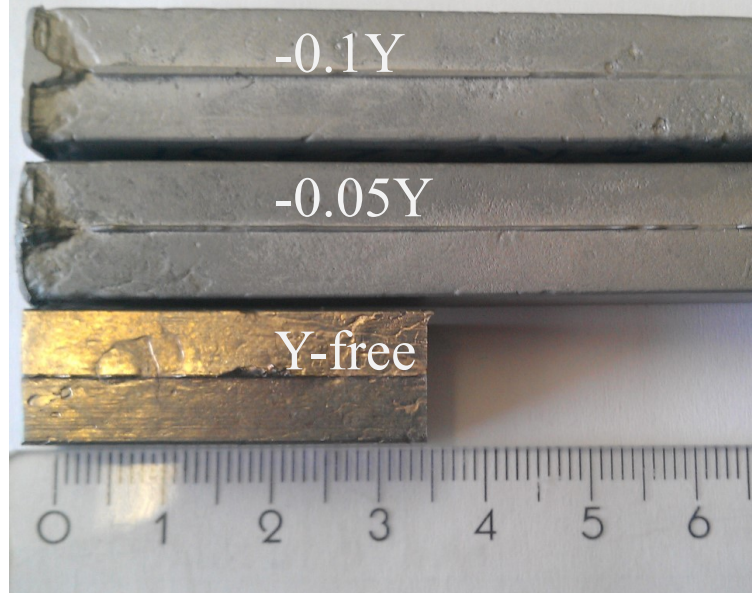
Figure 6.32: Optical images of Co-17Re-25Cr-2Si-xY alloys as received after solution heat treatment

By a further assumption that either evacuation or argon-purging limits the oxygen partial pressure in the arc furnace chamber to about 10^{-6} bar at room temperature, the theoretical volume of such ambient atmosphere required to oxidize the Y in the alloy completely can be calculated using the ideal gas law:

$$V = \frac{n_{O_2} RT}{p_{O_2}} = \frac{9.6 \times 10^{-4} \, mol \, \times 0.08314 \frac{l \cdot bar}{K \cdot mol} \times 298.15 \, K}{10^{-6} \, bar} = 23.8 \, m^3 \qquad (6.3)$$

Similarly, the value for alloy Co-17Re-25Cr-2Si-0.05Y is calculated to be 11.9 m^3. This is apparently far bigger than the actual volume of the applied arc furnace chamber. Considering that all elements in both Y-containing alloys could thermodynamically be oxidized under the same oxygen partial pressure and some Y additionally reacts with the S impurity, the amount of Y depleted through a reaction with the remaining oxygen in the chamber could be considerably neglected. Also, it can be inferred that most of the Y alloyed should be additionally present as solid solutes within the alloy apart from the Y-S-O-rich particles, although the techniques used could not directly detect it. Nevertheless, due to the extremely high oxygen affinity of Y (much higher than Ti, which is generally used in the laboratory arc-melting process to absorb the rest of oxygen in the chamber) and its general minor addition requirement, a reversing of the calculation introduced above should be taken into account in the further development of an optimized RE concentration. Based on the assumptions above, if the total Y in an alloy can just be

exhausted by the rest of the oxygen in the furnace chamber, the following relationship can be established according to the conservation of oxygen:

$$\frac{3}{4} \cdot \frac{m_{alloy} w_Y^*}{M_Y} = \frac{p_{O_2} V_{ch}}{RT} \tag{6.4}$$

or in another form

$$w_Y^* = \frac{4 p_{O_2} V_{ch} M_Y}{3RT m_{alloy}} \tag{6.5}$$

where w_Y^* is the critical yttrium weight concentration additionally required to compensate for reaction with the rest of oxygen in the furnace, V_{ch} is the volume of the furnace chamber, M_Y is the molar masse of Y, and m_{alloy} is the weight of the alloy to be produced. For instance, under the same condition as discussed above but with a chamber volume of about 0.2 m^3, the w_Y^* for alloy Co-17Re-25Cr-2Si-0.1Y is calculated to be 9.5 ppm.

Regarding the effectiveness of RE concentration, more recent researches have suggested that only a few hundred ppm seem to be more favorable than the content proposed in earlier studies, which usually quote a few tenths of a weight percent to ensure the REE [125]. Even it has been reported by Klöwer [126] that the over-doping of RE could produce detrimental effects by decreasing the scale adhesion through enhanced internal oxidation. On the other hand, some other researchers have emphasized that the REE may have less than optimal performance if the critical concentration Y/S ratio is not exceeded [127]. In light of this, the laboratory fabrication process needs to be taken into account, especially if the optimization of Y concentration in the Co-Re-base alloy system comes down to the ppm range.

In this study, except for the Y-rich particles in the alloy, no Y could be detected by the used techniques within the oxide scale or at the scale/alloy interface. However, a significant improvement in the oxidation resistance of the alloy through Y addition has been clearly observed. To comprehensively and precisely understand the exact mechanism of these positive effects of Y addition in the Co-Re-Cr-base alloys, further examinations, in particular, using high-resolution analytical TEM, still need to be carefully conducted. This goes, however, beyond the scope of the current study.

Nevertheless, based on the results and discussions presented above, the effect of the Y addition to alloy Co-17Re-25Cr-2Si could be stated as follows:

- The addition of Y removes the S contamination from the alloy, which is supposed to be beneficial for the scale adhesion

- Y addition to the alloy favors the nucleation and growth of SiO$_2$, particularly at the alloy/scale interface and the alloy grain boundaries, which further enhances the Si-effect to facilitate the formation of protective chromia scale by selective oxidation.

- The chromia scale growth is governed by inward oxygen diffusion. The inwardly transported oxygen is thermodynamically more in favor of reacting with Y and Si instead of Cr, resulting in a slower growth rate of the Cr$_2$O$_3$ scale but a greater SiO$_2$ internal oxidation than the Y-free alloy.

- The growth of the Cr$_2$O$_3$ scale over the alloy grain boundaries is partially suppressed due to the competition of the formation of internal SiO$_2$ at the grain boundaries, which is benefited by the faster diffusion of oxygen and the lower nucleation energy there.

- The inhomogeneously developed Cr$_2$O$_3$ scale thickness over the alloy provides a special interspace for scale relaxation, which is supposed to improve scale adherence significantly.

Since this part of the work has been carried out in parallel with the preliminary investigation of the Al$_2$O$_3$ scale formation on the Co-Re-Cr-Al alloys, the REE on the alumina-forming Co-Re-base alloys has not yet been studied. Based on the result of beneficial REE on the chromia-forming Co-Re-base alloys in this work and many other alumina-forming alloys in the literature [128], it would be worthful to consider the Y addition to Co-Re-Cr-Al alloy aiming to facilitate the formation of complete and adherent Al$_2$O$_3$ scale at elevated temperatures.

6.3 Effect of nickel addition

As mentioned in Chapter 2, the Ni addition to the reference alloy Co-17Re-23Cr significantly refines the particle size of the σ phase, enhancing the intrinsic ductility of the alloy without weakening its strength and being beneficial for high-temperature creep resistance. Consequently, it is of great interest to investigate the effect of Ni addition on the oxidation behavior of the Co-Re-Cr-base alloys.

6.3.1 Alloy Co-17Re-23Cr-15Ni-(AT)

Figure 6.33 shows the micrographs of two Ni-containing alloys in comparison with the reference alloy Co-17Re-23Cr. The two Ni-containing alloys, namely the Co-17Re-23Cr-15Ni and Co-17Re-23Cr-15Ni-AT, are in fact the same materials with 15% Ni addition. The principal difference is their heat treatment condition and, thereby, their microstructure. Unlike most of the alloys investigated in this study, including Co-17Re-23Cr and Co-17Re-23Cr-15Ni, the alloy Co-17Re-23Cr-15Ni-AT was additionally annealed at 1050°C for 4 h after the typical solution heat treatment, which is described in Table 3.1.

Compared to the reference alloy Co-17Re-23Cr, the primary σ phase can be merely observed on alloy Co-17Re-23Cr-15Ni after the solution heat treatment. Subsequent annealing heat treatment allows the precipitation of many fine secondary σ particles in the matrix of alloy Co-17Re-23Cr-15Ni-AT (see

Figure 6.33c). The chemical compositions of the alloys obtained by EDS measurement are presented in Table 6.3. The Ni content in the secondary σ particles is about half of that in the matrix in alloy Co-17Re-23Cr-15Ni-AT.
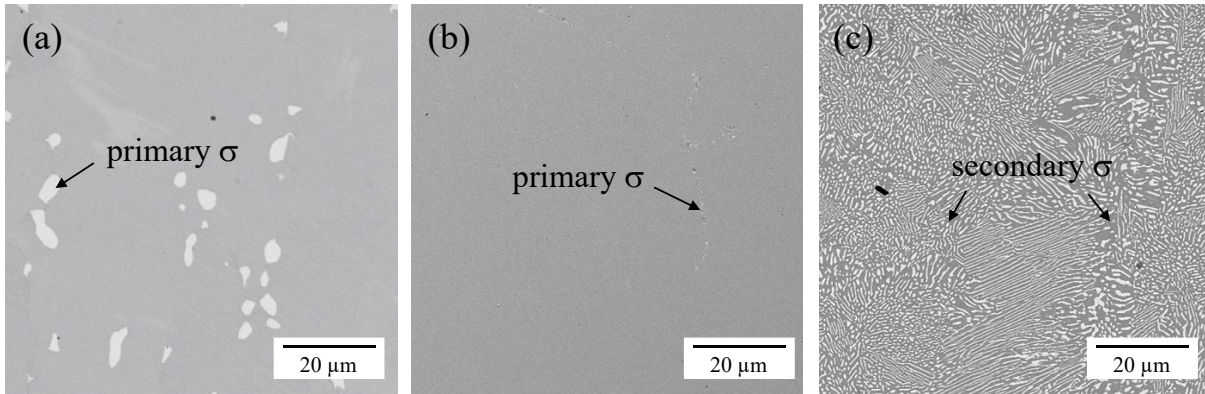
Figure 6.33: BSE-SEM micrograhs of alloy (a) Co-17Re-23Cr; (b) Co-17Re-23Cr-15Ni; (c) Co-17Re-23Cr-15Ni-AT

Table 6.3: Alloy heat treatment conditions and phase compositions measured by EDS

Alloy	matrix composition [at.%]				σ phase composition [at.%]			
	Co	Re	Cr	Ni	Co	Re	Cr	Ni
Co-17Re-23Cr	58.2	19.2	22.6	-	33.4	38.3	28.3	-
Co-17Re-23Cr-15Ni	43.4	18.2	22.6	15.8	-	-	-	-
Co-17Re-23Cr-15Ni-AT*	48.1	12.6	21.0	18.3	29.3	33.5	28.2	9.0

*AT for additional annealing heat treatment (1050°C/4h) after the general solution heat treatment

Further microstructural examination using EBSD indicates the presence of an additional fcc phase in the Ni-containing alloys. As the example shown in Figure 6.34 demonstrates, apart from the very few primary σ particles at the grain boundaries, the matrix of alloy Co-17Re-23Cr-15Ni is a mixture of hcp single-phase grains and grains with hcp/fcc lamellar structure.
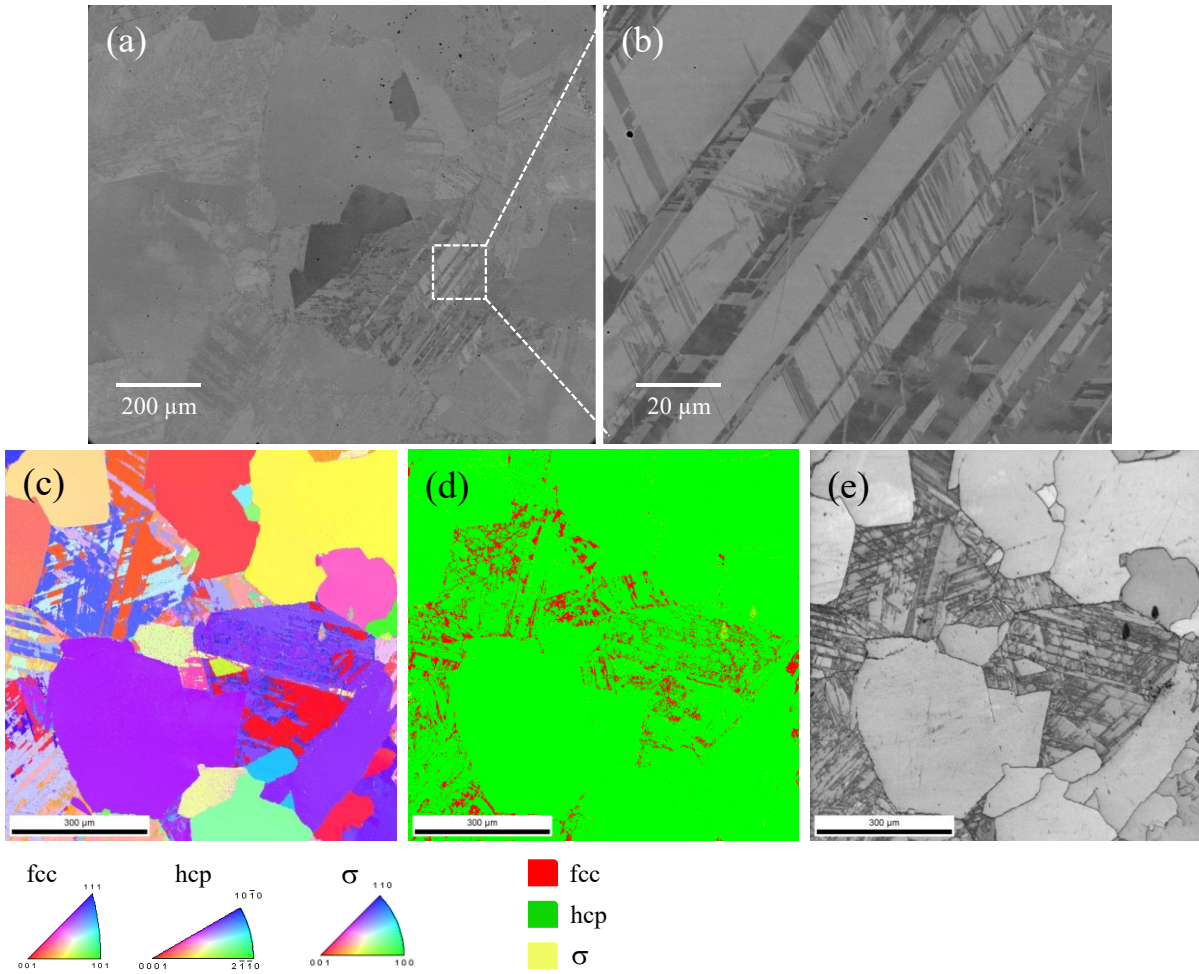
Figure 6.34: BSE-SEM images (a,b) and EBSD-SEM analysis of Co-17Re-23Cr-15Ni showing the presence of fcc phase: (c) orientation map; (d) phase map; (e) image quality map

6.3.2 Oxidation behavior

Figure 6.35 shows the TGA results of the alloys during exposure to laboratory air at 1000°C. Comparing with the reference alloy Co-17Re-23Cr, it seems that an improvement in oxidation performance is demonstrated by both Ni-containing alloys, leading to very small weight changes. Figure 6.35b shows the comparison of the TGA curves of both Ni-containing alloys in a high resolution of the weight change. A kind of parabolic kinetics is observed on alloy Co-17Re-23Cr-15Ni-AT along with the test, whereas the alloy Co-17Re-23Cr-15Ni exhibits a transient mass loss before steady-state weight-gain kinetics is achieved.
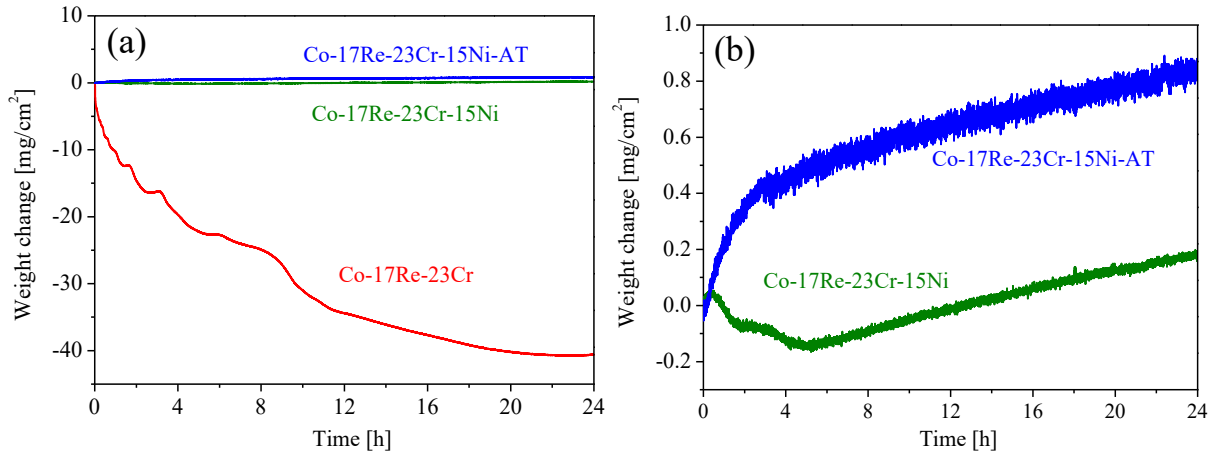
Figure 6.35: (a) TGA measurements of the investigated alloys during exposure to air at 1000°C; (b) high-resolution representation for the Ni-containing alloys

Figure 6.36 compares the surface and cross-sectional micrographs of the alloys after oxidation at 1000°C for 72 h. It is seen that the outermost oxide formed on both Ni-containing alloys is much thinner than that formed on the reference alloy Co-17Re-23Cr, and the total thickness of the oxide scales formed on both Ni-containing alloys is about fifty times smaller than that formed on Co-17Re-23Cr. Similar fine secondary σ particles are found in both Ni-containing alloys after the exposure.

EDS and XRD analyses were conducted to identify the nature of the oxides formed. A detailed analytical discussion on the results obtained was published elsewhere [129]. Surprisingly, the scale formed on alloy Co-17Re-23Cr-15Ni-AT consists of almost pure dense chromia, only an extremely thin spinel layer ca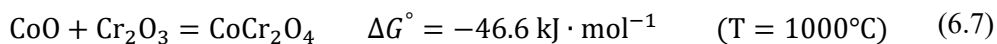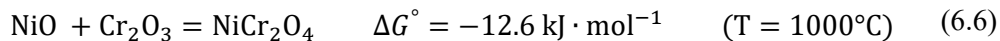n be detected over the chromia layer. In contrast to the typical non-protective $CoO/CoCr_2O_4$ scale formed on the reference alloy, a compact Cr_2O_3 layer is found on alloy Co-17Re-23Cr-15Ni underneath an outermost Co/Ni monoxide solid solution layer as well as a Ni-doped $CoCr_2O_4$ spinel intermediate layer. The Ni content detected by EDS analysis in the (Co,Ni)O layer and the intermediate $CoCr_2O_4$ spinel layer is 19.3% and 2.3% (in atomic percent), respectively. The preferential formation of $CoCr_2O_4$ instead of $NiCr_2O_4$ or $Co(Ni)Cr_2O_4$ is not only due to the higher amount of cobalt in the bulk material but also a consequence of the order of thermodynamic stabilities since the Gibbs free energy reduction by the $CoCr_2O_4$ formation reaction is almost four times higher than that of $NiCr_2O_4$ formation:

$$NiO + Cr_2O_3 = NiCr_2O_4 \qquad \Delta G° = -12.6 \, kJ \cdot mol^{-1} \qquad (T = 1000°C) \qquad (6.6)$$

$$CoO + Cr_2O_3 = CoCr_2O_4 \qquad \Delta G° = -46.6 \, kJ \cdot mol^{-1} \qquad (T = 1000°C) \qquad (6.7)$$

Examination of discontinuously oxidized specimens reveals that the scaling process on alloy Co-17Re-23Cr-15Ni is dominated by (Co,Ni)O and spinel layers growth for a few hours before a continuous Cr_2O_3 layer forms, while the Cr_2O_3 layer on alloy Co-17Re-23Cr-15Ni-AT forms almost immediately after exposure. This is, for example, shown in Figure 6.37.

Despite the oxygen uptake through the formation of the oxide scale, the TGA curve of alloy Co-17Re-23Cr-15Ni shows weight loss during the first few hours, indicating the evaporation of Re oxides due to the lack of a protective chromia layer. However, it is important to point out that a semi-continuous Cr$_2$O$_3$ scale is established at the spinel/alloy interface after exposure for 1 h (Figure 6.37b). Further, the EDS line scan run from the oxide scale to the alloy shows a sharp increase of the Cr intensity at the spinel/alloy interface, indicating a strong tendency to form a dense Cr$_2$O$_3$ layer.

On alloy Co-17Re-23Cr-15Ni-AT, a compact and continuous Cr$_2$O$_3$ layer forms quickly during exposure (Figure 6.37c). The transient oxidation period is relatively short and, hence, negligible in a first approach. However, a very thin CoCr$_2$O$_4$ layer over the chromia layer retains. The later oxidation of the alloy is then governed by the growth of the protective chromia layer, resulting in a parabolic weight-gain kinetics and the dissolution of the Cr-rich σ phase in the vicinity of the alloy surface.

It is noteworthy that no significant difference in oxidation behavior can be observed between the hcp grains and the grains with a mixture of hcp and fcc phases in the Ni-containing alloys.
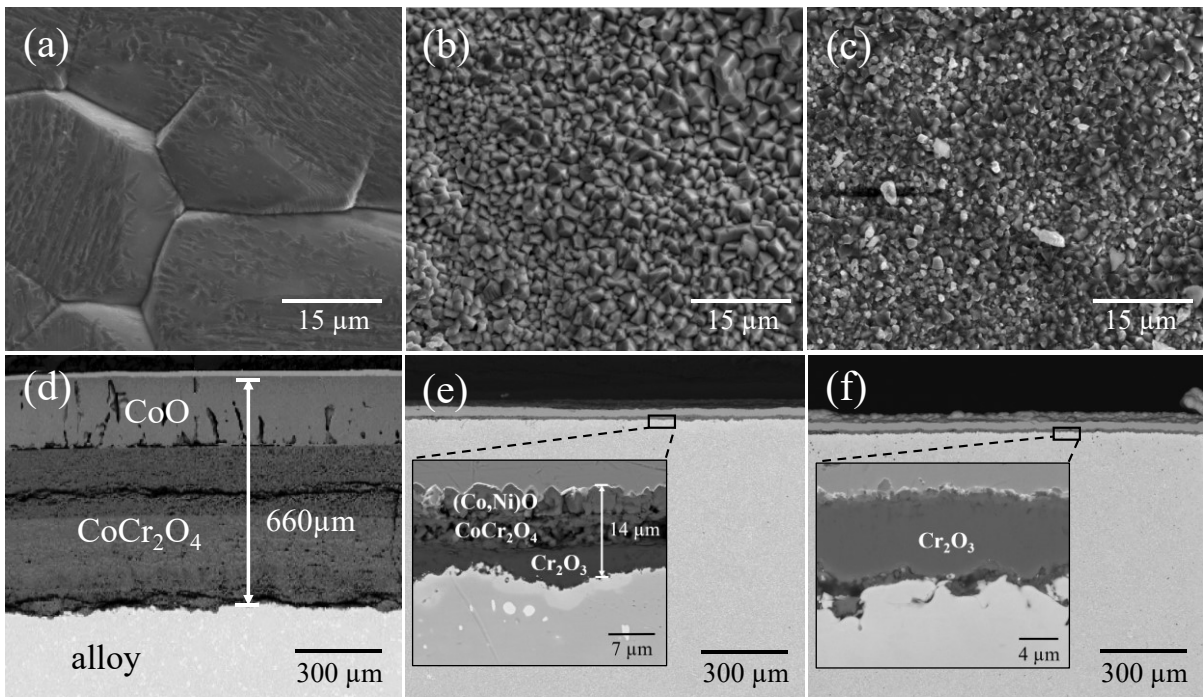
Figure 6.36: SEM surface (top, SE mode) and cross-sectional (bottom, BSE mode) images of (a, d) Co-17Re-23Cr, (b, e) Co-17Re-23Cr-15Ni, and (c, f) Co-17Re-23Cr-15Ni-AT after exposure to air at 1000°C for 72 h

101
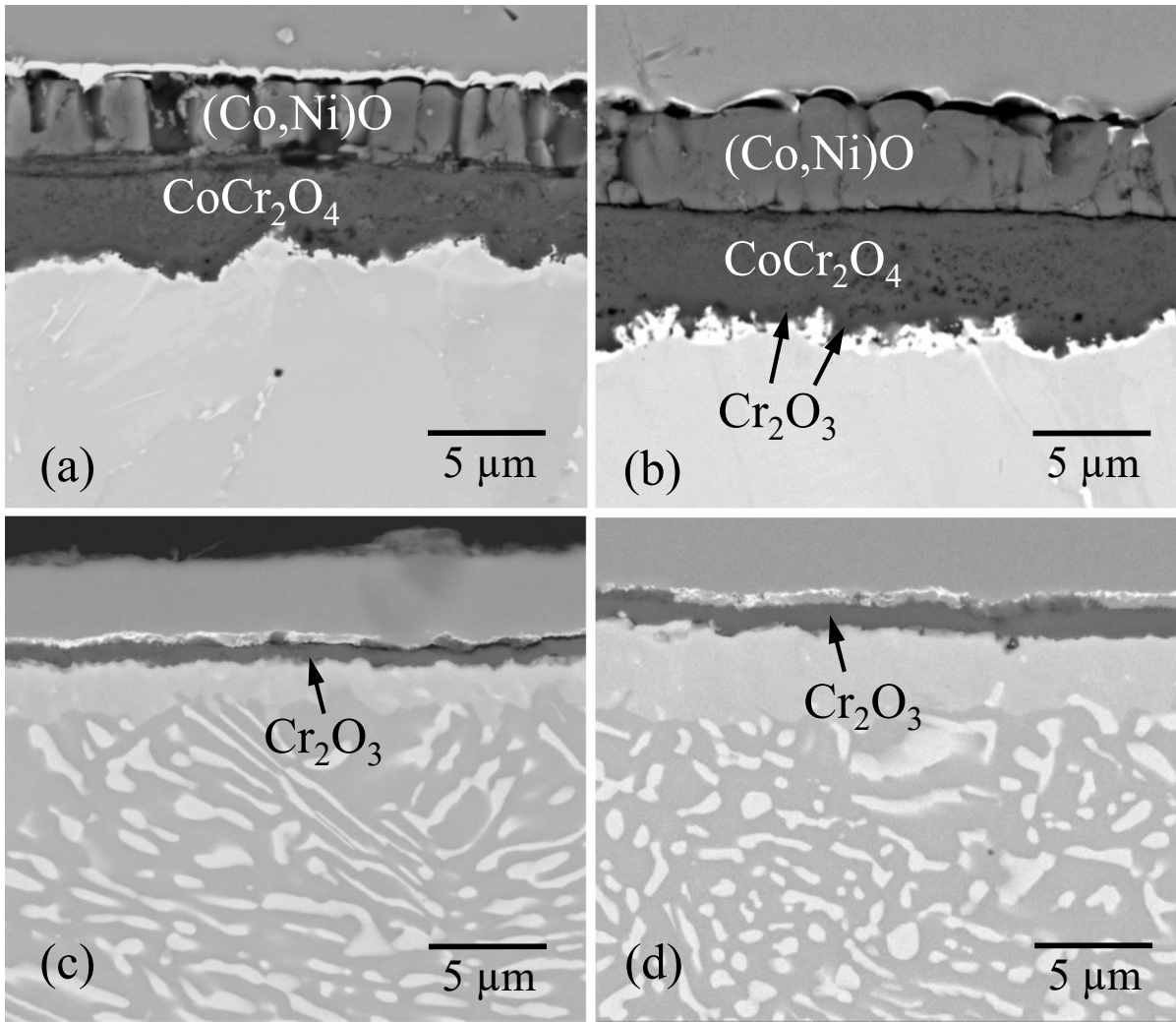
Figure 6.37: Cross-sectional BSE-SEM images of specimens oxidized at 1000°C: Co-17Re-23Cr-15Ni for 10 min (a) and 1 h (b); Co-17Re-23Cr-15Ni-AT for 10 min (c) and 1 h (d)

Combining the TGA results and the results of the microstructural investigations presented above, it is apparent that the Ni addition to alloy Co-17Re-23Cr significantly improves the oxidation resistance of the alloys by promoting the formation of a Cr$_2$O$_3$ layer. From the viewpoint of thermodynamics, the calculated Gibbs free energy change of the NiO formation reaction is even lower in absolute values than that of CoO formation at 1000°C, while the Gibbs free energy reduction of Cr$_2$O$_3$ formation is about twice as high as that of CoO formation, as shown in the following equations:

$$2Ni + O_2 = 2NiO \qquad \Delta G^\circ = -252.3 \text{ kJ} \cdot \text{mol}^{-1} O_2 \qquad (T = 1000°C) \qquad (6.8)$$

$$2Co + O_2 = 2CoO \qquad \Delta G^\circ = -290.1 \text{ kJ} \cdot \text{mol}^{-1} O_2 \qquad (T = 1000°C) \qquad (6.9)$$

$$\frac{4}{3}Cr + O_2 = \frac{2}{3}Cr_2O_3 \qquad \Delta G^\circ = -532.5 \text{ kJ} \cdot \text{mol}^{-1} O_2 \qquad (T = 1000°C) \qquad (6.10)$$
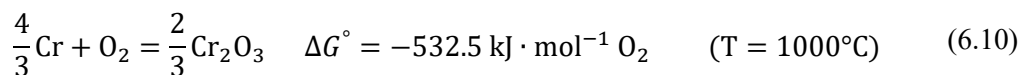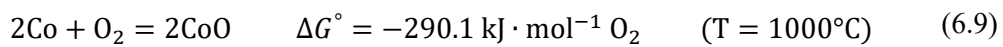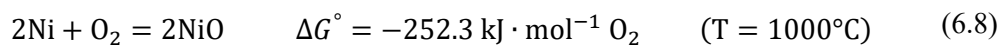
Consequently, Ni cannot promote the nucleation of Cr$_2$O$_3$ through the so-called "reactive element effect", where the reactive element involved usually possesses a higher oxygen affinity than the scale former [65]. Therefore, the significant improvement of the oxidation behavior of the Ni-containing alloy Co-17Re-23Cr-15Ni seems to be connected to the changes in the diffusion kinetics. Figure 6.38 shows the comparison of BSE images of alloy Co-17Re-23Cr and alloy Co-17Re-23Cr-15Ni with high contrast, indicating that the average grain size of the matrix in the alloy Co-17Re-23Cr-15Ni (~200 μm) is about fourfold of that in the reference alloy Co-17Re-23Cr (~50 μm). This is in principle disadvantageous for a high Cr flux towards oxidation front through short-circuit diffusion in the Ni-containing alloy Co-17Re-23Cr-15Ni.

However, Chattopadhyay and Wood [130] reported that the alloy interdiffusion coefficient in binary Co-xCr (x: 0-40 wt.%) alloys is between 3×10^{-16} and 6×10^{-16} m^2·s^{-1} at 1000°C, while that in binary Ni-xCr (x: 0-30 wt.%) alloys lies between 1×10^{-15} to 4×10^{-15} m^2·s^{-1}, which is about an order of magnitude higher, referring to faster diffusion of Cr in the Ni-Cr alloys than in the Co-Cr alloys. Also, the value of the critical concentration of Cr required for developing a protective external Cr$_2$O$_3$ scale on Ni-Cr-base alloys was commonly observed to be lower than that for the Co-Cr-base alloys [34]. All these pieces of evidence indicate that the Ni addition may accelerate the lattice diffusivity of Cr in the alloy Co-17Re-23Cr-15Ni.

In alloy Co-17Re-23Cr-15Ni-AT, the high density of phase boundaries between the fine σ particles and the matrix, which are considered as additional fast diffusion paths, facilitates the formation of a compact and continuous Cr$_2$O$_3$ layer further.
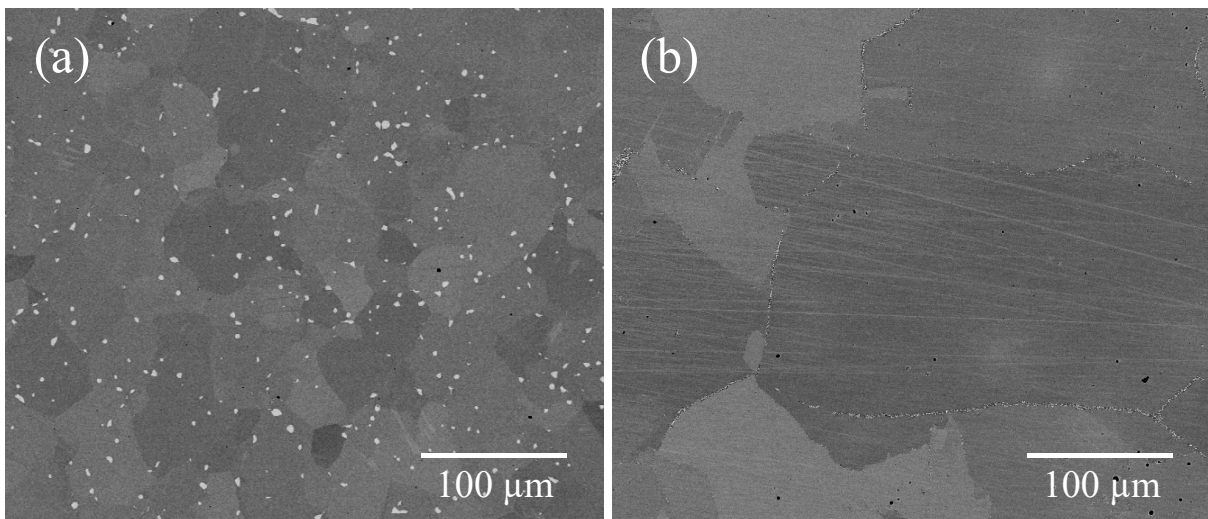

Figure 6.38: High contrast BSE-SEM images of alloy Co-17Re-23Cr (a) and Co-17Re-23Cr-15Ni (b)

6.3.3 Effect of shot-peening

Since the diffusivity of Cr plays such an essential role in the oxidation behavior of the Co-Re-Cr-base alloys, a reasonable question is, whether or not a pre-treatment such as shot-peening could further improve the alloy oxidation resistance by providing higher dislocation density in the alloy subsurface region, i.e., enhancing short-circuit diffusion of Cr, and thus, promoting the formation of a compact external Cr$_2$O$_3$ scale.

The preliminary shot-peening attempt on the Co-Re-Cr-Si alloys shows a detrimental effect on the mechanical properties though it is beneficial for oxidation resistance [131]. The fundamental limitation of using shot-peening on the Co-Re-Cr-Si alloys is mainly connected with the brittleness of their coarse primary σ phase. Figure 6.39 shows the cross-sectional micrograph of a shot-peened Co-17Re-23Cr-2Si specimen. Many shot-peening induced micro-cracks within the primary σ particles in the subsurface region are evident, which are arrested by the ductile matrix. The depth of such crack-affect zone is about 50 μm in good accordance with the micro-hardness profile in the matrix, which continuously decreases from about 800 HV at the shot-peened surface and reaches the value of the ground specimen at about 50 μm from the surface. The hardness increment in the subsurface region indicates the presence of shot-peening-induced dislocations.

Owing to the lack of coarse primary σ phase, alloy Co-17Re-23Cr-15Ni shows no micro-cracks after the shot-peening treatment under the same condition. The corresponding micro-hardness profile is depicted in Figure 6.40, indicating a similar hardness increment compared to alloy Co-17Re-23Cr-2Si but with a relatively deeper affected zone (~100 μm). This phenomenon is supposed to be related to the relatively larger matrix grain size in alloy Co-17Re-23Cr-15Ni.
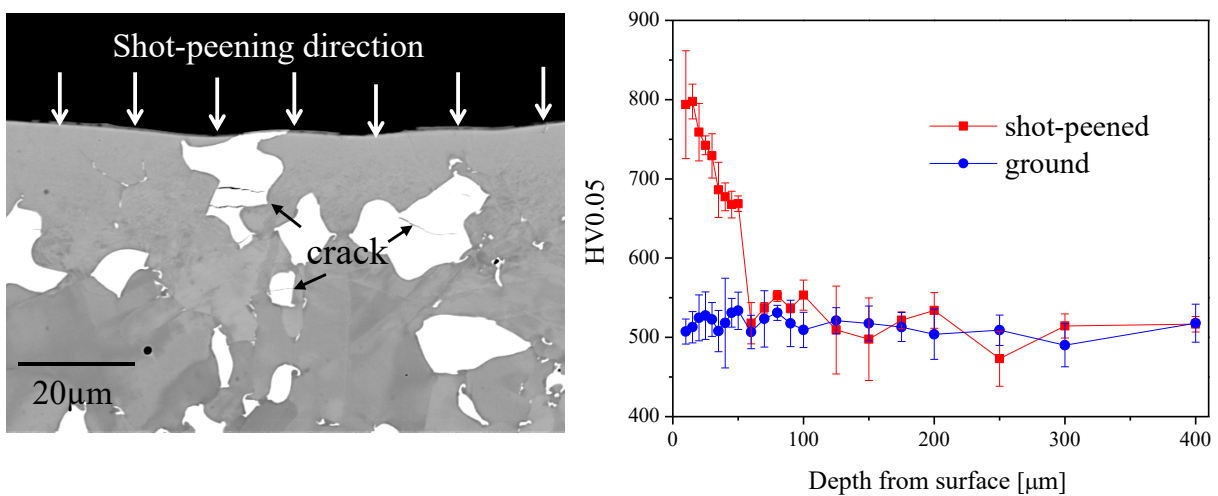

Figure 6.39: Cross-sectional BSE-SEM image of a shot-peened Co-17Re-23Cr-2Si sample (left); comparison of the micro-hardness profile of the matrix phase in Co-17Re-23Cr-2Si (right)
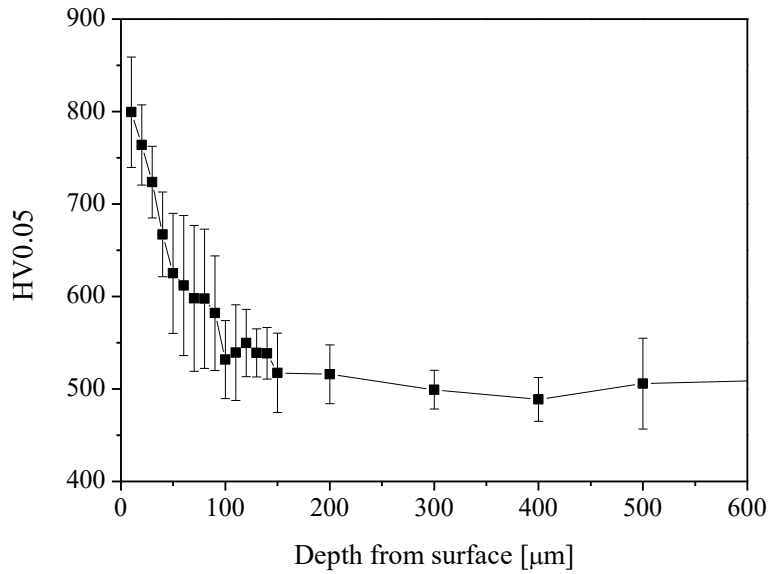
Figure 6.40: Micro-hardness profile of shot-peened alloy Co-17Re-23Cr-15Ni

Figure 6.41 shows the weight change curves of shot-peened and non-shot-peened (ground) Co-17Re-23Cr-15Ni specimens during the oxidation test at 1000°C. Unlike the ground specimen, which exhibits a weight loss behavior at the early reaction stage, weight-gain kinetics is observed for the shot-peened alloy directly after exposure.

Micrographs of the gound and the shot-peened Co-17Re-23Cr-15Ni specimen after oxidation at 1000°C for one hour are compared and shown in Figure 6.42. On the ground specimen, (Co,Ni)O/spinel double-layer scale forms all over the alloy surface. A slower growth rate of the inner spinel layer is observed at the alloy grain boundaries. Some fine secondary σ particles are precipitated in the substrate along the alloy grain boundaries (Figure 6.42b). Both phenomena are supposed to be connected with the relatively faster Cr diffusivity along the alloy grain boundaries. On the shot-peened specimen, a continuous and protective chromia layer forms quickly after the exposure, retaining only a few transient spinel grains over the scale. Further, fine secondary σ particles are homogenously and fully precipitated in the shot-peened affected zone, whereas the σ-precipitation can only be observed along the alloy grain boundaries in the substrate region that is not affected by shot-peening (Figure 6.42e). In comparing the oxidation products and the microstructural changes in the subsurface between the ground and shot-peened alloy Co-17Re-23Cr-15Ni, it becomes clear that the shot-peening induced dislocations in the subsurface significantly enhance the Cr diffusion in this region and thus promote the quick formation of protective chromia layer and the faster precipitation of the secondary σ phase.

Figure 6.41: TGA results of alloy Co-17Re-23Cr-15Ni in two different initial surface conditions after exposure to air at 1000°C

Figure 6.42: Surface (a,d) and cross-sectional (b,c,e,f) SEM images of ground (top) and shot-peened (bottom) alloy Co-17Re-23Cr-15Ni after exposure to air at 1000°C for 1 h

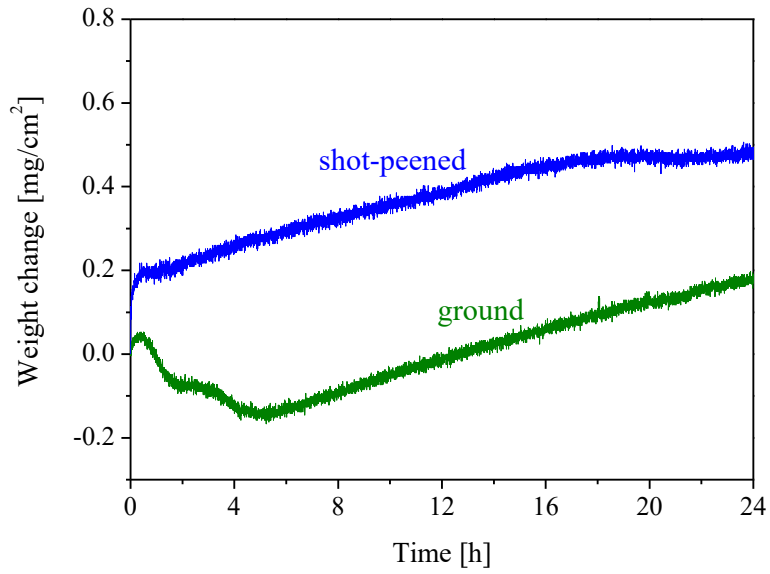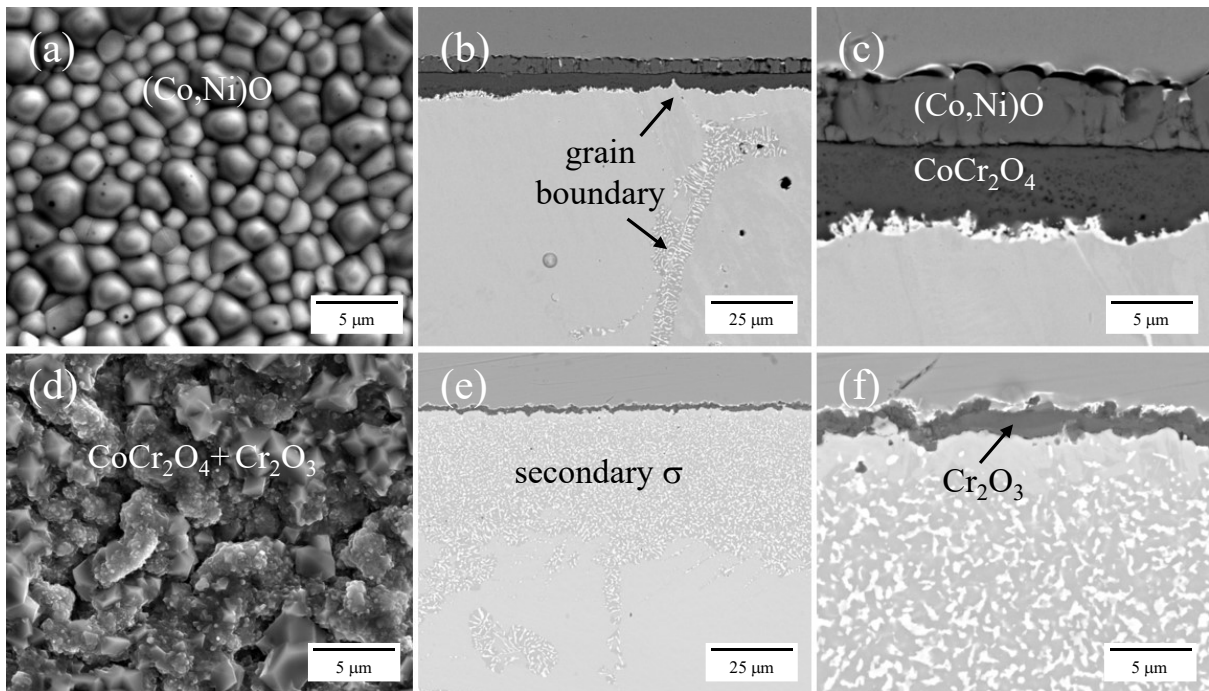## 6.3.4 Discussion

The results presented above clearly show that the addition of 15% Ni to the reference alloy Co-17Re-23Cr significantly improves the oxidation resistance by promoting the formation of a Cr$_2$O$_3$ scale. The results also imply that the lattice diffusivity of Cr might be enhanced by the Ni addition and consequently contributes to the significant improvement.

To assess the effect of Ni on the diffusivity of Cr in the Co-Re-Cr-Ni system, in a first approach, the ternary system Co-Cr-Ni is considered, and the interdiffusion coefficient of chromium, D_{CrCr}, is expressed following the treatment given in ref. [132] as a function of the tracer diffusion coefficients D_{CrCr}^*, D_{NiNi}^*, and D_{CoCo}^*, the thermodynamic factors g_{CrCr}, g_{NiNi}, and g_{NiCr}, and the mole fractions x_{Cr} and x_{Ni}. As shown in detail in ref. [129], the following equation results:

$$D_{CrCr} = (1 - x_{Cr})g_{CrCr}D_{CrCr}^* - x_{Ni}g_{NiCr}D_{NiNi}^* + (x_{Cr}g_{CrCr} + x_{Ni}g_{NiCr})D_{CoCo}^* \qquad (6.11)$$

The diffusivity of Cr in the Co-Cr-(Ni) system is dependent not only on the composition but also on the related thermodynamic factors. The values of the tracer diffusion coefficients D_{CrCr}^*, D_{NiNi}^*, D_{CoCo}^* at 1000°C were taken from ref. [133, 134] as 5.22×10^{-16} m^2/s, 3.07×10^{-16} m^2/s, and 2.82×10^{-16} m^2/s, respectively. It must be noticed that D_{NiNi}^* and D_{CoCo}^* were directly taken from experimental results on [63]Ni impurity diffusion in fcc Co and the tracer diffusion coefficient of ^{60}Co in fcc Co [133], respectively, whereas D_{CrCr}^* refers to experimental interdiffusion results in Co-Cr alloys with relatively low Cr concentration [134], since there is no published data for Cr impurity diffusion in fcc Co available to the best knowledge of the author. The values of g_{CrCr} and g_{NiCr} as a function of both x_{Cr} and x_{Ni} in a fcc Co-Cr-(Ni) solid solution at 1000°C were calculated with FactSage. The results obtained are shown in Figure 6.43. Finally, D_{CrCr} was calculated, and the results are plotted in Figure 6.44.
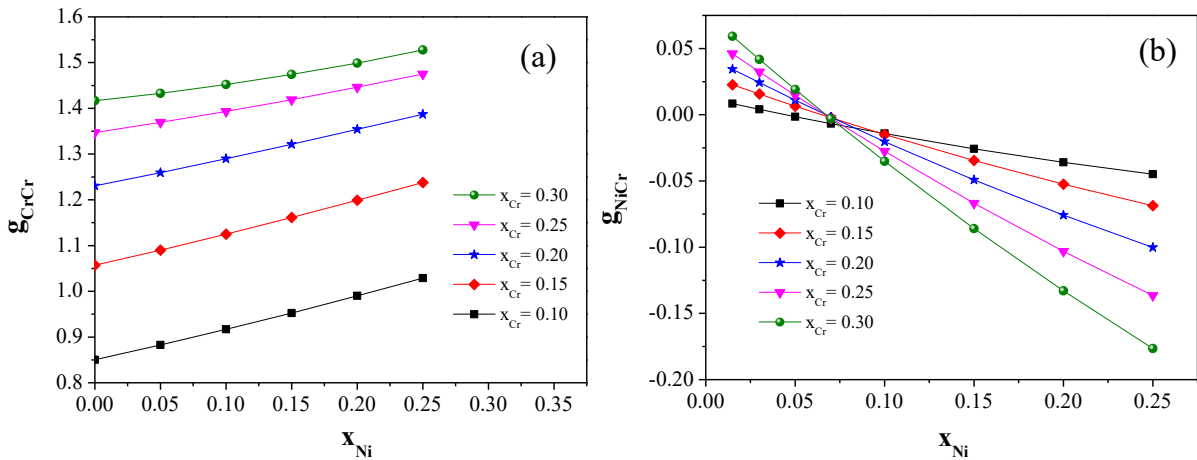
Figure 6.43: Thermodynamic factors as a function of composition in ternary Co-Cr-Ni fcc solid solution:
(a) g_{CrCr}; (b) g_{NiCr}
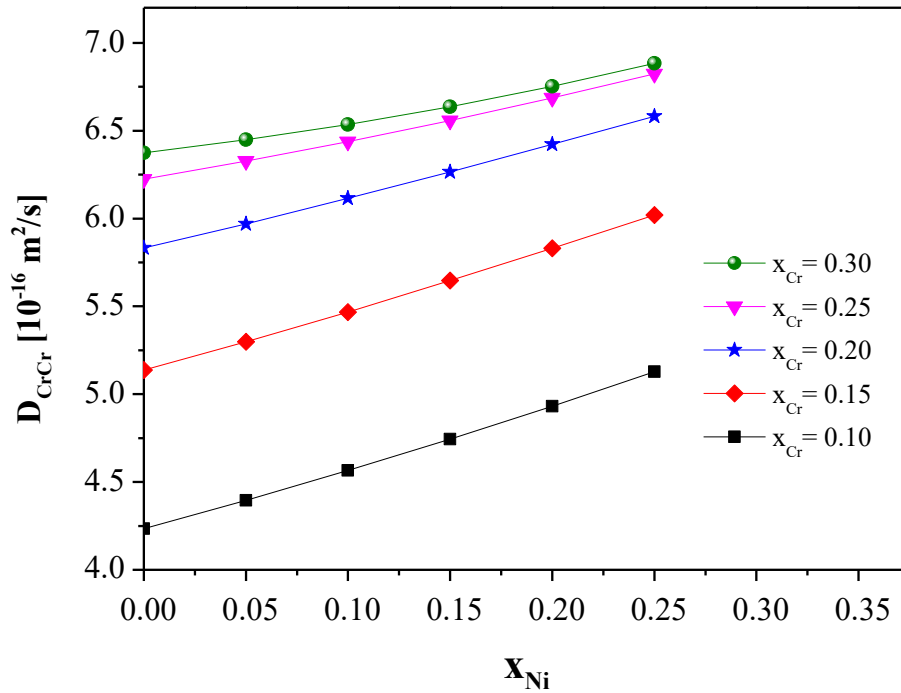
Figure 6.44: Concentration dependence of interdiffusion coefficient D$_{CrCr}$ in Co-Cr-Ni system at 1000°C

The calculated values shown in Figure 6.44 indicate that the interdiffusion coefficient D_{CrCr} increases slightly with increasing Ni content. This result is in good agreement with the experimental observation obtained by Minamino et al. [135], who demonstrated that D_{CrCr} shows a slight increase with increasing Ni concentration for the alloys Co-(15-30)Ni-15Cr at 1200°C.

However, in the calculation given above, the influence of Re is not considered. Therefore, additional studies taking Re into account are necessary to provide further clarification of this proposal. In a successional study based on this work, Esleben [136] intensively investigated the oxidation behavior of quaternary Co-17Re-xCr-yNi alloys. By means of specifically designed oxidation test carried out at very low oxygen partial pressure, it was possible to prove experimentally and quantitatively that a Ni addition accelerates the Cr diffusion in Co-Re-Cr-Ni alloys.

On the other hand, the Ni addition-induced formation of the outer (Co,Ni)O solid solution layer is supposed to be another essential contributor to the significant improvement. Wood et al. [115] reported that the parabolic rate constant of NiO growth on pure Ni (2.9×10^{-10} g^2·cm^{-4}·s^{-1}) in oxygen at 1000°C is about two orders of magnitude lower than that of CoO growth on pure Co (2.1×10^{-8} g^2·cm^{-4}·s^{-1}) under the same conditions. The significant difference of the oxidation rates is suggested to be related to the cation vacancy concentration of the oxides, where the cation vacancy concentration of NiO formed on Ni is much lower than that of CoO formed on Co (0.07% compared to 0.86%), leading to a slower outwards transport of the Ni cations to the oxidation front, i.e., the scale/gas interface [115]. Further, Stiglich et al. [137] studied the interdiffusion in (Co,Ni)O solid solution and reported that the isothermal

values of the interdiffusion coefficients in the CoO-NiO system increased exponentially with the CoO concentration.

As a solid solution of CoO and NiO, the growth rate of the outer (Co,Ni)O layer formed on the alloy Co-17Re-23Cr-15Ni is reasonably observed to be much lower than that of the CoO formed on the reference alloy Co-17Re-23Cr, as shown in Figure 6.37. By extension of Wagner's original analysis on the transition from internal to external oxidation, Gesmundo und Viani stated [53] that the critical concentration of the more reactive component in a binary alloy required to form the corresponding external layer is positively correlated to the growth rate of the outer oxide layer of the less reactive component. Therefore, it is very likely that the slower growth rate of (Co,Ni)O, for the same reason, reduces the critical concentration of Cr in the Ni-containing alloy compared to the reference alloy Co-17Re-23Cr.

Finally, both the additional annealing and short-peening treatment further promote chromia scale formation through short-circuit diffusion. In the first case, the improvement through the pre-treatment results from the increase of the phase boundary area between the matrix and the fine secondary σ particles, while in the second pre-treatment applied in this study the dislocation density increase in the subsurface favors the Cr$_2$O$_3$ scale formation.

7 Conclusions and perspectives

This work aimed to fundamentally investigate and improve the intrinsic high-temperature oxidation behavior of Co-Re-base alloys. The key concept is to develop a compact, adherent, and slow-growing external oxide scale on the alloy surface during exposure, which separates the alloy substrate from the oxidizing environment and, therefore, limits the further degradation of the substrate material. For this purpose, the formation of the most effective scales, i.e., SiO_2, Al_2O_3, and Cr_2O_3, on the Co-Re-base alloys were studied.

The SiO₂ scale formation

In a previous work, B. Gorr [26] had stated that the addition of Si from 1% to 3% to the reference alloy Co-17Re-23Cr significantly and incrementally improved the oxidation resistance of the alloy by promoting chromia scale formation. SiO_2 was generally found as internal oxidation particles at alloy subsurface and was observed to be more laterally connected as the Si content increases. Based on Gorr's contribution, alloy Co-17Re-23Cr-4Si containing 4% Si was additionally investigated in this study to verify the possibility of the formation of a continuous SiO_2 layer for high-temperature applications.

However, results show that instead of forming a continuous and protective SiO_2 layer, the increase of Si content up to 4% leads to severe spallation of the chromia scale formed. Moreover, Si addition also dramatically increases the volume fraction and size of the primary σ phase, which is detrimental to mechanical properties, leads to poor oxidation resistance, and cannot be reduced or refined by further annealing heat treatment. For instance, the volume fraction of the primary σ phase in alloy Co-17Re-23Cr-4Si is measured to be around 23%, whereas for the reference alloy Co-17Re-23Cr, only about 2% can be observed.

Thermodynamic considerations imply that the formation of an intrinsic SiO_2 layer on chromium-free Co-Re alloys through macro-alloying with Si is problematic with respect to high-temperature applications of such an alloy system. The main limiting factor is that the Si addition to Co-Re alloys strongly reduces their melting temperature. Moreover, the study on the model alloy Co-17Re-9Si-8B revealed that the formation of thermodynamically stable but fast-growing $CoSi_2O_4$ continually consumes the Si solved in the alloy or the SiO_2 particles formed in the alloy during exposure at intermediate temperature (around 1000°C), making the formation of a continuous SiO_2 layer even more difficult.

The Al₂O₃ scale formation

Alternatively, two Al-containing model alloys, Co-17Re-23Cr-5Al and Co-17Re-23Cr-10Al, were investigated in a wide temperature range from 800°C to 1300°C to elucidate the possibility of alumina

scale formation on the Co-Re alloy system. Results show that the addition of both 5% and 10% Al improves the oxidation resistance of the reference alloy Co-17Re-23Cr. However, in different ways.

The main contribution of 5% Al addition is that it "getters" the oxygen preferentially by internal oxidation and, consequently, facilitates the formation of a protective chromia scale at 1000°C and 1100°C. At lower temperatures, i.e., 800°C and 900°C, the temperature-dependent Cr and Al diffusivity in the alloy leads to an insufficient supply of Cr and Al to the reaction front, resulting in the formation of non-protective $CoO/Co(Cr,Al)_2O_4$ double-layer scale. At 1200°C and higher, neither Al_2O_3 nor Cr_2O_3 can be formed, rather severe oxidation occurs.

The addition of 10% Al to alloy Co-17Re-23Cr is almost, but not completely, sufficient to ensure the formation of a complete Al_2O_3 layer at 800-1100°C. At 1200°C and above, Al_2O_3 is only observed as internal oxidation precipitates, since a severe nitridation of Al takes place. Results also reveal that the Cr_2O_3 scale possesses a much weaker protectiveness against nitrogen penetration than the Al_2O_3 scale.

In terms of microstructure, the addition of Al to alloy Co-17Re-23Cr strongly promotes the formation of the σ phase. In alloy Co-17Re-23Cr-10Al, the Co-Al-rich bcc phase (B2) is additionally observed.

The Cr_2O_3 scale formation

In addition to the layer formation of SiO_2 and Al_2O_3, the formation of the Cr_2O_3 scale and its stability were studied in detail for intermediate temperature applications. The investigations were mainly focused on developing a fundamental understanding of the oxidation mechanisms relevant to Co-Re-Cr-base alloys, in order to provide a solid mechanistic basis for future optimization strategies.

As mentioned above, the Si content in the first generation of Co-Re-Cr-base alloys was limited to 2% to avoid the detrimental effects of high Si contents. Studies on alloys Co-17Re-(23/25/27/30)Cr-2Si indicate that an increase of the Cr content from 23% to 25% significantly improves the oxidation behavior of the alloy, changing the scale from a non-protective $CoO/CoCr_2O_4$ double-layer scale to a dense and continuous Cr_2O_3 scale at 1000°C and 1100°C. Although, alloy Co-17Re-30Cr-2Si possesses similar excellent oxidation behavior, the volume fraction of the primary σ phase in alloy Co-17Re-25Cr-2Si is only half of that in alloy Co-17Re-30Cr-2Si.

Nevertheless, the oxidation behavior of alloy Co-17Re-25Cr-2Si is strongly temperature-dependent. At 800°C and 900°C, the reduced Cr diffusional flux towards the reaction front, especially in the σ phase, leads to the formation of a non-protective $CoO/CoCr_2O_4$ scale. Moreover, the Cr_2O_3 scales formed on alloy Co-17Re-25Cr-2Si at 1000°C and 1100°C exhibit an unsatisfactory spallation behavior.

The experimental results clearly demonstrate that the addition of 0.1% Y to alloy Co-17Re-25Cr-2Si significantly facilitates the formation of chromia scale even at a lower temperature (900°C). Most importantly, the small Y alloy concentration tremendously enhances the adhesion of the Cr_2O_3 scale formed, manifesting itself most strongly under thermocyclic conditions.

In all Co-Re-base alloys investigated, the primary σ phase always shows inferior oxidation performance. By adding Ni, it is possible to avoid to a large extent the coarse, primary σ-precipitates so that only the much finer, secondary precipitation takes place during the corresponding heat treatment of a high-temperature exposure. A 15% Ni addition to alloy Co-17Re-23Cr is not only beneficial for the mechanical properties but also improves the oxidation resistance significantly. Without the brittle coarse primary σ phase, short-peening treatment further facilitates the formation of chromia scale on alloy Co-17Re-23Cr-15Ni.

Perspectives

The development of Co-Re-base alloys has been just started several years ago, and there are still a limited number of publications on this relatively unknown alloy system. In terms of oxidation behavior, the present work fundamentally studied the formation of the three most effective oxides with respect to their capability to establish protective scales on Co-Re-base alloys. It has been proved that silica is not a suitable solution for the system. Although a chromia scale turned out to be very promising for applications at intermediate temperatures, there are still some open questions or optimization potentials that need to be further investigated, including but not limited to the following:

- Can the Ni content be further optimized in such a way that the Cr concentration can be reduced? (This topic forms the basis for the Ph.D. work conducted by Esleben [136].)

- What is the exact mechanism of the positive Y addition? Can the Y content be further optimized? What about other RE?

- Can the positive Si and Y effects be transferred to the Co-Re-Cr-Ni alloys? (This topic is also addressed in the Ph.D. thesis of Esleben [136].)

- Can the grain size of the Co-Re-Cr-Ni alloys be metallurgically modified (i.e., reduced) for an increased Cr transport towards the surface?

- What is the influence of the internal oxidation and phase transformation beneath the scale on the mechanical properties of the alloy, particularly under thermomechanical cyclic conditions?

As the target application temperature of the Co-Re-base alloys is 1200°C and more, it is necessary to investigate further the possibility of the alumina scale formation on the Co-Re-base alloys. Based on the results of this work, some possible strategies for a further development in this direction can be stated as follows:

- Reduction of the Cr content in alloy Co-17Re-23Cr-10Al to decrease the size and amount of the coarse primary σ phase.

- Examine the Ni-effect in the Co-Re-Cr-Al alloys towards promoting Al_2O_3 scale formation.

- Minor addition of elements with higher oxygen affinity, such as Y (Figure 7.1), to promote the selective oxidation of Al and improve the adhesion of the oxide scale formed.

- Minor addition of elements with higher nitrogen affinity than Al, such as Ti (Figure 5.16), to bind the inwardly diffusing nitrogen from the environment, avoid the internal AlN precipitation and, thus, promote the formation of a continuous and protective alumina external scale at elevated temperatures.
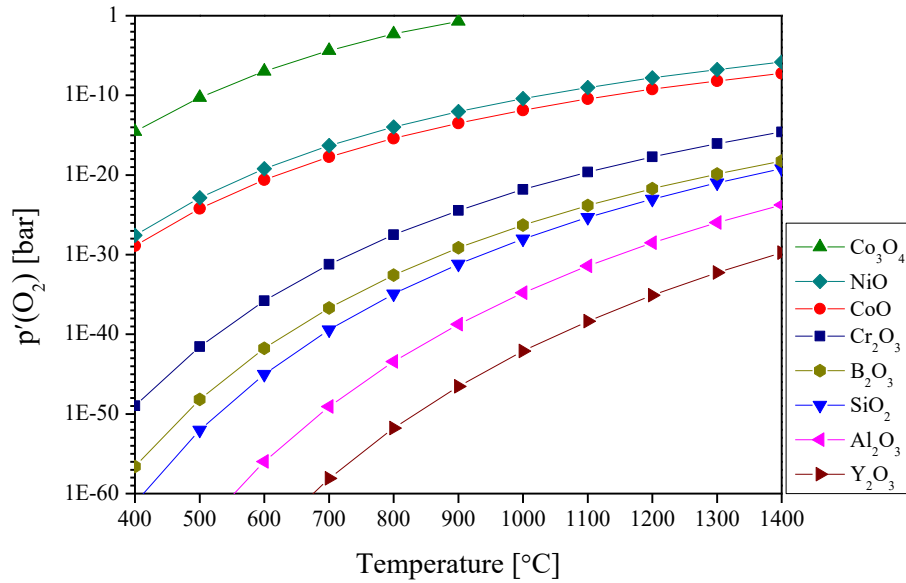
Figure 7.1: Equilibrium oxygen partial pressure of the essential oxides in the Co-Re system

References

1. J.H. Perepezko, The Hotter the Engine, the Better, Science 326 (2009) 1068-1069.

2. A. Kracke, Superalloys, the Most Successful Alloy System of Modern Times-Past, Present, and Future, in: E.A. Ott, J.R. Groh, A. Banik, I. Dempster, T.P. Gabb, R. Helmink, X. Liu, A. Mitchell, G.P. Sjöberg, A. Wusatowska-Sarnek (Eds.) Superalloy 718 and Derivatives, John Wiley & Sons, Boston, 2010, pp. 13-50.

3. D.G. Backman, J.C. Williams, Advanced Materials for Aircraft Engine Applications, Science 255 (1992) 1082-1087.

4. B.H. Kear, E.R. Thompson, Aircraft Gas Turbine Materials and Processes, Science 208 (1980) 847-856.

5. T.M. Pollock, S. Tin, Nickel-Based Superalloys for Advanced Turbine Engines: Chemistry, Microstructure and Properties, J. Propul. Power 22 (2006) 361-374.

6. Y. Koizumi, T. Kobayashi, T. Yokokawa, J. Zhang, M. Osawa, H. Harada, Y. Aoki, M. Arai, Development of Next-Generation Ni-Base Single Crystal Superalloys, in: K.A. Green, T.M. Pollock, H. Harada (Eds.) Superalloys 2004, TMS, Warrendale, 2004, pp. 35-43.

7. Rolls-Royce Website, cited in 2020, available from: https://www.rolls-royce.com/products-and-services/civil-aerospace/airlines/trent-800.

8. M. Kushan, S. Çevik, Y. Uzunonat, S. Diltemiz, ALLVAC 718 Plus Superalloy for Aircraft Engine Applications, in: A. Agarwal (Ed.) Recent advances in aircraft technology, InTech, Rijeka, 2012, pp. 75-96.

9. Y. Takebe, T. Yokokawa, T. Kobayashi, K. Kawagishi, H. Harada, C. Masuda, Effect of Ir on the Microstructural Stability of the 6th Generation Ni-Base Single Crystal Superalloy TMS-238, J. Jpn. Inst. Met. Mater. 79 (2015) 227-231.

10. H. Long, S. Mao, Y. Liu, Z. Zhang, X. Han, Microstructural and Compositional Design of Ni-Based Single Crystalline Superalloys-A Review, J. Alloys Compd. 743 (2018) 203-220.

11. K. Kawagishi, A.-C. Yeh, T. Yokokawa, T. Kobayashi, Y. Koizumi, H. Harada, Development of an Oxidation-Resistant High-Strength Sixth-Generation Single-Crystal Superalloy TMS-238, in: E.S. Huron, R.C. Reed, M.C. Hardy, M.J. Mills, R.E. Montero, P.D. Portella, J. Telesman (Eds.) Superalloys 2012, Wiley, Hoboken, 2012, pp. 189-195.

12. P. Tsakiropoulos, Beyond Nickel Based Superalloys, in: R. Blockley, W. Shyy (Eds.) Encyclopedia of Aerospace Engineering, John Wiley & Sons, Hoboken, 2010.

13. D. Young, High Temperature Oxidation and Corrosion of Metals, Elsevier, Oxford, 2016.

14. S. Vorberg, M. Wenderoth, B. Fischer, U. Glatzel, R. Völkl, Pt-Al-Cr-Ni Superalloys: Heat Treatment and Microstructure, JOM 56 (2004) 40-43.

15. Y. Yamabe-Mitarai, Y. Ro, H. Harada, T. Maruko, Ir-Base Refractory Superalloys for Ultra-High Temperatures, Metall. Mater. Trans. A 29 (1998) 537-549.

16. Y. Yamabe-Mitarai, Y. Koizumi, H. Murakami, Y. Ro, T. Maruko, H. Harada, Rh-Base Refractory Superalloys for Ultra-high Temperature Use, Scripta Mater. 36 (1997) 393-398.

17. B.P. Bewlay, M.R. Jackson, P.R. Subramanian, J.C. Zhao, A Review of Very-High-Temperature Nb-Silicide-Based Composites, Metall. Mater. Trans. A 34 (2003) 2043-2052.

18. S. Burk, B. Gorr, V.B. Trindade, H.-J. Christ, Effect of Zr Addition on the High-Temperature Oxidation Behaviour of Mo-Si-B Alloys, Oxid. Met. 73 (2009) 163-181.

19. S. Majumdar, A. Kumar, D. Schliephake, H.-J. Christ, X. Jiang, M. Heilmaier, Microstructural and Micro-Mechanical Properties of Mo-Si-B Alloyed with Y and La, Mater. Sci. Eng., A 573 (2013) 257-263.

20. M. Azim, S. Burk, B. Gorr, H.-J. Christ, D. Schliephake, M. Heilmaier, R. Bornemann, P.H. Bolívar, Effect of Ti (Macro-) Alloying on the High-Temperature Oxidation Behavior of Ternary Mo-Si-B Alloys at 820-1300°C, Oxid. Met. 80 (2013) 231-242.

21. J. Schneibel, Beyond Nickel-Base Superalloys, in: M. Gupta, T.S. Srivatsan, C.Y.H. Lim, R.A. Varin (Eds.) Processing and Fabrication of Advanced Materials XIII, Stallion Press, Singapore, 2005, pp. 563-574.

22. Y. Yang, H. Bei, S. Chen, E.P. George, J. Tiley, Y.A. Chang, Effects of Ti, Zr, and Hf on the Phase Stability of Mo_ss+Mo$_3$Si+Mo$_5$SiB$_2$ Alloys at 1600°C, Acta Mater. 58 (2010) 541-548.

23. B.P. Bewlay, J.J. Lewandowksi, M.R. Jackson, Refractory Metal-Intermetallic In-Situ Composites for Aircraft Engines, JOM 49 (1997) 44-45.

24. B. Gorr, L. Wang, S. Burk, M. Azim, S. Majumdar, H.J. Christ, D. Mukherji, J. Rösler, D. Schliephake, M. Heilmaier, High-Temperature Oxidation Behavior of Mo-Si-B-Based and Co-Re-Cr-Based Alloys, Intermetallics 48 (2014) 34-43.

25. J. Rösler, D. Mukherji, T. Baranski, Co-Re-Based Alloys: A New Class of High Temperature Materials?, Adv. Eng. Mater. 9 (2007) 876-881.

26. B. Gorr, Hochtemperaturoxidationsuntersuchungen an Co-Re-Modelllegierungen zur Entwicklung einer technischen Legierung der ersten Generation, Doctoral Thesis, H.-J. Christ (Ed.) Siegener werkstoffkundliche Berichte, Vol. 2, Siegen, 2011.

27. B. Gorr, V.B. Trindade, S. Burk, H.-J. Christ, Oxidation Behaviour of Model Co-Re Alloys During Exposure to Laboratory Air at 1000°C, Corros. Eng. Sci. Technol. 44 (2009) 176-181.

28. B. Gorr, V. Trindade, S. Burk, H.-J. Christ, M. Klauke, D. Mukherji, J. Rösler, Oxidation Behaviour of Model Cobalt-Rhenium Alloys During Short-Term Exposure to Laboratory Air at Elevated Temperature, Oxid. Met. 71 (2009) 157-172.

29. B. Gorr, H.-J. Christ, High-Temperature Oxidation Behaviour of Co-Re-Cr-Based Alloys: Limitations and Ways to Improve, Adv. Mater. Res. (Switzerland) 278 (2011) 545-550.

30. B. Gorr, S. Burk, V.B. Trindade, H.-J. Christ, High-Temperature Oxidation Behaviour of Model Co-Re-Cr Alloys at Low Oxygen Partial Pressure, Mater. Corros. 61 (2010) 741-747.

31. B. Gorr, S. Burk, V.B. Trindade, H.-J. Christ, The Effect of Pre-Oxidation Treatment on the High-Temperature Oxidation of Co-Re-Cr Model Alloys at Laboratory Air, Oxid. Met. 74 (2010) 239-253.

32. B. Gorr, S. Burk, T. Depka, C. Somsen, H. Abu-Samra, H.-J. Christ, G. Eggeler, Effect of Si Addition on the Oxidation Resistance of Co-Re-Cr-alloys: Recent Attainments in the Development of Novel Alloys, Int. J. Mater. Res. 103 (2012) 24-30.

33. B. Gorr, S. Burk, H.J. Christ, The High-Temperature Oxidation Behavior of Co-Re-Cr-Based Alloys, JOM 63 (2011) 37-40.

34. N. Birks, G.H. Meier, F.S. Pettit, Introduction to the High Temperature Oxidation of Metals, Cambridge University Press, Cambridge, 2006.

35. H.J.T. Ellingham, Transactions and Communications, J. Soc. Chem. Ind. 63 (1944) 125-160.

36. F.D. Richardson, J.H.E. Jeffes, The Thermodynamics of Substances of Interest in Iron and Steel Making from 0°C to 2400°C: I-Oxides, J. Iron and Steel Inst. 160 (1948) 261.

37. University of Cambridge Website, cited in 2020, available from: http://www.doitpoms.ac.uk/tlplib/ellingham_diagrams/ellingham.php.

38. P.J. Spencer, A Brief History of CALPHAD, Calphad 32 (2008) 1-8.

39. G. Kostorz, Phase Transformations in Materials, WILEY-VCH Verlag, Weinheim, 2001.

40. B. Gorr, H.-J. Christ, D. Mukherji, J. Rösler, Thermodynamic Calculations in the Development of High-Temperature Co-Re-Based Alloys, J. Alloys Compd. 582 (2014) 50-58.

41. H. Mehrer, Diffusion in Solids: Fundamentals, Methods, Materials, Diffusion-Controlled Processes, Springer, Berlin, 2007.

42. W.D. Callister, D.G. Rethwisch, Fundamentals of Materials Science and Engineering: An Integrated Approach, Wiley, Hoboken, 2012.

43. P. Heitjans, J. Kärger, Diffusion in Condensed Matter: Methods, Materials, Models, Springer, Berlin, 2006.

44. H.V. Atkinson, A Review of The Role of Short-Circuit Diffusion in the Oxidation of Nickel, Chromium, and Nickel-Chromium Alloys, Oxid. Met. 24 (1985) 177-197.

45. G.R. Wallwork, The Oxidation of Alloys, Rep. Prog. Phys. 39 (1976) 401-485.

46. P. Kofstad, High-temperature Oxidation of Metals, Wiley, New York, 1966.

47. G.Y. Lai, High-Temperature Corrosion and Materials Applications, ASM International, Geauga, 2007.

48. B.A. Pint, Design Strategies for New Oxidation-Resistant High Temperature Alloys, in: W. Gao, Z. Li (Eds.) Developments in High Temperature Corrosion and Protection of Materials, Woodhead Publishing, Cambridge, 2008, pp. 398-432.

49. H. Hirata, K. Ogawa, Effect of Chromium Content on Loss of Creep Rupture Strength in the Heat Affected Zone of Heat-Resistant Ferritic Steel, Weld. Int. 19 (2005) 118-124.

50. P. Maziasz, B. Pint, J. Shingledecker, N. Evans, Y. Yamamoto, M. Library, E. Lara-Curzio, Advanced Alloys for Compact, High-Efficiency, High-Temperature Heat-Exchangers, Int. J. Hydrogen Energy 32 (2007) 3622-3630.

51. M.P. Brady, I.G. Wright, B. Gleeson, Alloy Design Strategies for Promoting Protective Oxide-Scale Formation, JOM 52 (2000) 16-21.

52. C. Wagner, Oxidation of Alloys Involving Noble Metals, J. Electrochem. Soc. 103 (1956) 571.

53. F. Gesmundo, F. Viani, Transition from Internal to External Oxidation for Binary Alloys in the Presence of an Outer Scale, Oxid. Met. 25 (1986) 269-282.

54. G.H. Meier, K. Jung, N. Mu, N.M. Yanar, F.S. Pettit, J. Pirón Abellán, T. Olszewski, L. Nieto Hierro, W.J. Quadakkers, G.R. Holcomb, Effect of Alloy Composition and Exposure Conditions on the Selective Oxidation Behavior of Ferritic Fe-Cr and Fe-Cr-X Alloys, Oxid. Met. 74 (2010) 319-340.

55. H.J. Grabke, E.M. Muller-Lorenz, S. Strauss, E. Pippel, J. Woltersdorf, Effects of Grain Size, Cold Working, and Surface Finish on the Metal-Dusting Resistance of Steels, Oxid. Met. 50 (1998) 241-254.

56. R. Naraparaju, H.-J. Christ, F.U. Renner, A. Kostka, Effect of Shot-Peening on the Oxidation Behaviour of Boiler Steels, Oxid. Met. 76 (2011) 233-245.

57. P. Berthod, Kinetics of High Temperature Oxidation and Chromia Volatilization for a Binary Ni-Cr Alloy, Oxid. Met. 64 (2005) 235-252.

58. D.J. Young, B.A. Pint, Chromium Volatilization Rates from Cr_2O_3 Scales into Flowing Gases Containing Water Vapor, Oxid. Met. 66 (2006) 137-153.

59. D.R. Sigler, Oxidation Behavior of Fe-20Cr-5Al Rare Earth Alloys in Air and Synthetic Exhaust Gas, Oxid. Met. 36 (1991) 57-80.

60. M. Bensch, J. Preußner, R. Hüttner, G. Obigodi, S. Virtanen, J. Gabel, U. Glatzel, Modelling and Analysis of the Oxidation Influence on Creep Behaviour of Thin-Walled Structures of the Single-Crystal Nickel-Base Superalloy René N5 at 980°C, Acta Mater. 58 (2010) 1607-1617.

61. U. Brill, J. Kloewer, Vergleichende Untersuchung des Oxidationsverhaltens der Werkstoffe Nicrofer 7216 H, 6023 H und 6025 HT, Metall 51 (1997) 263-266.

62. V.P. Deodeshmukh, S.J. Matthews, D.L. Klarstrom, High-Temperature Oxidation Performance of a New Alumina-Forming Ni-Fe-Cr-Al Alloy in Flowing Air, Int. J. Hydrogen Energy 36 (2011) 4580-4587.

63. R. Prescott, M.J. Graham, The Formation of Aluminum Oxide Scales on High-Temperature Alloys, Oxid. Met. 38 (1992) 233-254.

64. W.J. Quadakkers, K. Bongartz, The Prediction of Breakaway Oxidation for Alumina Forming ODS Alloys Using Oxidation Diagrams, Mater. Corros. 45 (1994) 232-241.

65. D.P. Whittle, J. Stringer, Improvements in High Temperature Oxidation Resistance by Additions of Reactive Elements or Oxide Dispersions, Philos. Trans. R. Soc. London, Ser. A 295 (1980) 309-329.

66. R. Cueff, H. Buscail, E. Caudron, C. Issartel, F. Riffard, Influence of Yttrium-Alloying Addition on the Oxidation of Alumina Formers at 1173 K, Oxid. Met. 58 (2002) 439-455.

67. T.J. Nijdam, W.G. Sloof, Effect of Y Distribution on the Oxidation Kinetics of NiCoCrAlY Bond Coat Alloys, Oxid. Met. 69 (2007) 1-12.

68. Y. Wu, S.K. Hwang, S.W. Nam, N.J. Kim, The Effect of Yttrium Addition on the Oxidation Resistance of EPM TiAl-Based Intermetallics, Scripta Mater. 48 (2003) 1655-1660.

69. P.Y. Hou, J. Stringer, The Influence of Ion-Implanted Yttrium on the Selective Oxidation of Chromium in Co-25 wt.% Cr, Oxid. Met. 29 (1988) 45-73.

70. P.Y. Hou, J. Stringer, The Effect of Reactive Element Additions on the Selective Oxidation, Growth and Adhesion of Chromia Scales, Mater. Sci. Eng., A 202 (1995) 1-10.

71. D.G. Lees, On the Reasons for the Effects of Dispersions of Stable Oxides and Additions of Reactive Elements on the Adhesion and Growth-Mechanisms of Chromia and Alumina Scales-the "Sulfur Effect", Oxid. Met. 27 (1987) 75-81.

72. C. Mennicke, E. Schumann, C. Ulrich, M. Rühle, The Effect of Yttrium and Sulfur on the Oxidation of FeCrAl, Mater. Sci. Forum 251-254 (1997) 389-396.

73. T.A. Ramanarayanan, R. Ayer, R. Petkovic-Luton, D.P. Leta, The Influence of Yttrium on Oxide Scale Growth and Adherence, Oxid. Met. 29 (1988) 445-472.

74. J. Stringer, The Reactive Element Effect in High-Temperature Corrosion, Mater. Sci. Eng., A 120 (1989) 129-137.

75. D. Coutsouradis, A. Davin, M. Lamberigts, Cobalt-Based Superalloys for Applications in Gas Turbines, Mater. Sci. Eng. 88 (1987) 11-19.

76. J. Sato, T. Omori, K. Oikawa, I. Ohnuma, R. Kainuma, K. Ishida, Cobalt-Base High-Temperature Alloys, Science 312 (2006) 90-91.

77. A. Suzuki, T.M. Pollock, High-Temperature Strength and Deformation of $\gamma / \gamma '$ Two-phase Co-Al-W-base Alloys, Acta Mater. 56 (2008) 1288-1297.

78. R.C. Reed, The Superalloys: Fundamentals and Applications, Cambridge University Press, Cambridge, 2006.

79. P. Caron, T. Khan, Evolution of Ni-Based Superalloys for Single Crystal Gas Turbine Blade Applications, Aerosp. Sci. Technol. 3 (1999) 513-523.

80. M. Huang, J. Zhu, An Overview of Rhenium Effect in Single-Crystal Superalloys, Rare Met. 35 (2016) 127-139.

81. W.S. Walston, J.C. Schaeffer, W.H. Murphy, A New Type of Microstructural Instability in Superalloys-SRZ, in: R.D. Kissinger, D.J. Deye, D. L. Anton, A.D. Cetel, M.V. Nathal, T.M. Pollock, D.A. Woodford (Eds.) Superalloys 1996, TMS, Warrendale, 1996, pp. 9-18.

82. D. Mukherji, R. Gilles, L. Karge, P. Strunz, P. Beran, H. Eckerlebe, A. Stark, L. Szentmiklosi, Z. Mácsik, G. Schumacher, I. Zizak, M. Hofmann, M. Hoelzel, J. Rösler, Neutron and Synchrotron Probes in the Development of Co-Re-Based Alloys for Next Generation Gas Turbines with An Emphasis on the Influence of Boron Additives, J. Appl. Crystallogr. 47 (2014) 1417-1430.

83. K. Przybylski, D. Szwagierczak, Kinetics and Mechanism of High-temperature Oxidation of Dilute Cobalt-Chromium Alloys, Oxid. Met. 17 (1982) 267-295.

84. D. Mukherji, J. Rosler, J. Wehrs, H. Eckerlebe, R. Gilles, Co-Re-based Alloys: a New Class of Material for Gas Turbine Applications at very High Temperatures, Adv. Mater. Res. (Korea) 1 (2012) 205-219.

85. D. Mukherji, J. Rösler, Design Considerations and Strengthening Mechanisms in Developing Co-Re-Based Alloys for Applications at +100°C above Ni-Superalloys, Adv. Mater. Res. (Switzerland) 278 (2011) 539-544.

86. T. Depka, C. Somsen, G. Eggeler, D. Mukherji, J. Rösler, M. Krüger, H. Saage, M. Heilmaier, Microstructures of Co-Re-Cr, Mo-Si and Mo-Si-B High-Temperature Alloys, Mater. Sci. Eng., A 510-511 (2009) 337-341.

87. T. Depka, C. Somsen, G. Eggeler, D. Mukherji, J. Rösler, Sigma Phase Evolution in Co-Re-Cr-based Alloys at 1100 °C, Intermetallics 48 (2014) 54-61.

88. D. Mukherji, J. Rösler, P. Strunz, R. Grilles, G. Schumacher, S. Piegert, Beyond Ni-based Superalloys: Development of CoRe-based Alloys for Gas Turbine Application at very High Temperatures, Int. J. Mater. Res. 102 (2011) 1125-1132.

89. M. Heilmaier, M. Krüger, H. Saage, J. Rösler, D. Mukherji, U. Glatzel, R. Völkl, R. Hüttner, G. Eggeler, C. Somsen, T. Depka, H.-J. Christ, B. Gorr, S. Burk, Metallic Materials for Structural Applications Beyond Nickel-Based Superalloys, JOM 61 (2009) 61-67.

90. D. Mukherji, J. Rösler, Co-Re-based Alloys for High Temperature Applications: Design Considerations and Strengthening Mechanisms, J. Phys. Conf. Ser. 240 (2010) 012066.

91. M. Brunner, R. Hüttner, M.-C. Bölitz, R. Völkl, D. Mukherji, J. Rösler, T. Depka, C. Somsen, G. Eggeler, U. Glatzel, Creep Properties Beyond 1100°C and Microstructure of Co-Re-Cr Alloys, Mater. Sci. Eng., A 528 (2010) 650-656.

92. D. Mukherji, P. Strunz, R. Gilles, L. Karge, J. Rösler, Current Status of Co-Re-Based Alloys being Developed to Supplement Ni-Based Superalloys for Ultra-High Temperature Applications in Gas Turbines, Kovove Mater. 53 (2015) 287-294.

93. D. Mukherji, J. Rösler, M. Krüger, M. Heilmaier, M.C. Bölitz, R. Völkl, U. Glatzel, L. Szentmiklósi, The Effects of Boron Addition on the Microstructure and Mechanical Properties of Co-Re-Based High-Temperature Alloys, Scripta Mater. 66 (2012) 60-63.

94. T.C. Chou, A. Joshi, C.M. Packer, Oxidation Behavior of Rhenium at High Temperatures, Scr. Metall. Mater. 28 (1993) 1565-1570.

95. R. Durham, B. Gleeson, D.J. Young, Silicon Contamination Effects in the Oxidation of Carbide-Containing Cobalt-Chromium Alloys, Mater. Corros. 49 (1998) 855-863.

96. P.Y. Hou, J. Stringer, Effect of Internal Oxidation Pretreatments and Si Contamination on Oxide-Scale Growth and Spalling, Oxid. Met. 33 (1990) 357-369.

97. D.E. Jones, J. Stringer, The Effect of Small Amounts of Silicon on the Oxidation of High-Purity Co-25 wt. % Cr at Elevated Temperatures, Oxid. Met. 9 (1975) 409-413.

98. B. Li, B. Gleeson, Effects of Silicon on the Oxidation Behavior of Ni-Base Chromia-Forming Alloys, Oxid. Met. 65 (2006) 101-122.

99. Y. Liu, W. Wei, L. Benum, M. Oballa, M. Gyorffy, W. Chen, Oxidation Behavior of Ni-Cr-Fe-Based Alloys: Effect of Alloy Microstructure and Silicon Content, Oxid. Met. 73 (2009) 207-218.

100. S. Uran, B. Veal, M. Grimsditch, J. Pearson, A. Berger, Effect of Surface Roughness on Oxidation: Changes in Scale Thickness, Composition, and Residual Stress, Oxid. Met. 54 (2000) 73-85.

101. FactSage-Teach Website, cited in 2020, available from: https://gtt-technologies.de/software/factsage/teach/.

102. D.L. Douglass, J.S. Armijo, The Effect of Silicon and Manganese on the Oxidation Mechanism of Ni-20 Cr, Oxid. Met. 2 (1970) 207-231.

103. H.E. Evans, D.A. Hilton, R.A. Holm, S.J. Webster, Influence of Silicon Additions on the Oxidation Resistance of a Stainless Steel, Oxid. Met. 19 (1983) 1-18.

104. S. Burk, Hochtemperaturoxidation molybdän-basierter Legierungen unter Berücksichtigung von Einflüssen aus Umgebungsatmosphäre und legierungstechnischen Maßnahmen, Doctoral Thesis, H.-J. Christ (Ed.) Siegener werkstoffkundliche Berichte, Vol. 1, Siegen, 2011.

105. L.T.F. Eleno, C. Geraldo Schön, CVM Calculation of the b.c.c. Co-Cr-Al Phase Diagram, Calphad 27 (2003) 335-342.

106. F.H. Stott, G.C. Wood, Internal Oxidation, Mater. Sci. Technol. 4 (1988) 1072-1078.

107. S.Y. Chang, U. Krupp, H.-J. Christ, Formation and Compensation of Internal Stresses During Internal Nitridation of Nickel-base Alloys, Mater. Sci. Eng., A 301 (2001) 196-206.

108. K. Taneichi, T. Narushima, Y. Iguchi, C. Ouchi, Oxidation or Nitridation Behavior of Pure Chromium and Chromium Alloys Containing 10 mass% Ni or Fe in Atmospheric Heating, Mater. Trans. 47 (2006) 2540-2546.

109. C. Geers, V. Babic, N. Mortazavi, M. Halvarsson, B. Jönsson, L.-G. Johansson, I. Panas, J.-E. Svensson, Properties of Alumina/Chromia Scales in N_2-Containing Low Oxygen Activity Environment Investigated by Experiment and Theory, Oxid. Met. 87 (2017) 321-332.

110. J. Litz, A. Rahmel, M. Schorr, Selective Carbide Oxidation and Internal Nitridation of the Ni-Base Superalloys IN 738 LC and IN 939 in Air, Oxid. Met. 30 (1988) 95-105.

111. L. Wang, B. Gorr, H.-J. Christ, D. Mukherji, J. Rösler, Optimization of Cr-Content for High-Temperature Oxidation Behavior of Co-Re-Si-Base Alloys, Oxid. Met. 80 (2013) 49-59.

112. S. Espevik, R.A. Rapp, P.L. Daniel, J.P. Hirth, Oxidation of Ternary Co-Cr-W Alloys, Oxid. Met. 20 (1983) 37-65.

113. I.G. Wright, G.C. Wood, The Isothermal Oxidation of Co-Cr Alloys in 760 Torr Oxygen at 1000°C, Oxid. Met. 11 (1977) 163-191.

114. P.K. Kofstad, A.Z. Hed, Oxidation of Co-10 w/o Cr Interrupted by Vacuum Annealing, Oxid. Met. 2 (1970) 101-117.

115. G.C. Wood, I.G. Wright, T. Hodgkiess, D.P. Whittle, A Comparison of the Oxidation of Fe-Cr, Ni-Cr and Co-Cr Alloys in Oxygen and Water Vapour, Mater. Corros./Werkst. Korros. 21 (1970) 900-910.

116. T. Biegun, A. Brückman, S. Mrowec, High-temperature Sulfide Corrosion of Cobalt-Chromium Alloys, Oxid. Met. 12 (1978) 157-172.

117. E.M. Fryt, G.C. Wood, F.H. Stott, D.P. Whittle, Influence of Prior Internal Oxidation on the Oxidation of Dilute Co-Cr Alloys in Oxygen, Oxid. Met. 23 (1985) 77-106.

118. P.K. Kofstad, A.Z. Hed, On the Oxidation of Co-35 w% Cr at High Temperatures, Mater. Corros./Werkst. Korros. 21 (1970) 894-899.

119. L. Wang, B. Gorr, H.J. Christ, D. Mukherji, J. Rösler, Microstructure and Oxidation Mechanism Evolution of Co-17Re-25Cr-2Si in the Temperature Range 800-1100 °C, Oxid. Met. 83 (2015) 465-483.

120. J.W. Weeton, Diffusion of Chromium in Alpha Cobalt-Chromium Solid Solutions, U. S. Government Printing Office, Washington, D.C, 1951.

121. M. Skeldon, J.M. Calvert, D.G. Lees, An Investigation of the Growth-Mechanism of Cr_2O_3 on Pure Chromium in 1 atm Oxygen at 950°C, Oxid. Met. 28 (1987) 109-125.

122. W.T. Griffiths, L.B. Pfeil, Improvement in Heat-Resisting Alloys, U.K. Patent Number 459848, 1937.

123. P.Y. Hou, J. Ager, J. Mougin, A. Galerie, Limitations and Advantages of Raman Spectroscopy for the Determination of Oxidation Stresses, Oxid. Met. 75 (2011) 229-245.

124. R. Swadźba, L. Swadźba, J. Wiedermann, M. Hetmańczyk, B. Witala, Characterization of Alumina Scales Grown on a 2nd Generation Single Crystal Ni Superalloy During Isothermal Oxidation at 1050, 1100 and 1150 °C, Oxid. Met. 82 (2014) 195-208.

125. B.A. Pint, Optimization of Reactive-Element Additions to Improve Oxidation Performance of Alumina-Forming Alloys, J. Am. Ceram. Soc. 86 (2003) 686-695.

126. J. Klöwer, Factors Affecting the Oxidation Behaviour of Thin Fe-Cr-Al foils. Part II: The Effect of Alloying Elements: Overdoping, Mater. Corros. 51 (2000) 373-385.

127. J.G. Smeggil, Some Comments on the Role of Yttrium in Protective Oxide Scale Adherence, Mater. Sci. Eng. 87 (1987) 261-265.

128. D. Naumenko, B.A. Pint, W.J. Quadakkers, Current Thoughts on Reactive Element Effects in Alumina-Forming Systems: In Memory of John Stringer, Oxid. Met. 86 (2016) 1-43.

129. L. Wang, B. Gorr, H.-J. Christ, D. Mukherji, J. Rösler, The Effect of Alloyed Nickel on the Short-Term High Temperature Oxidation Behaviour of Co-Re-Cr-based Alloys, Corros. Sci. 93 (2015) 19-26.

130. B. Chattopadhyay, G.C. Wood, The Transient Oxidation of Alloys, Oxid. Met. 2 (1970) 373-399.

131. E. Azim, Untersuchung des Einflusses der Oberflächenbehandlung mittels Kugelstrahlen auf das Oxidationsverhalten von Cobalt-Rhenium-Basislegierungen, Master Thesis, University of Siegen, Siegen, 2012.

132. J.S. Kirkaldy, D.J. Young, Diffusion in the Condensed State, Institute of Metals, London, 1987.

133. K. Hirano, R.P. Agarwala, B.L. Averbach, M. Cohen, Diffusion in Cobalt-Nickel Alloys, J. Appl. Phys. 33 (1962) 3049-3054.

134. A. Green, D.P. Whittle, J. Stringer, N. Swindells, Interdiffusion in the Cobalt-Chromium System, Scr. Metall. 7 (1973) 1079-1082.

135. Y. Minamino, Y. Koizumi, N. Tsuji, T. Yamada, T. Takahashi, Interdiffusion in Co Solid Solutions of Co-Al-Cr-Ni System at 1423 K, Mater. Trans. 44 (2003) 63-71.

136. K. Esleben, Erforschung des Einflusses von Nickel, Silizium und Yttrium auf die Mikrostruktur und das Hochtemperaturoxidationsverhalten von Co-Re-Cr-Legierungen, Doctoral Thesis, H.-J. Christ (Ed.) Siegener werkstoffkundliche Berichte, Vol. 26, Siegen, 2020.

137. J.J. Stiglich, J.B. Cohen, D.H. Whitmore, Interdiffusion in CoO-NiO Solid Solutions, J. Am. Ceram. Soc. 56 (1973) 119-126.